A Study of the Expansion of a Laser Produced Lithium Plasma using Spatially and Temporally Resolved Imaging and Spectroscopic Techniques.

A Thesis for the Degree of
Doctor of Philosophy

By

William Whitty, B.Sc.

School of Physical Sciences
Dublin City University.

Research Supervisor

Dr. Jean-Paul Mosnier
September 1998.

To the memory of John

(8th August 1996)

Declaration

I hereby certify that this material, which I now submit for assessment on the programme of study leading to the award of Doctor of Philosophy, is entirely my own work and has not been taken from the work of others save and to the extent that such work has been cited and acknowledged within the text of my work.

Signature: _Willi Whatt_   ID No.:   93701349

Date: _28/9/98_

Introduction

The development of three diagnostic techniques, and their application to the quantitative analysis of a laser produced lithium plasma is described. Two of the diagnostic techniques, the fast-frame photography technique and the shadowgraph technique, are new to the Centre for Laser Plasma Research laboratory, while a novel approach to the analysis of the results of the established Dual Laser Plasma (DLP) photoabsorption technique is also presented. The organisation of the thesis is as follows: Chapter 1 introduces the theory of the creation and expansion of a laser produced plasma both in vacuum and in a gaseous environment. The emission or absorption of radiation by a plasma is also outlined, leading to a solution to the equation of radiative transfer. Finally, theoretical aspects of the experimental procedures used during the course of this work are described. Chapter 2 outlines the three experimental set-ups used during this study. Fast-frame images, shadowgraphs and extreme ultraviolet (EUV) photoabsorption spectra of an expanding lithium plasma are presented. Chapter 3 is concerned with the quantitative analysis and discussion of the results presented in chapter 2 using the plasma models developed in chapter 1. Finally, suggestions for future work are presented. SI units are used throughout this thesis, unless explicitly stated otherwise.

Table Of Contents

Chapter 2   Experimental and Results

Chapter 3   Analysis and Discussion

Conclusions and Suggestions for Future Work   153

References   155

Appendices

Acknowledgements

I would also like to take this opportunity to thank Prof. Eugene Kennedy and Dr. James Lunney for their useful suggestions upon proof reading this thesis.

Finally, I wish to express my sincerest thanks to my parents and to my sister (who would most modestly admit to "teaching me everything I know"). Their support both financial and otherwise will always be remembered.

Abstract

The study of the expansion of a laser produced lithium plasma using spatially and temporally resolved imaging and spectroscopic diagnostic techniques is described. The diagnostic system consists of three separate components: a 2.2m grazing incidence spectrometer (coupled to an Extreme Ultra-Violet (EUV) sensitive photodiode array), a recently developed fast-frame photography apparatus comprising a CCD camera coupled to a gated image intensifier, and a newly developed shadowgraphy apparatus consisting of a combination of a Nd:YAG pumped dye laser and a CCD camera. The development and capabilities of the diagnostic techniques used to characterise the plasma expansion are outlined. Furthermore, the characterisation of new or additional instrumental parameters pertinent to the quantitative interpretation of the experimental data is explored.

Using the 2.2m grazing incidence spectrometer, temperature and density profile estimates for a laser produced lithium plasma are inferred. Photoabsorption spectra using this instrument and a newly developed model, for the $1s^2 \rightarrow 1snp$ (n = 4,5,6 and 7) in Li^+, are synthesised for the first time. Employing the fast-frame photography technique, species velocities and corresponding temperature estimates are obtained. Additionally, excited state density distributions are extracted by application of the Abel transform. Finally, the shadowgraph technique is used to furnish electron density distribution information. In all cases plasma parameters, determined using the diagnostic techniques proposed, are correlated with novel computer codes developed, based on established plasma expansion models.

The thesis concludes with a description of future work with an emphasis on prospective extensions to the diagnostic techniques developed.

Chapter 1

This chapter first introduces the theory of the creation and expansion of a laser produced-plasma (LPP) by a nanosecond pulsed laser on a planar metallic surface, both in vacuum and in gaseous environments. Second, the formation and broadening of spectral lines is discussed and a solution to the equation of radiative transfer is developed. Finally, theoretical aspects of the experimental methods used during the course of this work are outlined.

1.1 The Interaction of High Powered Radiation with Metals – The Creation of a Laser Produced Plasma (LPP)

When the output of an intense beam of Q-switched laser radiation (typically 1 J, 10 ns) is focussed onto a solid metal target, a hot dense plasma is formed. The sequence of interactions ultimately leading to plasma formation are complex and manifold. Initially, a certain fraction of the incident laser light is reflected from the target surface. In the case of a lithium target irradiated at normal incidence with a Nd:YAG (1.064 μm) laser, ~95% of the incident light is reflected [1]. The remainder is usually absorbed by electrons in the conduction band, which are consequently raised to higher energy states. Momentum balance is maintained by collisions with other electrons and with phonons. Through electron-phonon interaction, the absorbed energy is transferred, in part, to the motion of the atoms or ions making up the metallic lattice. In this manner the solid tends to reach equilibrium at a higher temperature. Typical transfer times between hot electrons and the lattice are of the order of 10^{-12} to 10^{-13} s for most solids

1

[2][3]. The initial interaction between the laser radiation and the solid takes place over a very thin surface layer referred to as the skin depth, δ, given by [4]

$$\delta = \left(\pi \nu \mu_o \sigma'\right)^{-\frac{1}{2}} \qquad [1.1]$$

In the case of lithium having a conductivity, $\sigma' = 1.076 \times 10^7$ mhos m^{-1} [5] irradiated with a Nd:YAG laser of frequency, $\nu = 2.818 \times 10^{14}$ Hz, the corresponding skin depth $\delta \approx 9$ nm. It is within this thin layer that the initial heat production takes place. Thermal conduction will carry the heat deeper into the metal to a penetration depth, δ', typically of the order of

$$\delta' \cong \sqrt{\kappa_D t_p} \qquad [1.2]$$

[3], where κ_D is the thermal diffusivity, and t_p is the duration (FWHM) of the laser pulse. The penetration depth for a Nd:YAG laser ($t_p = 15$ ns) incident on a lithium target ($\kappa_D = 4.5 \times 10^{-5}$ m^2 s^{-1} [5]) is ≈ 1 μm.

In general three laser irradiance regimes can loosely be defined [3]. These constitute the low ($I < 10^{10}$ W m^{-2}), the medium (10^{10} W m$^{-2} < I < 10^{16}$ W m^{-2}) and the high ($I > 10^{16}$ W m^{-2}) irradiance regimes. The limiting irradiances in each case are dependent upon, for example, the wavelength of the laser and the target material chosen [6]. In the low irradiance regime ($I < 10^{10}$ W m^{-2}) thermal processes can give rise to a heating of the solid by conduction leading to a possible change of phase of the metal. This regime generally finds application in a diverse number of fields ranging from optical data storage to laser treatment, cutting and welding. Due to the short relaxation times involved reasonably accurate calculations can be performed using a single (averaged) value for the thermal conductivity and other material parameters [2]. As the laser spot size is generally orders of magnitude greater than the penetration depth, the temperature rise at the surface of the material can be estimated from a classical one-dimensional thermodynamic formalism, i.e.

$$\sqrt{\kappa_D t_p} \rho_o C\left(T - T_o\right) \approx \left(1 - R\right) I t_p \qquad [1.3]$$

2

[3], where ρ_o is the target material density, C is the specific heat, T and T_o are the final and initial temperatures at the surface respectively, R is the reflectance, and I is the incident intensity of the laser. Using typical parameters for lithium [5], coupled with a reflectance of 95%, one estimates that an irradiance of ~10^{11} W m^{-2} is required to heat the metal surface to its boiling point (1615 K [5]) from room temperature. This simplified calculation assumes that losses through re-radiation and convection are negligible. It also neglects the dependence of material parameters, and in particular reflectance, on temperature.

The second regime to be considered is that of high irradiance (I > 10^{15} W m^{-2}). Here, ionisation takes place within the first few cycles of the incident electromagnetic radiation. The incident energy is quickly redistributed into thermal conduction and re-radiation. In this regime many models ignore the initial stages of plasma formation, since the energy required for melting and subsequent vaporisation is negligible compared to that required for ionisation and heating. The plasma is assumed to be uniformly 'cold' with initial electron and ion densities equal to the solid atom density [2]. In extreme cases (I > 10^{22} W m^{-2}) hole boring, due to the radiation pressure of the light beam, is a key feature of the interaction [7]. Generally however the irradiance is low enough so that the ablation pressure exceeds the radiation pressure by a factor of 10^4 or more [2]. The thin plasma vapour thus formed is sufficiently dense and ionised such that the laser light is significantly absorbed by the plasma, subsequently decoupling the laser radiation from the target surface. The main absorption mechanism is via Inverse Bremsstrahlung (IB) whereby electrons accelerated by the electric field of the focused laser light undergo momentum transfer collisions with ions via their Coulomb interaction. As the energy absorbed increases, so too does T_e, the electron temperature, and T_i, the ion temperature. Consequently this produces further ionisation through collisions, thus increasing the electron density still further until it eventually reaches a critical value N_{ec} at some distance from the target surface where N_{ec} is defined by [6]

$$N_{ec} = \frac{m_e n^2 \varepsilon_o \omega^2}{e^2} \cong \frac{10^{15}}{\lambda^2} \qquad \text{[1.4]}$$

3

Here n is the refractive index of the surrounding medium, and ω is the laser frequency (radians). The surface or narrow slab at which $N_e \approx N_{ec}$ is termed the deflagration zone. For a Nd:YAG laser $N_{ec} \approx 9.9 \times 10^{26}$ m^{-3}. Radiation will propagate into the plasma until at some depth it reaches the layer of critical density, whereupon the absorption coefficient for Inverse Bremsstrahlung tends towards infinity, i.e. $\kappa_\nu \rightarrow \infty$ [8][9], after which the wave becomes evanescent and is eventually reflected. Although laser radiation no longer reaches the target surface, plasma growth continues due to the heating of the layers in front of the critical density surface. The plasma is driven out from the target as a consequence of pressure gradients, causing a decrease in the electron density. As a result of momentum conservation, the deflagration front simultaneously moves rapidly into the target, driving before it a shock wave of even greater velocity [10]. Radiation can thus penetrate the plasma to reach the target surface again. These processes are schematically illustrated in fig. 1.1.
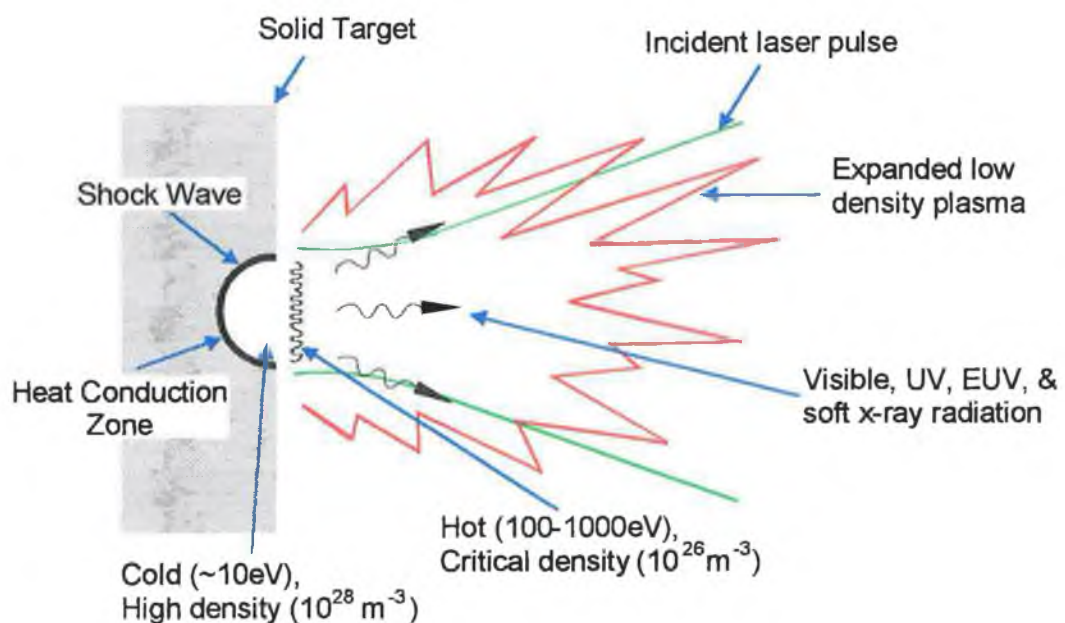
Fig. 1.1: A schematic representation of the creation of a laser produced plasma.

The final regime to be considered is that of medium irradiance (10^{10} W m^{-2} < I < 10^{16} W m^{-2}). Here, plasma effects become significant. One is concerned with the heating, melting and subsequent vaporisation and ionisation of the target material. The primary considerations are thus the dependence of the material properties on temperature and

pressure. Unlike plasma formation in the high irradiance regime, the free electron density in the plasma vapour is lower than the critical density and thus laser-target interaction is sustained throughout the duration of the pulse. The classical electron-ion Inverse Bremsstrahlung process may no longer be the sole mechanism by which laser radiation is absorbed by the plasma [11]. Other processes such as electron-atom Inverse Bremsstrahlung, direct photoionisation and neutral atom resonance absorption must be accounted for [11][12][13]. This irradiance regime is of general importance to materials processing applications, e.g. pulsed laser deposition (PLD) of thin superconducting films [14].

In the following sections plasma formation and expansion in the medium irradiance regime (10^{10} W m^{-2} < I < 10^{16} W m^{-2}) will be considered. This is based on the range of irradiances used to generate a lithium plume during the course of these experiments.

1.2   The Expansion of a Laser Produced Plasma

When a Q-switched laser is focused onto a solid metal target, the surface is heated to its melting temperature or higher on a time scale of 10^{-10} s or less. The result is a plasma plume that expands as a consequence of thermally induced pressure gradients, mainly along a direction normal to the target surface [15]. Expansion continues long after the laser pulse duration, lasting typically of the order of microseconds [16]. As the plasma expands the density and temperature rapidly decrease, with an adiabatic transfer of thermal energy into kinetic energy of expansion [17].

Two expansion regimes are considered in the following paragraphs. The first involves the free expansion of the plume in vacuum, while the second pertains to the expansion of the plasma in a gaseous environment.

1.2.1   The Expansion of a Laser Produced Plasma in Vacuum

The temperature decrease for a plasma generated on a planar target *in vacuo* as a result of plasma expansion can be described by the adiabatic relation [17][18]

$$T(r) \propto r^{-(\gamma-1)} \qquad \text{[1.5]}$$

where T(r) represents the plasma temperature as a function of the radial co-ordinate r, and γ is the ratio of specific heats. The spatial density distributions of the species comprising the plasma are also modified as a result of plume expansion. Assuming radial symmetry about the expansion axis (O_x), a conical annular structure, as depicted in fig. 1.2 for the case of a singly ionised lithium plasma, can be envisaged viz. ions of increasing charge are located closer to the front of the expanding plasma and closer to the expansion axis [19]. This structure was observed experimentally by Irons et al. [20] for a laser produced carbon plasma. The results are reproduced in fig. 1.3.
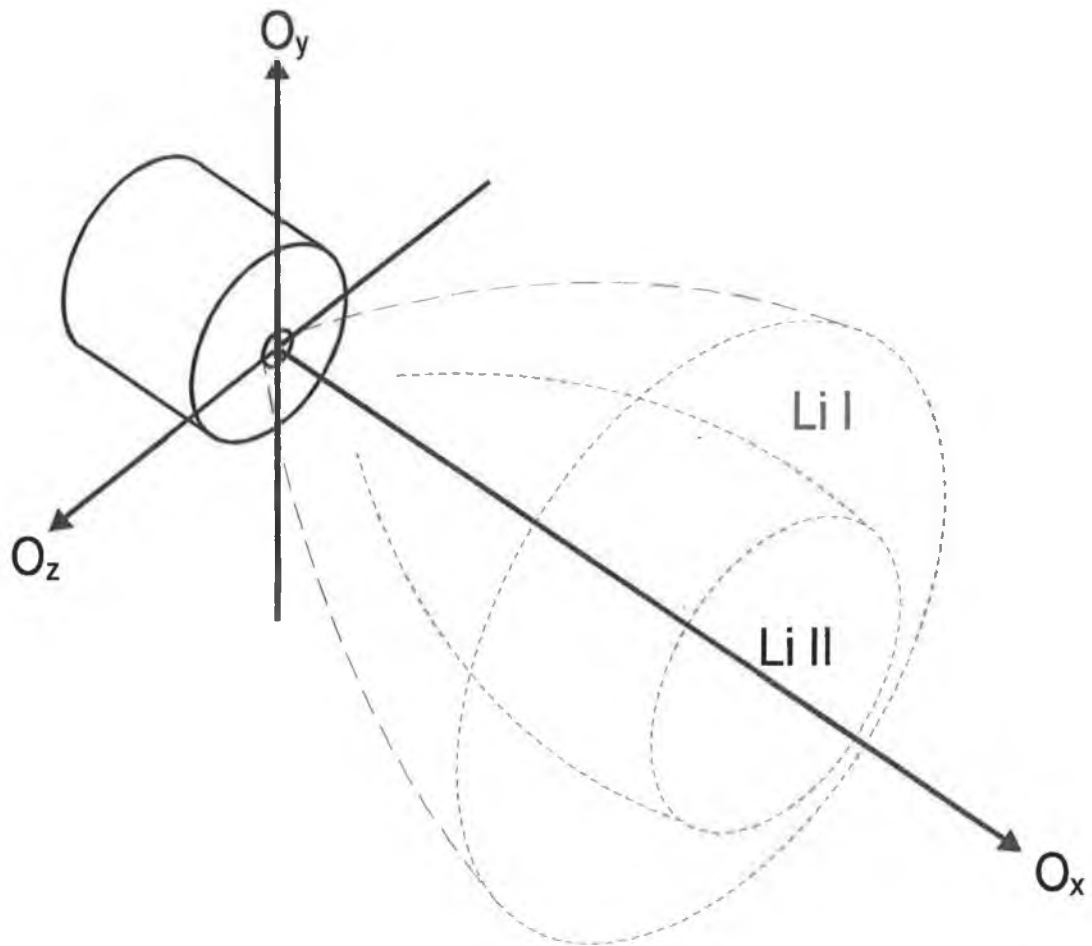

Fig. 1.2: An idealised picture of the spatial distribution of an expanding singly ionised laser produced lithium plasma in vacuum according to [20].
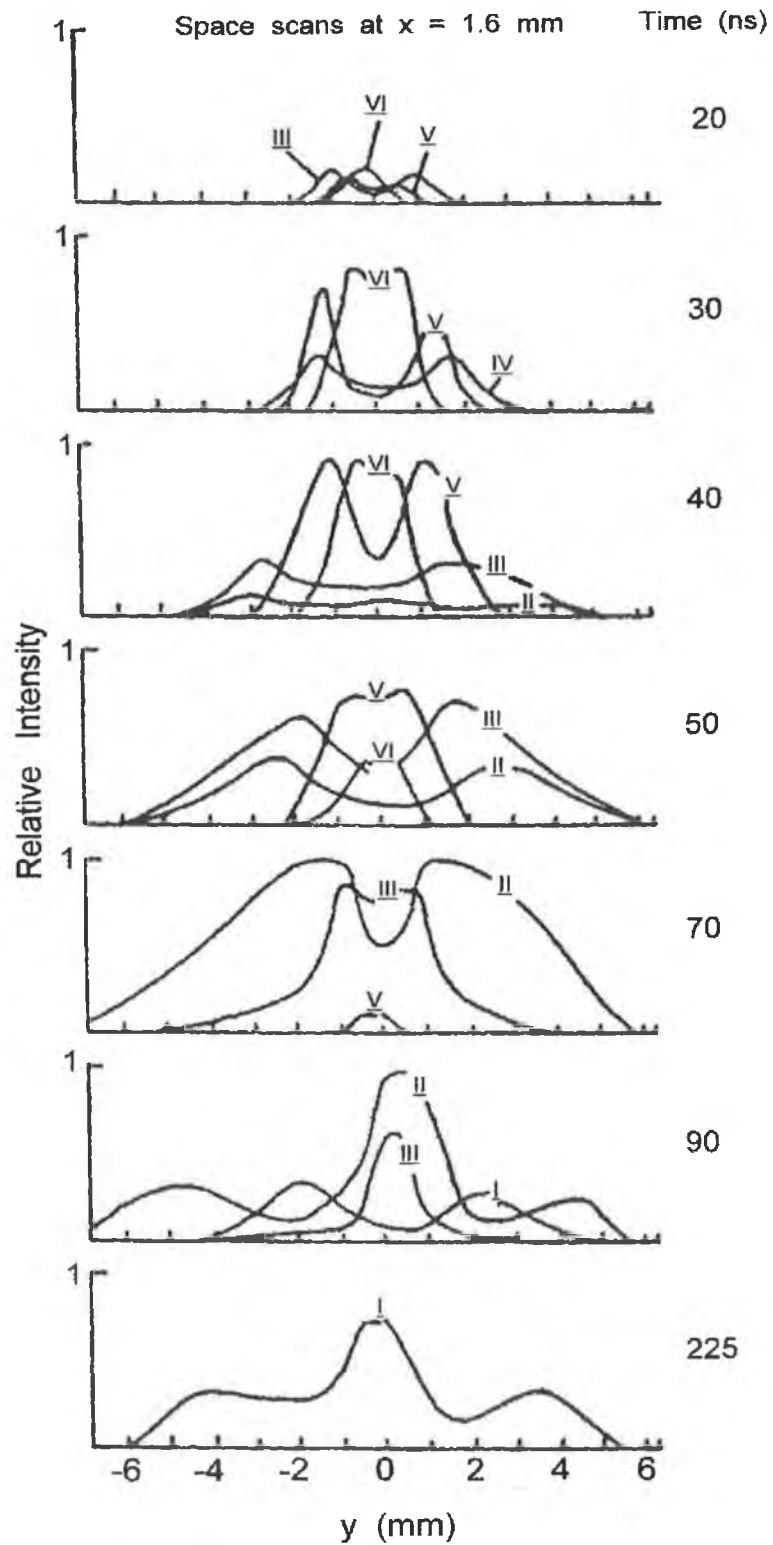
6

Fig. 1.3: A sequence in time showing the development of the spatial distribution of C I – VI (indicated by I - VI respectively) at 1.6 mm. The peak laser intensity occurs at 20 ns (after [20]).

7

The radial velocity, v(r), of a spherical plasma expanding into vacuum can be described by the so-called self-similar expansion model, whereby v(r) is found to be a linear function of the plasma radius [21], i.e.

$$v(r) = Kr \qquad\qquad [1.6]$$

where K is a constant which may vary with time and the spatial co-ordinate x (along O_x). Typical values for K lie in the range 10^6 s^{-1} to 10^9 s^{-1}, depending on the experimental conditions. The complete radially symmetric hydrodynamic calculation leading to [1.6], for example by Fader [21], with *any* initial radial velocity profile and ion density profile, resulted after some time, t, in a solution where the density distribution evolved into a Gaussian profile, while the velocity distribution became linear. The linear velocity relation of [1.6] remains valid when a drift velocity component parallel to the axis of expansion is superimposed uniformly on all ions. The term 'self-similar' is used to describe the plasma expansion in this model, as the density and velocity profiles retain their respective forms after a time t [21]. The constant density profile is, however, only maintained as an average value. Dawson [22] and Singh and Narayan [17] extended this model to the general case of a non-symmetric expanding plume. The plasma is assumed to behave as a high-temperature high-pressure gas initially expanding isothermally for the duration of the time interval of the laser pulse, and subsequently expanding adiabatically after termination of the laser pulse. Solving the appropriate equations one obtains [17]

$$X(t)\left(\frac{1}{t}\frac{dX}{dt} + \frac{d^2X}{dt^2}\right) = Y(t)\left(\frac{1}{t}\frac{dY}{dt} + \frac{d^2Y}{dt^2}\right) = Z(t)\left(\frac{1}{t}\frac{dZ}{dt} + \frac{d^2Z}{dt^2}\right) = \frac{k_B T_o}{M} \qquad [1.7]$$

describing the isothermal expansion during the time interval of the laser pulse and

$$X(t)\left(\frac{d^2X}{dt^2}\right) = Y(t)\left(\frac{d^2Y}{dt^2}\right) = Z(t)\left(\frac{d^2Z}{dt^2}\right) = \frac{k_B T_o}{M}\left(\frac{X_o Y_o Z_o}{X(t)Y(t)Z(t)}\right)^{\gamma-1} \qquad [1.8]$$

which describes the subsequent adiabatic expansion after the laser pulse terminates. X_o, Y_o and Z_o are the initial orthogonal edges of the plasma after the termination of the

laser pulse, T_o is the isothermal plasma temperature, M is the atomic weight of the plasma species and γ is the ratio of the specific heats. Generally the self-similarity model is restricted to the $10^{14} \rightarrow 10^{16}$ W m^{-2} irradiance regime, below the threshold where non-linear processes become significant [23]. This model has been applied to describe the expansion of laser produced plasmas, both in spherical and other geometries, by Dawson [8][20] and Bobin *et al.* [24] among others ([21] and references therein) and more recently by Chen *et al.* [25] and Al-Wazzan *et al.* [26].

The linear velocity relation proposed by the self-similarity model has been observed experimentally by Irons *et al.* [20] and Al-Wazzan *et al.* [26] to mention but a few.

1.2.2 The Expansion of a Laser Produced Plasma in a Gaseous Environment

Laser ablation in a suitable background gas promotes gas-phase reactions between target atoms and the background gas as well as between the target atoms themselves. These interactions can be tailored to produce novel species and materials for basic study, for chemical analysis, and for applications in advanced devices [27]. Thus, gas dynamic effects play an important role in determining the spatial and velocity distributions of the various species in the expanding plume [28].

As a laser produced plasma expands in a gaseous environment, energy is expended in heating and moving the ambient gas with the result that the plasma-gas contact front decelerates. The expansion shows a distance (from the target surface) related pressure threshold, above which the dynamics differ from that of the free expansion regime observed in vacuum [29]. For a sufficiently dense gas a blast wave is produced by the piston like action of the quickly expanding ablated material pushing outward on the background gas at the contact front, compressing the gas into a relatively thin shell at the shock front [27][30]. Under these circumstances, the mass of the ablated material is small in comparison with the mass of the buffer gas. The Taylor-Sedov ideal blast wave model can be used to predict the expansion of the ablated plume in spherical geometry using the relationship [29][31]

$$r = \left(\frac{E_B \times 75(\gamma - 1)(\gamma + 1)^2}{16\pi(3\gamma - 1)\rho_o} \right)^{\frac{1}{5}} (t - t_s)^{\frac{2}{5}}$$

[1.9]

where E_B is the laser energy that contributes to the blast wave, ρ_o is the gas density, t_s is a boundary condition which takes account of the fact that the shock wave model can strictly be applied only a time after the mass of the gas surrounding the shock wave is higher than the mass of the ablated material, i.e. a time t_s after the laser pulse. As pointed out by Dyer *et al.* [33], the blast wave model has two limiting characteristic distances outside which [1.9] is no longer valid. These limiting conditions depend not only on the pressure of the gas, but also on the nature of the gas, i.e. at a given pressure, shorter distances are obtained for gases of larger atomic mass [34]. Generally the blast wave model can be applied for high background pressures and later times of expansion. For limited improvement at earlier times of expansion, fits of the form

$$r = C_o t^p$$

[1.10]

have been suggested [28], where the exponent, $p > \frac{2}{5}$.

The classical drag force model, in which the ejected species are subjected to a viscous resistive force, which is proportional to the velocity of the plume species, has been used to describe the expansion at lower pressures and earlier times of expansion. In this model one can solve the equation of motion to obtain [28]

$$r = x_f[1 - \exp(-\beta t)]$$

[1.11]

where β is a slowing coefficient, $x_f = \frac{v_o}{\beta}$ is the stopping distance of the plume and v_o is the velocity of the plume at time $t = 0$. This model has been applied extensively to the expansion of a laser ablated plasma in various gas environments [28][29][34][35]. Furthering the argument on the basis that the drag force is produced by both viscous and form resistances, the Reynolds number described by

10

$$R_n = \frac{\rho_o v d_\phi}{\upsilon}$$

[1.12]

can be used to estimate whether the drag is mainly the result of viscous or form resistance, where ρ_o is the fluid (gas) density, υ is the viscosity, v is the relative velocity of the flow and d_ϕ is the cross-sectional diameter of the object at right angles to the flow. Assuming a plasma diameter of 1 cm propagating at a velocity of 3×10^6 cm s^{-1} in an argon environment for which $\upsilon = 3.685 \times 10^{-4}$ g s^{-1} cm^{-1} [1] and $\rho = 0.001784$ g cm^{-3} [5], the corresponding Reynolds number is of the order of 10^7. As the viscous drag predominates when the Reynolds number is very small $(R_n \leq 1)$, it may be postulated that the form resistance which is $\propto v^2$ predominates. This is the case for high-speed motion. Solving the equation of motion $(a = -\beta'v^2)$ one obtains

$$r = \frac{1}{\beta'} Ln(1 + \beta' v_o t)$$

[1.13]

Using the non-viscous drag force model relationship of [1.13], improved agreement between experiment and theory is obtained for lower pressures and later times of expansion, than those predicted by the viscous drag force model of [1.12]. This can be seen from fig. 1.4. This topic is re-addressed in §3.1.2 where agreement between the viscous drag force model is attained at early stages of expansion, while at later times the trend is more towards the ideal blast wave model.
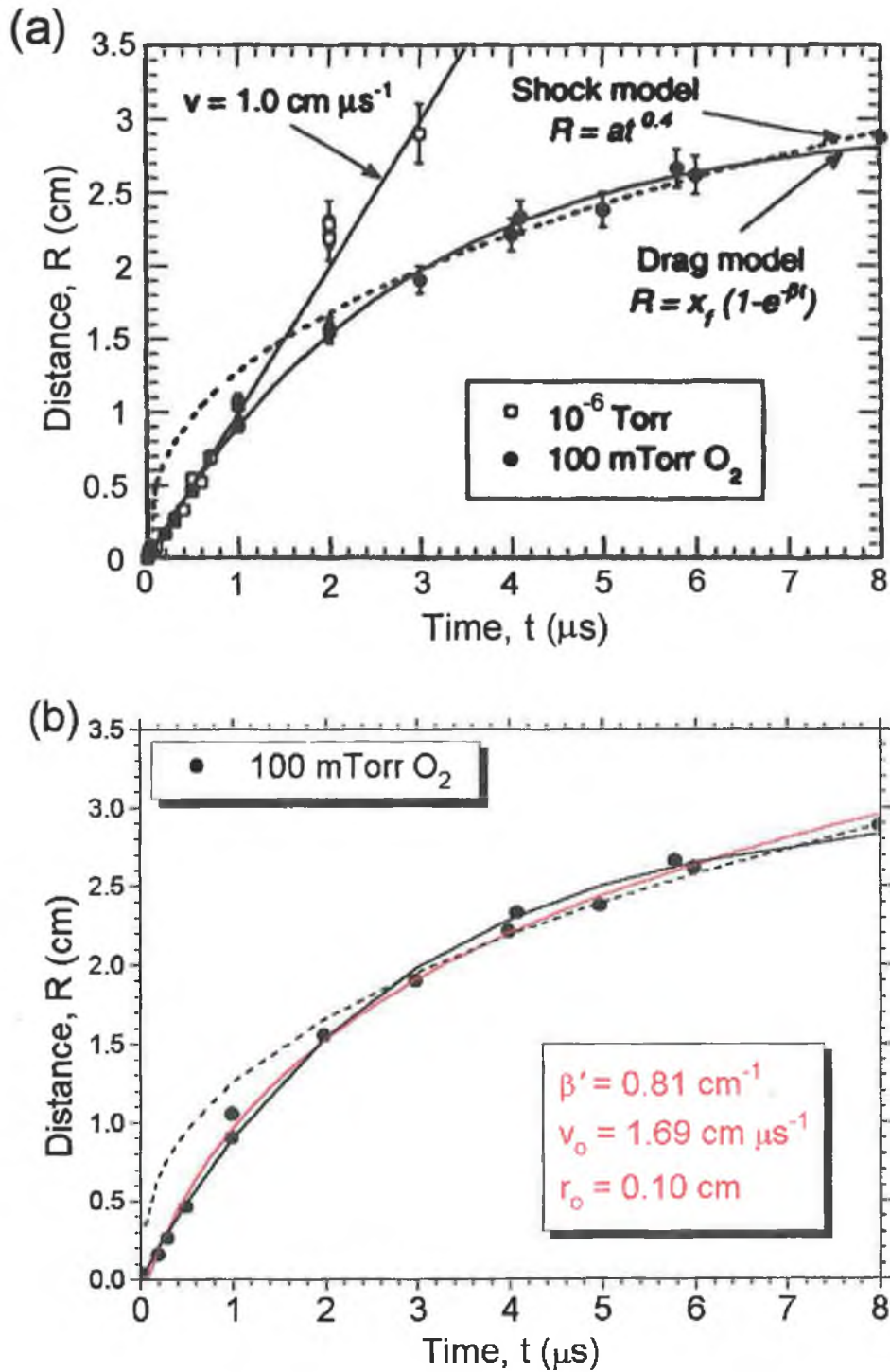
(a)

v = 1.0 cm µs^{-1}

Shock model
$R = at^{0.4}$

Drag model
$R = x_f (1-e^{-\beta t})$

□ 10^{-6} Torr
● 100 mTorr O$_2$

Distance, R (cm)

Time, t (µs)

(b)

● 100 mTorr O$_2$

$\beta' = 0.81$ cm^{-1}
$v_o = 1.69$ cm µs^{-1}
$r_o = 0.10$ cm

Distance, R (cm)

Time, t (µs)

Fig. 1.4: (a) z-t plot of the expansion front boundary of the luminous plume along the normal to the YBCO pellet measured from gated ICCD images in 100 mTorr of oxygen (after [28]). (b) z-t plot of the expansion front of the YBCO plume in 100 mTorr of oxygen. Indicated in red is the fit obtained using the non-viscous relationship of [1.13].

12

1.3 Plasma Equilibrium and Radiation Models

Heretofore, plasma equilibrium considerations have been neglected. In many physical situations however, despite its dynamic nature, a plasma can be considered to be in thermodynamic equilibrium. In such circumstances a plasma can be characterised by its temperature. Radiative processes are governed by Planck's distribution law, the velocities of the plasma particles follow a Maxwellian distribution, the plasma particles are distributed in their accessible internal energy levels according to a Boltzmann distribution, while the ionisation states of the plasma follow a Saha-Boltzmann distribution, all of which are characterised at a temperature T. Such a system obeys the principle of detailed balance, i.e. every atomic process is as frequent as its inverse process. In real situations thermodynamic equilibrium is seldom, if ever, achieved as this would require the plasma to be optically thick at all frequencies. Thus, approximate models are required to solve the differential rate equations describing the population and depopulation of levels. A multitude of atomic processes must be considered including three-body recombination, collisional ionisation, radiative recombination, photoionisation, collisional excitation and de-excitation, spontaneous and stimulated emission, photoexcitation, dielectronic recombination etc. The rate coefficient for each of these processes is defined as the product of the process dependent cross-section times the velocity, averaged over the velocity distribution, i.e. $\langle \sigma v \rangle$. These rate coefficients are essential for the prediction of ionisation balance etc. Introducing a time dependence complicates the solution still further. Often it is assumed that certain processes dominate thus allowing simplification of the rate equations and hence of the model descriptions.

In the brief plasma radiation model descriptions which follow, the electron velocity distribution is assumed to be Maxwellian at a temperature T_e. This is satisfied provided the electron-electron relaxation time is smaller than the electron heating time. It is also assumed that radiation escapes without interacting with the plasma. This is the optically thin approximation.

13

1.3.1 Local Thermodynamic Equilibrium (LTE)

At sufficiently high densities, collisional processes, especially those involving electrons, play a more important role than radiative processes in determining the excited state populations. Each process is accompanied by its inverse and these occur at equal rates by the principle of detailed balance. Thus, the distribution of population densities is the same as it would be in complete thermodynamic equilibrium at any instant and point in the plasma, determined entirely by local values of temperature, density and chemical composition. LTE requires that not only are the free electrons distributed according to a Maxwellian velocity distribution given by [4]

$$dn_v = N_e 4\pi \left(\frac{m_e}{2\pi k_B T_e}\right)^{3/2} \exp\left(\frac{-m_e v^2}{2k_B T_e}\right) v^2 dv \qquad [1.14]$$

where dn_v is the number of electrons of mass m_e with velocities between v and $v + dv$, but also that the bound electrons occupy discrete levels according to a Boltzmann distribution given by [36]

$$\frac{N(i)}{N(k)} = \frac{g(i)}{g(k)} \exp\left(\frac{-\chi(i,k)}{k_B T}\right) \qquad [1.15]$$

where i and k denote the lower and upper levels respectively, N is the population density, g is the statistical weight and $\chi(i,k)$ is the energy difference between the two levels. The free particle densities are required to follow the Saha relation given by [36]

$$\frac{N(Z)N_e}{N(Z-1)} = 6 \times 10^{27} T^{3/2} \exp\left[\frac{-\chi(Z-1)}{T}\right] \qquad [1.16]$$

where Z = 1 for a singly ionised atom, $\chi(Z-1)$ is the ionisation energy of the Z-1 times ionised atom in eV, and T is in eV. The fractional state charge densities for an electron density, $N_e = 9 \times 10^{23}$ m^{-3}, as a function of temperature, calculated using [1.16], are plotted in fig. 1.5 for lithium.

14

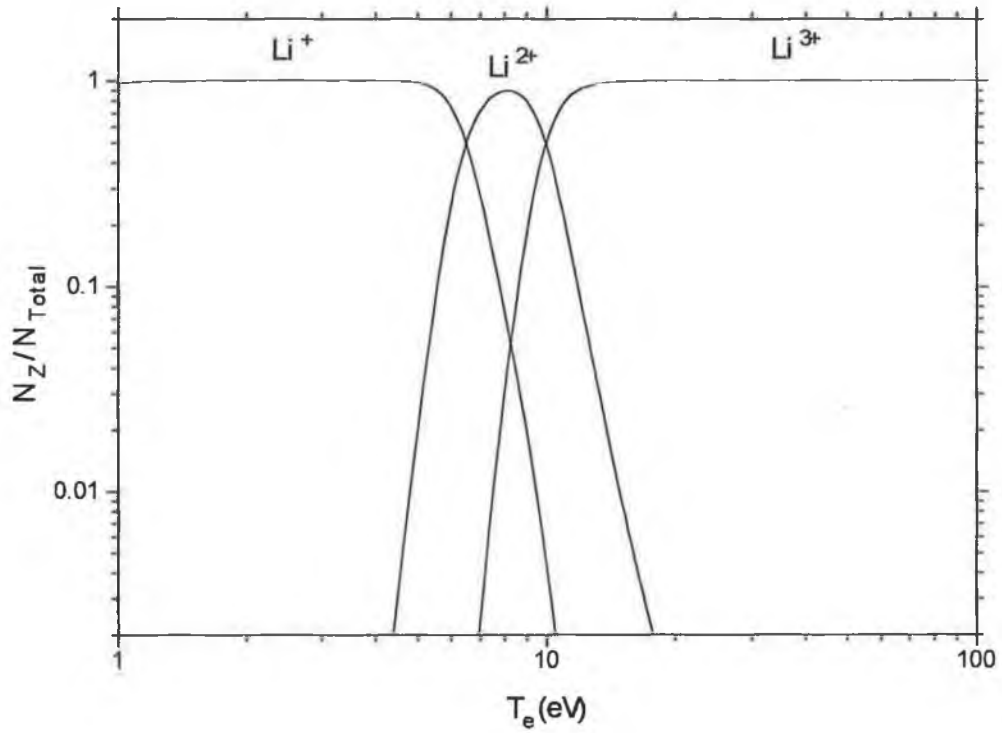Fig. 1.5: Fractional state charge densities as a function of temperature for lithium assuming LTE ($N_e = 9 \times 10^{23}$ m^{-3}). This electron density relates to the analysis of §3.3.1.

A necessary but not sufficient criterion for LTE to hold is that the electron density be sufficiently high that collisional de-excitation be, say, ten times more probable than radiative decay for all transitions. This is equivalent to the requirement that [36]

$$N_e \geq 1.4 \times 10^{20} T_e^{\frac{1}{2}} \chi^3(i,k) \qquad [1.17]$$

where T_e is in eV and $\chi(i,k)$ is the largest energy gap, in eV, between adjacent levels of the atoms and ions in the plasma. This lower limit of applicability is plotted for various species in fig. 1.6.

In an optically thick plasma the LTE model is valid at lower densities [36]. LTE generally applies to Nd:YAG laser produced plasmas generated from low atomic number elements (Z < 9) [37].

15
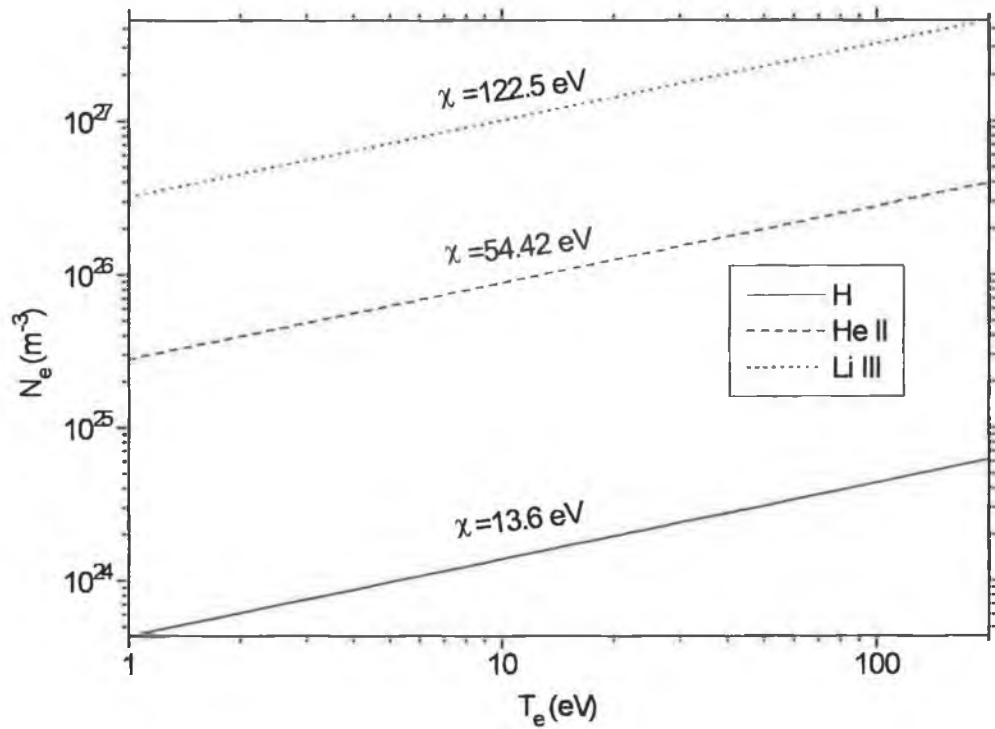
Fig. 1.6: LTE model lower limit of applicability using [1.17].

1.3.2 Coronal Equilibrium (CE)

At plasma densities, such as those found in the solar corona, equilibrium is maintained between excitation and ionisation by electronic collisions from the ground state and de-excitation and recombination by radiative processes from the upper levels to all lower levels. Since the rates of collisional ionisation and radiative recombination are proportional to the electron density, the populations of the various ion species in the plasma are independent of electron density. The Saha equation ([1.16]) no longer holds. It is replaced by the corona equation

$$\frac{N_{z+1}}{N_z} = \frac{S(Z, T_e)}{\alpha_r(Z+1, T_e)}$$ [1.18]

where $S(Z, T_e)$ is the collisional ionisation coefficient and $\alpha_r(Z+1, T_e)$ is the radiative recombination coefficient [4][37]. Unlike the LTE model, quantitative interpretation of

16

the CE model depends critically on atomic cross-sectional data [4]. Indeed, for improved accuracy generalised formulae for $S(Z,T_e)$ and $\alpha_r(Z+1,T_e)$ [37] should not be heavily relied upon, but rather reference should be made to the literature for species specific rate coefficients [4], e.g. [38]. Generally the CE model can be applied to Nd:YAG laser produced plasmas for $Z > 29$ [37].

1.3.3 Collisional Radiative Equilibrium (CR)

In the intermediate density range neither the LTE nor the CE model is valid. The collisional radiative (CR) model of Bates et al. (1962) was developed to breach this gap by modifying the coronal model to take into account collisional transitions from the higher bound levels as well as three-body and radiative recombination. Colombant and Tonon [37] extended this model and derived useful formulae to calculate both the electron temperature in the case of fully ionised plasmas, as well as equilibrium populations of various ion species in a laser produced plasma, i.e.

$$\frac{N_{z+1}}{N_z} = \frac{S(Z,T_e)}{\alpha_r(Z+1,T_e)+N_e\alpha_{3b}(Z+1,T_e)} \qquad [1.19]$$

where α_{3b} is the coefficient for three-body recombination. This model is particularly appropriate in the 10^{15} to 10^{17} W m^{-2} irradiance regime for medium to high atomic number elements. For low density plasmas $N_e\alpha_{3b} \ll 1$ and the CR model reduces to the CE model. In the limit of very high density, the CR model approaches the LTE model.

1.4 The Emission and Absorption of Radiation in a Plasma

The profile of a spectral line has a characteristic width and shape determined by the conditions existing in the source. In the absence of instrumental effects, the profile of such a line can be used to ascertain local conditions of, for example, temperature and density etc. in the source. In the following sections, the atomic processes governing the emission or absorption of radiation in a plasma are outlined. The emission and

absorption coefficients are introduced, along with the solution to the equation of radiative transfer. Finally, using the expansion geometry of §1.2 and §1.4.3, asymmetric emission or absorption profiles are discussed.

1.4.1 The Einstein Coefficients and the Atomic Frequency Response (AFR)

The emission or absorption intensities for a given transition are determined by the population of the upper and lower quantum levels of the line, respectively, by the Einstein transition probabilities and, in the case of absorption, by the intensity of the radiation field. Assuming thermal equilibrium the Einstein coefficients are deduced by application of the principle of detailed balance (dynamic equilibrium) [39], so that

$$A_{ki} = \frac{g_i}{g_k} B_{ik} \frac{8\pi h\nu^3}{c^3} \qquad\qquad [1.20]$$

$$g_k B_{ki} = g_i B_{ik} \qquad\qquad [1.21]$$

where A_{ki} is the Einstein A coefficient for spontaneous emission, B_{ik} the Einstein B coefficient for absorption, B_{ki} the Einstein B coefficient for stimulated emission, g_i and g_k are the statistical weights of the lower and upper levels respectively. As these coefficients are properties of the atom relationships [1.20] and [1.21] hold regardless of the actual situation of the atom, despite the initial assumption of thermal equilibrium. A direct result is that

$$f_{ik} = \frac{m_e h\nu}{\pi e^2} B_{ik} \qquad\qquad [1.22]$$

or equivalently (upon rearrangement)

$$f_{ik} = \frac{A_{ki}\lambda^2}{6.670\times 10^{15}} \qquad\qquad [1.23]$$

18

where λ is in Å. f_{ik} is the atomic absorption oscillator strength, tables for which can be obtained, for example, from the Opacity Project Database (TOPBASE)[1] [40]. In Einstein's classical treatment of the interaction of a two-level atom with a radiation field that is a slowly varying function of frequency, the transition probabilities are effectively averaged over the frequency response of the atom, i.e. over the line profile. In many applications and particularly in the case of lasers, the transition rates induced by a monochromatic wave of frequency ν are required. These are obtained by multiplying the frequency-averaged A or B coefficients by the appropriate *normalised* line shape function, ϕ_ν. This intrinsic line shape is denoted the Atomic Frequency Response (AFR) where

$$\int_{line} \phi_\nu d\nu = 1 \qquad\qquad [1.24]$$

is the normalised AFR. From [1.24] the physical meaning of the AFR becomes clear. It represents the probability per unit interval frequency to observe a photon emitted in the interval ν and $\nu + d\nu$ (in the vicinity of ν_0).

In the following treatment, the assumption that the atomic frequency response is identical in both emission and absorption shall be made without justification. This assumption often proves to be a very good one in astrophysics problems [41]. Three atomic frequency response profiles are considered.

(a)   The Lorentzian AFR

The normalised Lorentzian profile AFR is described by

$$\phi_{\nu_{Lorentzian}} = \frac{1}{\pi \Delta_L} \frac{1}{\left[1 + \left(\dfrac{\nu - \nu_0}{\Delta_L}\right)^2\right]} \qquad\qquad [1.25]$$

---

[1] Other sources include Martin *et al.* [42] and Reader *et al.* [43]. The oscillator strengths of hydrogenic systems are independent of nuclear charge i.e. $f_Z = f_H$.

where Δ_L is the half width at half maximum (HWHM = FWHM / 2) and ν_o is the resonance frequency between the two levels involved in the transition. Lorentzian profiles are normally associated with the natural width and the Stark width of a spectral line (see §1.5.1 and §1.5.3).

(b)   The Gaussian AFR

The normalised Gaussian profile AFR is characterised by

$$\phi_{\nu_{Gaussian}} = \left(\frac{Ln2}{\pi}\right)^{\frac{1}{2}} \frac{1}{\Delta_G} \exp\left[-Ln2\left(\frac{\nu - \nu_o}{\Delta_G}\right)^2\right] \qquad \textbf{[1.26]}$$

Here Δ_G is the HWHM (See Appendix A). Such a profile can readily be obtained by considering the Doppler shifts associated with a Maxwellian (thermal) distribution of molecular speeds in a gas. Δ_G is therefore related to the kinetic temperature of the emitting particles.

(c)   The Voigt AFR

Originally developed by W. Voigt (1912) from the basic theories of line broadening, this profile takes account of both a Lorentzian and a Gaussian contribution to the AFR, thus providing a versatile form. Several defining expression exist including

$$\phi_{\nu_{Voigt}} = C_n\left(\phi_{\nu_{Lorentzian}} \otimes \phi_{\nu_{Gaussian}}\right) = C_n\left(\int_{-\infty}^{+\infty} \phi_{Lorentzian}(\nu)\phi_{Gaussian}(\nu - \nu')d\nu'\right) \qquad \textbf{[1.27]}$$

where $\otimes$ denotes convolution, and C_n is a normalisation constant. A form to satisfy [1.24] is given by

$$\phi_{V_{Voigt}} = \left(\frac{Ln2}{\pi}\right)^{\frac{1}{2}} \frac{1}{\Delta_G} \frac{1}{\pi\Delta_L} \int_{-\infty}^{+\infty} \exp\left[-Ln2\left(\frac{v'}{\Delta_G}\right)^2\right] \frac{1}{\left[1+\left(\frac{v-v'}{\Delta_L}\right)^2\right]} dv' \qquad [1.28]$$

Unfortunately, the Voigt function cannot be expressed analytically. A much simpler form however, avoiding the convolution process (and thus reducing computational expense), for the Voigt profile has been developed by [44] whereby the core of the line profile is approximated by a rectangle, and the wings by a v^{-2} relationship. A further improved analytical approximation using four generalised Lorentzians in two variables, accompanied by numerical implementation is given in [45]. It should be noted that values returned by the 'C' programming language function $vs(\ldots)$, presented in [45], (and in Appendix B for reference), should be multiplied by the normalisation factor $\frac{1}{\pi\Delta_L}$ in order to satisfy [1.24].

1.4.2 The Equation of Radiative Transfer

(a) The Emission Coefficient

The radiation power emitted per unit solid angle from unit volume of a source is termed the emission coefficient. The resulting expression in cgs units is [39]

$$\varepsilon_v = N_k(r) \frac{2\pi e^2 h v^3}{m_e c^3} \frac{g_i}{g_k} f_{ik}\phi_v(r) \qquad [1.29]$$

where $N_k(r)$ is the spatially dependent density distribution of the upper quantum level, $\phi_v(r)$ as before is the normalised AFR, which may also be a function of the spatial coordinate as a result of the Doppler effect due to streaming (see §1.4.3).

(b) The Absorption Coefficient

It is a general principle that if a medium emits radiation, then it will absorb radiation at that same frequency. The absorption coefficient is related to the Einstein coefficient

21

for absorption B_{ik} as well as the Einstein coefficient for stimulated emission B_{ki} (which is normally treated as negative absorption, if it has the same frequency and direction as the incident radiation). In general stimulated emission will only be important if a population inversion is created between the two levels, resulting in a negative absorption coefficient. κ_v is defined in cgs units as [39]

$$\kappa_v = \frac{\pi e^2}{m_e c} N_i(r)\left(1 - \frac{g_i N_k(r)}{g_k N_i(r)}\right) f_{ik}\phi_v(r) \qquad [1.30]$$

where $N_i(r)$ and $N_k(r)$ are the spatially dependent population densities of the lower and upper levels respectively, and $\phi_v(r)$ may also be a function of the spatial coordinate in the general case, through the Doppler effect due to streaming (see §1.4.3). By definition

$$\kappa_v = \sigma_v N_i(r)\left(1 - \frac{g_i N_k(r)}{g_k N_i(r)}\right) \qquad [1.31]$$

where σ_v is the absorption cross-section (cgs units).

For the case of continuum states, a differential form for the oscillator strength is used, i.e.

$$f_c = \int_{S_L}^{\infty} \frac{\partial f_m}{\partial v}\, dv \qquad [1.32]$$

where f_c is the oscillator strength for the whole continuum associated with absorption for a level m, and S_L represents the series limit. By definition the corresponding cross-section writes (cgs)

$$\sigma_m(v) = \frac{\pi e^2}{m_e c} \frac{\partial f_m}{\partial v} \qquad [1.33]$$

22

(c)   *A Solution to the Equation of Radiative Transfer*

Radiative Transfer, or Radiative Trapping as it is known in the case of confined laboratory plasmas details the emission of radiation by a hot (excited) gas which is opaque to its own radiation.   The transfer equation is obtained by considering the change in radiant energy contained within a frequency interval $d\nu$ as the beam passes through a cylindrical volume element of cross-section dS and length dx during a time dt in a solid angle $d\Omega$ as shown in fig. 1.7.
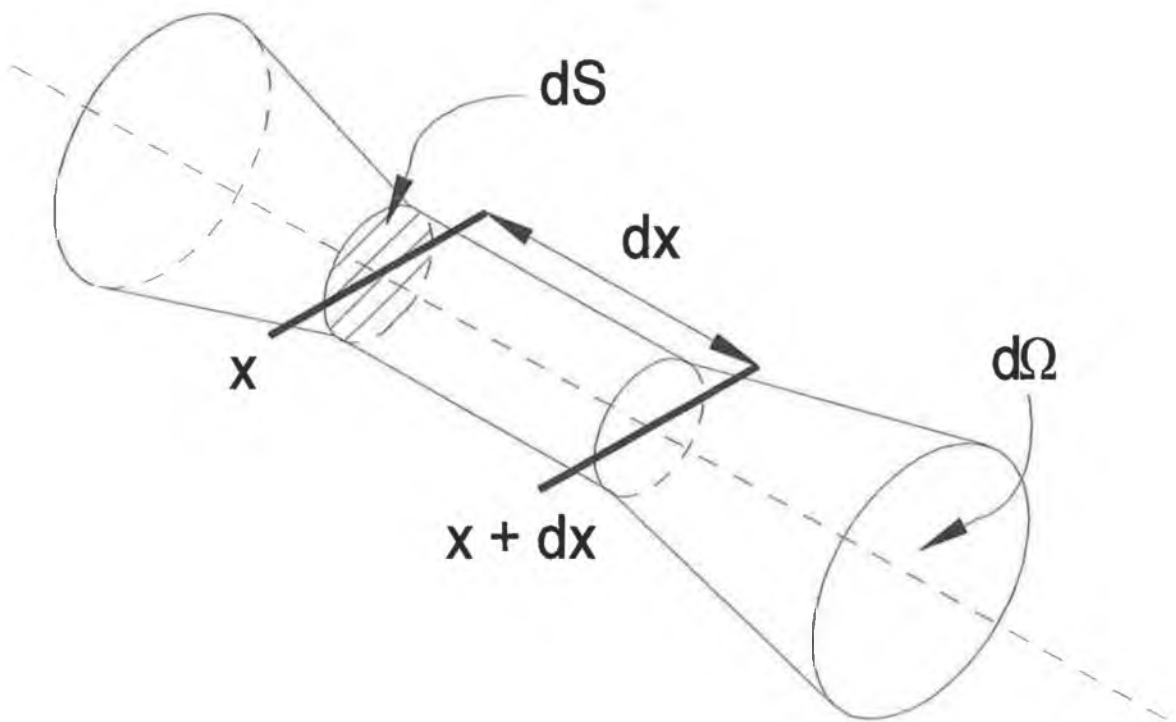
Fig. 1.7:   The geometric volume element considered in the derivation of the equation of radiative transfer (after [39]).

The absorbed energy in the frequency interval $d\nu$, solid angle $d\Omega$, surface element dS and time interval dt is the energy carried by one photon multiplied by the number of upward transitions in dt i.e.

$$E_{abs} = h\nu N_i dx dS d\nu dt B_{ik}\phi_\nu \frac{d\Omega}{4\pi} I_\nu(x) \hspace{2cm} [1.34]$$

23

where $I_\nu(x)$ is the intensity of light of frequency ν at x (see fig. 1.7). The term $\frac{d\Omega}{4\pi}$ takes account of the fact that the beam is confined to the solid angle $d\Omega$. Note that the frequency averaged B_{ik} has been multiplied by the AFR as discussed in §1.4.1. The atoms in the upper level (k) give energy to the beam by spontaneous transitions in the time interval dt so that

$$E_{emit} = h\nu dx dt dS d\nu A_{ki}\phi_\nu \frac{d\Omega}{4\pi}$$
[1.35]

where stimulated emission has been neglected. The variation in intensity in dx is therefore

$$\frac{dI_\nu}{dx} = \lim_{dx \to 0}[I(x+dx) - I(x)] = \frac{h\nu}{4\pi}(A_{ki}N_k - B_{ik}N_iI_\nu)\phi_\nu$$
[1.36]

which can be rewritten as

$$\frac{dI_\nu}{dx} = \varepsilon_\nu - \kappa_\nu I_\nu$$
[1.37]

This is a first order differential equation known as the equation of radiative transfer. Once the emission (ε_ν) and absorption (κ_ν) coefficients have been expressed as functions of frequency, the equation of radiative transfer may readily be solved. The usual procedure for solving this equation is by a change of variable, i.e. $d\tau_\nu = -\kappa_\nu dx$ called the optical depth. However in order to retain solutions which are explicit functions of $N_i(r)$ and $N_k(r)$, one may multiply [1.37] by $\exp\left(\int \kappa_\nu(x)dx\right)$ [46] to get

$$\frac{dI_\nu(x)}{dx}\exp\left(\int \kappa_\nu(x)dx\right) + \kappa_\nu(x)I_\nu(x)\exp\left(\int \kappa_\nu(x)dx\right) = \varepsilon_\nu(x)\exp\left(\int \kappa_\nu(x)dx\right)$$ [1.38]

Noting that the left hand side of [1.38] is equal to

24

$$\frac{d}{dx}\left[I_\nu(x)\exp\left(\int\kappa_\nu(x)dx\right)\right]$$

$$\Rightarrow \frac{d}{dx}\left[I_\nu(x)\exp\left(\int\kappa_\nu(x)dx\right)\right] = \varepsilon_\nu(x)\exp\left(\int\kappa_\nu(x)dx\right) \qquad [1.39]$$

Integrating [1.39] one obtains the solution

$$I_\nu(x) = \exp\left(-\int\kappa_\nu(x)dx\right)\left[\int\varepsilon_\nu(x)\exp\left(+\int\kappa_\nu(x)dx\right)dx + C_{int}\right] \qquad [1.40]$$

where ε_ν and κ_ν can be expressed in terms of N_k and N_i respectively (see §1.4.2(a) and §1.4.2(b)). Choice of $C_{int} = 0$ in [1.40] corresponds to $I_\nu(0) = 0$, i.e. no external radiation is incident on the plasma. The optically thin case corresponds to small optical depths, i.e. $\tau_\nu(L) = \int\kappa_\nu(x)dx \ll 1$, so that $\exp(\pm\tau_\nu(L)) \approx 1$ in which case [1.40] becomes the familiar

$$I_\nu(x) = \int\varepsilon_\nu(x)dx \qquad [1.41]$$

One can also generate an absorption spectrum from the above treatment. This is a different physical situation, corresponding to the case of radiation incident externally on a non-emitting ($\varepsilon_\nu = 0$) medium. In this circumstance [1.40] reduces to the familiar Beer-Lambert law, i.e.

$$I_\nu(x) = I_{\nu_o}\exp\left(-\int\kappa_\nu(x)dx\right) \qquad [1.42]$$

where C_{int} in [1.40] now equals I_{ν_o}, the intensity of the back-lighting radiation.

1.4.3 The Case of an Expanding Laser Produced Plasma

The following discussion is largely based on the work of [47]. Using the emission or absorption coefficient definitions of §1.4.2 it is shown that in the case of an expanding laser produced plasma, it is possible to observe asymmetric line profiles both in emission or absorption depending on the choice of K (see [1.6]), the atomic frequency response, as well as the upper and lower level density distributions. In the case of an emission spectrum, self-absorption may also be observed.

The geometries of expansion and observation of a laser-produced plasma created on a planar target are illustrated in figs. 1.8 and 1.9.
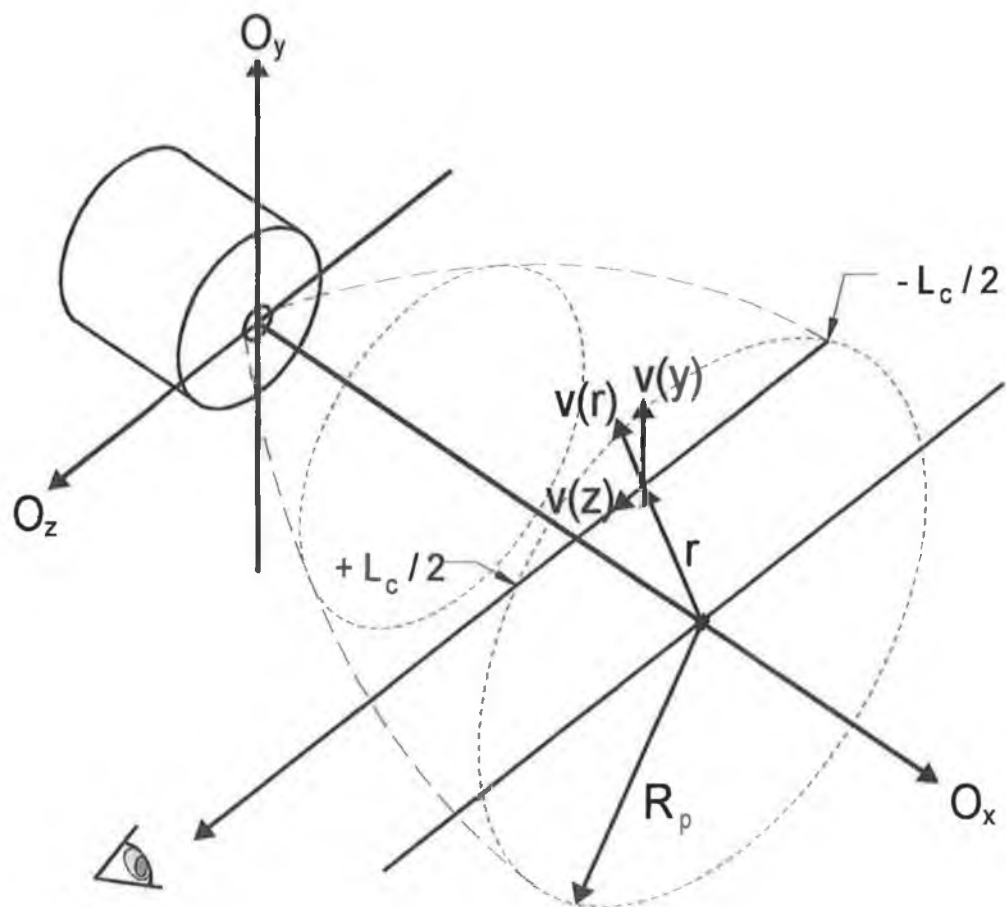
Fig. 1.8: The proposed expansion and observation geometries of a laser produced plasma created on a planar target.
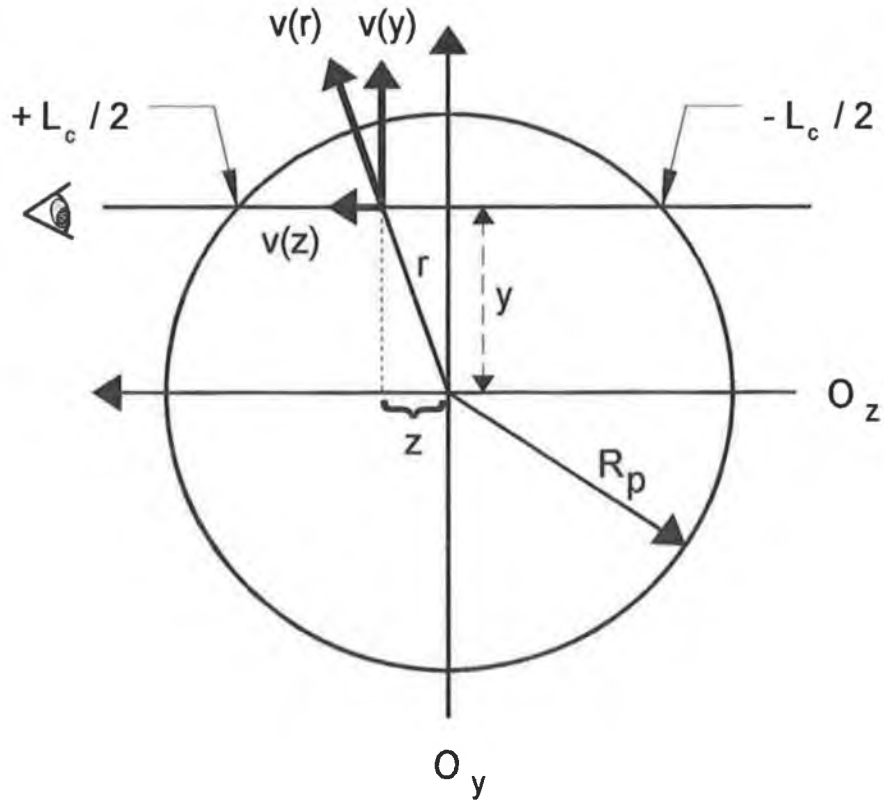
Fig. 1.9: The geometries of expansion and observation of a laser produced plasma in the y-z plane.

Two important assumptions are made in relation to the proposed model; (a) the expansion is axisymmetric about O_x, and (b) there is radial symmetry in planes normal to O_x, as previously outlined in §1.2. A fixed observer in the laboratory frame looking at the emitting plasma side-on will see Doppler shifted light proportionally to the sign and magnitude of the radial component of the instantaneous velocity v(r) (if the line-of-sight is along the diameter of the plume), or the corresponding v(z) projection (if the line-of-sight is along a chord as in fig. 1.9). It is assumed that the velocity of an absorbing (or emitting) ion (or atom) at any point in the plasma can be represented by the sum of a thermal component which contributes a Gaussian component to the total linewidth and a streaming component which contributes a frequency shift $\Delta v = v' - v_o$, where

$$v' = v_o \left(1 \pm \frac{v}{c}\right)$$ [1.43]

27

in the non-relativistic limit. v represents either v(r), the radial component, or v(z) the z component with

$$v(z) = v(r) \times z/r \qquad \qquad \textbf{[1.44]}$$

by simple geometry. The minus sign corresponds to a velocity component away from the observer (in emission) (red shift), while the plus sign corresponds to a velocity component towards the observer (blue shift). Therefore, one can deduce that atoms or ions moving away from the observer contribute to the short frequency side of the line profile, whereas atoms or ions moving towards the observer contribute to the long frequency side of the line profile. Knowledge of the variations of v(r) and v(z) as a function of r and z respectively are therefore required to accurately predict the line profile. It has been shown ([21]) that v(r) = K r (and thus v(z) = K z) is an acceptable self-similar solution (see §1.2.1) in the case of an expanding laser plasma from a plane target in vacuum. Using this linear velocity distribution, three test cases were chosen to illustrate the possible conditions for observing asymmetric self-reversed line profiles. Each was examined in the context of the low, medium and high velocity regimes corresponding to different K values in [1.6], as defined by [47]. Following the analysis of [47], the upper level density distribution was retained for each of the test cases, and was chosen such that it had a central minimum. Different ground level density distributions were then selected for each of the three test cases. This was done to illustrate the range of profiles which may emerge from an expanding laser produced plasma. The computed emission spectra for the low, medium and high velocity regimes along with their corresponding upper and ground level density distributions are plotted in figs. 1.10 through 1.12. The emission spectra shown were computed for the $1s^2 2s \leftarrow 1s^2 2p$ transition in Li° (670.78 nm) using a Gaussian AFR ϕ_v of half width $\Delta_G = 0.363$ nm.

28
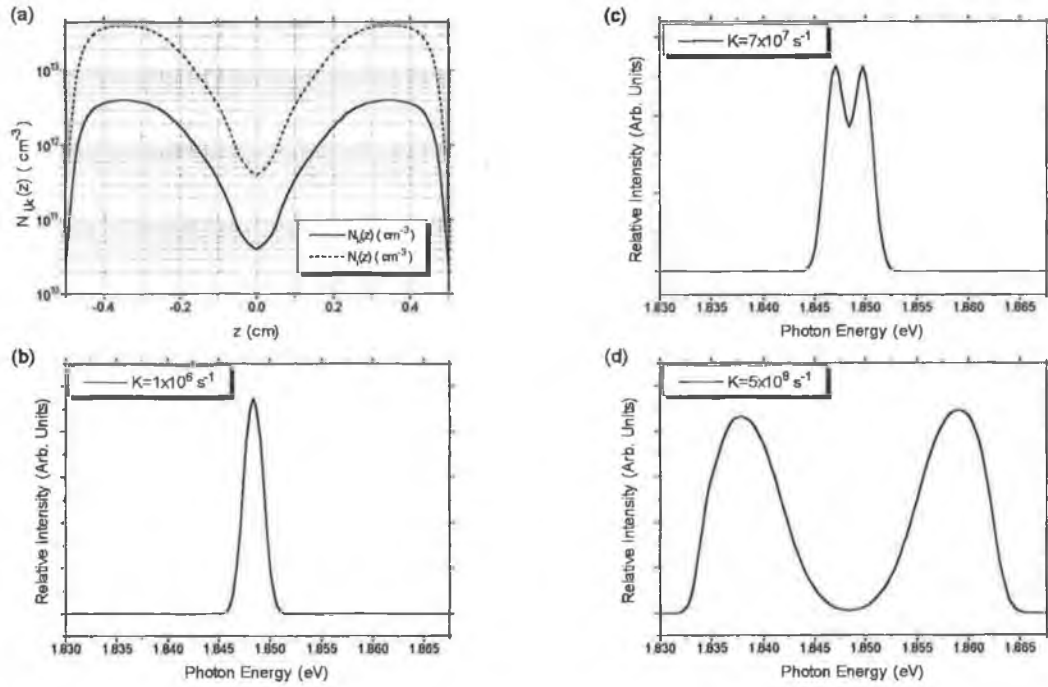
Fig. 1.10: Test case 1. (a) The upper ($N_k(z)$) and ground ($N_i(z)$) state density distributions used in the calculation. Also shown are the resultant emission spectra in the (b) low velocity (c) medium velocity and (d) high velocity regimes.
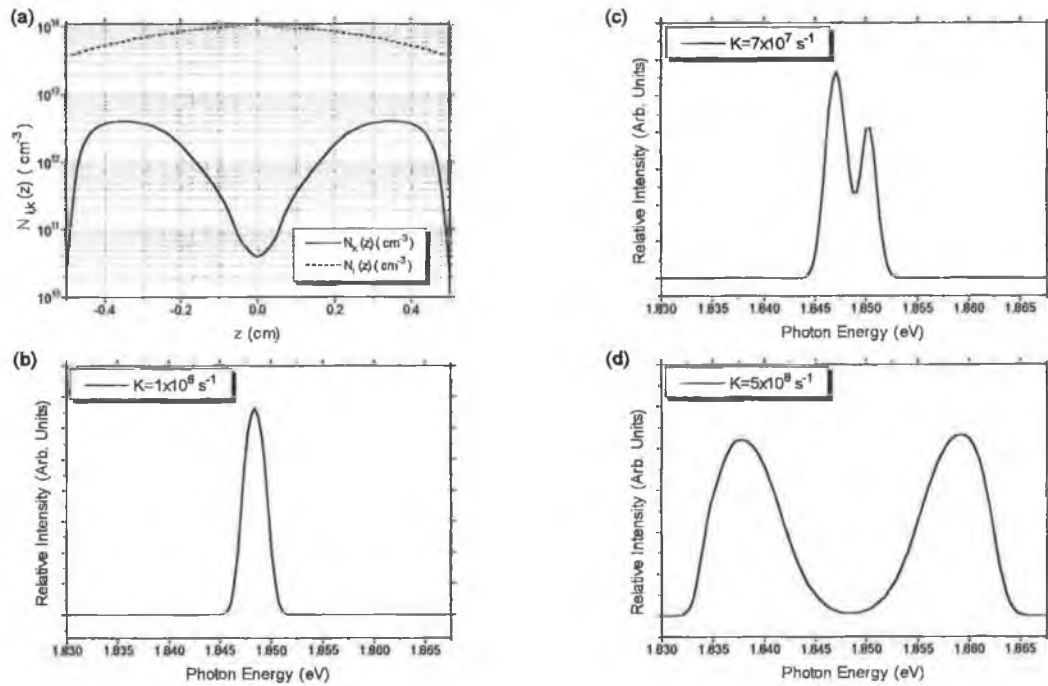
Fig. 1.11: Test case 2. (a) The upper ($N_k(z)$) and ground ($N_i(z)$) state density distributions used in the calculation. Also shown are the resultant emission spectra in the (b) low velocity (c) medium velocity and (d) high velocity regimes.
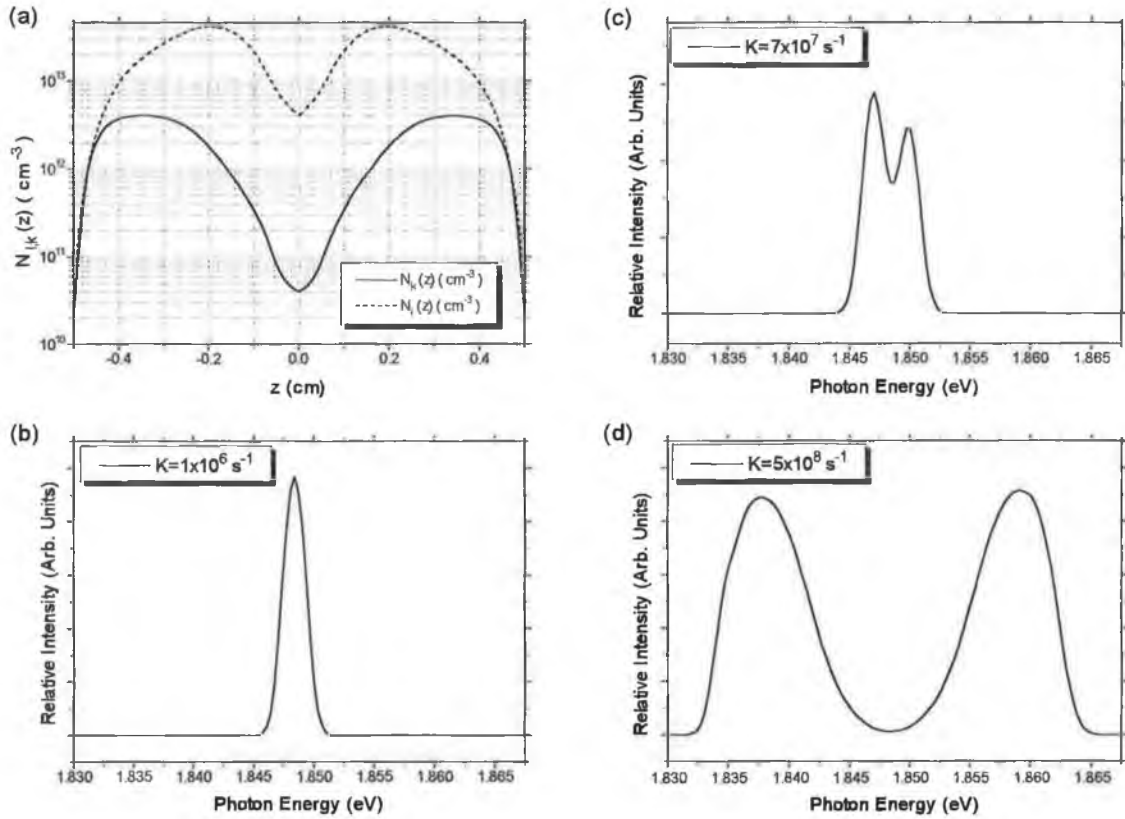
Fig. 1.12: Test case 3. (a) The upper ($N_k(z)$) and ground ($N_i(z)$) state density distributions used in the calculation. Also shown are the resultant emission spectra in the (b) low velocity (c) medium velocity and (d) high velocity regimes.

As already mentioned, one of the features of the self-similar expansion model is that due to the Doppler effect different parts of the emission profile will correspond to different parts of the emitting medium. Photons of different frequencies can therefore travel different absorbing path lengths possibly leading to a characteristic asymmetric profile as shown in figs. 1.11(c) and 1.12(c). A necessary condition for the asymmetry in this model is that the spatial emission coefficient be displaced relative to the spatial absorption coefficient [47] as shown in fig. 1.13, providing a suppression of either the red peak or the blue peak. This is most clearly shown in figs. 1.11(c) and 1.12(c) for cases 2 and 3 in the medium velocity regime, where the blue peak is suppressed.

30
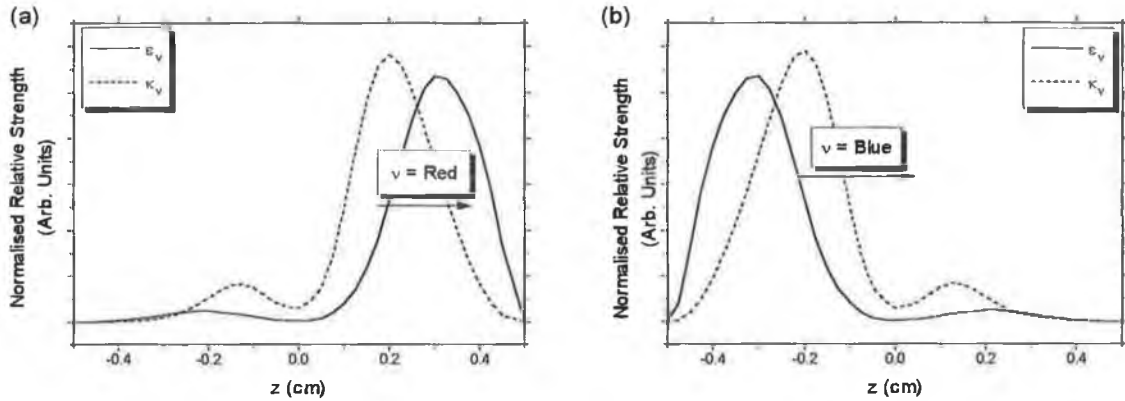
Fig. 1.13: (a) and (b) show the normalised spatial emission and absorption coefficients calculated at two different frequencies ($v=v_o\pm\Delta_G$) for case 3 in the medium velocity regime. A spatial displacement of the spatial emission and absorption coefficients relative to one another can be seen, thus explaining the origin of the spectral line asymmetry shown in fig. 1.12(c). The observer is positioned at z = +0.5 cm.

Thus, the solution to the equation of radiative transfer and hence the profile of a spectral line is strongly dependent on the density distributions of the upper and lower levels, the velocity distribution chosen, as well as the value of K (s^{-1}). As K decreases, a value is reached where the spatial emission and absorption curves approach one another so closely at all frequencies, that the resultant spectral profile is symmetric. This is also the case when the normalised density distributions of the upper and lower levels are equal as seen in fig. 1.10. Self-absorption or radiative trapping is also a feature of the model, as can be seen from the figures, whereby the plasma becomes opaque to its own radiation at certain frequencies. From [47], it appears that an enhancement of the red peak is most commonly reported on in the literature, although Irons comments on a study performed by Fraenkel et al. (1968) whereby satellites to the blue in resonance lines of Be III and IV from a vacuum spark were reported. In contrast Malvezzi et al. [48] have reported self-absorption, with enhancement of the red peak, in a laser produced carbon plasma where resonance lines of C V and VI were shifted to the short wavelength side. Tondello et al. observed similar results with beryllium [49]. Jones et al. [50] observed a very small asymmetry of the Ar I (696.543 nm) line profile produced by a wall stabilised arc, and attributed it to collisions between atoms and ions.

In the self-similar expansion model, the mechanism for the formation of an asymmetric self-reversal in line radiation originating from within an emitting plasma does not apply to light incident externally on a non-emitting plasma [47], as seen in the Dual Laser Plasma (DLP) photoabsorption technique [51][52]. Once the absorption coefficient κ_v is calculated one can generate an absorption spectrum using [1.42]. Even if the ground state density distribution, $N_i(r)$, is asymmetric, the resultant absorption spectrum line profile, in the self-similar expansion model, will be frequency-shifted but symmetric for large values of K. Symmetry is maintained if the excited level density distribution chosen is such that $N_k(r) \neq 0$, and approaches $N_i(r)$, in which case stimulated emission becomes significant. This *may not* be the case if the velocity distribution is described by a relationship other than v(r) = K r, i.e. if the AFR is asymmetric. This is especially evident in the case of an asymmetric AFR combined with a symmetric ground level density distribution as seen in fig. 1.14.
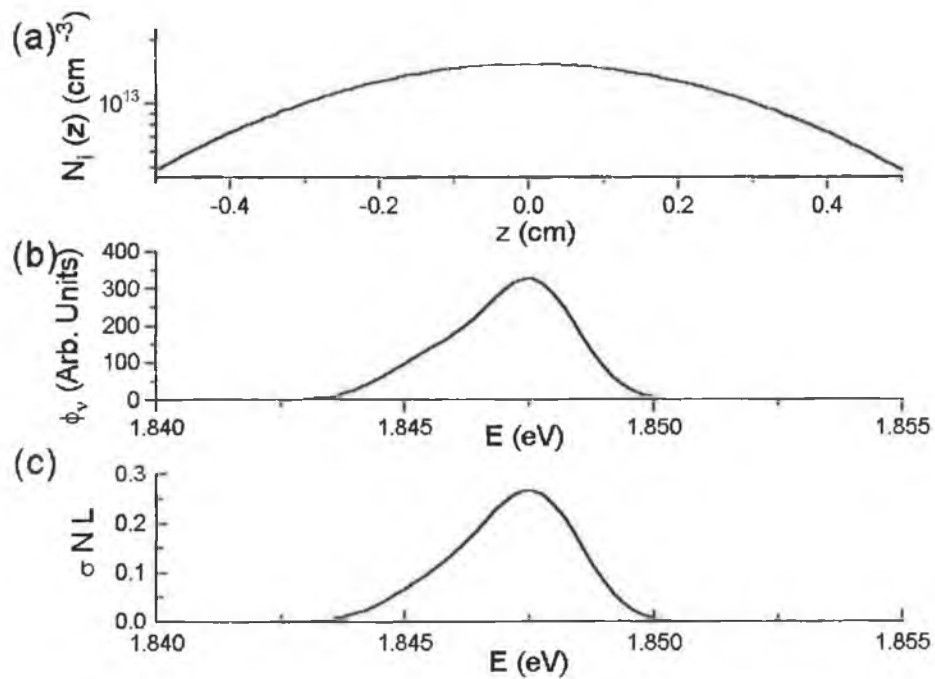
Fig. 1.14: The photoabsorption spectrum of the $1s^2 2s \rightarrow 1s^2 2p$ transition in Li^o (λ_o = 670.78 nm) (a) The ground level density distribution, $N_i(z)$ (b) the atomic frequency response $\phi_{Gaussian}$ (c) the resultant asymmetric absorption spectrum.

NOTE: The excited level density distribution $N_k(z) = 0$.

The velocity distribution chosen in fig. 1.14 was such that $v(z) = A_z z^4$; $z < 0$, $A_z = 1 \times 10^8$ cm^{-3} s^{-1}; $v(z) = K z$; $z \geq 0$. $K = 1 \times 10^8$ s^{-1}. This is conceivably a physically unrealistic velocity distribution. However, it is suitable for illustration purposes.

The velocity distribution for the ideal blast wave model (§1.2.2) can be obtained by differentiation of [1.9]. Using a velocity distribution of this form, i.e.

$$v(r) = a_r r^{3/2}$$ [1.45]

one obtains a symmetric atomic frequency response and hence a symmetric absorption spectrum, as shown in fig. 1.15. This is also the case using the self-similar expansion velocity distribution.
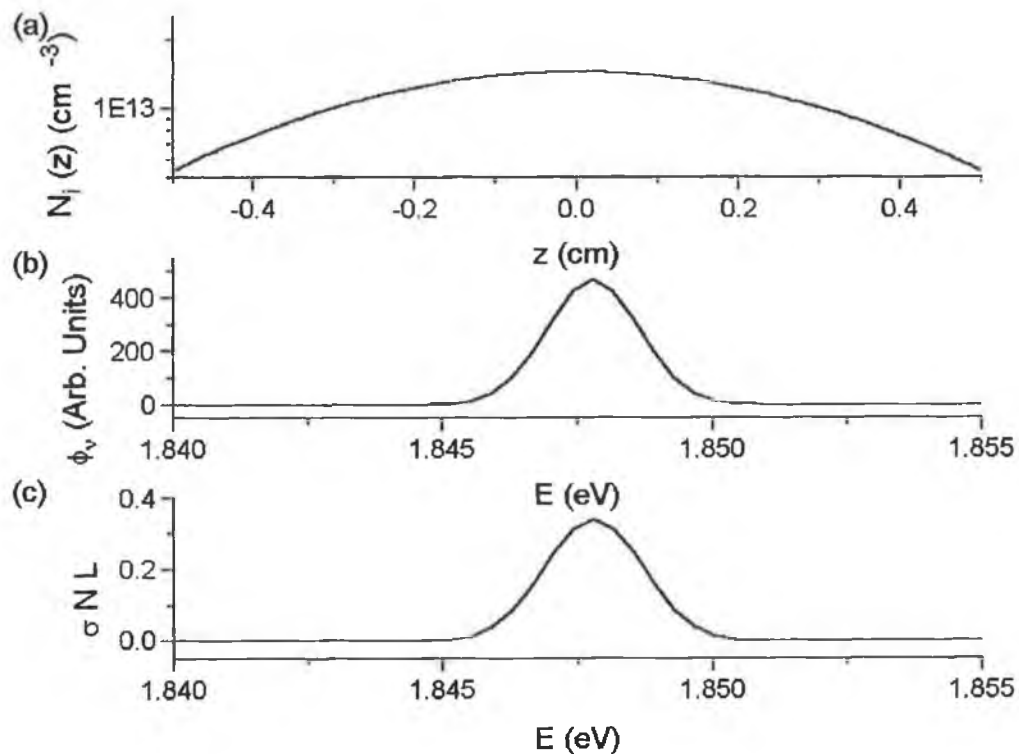
Fig. 1.15: The photoabsorption spectrum of the $1s^2 2s \rightarrow 1s^2 2p$ transition in Li^0 (λ_0 = 670.78 nm) (a) The ground level density distribution, $N_i(z)$ (b) the Gaussian atomic frequency response ϕ_v (c) the resultant symmetric absorption spectrum. The velocity distribution chosen is such that $v(r) = a_r r^{3/2}$; $a_r = 5 \times 10^6$ cm$^{-1/2}$ s^{-1}. This is the velocity distribution proposed by the ideal blast wave model.

1.5 Line Broadening Mechanisms

When an atom or ion makes a transition from one bound state to another of lower energy, the energy of the emitted photon is well defined (within the limits of Heisenberg's uncertainty principle). In the absence of perturbations, this transition gives rise to a spectral line whose profile is related to the spontaneous lifetime of the upper state, and on the distribution of velocities of the emitting species, resulting in a distribution of Doppler shifts. Collisions, electric and magnetic fields may all perturb the initial and final states of the transition, affecting the shape of the spectral line profile, though unaffecting the energy contained within it. Other mechanisms including Zeeman splitting, Van der Waals and resonance broadening will not be considered [39]. The observed profile thus contains valuable information about the conditions existing in the plasma. In the ensuing paragraphs three broadening mechanisms pertinent to the plasma model developed thus far, and to the plasma parameters obtained through the diagnostic techniques of the succeeding sections are described.

1.5.1 Natural Broadening

Natural line broadening arises from the fact that the quantum states of an atom do not have a single energy, but rather a small spread in energy. The effective spread is given by Heisenberg's uncertainty principle

$$\Delta E \approx \frac{\hbar}{\tau} \qquad \text{[1.46]}$$

where the lifetime τ is given by [39]

$$\frac{1}{\tau} = \sum_i A_{ki} \quad (s^{-1}) \qquad \text{[1.47]}$$

Typical values for τ in the optical region of the electromagnetic spectrum are of the order of 10^{-8} s, e.g. $\tau = 2.71 \times 10^{-8}$ s for the $1s^2 2s \rightarrow 1s^2 2p$ transition in lithium [40]. Natural broadening yields a dispersion profile that is Lorentzian in shape. It is usually negligible in the visible region of the spectrum but can become important in the case of

34

autoionising transitions, or for the case of extreme ultraviolet (EUV) lines of highly ionised impurities, due to the dependence of A_{ij} on v^3_{ij} (see [1.20]) [19].

1.5.2 Doppler Broadening

Doppler broadening is interpreted in terms of atom or ion thermal motions as discussed in §1.4.1. If the velocities of the atoms or ions are distributed according to a Maxwellian velocity distribution with temperature T, this gives rise to a Gaussian line profile of FWHM

$$\Delta\lambda_{D_{\frac{1}{2}}} = 2\sqrt{Ln2}\sqrt{\frac{2k_B T\lambda_o^2}{Mc^2}} \qquad\qquad [1.48]$$

$$\Delta\lambda_{D_{\frac{1}{2}}} = 7.16 \times 10^{-7}\lambda_o\sqrt{\frac{T}{\mu}} \qquad\qquad [1.49]$$

where M in [1.48] is the particle mass (kg), μ in [1.49] is the atomic mass $= M/m_u$ (amu), where $m_u = 1.66 \times 10^{-27}$ kg, λ_o is the centre wavelength (Å) and T the plasma temperature (Kelvin). This is plotted as a function of temperature for the lithium L_β line (113.9049 Å) (i.e. 1s $\rightarrow$ 3p in Li^{2+}) in fig. 1.16. Thermal Doppler broadening is most pronounced at high temperatures in light elements [4]. In the ultraviolet and visible region of the spectrum random thermal motion is the main contributor to the shape and width of the observed line profiles [39]. Additional Doppler broadening can occur in non-thermal plasmas stemming from the fact that the charged particles may not be distributed according to a Maxwellian velocity distribution. There may also be a large turbulent velocity component superimposed on the thermal components thus broadening the line further. Finally, there may be mass motion of the plasma or large clumps of it [53].
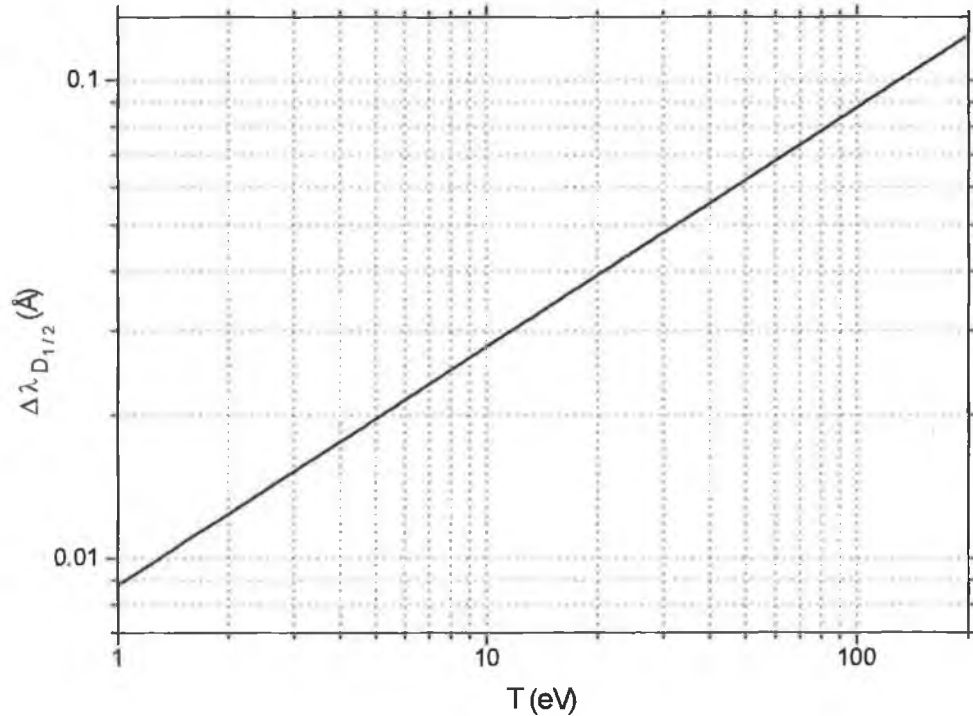
Fig. 1.16: The effect of temperature on $\Delta\lambda_{D_{\frac{1}{2}}}$ for the lithium L_β line (i.e. 1s → 3p in Li^{2+}) at 113.9 Å.

1.5.3 Stark Broadening

The theory of Stark or pressure broadening was initiated in 1905 by H.A. Lorentz. It arises from the influence of nearby particles and in particular their electric fields upon the emitting particle. These fields are due to electrons and ions that are within a Debye[2] length of the radiating species. Close to the target surface where the plasma density is highest, Stark broadening dominates. It decreases with increasing distance from the target, unlike Doppler broadening which remains fairly constant [20]. Stark broadening is a powerful diagnostic in the determination of electron density especially for the case of optical transitions. For the case of quasi-static Stark broadening of hydrogenic lines originally developed by Holtzmark (1919), in which the atom is

---

[2] The Debye length is the distance over which the electric field of an individual charge extends before it is effectively shielded by oppositely charged particles in its surroundings. The Debye length is defined as

$$\lambda_D = \left(\frac{\varepsilon_o k_B T_e}{N_e e^2}\right)^{\frac{1}{2}}$$

Beyond λ_D collective effects dominate [2].

36

assumed to radiate in an environment that is effectively static during the period of emission the full half width $\Delta\lambda_{1/2}$ is given by [53]

$$\Delta\lambda_{\frac{1}{2}} = 8.16 \times 10^{-19} \left(1 - 0.7 N_D^{-\frac{1}{3}}\right) \lambda_o^2 \left(n_k^2 - n_i^2\right) \left(\frac{Z_p^{\frac{1}{3}}}{Z_e}\right) N_e^{\frac{2}{3}} \quad (\text{Å}) \qquad [1.50]$$

$$N_D = 1.72 \times 10^9 \frac{T^{\frac{3}{2}}}{N_e^{\frac{1}{2}}} \qquad [1.51]$$

where it has been assumed that the plasma is electrically neutral, i.e. $N_p = {N_e}/{Z_p}$. N_p is the density of perturbers (ion density in this case), λ_o (Å) in [1.50] is the centre wavelength, N_e (cm^{-3}) is the electron density, n_k and n_i are respectively the upper and lower principal quantum numbers of the transition, Z_p is the ionic charge, Z_e is the nuclear charge and T (eV) is the temperature. N_D in [1.50] is the number of particles in a Debye sphere. It may be observed from [1.50] that the Stark width increases with increasing principal quantum number of the upper level. The quasistatic Stark width of the lithium L_β line (113.9049 Å) is plotted in fig. 1.17 as a function of temperature and density. As can be seen from the overlap of the curves in fig. 1.17, the half-width is particularly insensitive to temperature changes. A refinement to Holtzmark's theory involved the introduction of ion-ion correlation and shielding effects due to the presence of the surrounding ions and electrons, as well as the introduction of a time dependence of the ion microfields. The ionic contribution to the widths of Stark broadened lines is usually less than ~20% [54], and introduces some asymmetry to the line profile [4][50].
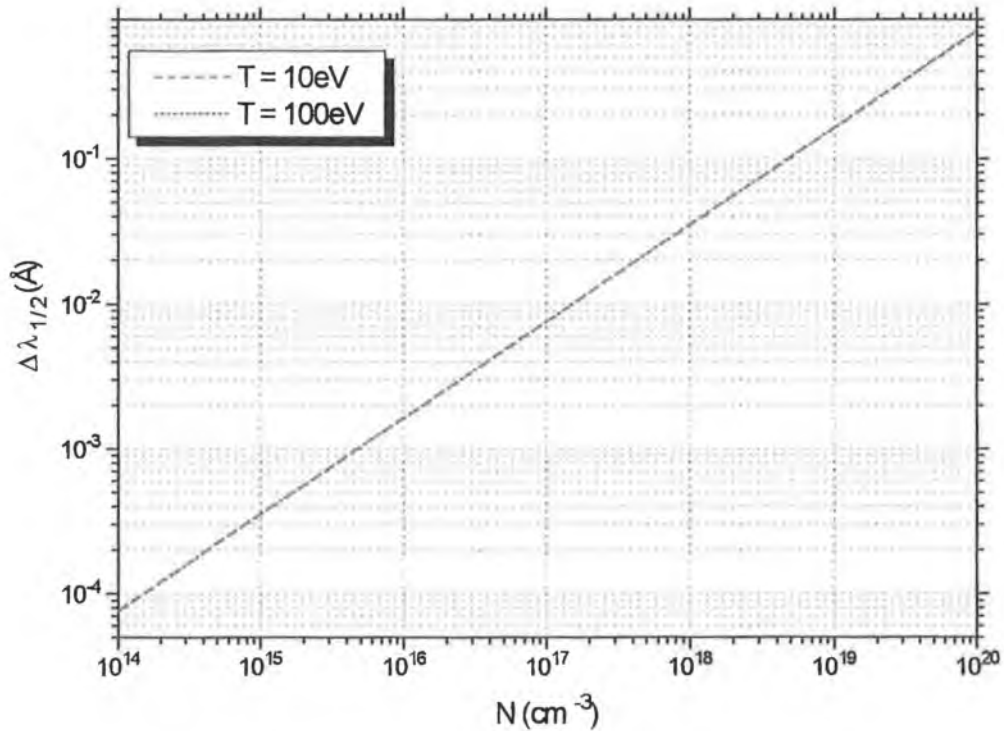
Fig. 1.17: $\Delta\lambda_{\frac{1}{2}}$ as a function of temperature and density for the lithium L_β line (λ_o = 113.9 Å).

Heretofore, the contribution to the half-width due to the plasma electrons, whereby a wave train of light emitted by an atom is perturbed by fast impacts (due to the high velocity of the electrons), well separated in time, has been neglected. This theory, referred to as the impact theory, was primarily developed by Lorentz, Lenz, Weisskopf and Lindholm, and was further refined by Baranger, Kolb and Griem [4]. However, despite the fact that the detailed features of the line profile are very dependent on the electron contribution, the half-widths are often insensitive. This is notably so for the L_β, L_δ etc. hydrogenic lines. On the other hand, the L_α etc. are strongly affected by electron collisional broadening (and sometimes dominated). Electron impact broadening also dominates isolated spectral lines of neutral atoms and singly ionised nonhydrogenic ions [50][55]. This leads to a shifted but symmetrical line profile of Lorentzian shape. Therefore, one can calculate the FWHM of these lines using the impact approximation, and then correct for the relatively unimportant quasistatic neutral or ion broadening contribution [53]. The width (FWHM) and lineshift are given to a good approximation (~20 → 30%) for neutral atoms by [53][56]

$$\Delta\lambda_{\frac{1}{2}\text{impact}} = \left\{ 2W\left(\frac{N_e}{10^{16}}\right) \right\} + \left\{ 3.5A\left(\frac{N_e}{10^{16}}\right)^{\frac{1}{4}}\left[1-\frac{3}{4}N_D^{-\frac{1}{3}}\right]W\left(\frac{N_e}{10^{16}}\right) \right\} \quad (\text{Å}) \quad \textbf{[1.52]}$$

$$\Delta\lambda_{\text{shift}} = \left\{ D\left(\frac{N_e}{10^{16}}\right) \right\} \pm \left\{ 2A\left(\frac{N_e}{10^{16}}\right)^{\frac{1}{4}}\left[1-\frac{3}{4}N_D^{-\frac{1}{3}}\right]W\left(\frac{N_e}{10^{16}}\right) \right\} \quad (\text{Å}) \quad \textbf{[1.53]}$$

where the first term (in chained brackets) in both equations represents the electron contribution, while the second term represents the correction for neutral atoms. The electron density N_e is given in cm^{-3}. The coefficients W, A and D are independent of density and slowly varying functions of temperature, comprehensive tables for which can be found in [55] (see table 1.1). The minus sign in [1.53] applies to the high temperature range of the few lines that have a negative $\frac{D}{W}$ value at low temperatures. In order to make [1.52] and [1.53] applicable to singly ionised species one need only replace the coefficient $\frac{3}{4}$ by 1.2 [53]. These formulae are valid only in the parameter range $N_D \geq 2$ and $0.05 < A\left(N_e/10^{16}\right)^{\frac{1}{4}} < 0.5$ [53]. Typical values for the coefficients W, A and D are given in table 1.1 for various transitions in lithium.

Transition	λ_{vac} (Å)	T (K)	W (Å)	A	D (Å)
$1s^2 \rightarrow 1s2p$	199.279	5000	0.279e-3		-0.165e-3
		10000	0.207e-3		-0.120e-3
		20000	0.156e-3		-0.861e-4
		40000	0.123e-3		-0.599e-4
$1s^2 \rightarrow 1s3p$	178.014	5000	0.236e-2		0.161e-2
		10000	0.178e-2		0.110e-2
		20000	0.137e-2		0.729e-3
		40000	0.108e-2		0.481e-3

Table 1.1: W, A, D Stark broadening coefficients for selected transitions in lithium (at $N_e = 10^{17}$ cm^{-3}) (after [55]). **NOTE:** For typical ion lines A values (a measure of the relative importance of ion broadening) are $<< 1$ [55].

Dimitrijevic and Sahal-Bréchot have published extensive Stark broadening parameters of spectral lines of multicharged ions (see references in [57]) including Li II [57] for perturber densities from $10^{15} \rightarrow 10^{18}$ cm^{-3} and temperatures T = 2500 $\rightarrow$ 50000 K for

which the electron impact approximation is valid. These are given in table 1.2 for a perturber density $N_e = 10^{17}$ cm^{-3}.

Transition	λ_{vac} (Å)	T (K)	Width (Å)	Shift (Å)
$1s^2 \rightarrow 1s2p$	199.3	5000	0.557e-03	0.391e-04
		10000	0.395e-03	0.401e-04
		20000	0.286e-03	0.274e-04
		40000	0.211e-03	0.175e-04
$1s^2 \rightarrow 1s3p$	178.0	5000	0.282e-02	-0.308e-03
		10000	0.228e-02	-0.246e-03
		20000	0.189e-02	-0.236e-03
		40000	0.161e-02	-0.197e-03
$1s^2 \rightarrow 1s4p$	171.6	5000	0.801e-02	-0.129e-02
		10000	0.704e-02	-0.118e-02
		20000	0.625e-02	-0.995e-03
		40000	0.555e-02	-0.806e-03
$1s^2 \rightarrow 1s5p$	168.7	5000	0.161e-01	-0.303e-02
		10000	0.155e-01	-0.289e-02
		20000	0.146e-01	-0.238e-02
		40000	0.134e-01	-0.194e-02

Table 1.2: Electron-impact full halfwidths and shifts for the $1s^2 \rightarrow 1snp$ (n = 2,3,4,5) transitions in Li$^+$ (after Dimitrijevic and Sahal-Bréchot [57]).

In order to derive densities with an accuracy of ~30 to 40% one must apply a convolution of the electron (impact) profile, requiring a temperature estimate, and the ion profile. Otherwise, it is advisable to pursue transitions dominated by quasi-static ion broadening [53], the criterion for the validity of which is given by [50][55].

Generally, at high densities the broadening by ions can be calculated with the quasi-static approximation, but at lower densities a transition into the impact domain may occur before the Doppler broadening becomes significant [58].

One should note that the impact approximation is not exclusive to the electron contribution, nor is the quasistatic approximation unique to the ion contribution, to Stark broadening. Broadening by protons and heavy (i.e. slow) ions can be described by the impact approximation for early members of hydrogen and hydrogenic line series [55][57].

40

1.6   Theoretical Aspects of the Experimental Techniques Employed

Fast frame photography, shadowgraphy and the dual laser plasma (DLP) photoabsorption technique were employed as diagnostic tools during the course of this work to facilitate the study of the expansion of a laser generated lithium plasma. The following sections outline the principles of these three techniques, indicating the plasma parameters that may be quantitatively ascertained either directly or indirectly through the introduction of various plasma radiation model assumptions.

1.6.1   The Fast Frame Photography Technique

Fast frame photography has long been used as a diagnostic aid in the study of laser produced plasmas, either through the usage of frame converter cameras [24][30], or digitally, by employing gated intensified charge coupled devices (ICCDs) [26][28], thus greatly enhancing sensitivity. The attraction of the technique lies in its relative ease of implementation. A sequence of short exposure (typically a few ns) frames of the self-emitting plume is obtained at various time delays during the course of the plasma's evolution, thus providing both spatial and temporal resolution. As in fig. 1.8, the observation is generally 'side on', at right angles to the axis of expansion. Introducing various narrow band interference filters in front of the camera, to limit the spectral range of the imaged light to that of known emission lines, introduces the possibility of tracking the spatio-temporal evolution of the corresponding excited states. The measured intensities in this case are integrated over the line profile. Spectrally resolved images can also be obtained if an imaging spectrometer is used [59]. In addition to the possibility of tracking the evolution of excited states, one may also estimate species velocities directly from the images, either using the leading luminous plume edge as a marker, thus providing an estimate of the maximum expansion velocity [28][33], or through the approach proposed by Boland *et al.* [60], whereby at fixed distances, d, from the target surface along the axis of expansion, the time, t, at which the maximum in intensity occurred was recorded. By plotting a graph of d against t, the most probable velocity was imparted. The fast frame photography technique has successfully been applied to the study of expanding plumes both in vacuum [16][61] and in a background gas [28][33][35].

The light intensity recorded at a single pixel (x,y) is given by (see figs. 1.8 and 1.9 for the expansion and observations geometries)

$$I_{(x,y)} = \int_{-\frac{L_c}{2}}^{+\frac{L_c}{2}} \int_{line} \varepsilon_\nu(r)dzd\nu \qquad [1.54]$$

in which $\varepsilon_\nu(r)$ is the emission coefficient (see §1.4.2(a)) at the photon frequency ν, and L_c is the total length of the emitting plasma chord. The radial distribution of emitters $N(r)$ can be obtained by Abel inversion of [1.54] assuming that:

(a)   The observed light rays are virtually paraxial.
(b)   The plasma is optically thin, in which case $\varepsilon_\nu(r)$ is linearly proportional to $N(r)$.
(c)   There is radial symmetry in the (y,z) plane.

Taking account the effect of a narrow band interference filter, [1.54] becomes

$$I_{(x,y)} = \int_{-\frac{L_u}{2}}^{+\frac{L_u}{2}} i(r)dz \qquad [1.55]$$

where $i(r) = \int_{line} \varepsilon_\nu(r)d\nu$. Finally, introducing a change of variable (with reference to fig. 1.9) so that

$$r^2 = z^2 + y^2$$
$$\Rightarrow 2rdr = 2zdz$$
$$\therefore dz = \frac{r}{z}dr$$

$$\text{But } z = \sqrt{r^2 - y^2}$$

$$\Rightarrow dz = \frac{r}{\sqrt{r^2 - y^2}}dr \qquad [1.56]$$

42

one obtains the integral equation

$$I_{(x,y)} = 2 \int_{r=y}^{R} \frac{i(r) r}{\sqrt{r^2 - y^2}} \, dr \qquad [1.57]$$

which is the Abel integral equation. $i(r)$ is recovered by inversion of [1.57]. This yields

$$i(r) = -\frac{1}{\pi} \int_{r}^{R} \frac{I'(x, y)}{\sqrt{y^2 - r^2}} \, dy \qquad [1.58]$$

where $I'(x, y)$ is the first derivative of the radiance function with respect to the lateral coordinate y (x is fixed).

The first application of Abel's integral to 'side on' measurements appears to have been carried out by Hörmann in 1935 [62]. Since then several methods have been devised to solve [1.58] without the need for differentiation. Differentiation tends to amplify enormously any inherently noisy data during the inversion process. Thus, least squares polynomial fit methods [63], piecewise cubic spline functions fitted by least square methods [64], iterative methods [65] and various transform methods [66][67] have been suggested as derivative free approaches to solving [1.58]. Several factors may influence the solution to [1.58]. Initially, the plasma may not be optically thin as assumed, and self-absorption, (which may be a function of intensity), may be significant. When taken into account, these effects yield a nonlinear integral equation [62]. This topic has been treated by [68] using the so-called two-path method. Also refraction effects may be non-negligible [69][70][71], and the initial assumption of radial symmetry may be invalid thus requiring a generalisation of the Abel method [72].

Furthermore, the Abel transform inversion procedure provides only the distribution of the corresponding excited state atomic densities in the plume. An appropriate radiation model for the plasma is then required in order to obtain ground state population densities and possibly electronic densities. This was accomplished by [73] by digitally imaging a hydrogen arcjet plume assuming LTE, while Elder *et al.* determined the

43

absorption and emission coefficients of a non-optically thin cylindrically symmetric source assuming LTE [74].

1.6.2 The Shadowgraph Technique

Shadowgraphy[3] records the modifications to the free space propagation of electromagnetic radiation, due to the abrupt variations in the electrical properties of the medium.
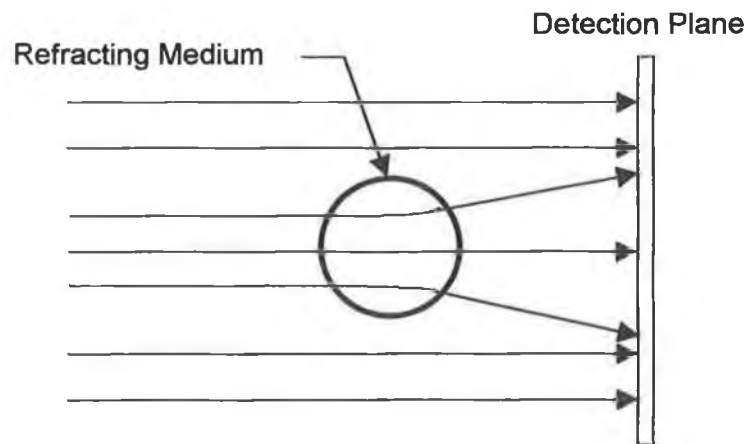
Fig. 1.18: The basic principle of the shadowgraph technique.

In its simplest form, a collimated beam of light passes through the test section under consideration and falls directly onto a recording device, such as a photographic plate or CCD camera, as in fig. 1.18. Assuming a non-absorbing medium, the variations in intensity occurring at the detection plane result from the different paths taken by rays traversing the medium. In the case of a laser produced plasma, self-emission from the refracting plasma is eliminated by using a relatively intense back-lighting radiation source. Provided the intensity of the probe beam is not too great, the technique is effectively non-perturbing. Temporal resolution is generally achieved by using short pulses of background radiation. Pulsed tunable laser light sources prove particularly useful in this regard, further introducing strong interference effects at the detector

---

[3] The inception and development of shadowgraphy (shadow photography) are usually attributed to Dvorak, who in 1880 used it to photograph air disturbances [75].

44

plane. One can show that the intensity modulations in the shadowgraph are sensitive to the second derivative of the index of refraction [75]. The technique thus proves suitable to the diagnosis of laser produced plasmas where steep spatial density gradients, and thus refractive index gradients exist. In general it is difficult to obtain high accuracy quantitative data from shadowgraphs without the supplementary information provided by, for example, Schlieren or interferometric techniques [76].

The strength of the interaction of electromagnetic radiation with "macroscopic" matter is embodied in the value of the index of refraction. The value of the refractive index of a plasma is due to the contributions from the plasma electrons, neutrals and ions. It is well known that the index of refraction of a plasma at optical frequencies is largely due to the free electron contribution [77][78][79]. However, in the vicinity of an atomic resonance significant additions must be made [78][80][81][82][83]. In addition, anomalous dispersion must be taken into account. Applying the dispersion theory of light (originally developed by H.A. Lorentz (1878)), which describes the dependence of the index of refraction on frequency, to the case of a laser produced plasma in the region of an atomic resonance, one obtains [80]

$$\tilde{n}(\omega,r)^2 - 1 = \left(\frac{1}{4\pi\varepsilon_o}\right)\frac{4\pi N(r)e^2 f_{ik}}{m_e}\frac{1}{\omega_o^2 - \omega^2 + i\zeta\omega} + n_e(\omega,r)^2 - 1 \qquad [1.59]$$

where $N(r)$ is the spatially variant number density of atoms or ions in the plume, $\tilde{n} = n - i\kappa$ is the complex refractive index, ζ is the resonance line-width (FWHM), and ω_o is the centre frequency. Here, it has been assumed that in the region near ω_o, the free electrons are the only other possible contributors to the refractive index. This contribution, as a function of frequency, is equal to

$$n_e(\omega,r) = \sqrt{1 - \frac{\omega_p(r)^2}{\omega^2}} \qquad [1.60]$$

where ω_p is the plasma frequency for an electron density N_e such that

$$\omega_p(r) = \left(\frac{1}{4\pi\varepsilon_o}\right)\frac{4\pi N_e(r)e^2}{m_e}$$

[1.61]

The particle densities and hence the magnitude of the refractive index largely determine the intensity distribution of light recorded at the detector plane, thereby explaining the principle of the diagnostic. From [1.59] and [1.60], one can see that the electron gas contribution to the phase index of refraction is negative and slightly less than unity. On the other hand, the atomic and ionic contributions are positive. The 'two' effective contributions to the plasma refractivity are thus opposite in sign [77]. This has been used as the basis of a resonance interferometry technique to study magnetically insulated pulsed ion sources [84]. The complex term in [1.60] gives rise to the effect of anomalous dispersion as illustrated in fig. 1.19.
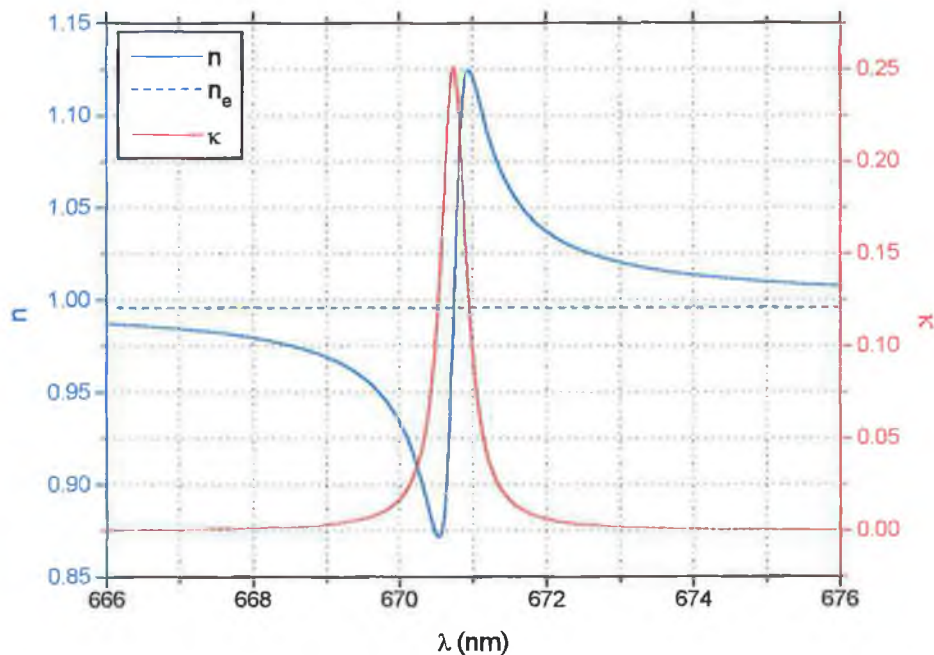
Fig. 1.19: The real (n) and imaginary (κ) parts of the plasma refractive index as a function of wavelength (nm) centred about the $1s^22s \rightarrow 1s^22p$ transition in lithium. ($\zeta \sim 0.4$ nm, $N(r) = 1 \times 10^{24}$ m^{-3}, $N_e(r) = 1 \times 10^{25}$ cm^{-3}, $f_{ik} = 0.75$, $\lambda_o = 670.78$ nm). Also shown is the electronic contribution, n_e, to the plasma refractive index.

The shadowgraph technique has been applied on numerous occasions during the 60's and 70's to the study of laser produced plasmas. References to such early works can be found in [2]. Michaelis and Willi [85] (and [86] for improved analysis) showed that

46

when probing a laser produced plasma of steep refractive index gradient with a pencil of laser light, the rays traversing the denser regions suffer greater refraction and may interfere with other rays, thus producing a pattern of bright and dark fringes – the so called refractive fringes. Using an optical path analysis, the authors showed that the generally 'unwanted' refractive fringes in shadowgraphy could be used to diagnose electron density distributions. Grid Image Refractometry (GIR) [87] whereby the probe beam is broken up into 'rays' by being passed through a grid before traversing the plasma, has been applied to the study of plasma formation on a CH target. By measuring the refraction angles, and introducing the assumption of cylindrical symmetry the resultant data was Abel inverted to yield population density distributions. Population densities have also been estimated using two- [77] and five- probe wavelength [78] measurements. The method assumes that far away from resonance, the contribution to the refractive index from the non-electronic species is constant with wavelength. Thus, by measuring the plasma refractivity at a number of wavelengths, the electron density can be ascertained. Using the strong variation of the plasma refractivity in the spectral vicinity of an atomic transition, an extension to the resonance interferometry technique called tomographic resonance interferometry has been applied [81] to measure chromium ground state densities, as well as Doppler and Lorentz widths in a helium pulsed plasma. Using a complex experimental set-up, the technique used involved scanning the probe wavelength of a dye laser over the investigated transition, and measuring both the spectral and spatial variations of the refractive index using a single shot tomographic method that provides simultaneous recording of all projections necessary for one tomogram. Dye laser resonance absorption photography (DLRAP) has also been used to probe the plasma created using aluminium [88][89], polyimide and polyethyleneterephthalate [89] targets. The basis of the technique involved back-lighting the plasma using the output of a probe laser tuned to a resonance transition. In this manner the spatial distribution of ablated products could be monitored.

It should be pointed out that shadowgraphs obtained using the basic principle illustrated in fig. 1.19 may be regarded as single beam holograms. Single beam

47

holograms of laser produced plasmas were first recorded[4] in the 60's [2]. The technique is reminiscent of the phase contrast imaging technique of nonabsorbing objects originally developed by Zernike [90]. Variations in the optical thickness of an object, as a result of refractive index variations or thickness variations or both, alter the phase of portions of the incoming wavefront, before interfering at the detector plane. Raven *et al.* [91] have applied this technique with great success to record phase contrast images of a 100 μm boron fibre using 60 keV coherent synchrotron x-ray radiation, while simultaneously computing the diffraction intensity distribution across the fibre in the detection plane, by means of the Kirchoff integral [92].

Following the analysis first proposed by Michaelis and Willi [85], and later refined by Cunningham *et al.* [86], the observed fringes in the detector plane (at a probe wavelength where the contribution to the refractive index from neutral and ionised species is negligible) can be employed to extract the refractive index profile of the plasma, and hence the electron density gradient. The path of a probe ray traversing a radially symmetric plasma, possessing a maximum electron density at the axis of symmetry and which decreases monotonically as a function of the radial co-ordinate is always in a direction of increasing refractive index [86][93]. Under these conditions, the plasma acts as a diverging lens. The equation governing the trajectory of a ray in a radially symmetric field is given by Bouguer's formula [79], i.e.

$$rn(r)\sin(i_r) = p_r \qquad \qquad \textbf{[1.62]}$$

The impact parameter p_r is constant along a ray, and its value thus serves as a label for each ray [79]. The geometry of an arbitrary probe ray traversing a radially symmetric plasma is illustrated in fig. 1.20.

---

[4] The technique of in-line holography was originally developed by Gabor in 1947. His work remained somewhat unnoticed until the 60's, when it experienced a resurgence of interest with the inception of the laser.
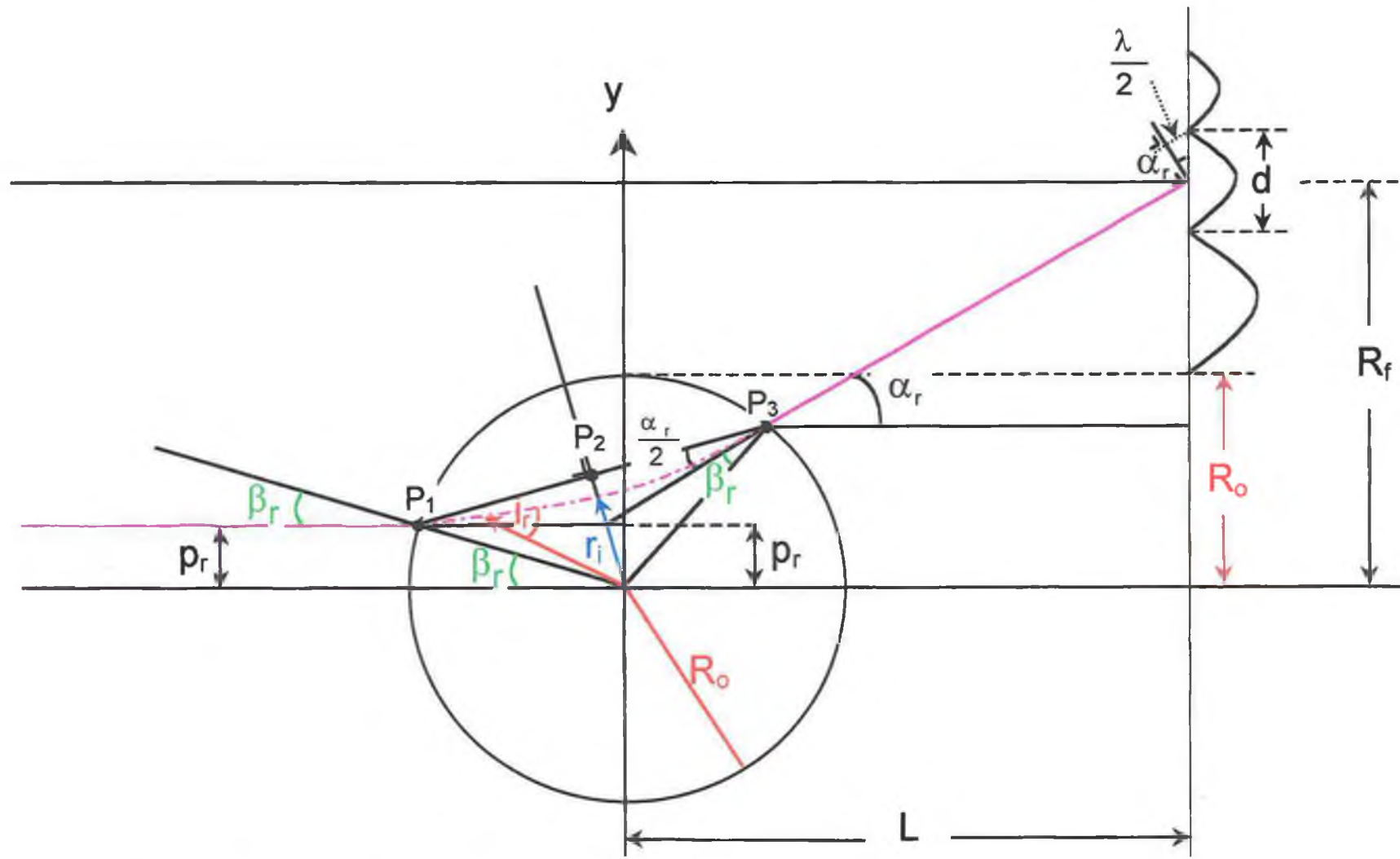
Fig. 1.20: The geometry of a probe ray traversing a radially symmetric plasma. The symbols used are explained in the text.

Six main assumptions are used in the analysis of Cunningham *et al.* [86]. These are as follows:

(1)   As previously mentioned, contributions from neutral and ionised species to the refractive index must be negligible. This assumes that the probe wavelength is not in the vicinity of an atomic resonance transition.

(2)   Geometric optics must be applicable. This places an upper limit on the maximum permissible refractive index gradient to be probed [94][95], i.e.

$$\left|\frac{\partial n}{\partial x}\right| << \frac{n}{\lambda_{vac}} \qquad\qquad \textbf{[1.63]}$$

where x is the co-ordinate in the direction of the density gradient perpendicular to the probe ray. For an electron gas [1.63] becomes [95]

$$\left|\frac{\partial n_e}{\partial x}\right| << 2\frac{N_{ec} - N_e}{\lambda_{vac}} \qquad\qquad \textbf{[1.64]}$$

Using condition [1.64] corresponding to the maximum value of N_e to be diagnosed, it is possible to determine the maximum permissible electron density gradient. This is plotted in fig. 1.21 for a probe wavelength of 669.7 nm. With reference to fig. 1.21 and [1.64] it is apparent that a gradient of $<< \sim 6 \times 10^{24}$ cm^{-4} can be tolerated if 669.7 nm radiation is used to probe an electron density not exceeding $\sim 8 \times 10^{20}$ cm^{-3} (0.8 times the critical density for an Nd:YAG laser).
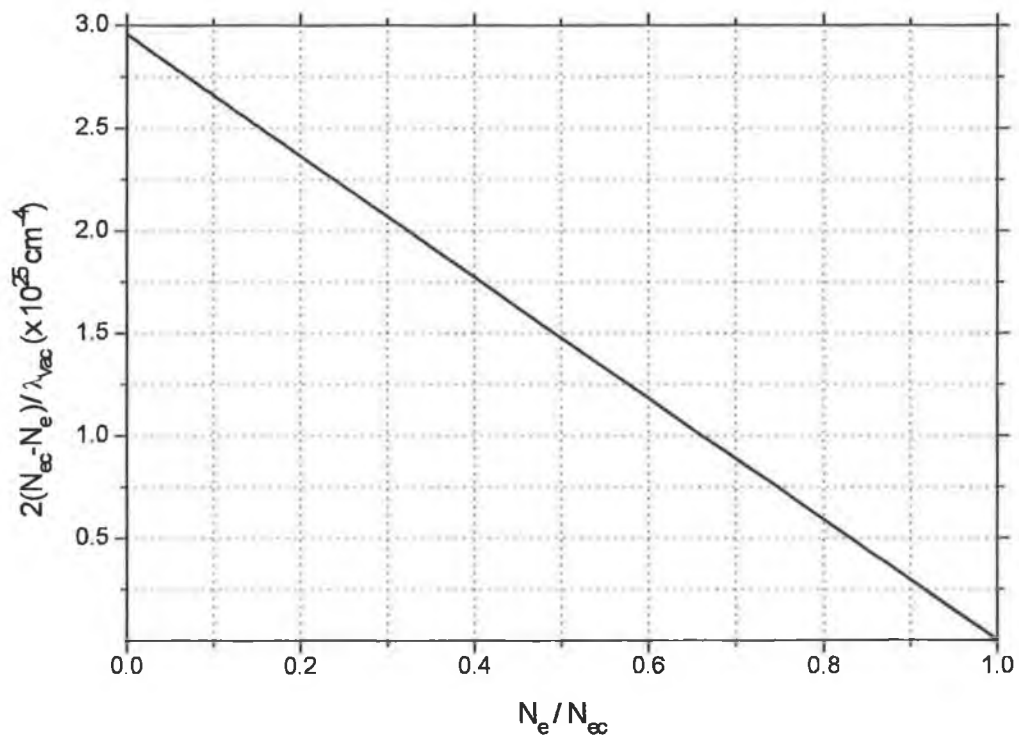
Fig. 1.21: The variation of $\dfrac{2(N_{ec} - N_e)}{\lambda_{vac}}$ as a function of electron density expressed as a fraction of N_{ec} for a probe wavelength (λ_{vac}) of 669.7 nm.

(3)   The ray trajectories must follow a parabolic path through the plasma. This is almost certainly the case provided the exit angle of the ray $\alpha_r(p_r)$ (see fig. 1.20) is small (<<1). Deviations from a parabolic path can be expected in strongly refracting plasmas.

(4)   Arguably the most severe assumption; the rays must be refracted solely in a plane parallel to the direction of propagation of the ray. This may only be the case for cylindrically symmetric plasmas, where refractive index changes along the axis of symmetry, perpendicular to the direction of ray propagation are negligible.

(5)   The existence of an 'optically effective plasma radius' (OEPR) is assumed. This is the radius of the dark region (R_o in fig. 1.20) interior to the last 'non-deviated' ray, i.e. the last ray experiencing negligible refraction, for the particular probe wavelength under consideration. It should be emphasised that the OEPR is a function of the probe beam wavelength utilised.

51

(6)   Finally the refracted wavefronts are assumed planar upon reaching the detector. This may be achieved by positioning the detector at large distances relative to the plasma.

Assuming the geometry of fig. 1.20, this final assumption combined with the path difference of λ between adjacent fringes in the detector plane, furnishes the geometrical relationship

$$\alpha_r = \sin^{-1}\left(\frac{\lambda}{d}\right)$$

[1.65]

where α_r is a function of p_r, the impact parameter of a ray. The equation of a ray exterior to the plasma exiting at point P_3 is given by

$$y = \tan(\alpha_r)x + b$$

[1.66]

However at $x = L$, $y = R_f$ and therefore

$$y(L) = R_f = \tan(\alpha_r)L + b$$
$$\Rightarrow b = R_f - \tan(\alpha_r)L$$

and thus

$$y = \tan(\alpha_r)(x - L) + R_f$$

[1.67]

The intersection of the plasma surface at the OEPR with the plane under consideration obeys the relation

$$x^2 + y^2 = R_o^{\,2}$$

[1.68]

Therefore the point of intersection of the two curves, at the exit point P_3, is determined by simultaneously solving [1.67] and [1.68], i.e.

52

$$[(x-L)t+R_f]^2 = R_o^2 - x^2 \qquad [1.69]$$

where $t = \tan(\alpha_r)$. Therefore

$$x^2(1+t^2) + x(2R_f t - 2Lt^2) - 2LR_f t + (Lt)^2 + (R_f^2 - R_o^2) = 0 \qquad [1.70]$$

The relevant root of [1.70] is

$$x_{P_3} = L - \frac{\left\{ R_f t + L - \left[(R_f t)^2 - (Lt)^2 + 2LR_f t - (R_f^2 - R_o^2)(1+t^2) \right]^{1/2} \right\}}{(1+t^2)} \qquad [1.71]$$

and thus

$$y_{P_3} = \sqrt{R_o^2 - x_{P_3}^2} \qquad [1.72]$$

Also from fig. 1.20 it is apparent that

$$\beta_r = \tan^{-1}\left(\frac{y_{P_3}}{x_{P_3}} \right) - \alpha_r \qquad [1.73]$$

Returning to the assumption of a parabolic path (assumption 3) through the plasma the co-ordinate 'b' in fig. 1.22 may be determined from the following. The equation of a parabola is

$$y = ax^2 \qquad [1.74]$$

53
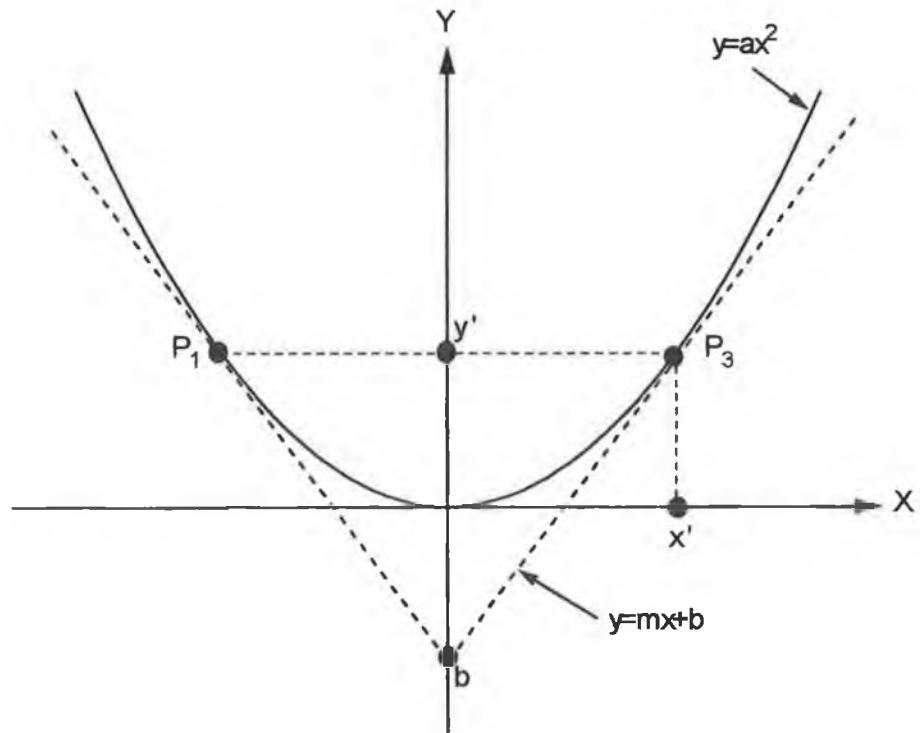
Fig. 1.22: The geometry of the parabolic path assumption used to describe a ray's trajectory through the plasma.

Differentiating [1.74] one obtains the slope of the line tangent to the an arbitrary point on the parabola, i.e. $\dfrac{dy}{dx} = 2ax$. The equation of the tangent may be described by the relation y=mx+b. Therefore, at $x = x'$, one obtains

$$y = 2a(x')^2 + b \qquad\qquad [1.75]$$

and therefore $b = y - 2a(x')^2$. However noting that $y' = a(x')^2$ by definition (using [1.74]), one obtains an expression for b, namely

$$b = -y' \qquad\qquad [1.76]$$

for all x'. Thus, with reference to fig. 1.22 it may be observed that the distance from the y-intercept (point b) of any tangent to the parabola at a point $(x'y')$ to the line segment $[P_1P_3]$ is $2y'$ for all x'.

54

Resuming the geometrical analysis of the RFD technique, it is apparent with reference to fig. 1.20 and using [1.76] that

$$r_i = R_o \sin\left(\beta_r + \frac{\alpha_r}{2}\right) - \frac{1}{2}\cos\left(\beta_r + \frac{\alpha_r}{2}\right)\tan\left(\frac{\alpha_r}{2}\right)$$

[1.77]

Finally, employing Bouguer's formula ([1.62]), and [1.77] and recognising that at r_i, the angle i_r equals $\frac{\pi}{2}$, it is possible to obtain a relation for $n(r_i)$, i.e.

$$n(r_i) = \frac{p_r}{r_i}$$

[1.78]

where p_r can be found from the geometrical relationship

$$p_r = R_o \sin(\beta_r)$$

[1.79]

Thus, by employing equations [1.65],[1.71],[1.72],[1.73],[1.77] and [1.78] to obtain α_r, x_{P_3}, y_{P_3}, β_r, r_i and $n(r_i)$ respectively, and determining R_o from the shadowgraphs it is possible to extract the refractive index profile of a radially symmetric plasma (through different values of r_i for different refracted rays).

One may also use Fermat's principle to describe the path of a ray which traverses the the plasma. This is based on an extremum principle expressed as

$$\partial \int_{P_1}^{P_3} n_r ds = 0$$

[1.80]

where the points P_1 and P_3 are shown in fig. 1.20, and ds is a differential arc length along the ray path. Equivalently Fermat's principle can be expressed in cylindrical co-ordinates as [82][86]

55

$$\frac{d\theta}{dr} = \frac{\pm n_r(R_o)p_r}{r\left[n_r(r)^2 r^2 - n_r(R_o)^2 p_r^2\right]^{\frac{1}{2}}} \qquad [1.81]$$

The + sign is used to the left of the turning point P_2, while the − sign is used to the right of P_2. The exit angle of any ray can then readily be computed using the relation [82]

$$\alpha_r(p_r) = (\pi - 2\beta_r) + 2p_r n_r(R_o) \int_{R_o}^{r_t} \frac{dr}{r\left[n_r(r)^2 r^2 - n_r(R_o)^2 p_r^2\right]^{\frac{1}{2}}} \qquad [1.82]$$

The ordinary differential relation of [1.81] may be solved using a Runge-Kutta integration technique, without the restrictive assumption of a parabolic path.

1.6.3 The Dual Laser Plasma (DLP) Photoabsorption Technique

The technique of probing the electronic structure and ion decay dynamics of a laser produced plasma using the radiation emitted by another plasma is known as the Dual Laser Plasma (DLP) photoabsorption technique [96]. DLP photoabsorption involves probing the absorbing plasma under different experimental conditions. Spectra of multiply or singly charged ions or neutrals are obtained when probing the plasma in different spatio-temporal regimes, thus introducing selectivity of absorbing species. The technique basically involves recording two spectra. The first, denoted I_{ν_o}, is that of a backlighting plasma generated from (usually) a high Z material such as tungsten. The second, denoted I_ν, involves generating a second plasma (the sample plasma) from a different target material using a separate laser. The radiation from the backlighting plasma passes through, and is absorbed by the sample plasma before falling on the detector. By application of Beer's law, i.e.

$$I_\nu = I_{\nu_o} \exp(-\sigma NL) \qquad [1.83]$$

where σ is the absorption cross-section, N is the density of absorbing atoms or ions and L is the absorbing column length, it is possible to generate an absorption

spectrum. Most DLP experiments have hitherto been concerned with the study of the fundamental aspects of the photoionisation process [97]. In the following sections, the extension of the technique to the interpretation of the Extreme UV (EUV) photoabsorption spectrum of a laser produced lithium plasma is outlined. In particular, using the models developed to describe the basic physical mechanisms of plume formation and expansion, as well as spectral line formation and broadening, coupled with values of the relevant atomic parameters characterising the transitions under consideration, it is shown that the quantitative interpretation of such spectra is practicable. Indeed, under certain conditions the interpretation of the EUV absorption spectra of laser plasmas is comparatively simpler than optical spectra. The broadening or distortion effects resulting from local plume conditions affect electronic inner-shells less severely than valence levels and may even be purely instrumental. In addition refractive effects are minimised for probe frequencies much larger than the plasma frequency. Thus, the technique proves suitable to the quantitative analysis of EUV spectra.

Chapter 2

This chapter describes the essential features of the experimental set-ups used during the course of this work. In all, three separate arrangements were used. A description of the operating characteristics and capabilities of each will be given including, where characterised, instrumental considerations. Finally, results pertaining to each diagnostic technique are presented. Specifications relating to the lasers, delay generator etc. used can be found in the Appendices.

2.1 The Fast-Frame Photography Technique

2.1.1 Experimental Set-up

Using a gated intensifier coupled to a charge coupled device (ICCD), a sequence of frames of the luminous plume of a laser produced lithium plasma was recorded expanding both in vacuum and in a low pressure argon atmosphere, at pressures of ~1 x 10^{-5} mbar and ~200 mTorr (~0.27 mbar) respectively. The experimental set-up is shown in figs. 2.1 and 2.2.
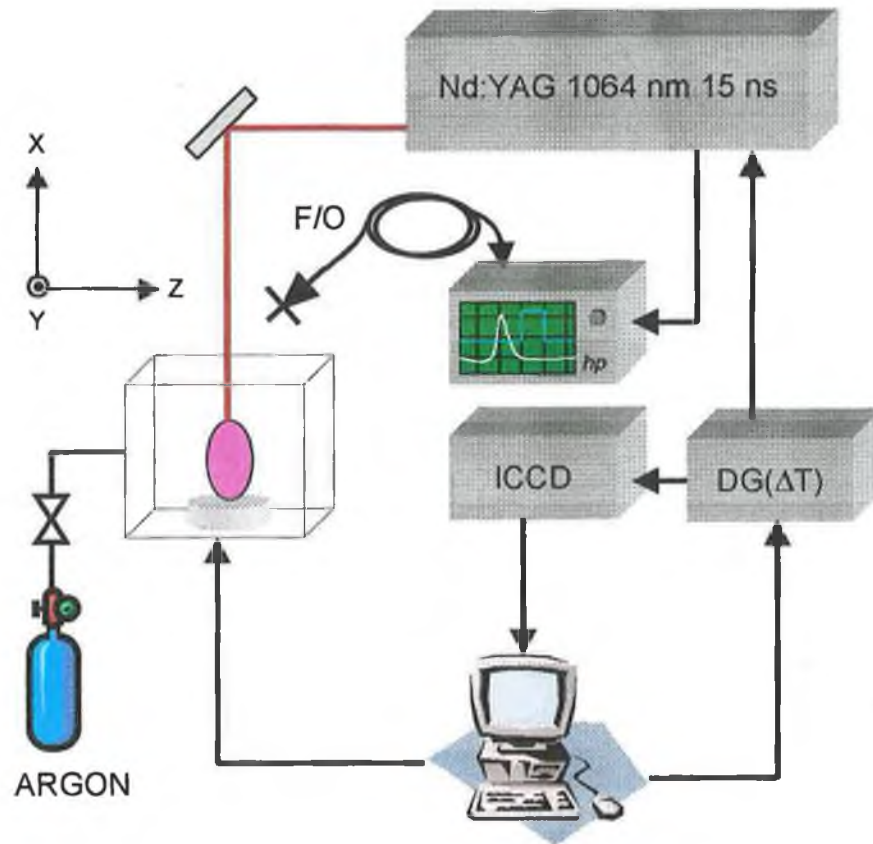
Fig. 2.1: The experimental set-up used to record a sequence of frames of the luminous plume of a laser produced lithium plasma: (ICCD) Intensified charge coupled device, (DG(ΔT)) Stanford digital delay generator, (F/O) BPX 65 Fast photodiode connected to ~14.2 m of fibre optic cable.
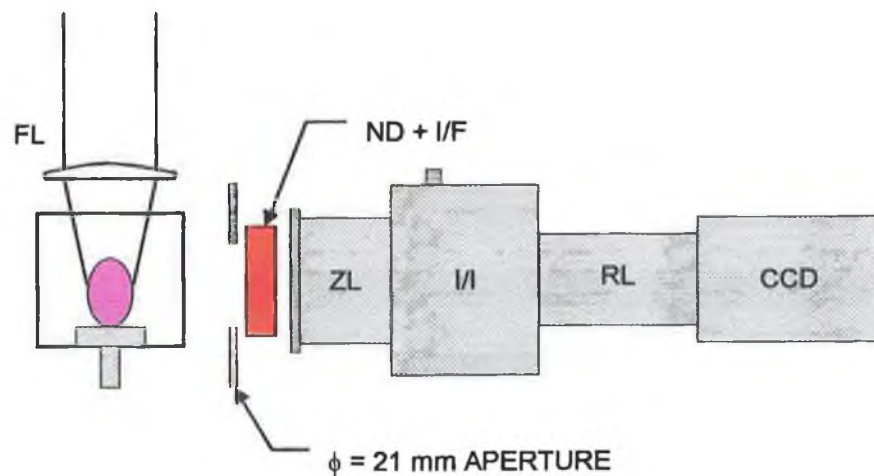
Fig. 2.2: A detailed view of the target chamber area and detection system: (FL) Plano-convex focussing lens (f = 190 mm), (ND + I/F) Neutral density + tuned interference filters, (ZL) Zoom lens f/2.8, (I/I) Gated image intensifier, (RL) Relay lens, (CCD) Charge coupled device.

The lithium plasma was generated by focussing the output from a Nd:YAG (0.8 J, 15 ns) laser, using an uncorrected plano-convex lens (FL) of 190 mm focal length, onto a planar lithium target. The target spot size was ~5 mm in diameter resulting in an irradiance of ~3 x 10^8 W cm^{-2} (~4 J cm^{-2}). Synchronisation between the laser trigger pulse and the gate pulse to the ICCD was achieved using a Stanford digital delay generator (DG(ΔT)), the timing diagram for which is illustrated in fig. 2.3. The resultant system jitter was less than 3 ns.
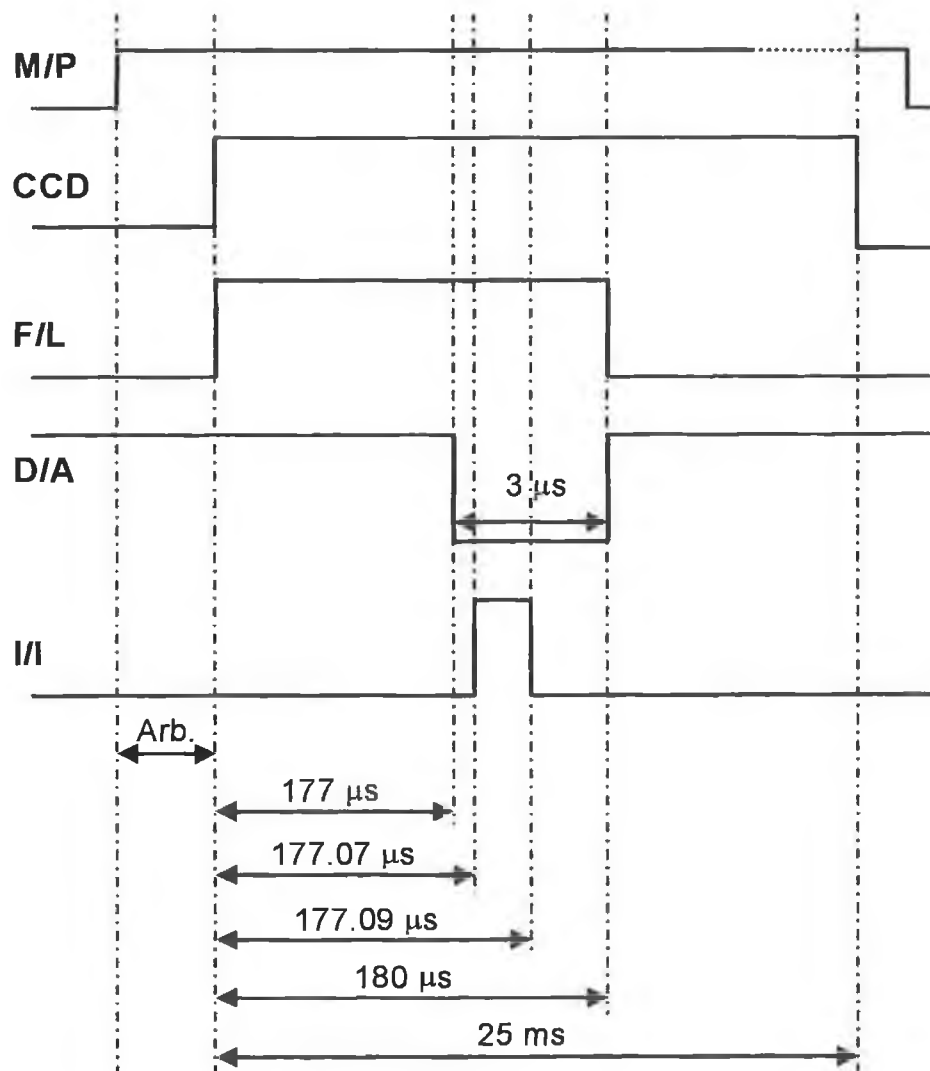
Fig. 2.3: A diagram of the triggering sequence used to capture frames of the luminous plume: (M/P) Master pulse (TTL), (CCD) CCD Shutter trigger, (F/L) Nd:YAG Flashlamp trigger (15 V), (D/A) Nd:YAG Direct Access trigger (-15 V), (I/I) Gated Image Intensifier trigger (TTL). In relation to the image intensifier, an electronic gate width of 20ns corresponds to an optical gate width of ~9 ns (see Appendix D).

Successive frames of the lithium plasma averaged over five shots were obtained by varying the triggering delay between the laser (Nd:YAG 0.8 J, 15 ns) used to create the plasma and the gating pulse (9 ns optical FWHM) to the image intensifier. The delay of 177.07 μs indicated in fig. 2.3 corresponds to a zero time delay. The target was rotated every five shots in order to present a fresh surface. The complete data acquisition procedure, including target rotation, was maintained under computer control. Frames were recorded using the CCIR standard in 8-bit gray-scale format; each frame measuring 544 x 290 pixels in size. The automatic gain control (AGC) feature of the CCD was disabled during the course of the experiments[1]. Gamma correction, where

$$G = I_T^{\gamma_c}$$ [2.1]

was set to unity. Here G is the quantised gray level while I_T is the true intensity. Generally, to accommodate the human eye γ_c is set to 0.4. Setting $\gamma_c = 1$ however ensures that the CCD response is a linear function of incident intensity (see §2.1.2(d)). The interference filter combined with neutral density filters (ND+IF) served to reduce the intensity of the detected radiation, as well as to narrow the spectral range of the imaged light to that of a known emission line. The opportunity to track the evolution of the corresponding excited species was thus provided. Due to the finite bandpass of the interference filters, the measured intensities are necessarily integrated over the line profile. The distance from the target centre to the 21 mm diameter circular aperture was ~190 mm. The separation between the target and the zoom lens (ZL) was ~220 mm.

---

[1] Automatic Gain Control (AGC) is a feature whereby the CCD automatically adjusts to ambient light levels. This was switched off during the course of this work. With the OS-25 CCD camera, unless the electronic shutter enable feature is selected (S5 UP), the camera automatically adjusts the exposure time to adapt to the incident light level. The result is similar to enabling automatic gain control.

2.1.2 System Characterisation

This section outlines the characterisation of the CCD parameters pertinent to the quantitative interpretation of the data recorded using the fast-frame photography diagnostic technique. A summary of the image intensifier test data supplied by Andor Technology can be found in Appendix D.

(a)   Spatial Resolution Measurement

The spatial resolution of an imaging system is defined as the minimum separation between two objects in the image plane before they become unresolved. This is often equated to the Rayleigh, or Sparrow criterion [98]. The spatial resolution of the combined image intensifier and CCD was measured using a Kodak TL-5003 imaging test chart. The resulting image is shown in fig. 2.4.
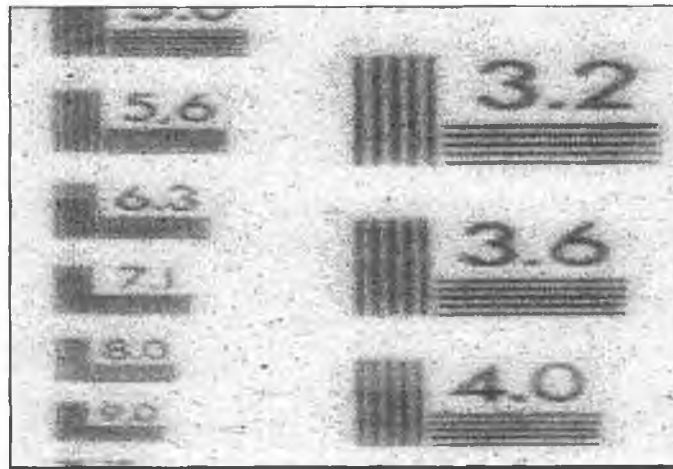
Fig. 2.4: Image of the Kodak TL-5003 imaging test chart. The numerals indicate the number of line pairs per mm.

From fig. 2.4, one can ascertain, using for example the Rayleigh criterion [98], the minimum separation between two consecutive dark lines before they become indiscernible from one another. With reference to figs. 2.5 and 2.6, one can see that this criterion is satisfied for a resolution of ~3.6 line pairs per mm (lp / mm) in the horizontal direction and slightly less than 3.6 lp / mm in the vertical direction.
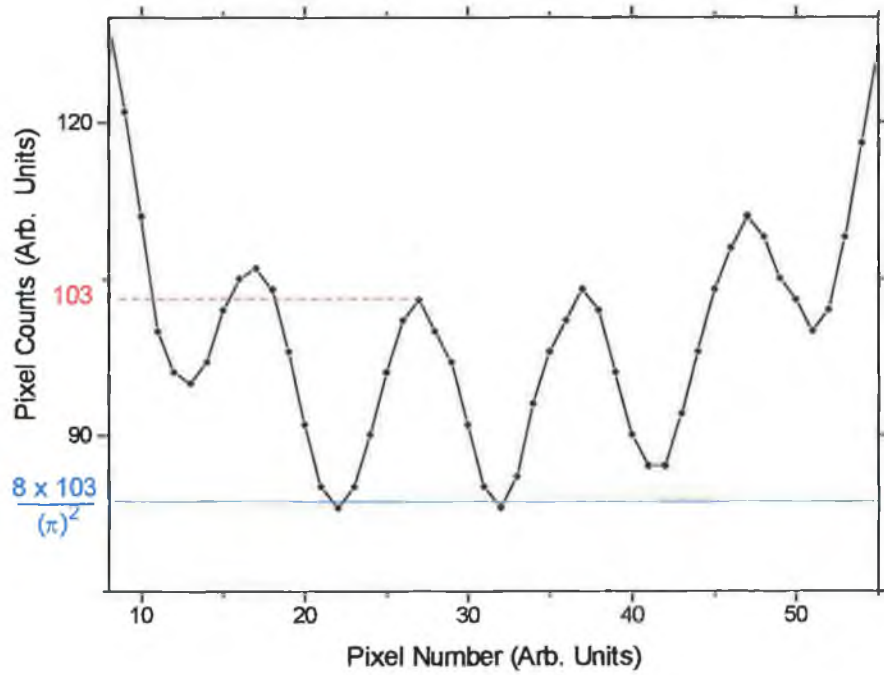
Fig. 2.5: Typical scan across the resolution test chart image in the horizontal direction (at 3.6 lp / mm) indicating the saddle point pixel value required to satisfy Rayleigh's criterion.
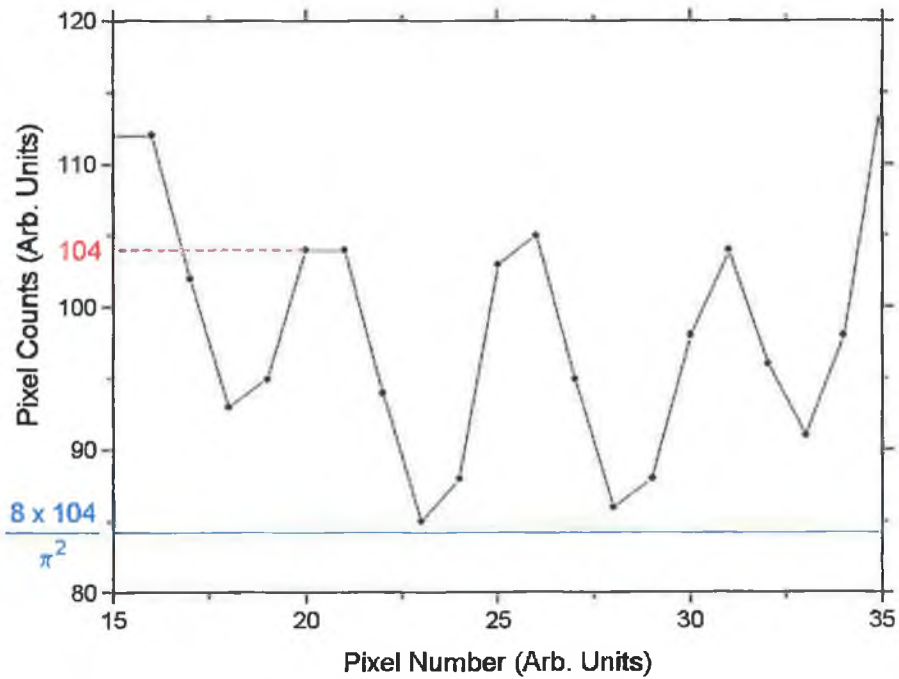
Fig. 2.6: Typical scan across the resolution test chart image in the vertical direction (at 3.6 lp / mm) indicating the saddle point pixel value required to satisfy Rayleigh's criterion.

63

The minimum spatial resolution of the gated intensifier as a standalone device is supplied as < 80 μm [99], corresponding to a spatial resolution of > 6.25 lp / mm, while the CCD resolution is < 12 μm [100] corresponding to a resolution of > 40 lp /mm.

(b)   Photon Statistics

The total number of photons emitted by a steady source over any time interval exhibits random fluctuations that vary according to a Poisson distribution given by

$$f(x) = \frac{\mu_s{}^x}{x!} \exp(-\mu_s)$$

[2.2]

where μ_s is equal to the square of the standard deviation defined as

$$\mu_s = \sigma_s{}^2 = \frac{\sum x^2}{N} - x_{AV}$$

[2.3]

Here N is the number of 'x' observations; x_{AV} is the average value. The charge collected by a CCD exhibits this same distribution so that the fluctuation, usually referred to as shot noise, is equal to the square root of the mean number of photons detected [101]. Shot noise or photon noise is independent of frequency and is always present in imaging systems. It simply represents the uncertainty in the data.

Employing the set-up depicted in fig. 2.7, a constant illumination source positioned ~40 cm from the front of the CCD was used to make 3000 observations; each observation having an exposure lasting 25 ms. The effect of the diffuser was to scatter the incident light to produce a uniform irradiance on the detector. By recording the pixel value of a single pixel located in the centre of the CCD matrix at pixel position (272,145), the random nature of the photoelectric process was examined. The results are plotted in fig. 2.8.
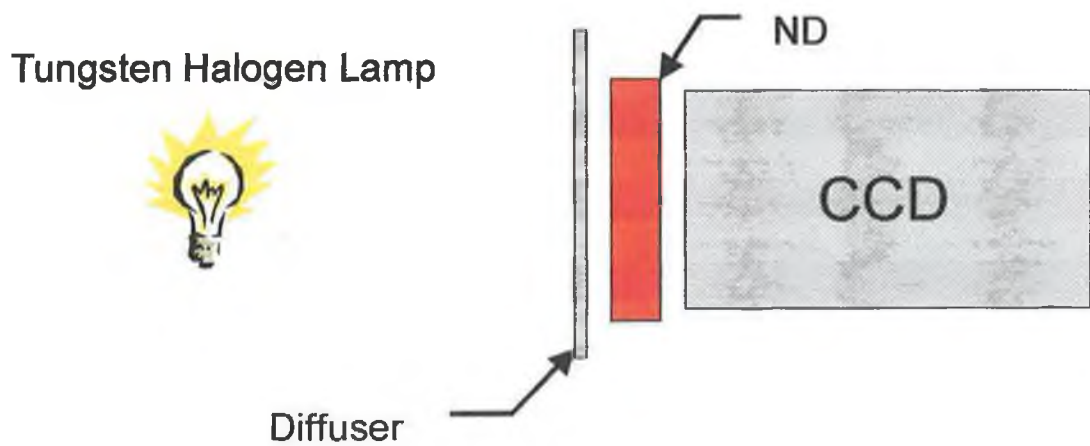
Fig. 2.7: The experimental set-up used in various calibration measurements to characterise the OS-25 CCD.
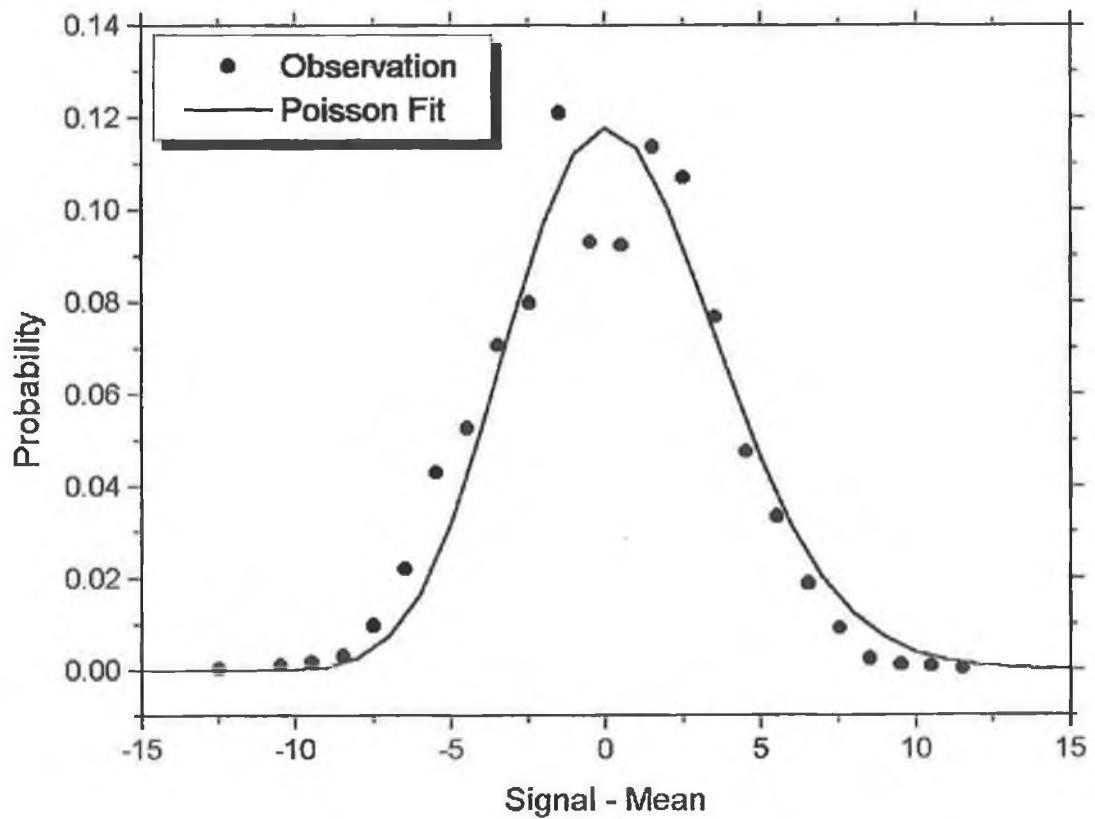
Fig. 2.8: Random fluctuations in the observed detector output as a result of the discrete nature of the photoelectric process fitted to a Poisson probability distribution.

From the graph one can see that the distribution is symmetric about the mean value. Therefore the probability of detecting a photon depends solely on the absolute value of the deviation of any value from the mean.

(c)   Quantum Efficiency

Quantum efficiency measures the sensor's efficiency is generating electronic charge from incident photons. Within the visible spectrum (400 → 700 nm), the photon to electron conversion efficiency (QE) of silicon is less than unity, and varies with the wavelength of the incident photons. The creation of charge from incident radiation of fixed wavelength is intrinsically linear (see (d)) [102]. The quantum efficiency for a typical OS-25 CCD camera is displayed in fig. 2.9.
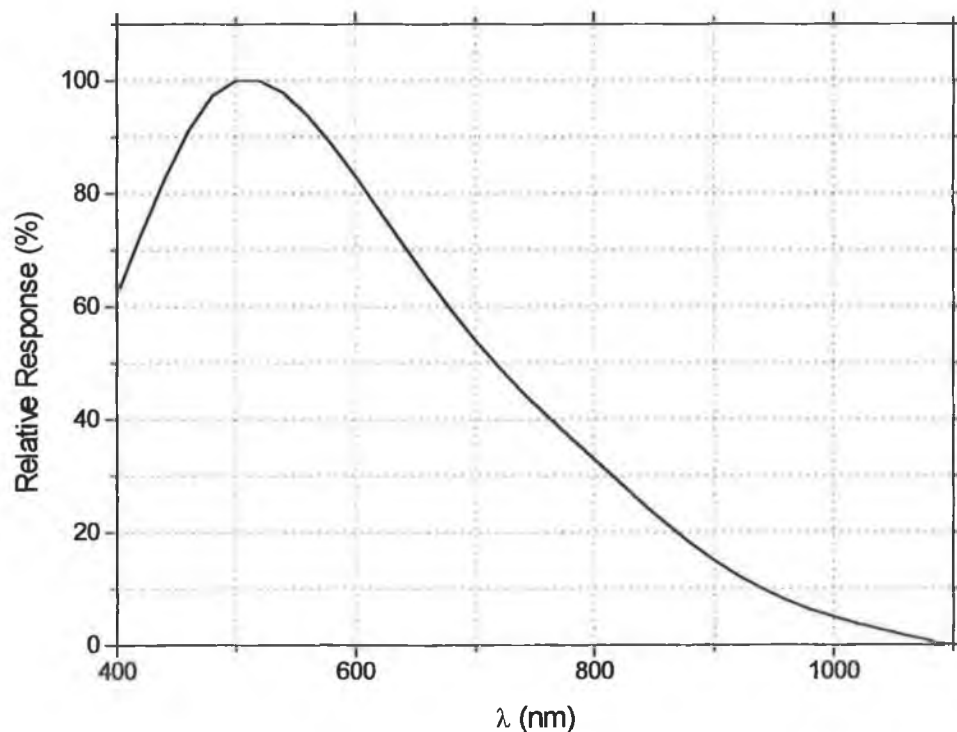
Fig. 2.9: A typical quantum efficiency curve of an OS-25 CCD camera [100].

In the analysis of §3.1, the CCD quantum efficiency is not a determining factor, as the image intensifier phosphor (P43) emits over a narrow band of radiation over which the QE of the CCD camera does not vary substantially. This is plotted in fig. 2.10.
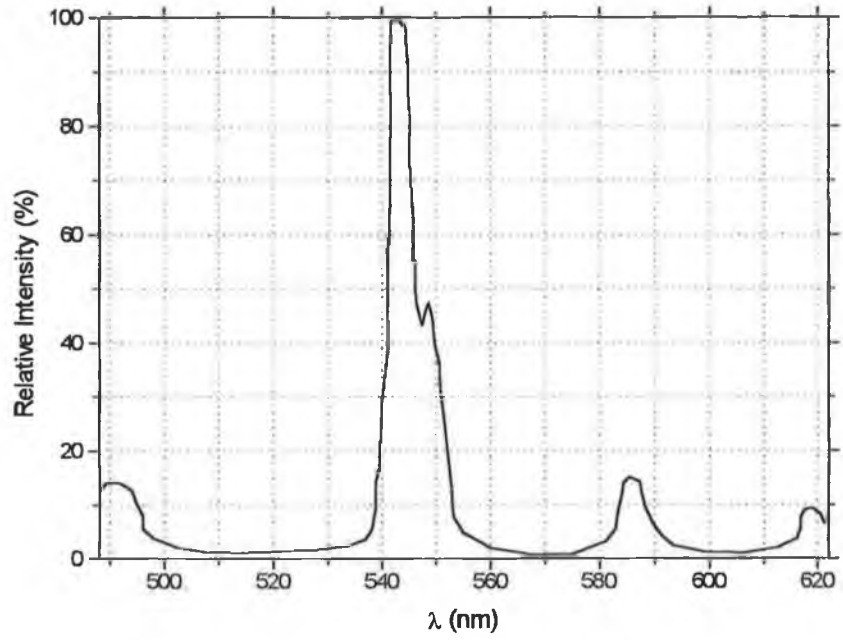
Fig. 2.10: The relative intensity as a function of wavelength of a P43 phosphor [103].

The quantum efficiency of the image intensifier photocathode (S 25) is plotted in fig. 2.11.
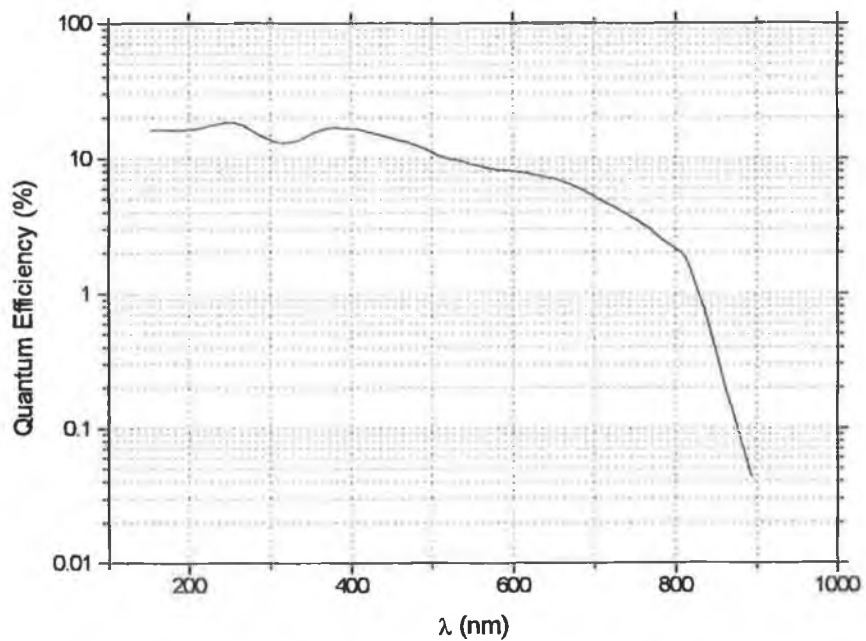
Fig. 2.11: The quantum efficiency of a typical modified S 25 photocathode [99].

67

This is important only if relative comparisons are to be made between detected intensity levels of the various transitions considered. The peak quantum efficiency of the gated intensifier used during the course of these experiments was ~16.6% [99]. The efficiency of the gated intensifier is not a determining factor in the analysis of §3.1.

(d)   Linearity

As previously mentioned (see (c)), at any given wavelength a linear relationship between the light level incident on each pixel and the digitally quantised gray level representing that signal should ideally exist. Scientific grade CCDs exhibit this linear relationship over several orders of magnitude to within a few hundredths of a percent. Non-linearity in an imaging system can introduce serious errors into image processing results and can thus lead to the erroneous interpretation of data. The linearity of the OS-25 CCD was experimentally measured using the set-up depicted in fig. 2.7. Using a tungsten halogen illumination source positioned ~40 cm from the CCD, and maintained at a constant current of 5 A (19.7 V), the transmittance of various sets of neutral density filters were measured, and averaged over five consecutive 25 ms exposures. Placing different tuned interference filters in front of the CCD effected the measurements at a number of 'discrete' wavelengths. The results are plotted in fig. 2.12. In each case the data has been corrected for the relative transmission of the appropriate narrowband interference filter. From the graph, one can ascertain that the response of the CCD is linear at the specified wavelengths. The difference in slopes between the various response curves may be attributed to a combination of the difference in the CCD quantum efficiency, and also the relative intensities of the spectrum of tungsten at these wavelengths, the temperature of which was estimated to be 2050 K using a CYCLOPS 152 pyrometer (see Appendix C), assuming an emissivity of 0.4 [1].
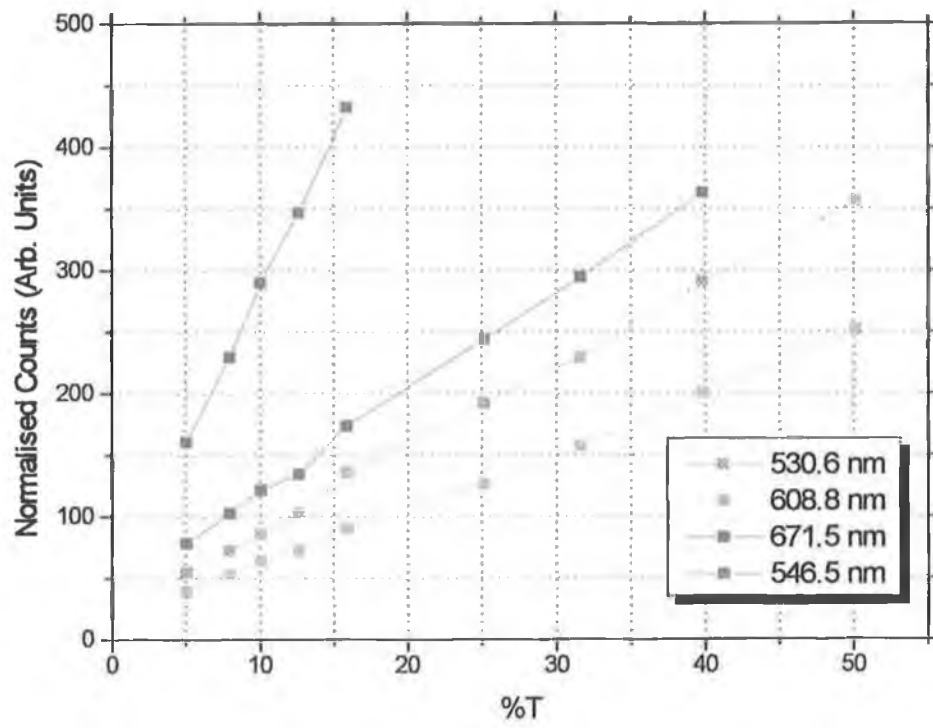
Fig. 2.12: The measured linearity of the OS-25 CCD at different wavelengths.

2.1.3 Experimental Results

The temporal and spatial evolution of a lithium plume expanding into vacuum ($\sim 1 \times 10^{-5}$ mbar) as well as into a low-pressure gas (~ 200 mTorr of argon) is shown in figs. 2.14 through 2.23, for a number of different time delays. In figs. 2.14 and 2.15, the camera was tuned to the $1s^2 2s \leftarrow 1s^2 2p$ (670.7 nm) Li^o transition using an interference filter centred at 671.5 nm. Similar figures for the $1s^2 2p \leftarrow 1s^2 3d$ transition (610.3 nm) in Li^o are shown in figs. 2.16 and 2.17, and for the $1s2s \leftarrow 1s2p$ transition (548.4 nm) in Li^+ in figs. 2.18 and 2.19. Temporally and spatially resolved spectrally broadband images and also broadband filtered images using a high (wavelength) pass filter for both the expansion into vacuum and argon cases are shown in figs. 2.20 and 2.21 and figs. 2.22 and 2.23 respectively. In each case a false coloured palette has been used to distinguish the recorded light intensities. The spectral transmission curves, recorded using a Shimadzu UV-1201 spectrophotometer, for the broadband filter as well as the tuned interference filters are illustrated in fig. 2.13.
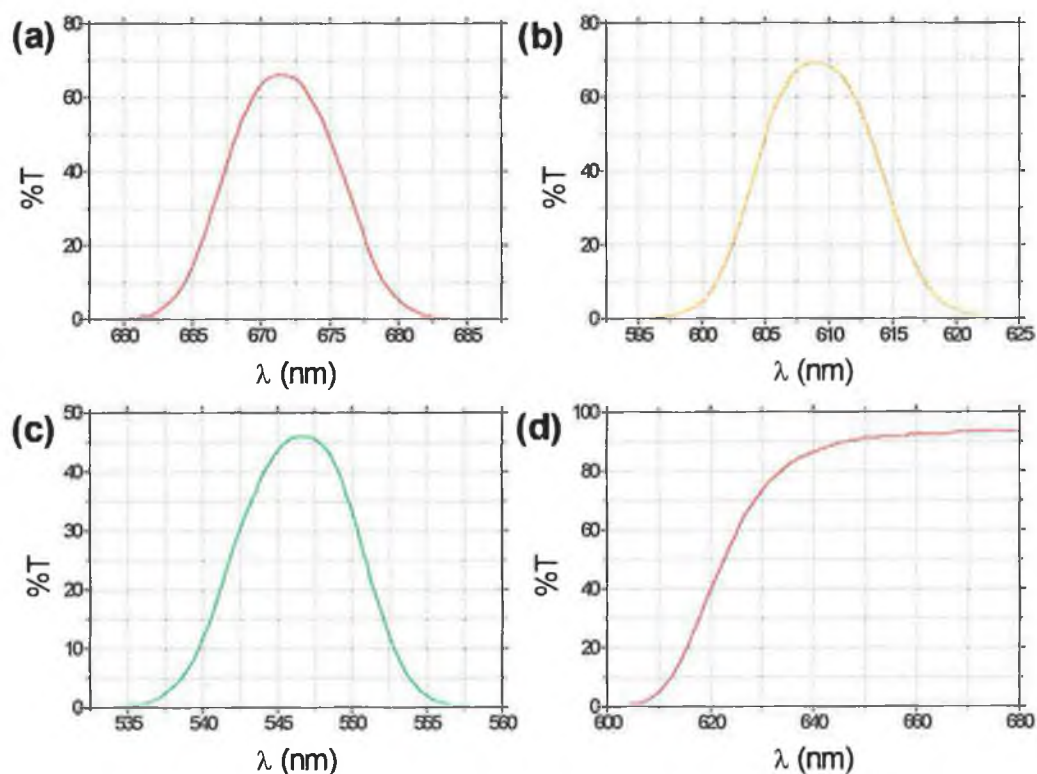
Fig. 2.13: The spectrophotometer transmission curves of (a) I/F 67IFS10-25 (λ_{centre} = 671.5 nm) (b) I/F 59405#1 λ_{centre} = 608.8 nm (c) I/F A43125 λ_{centre} = 546.5 nm (d) R-62 broadband high wavelength pass filter.
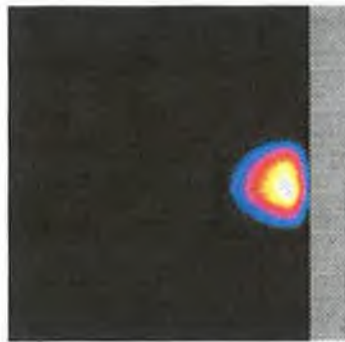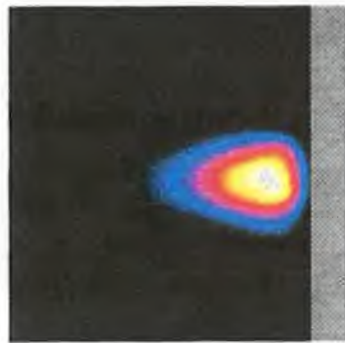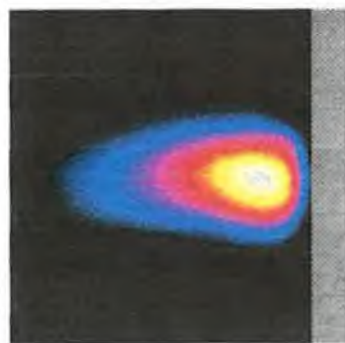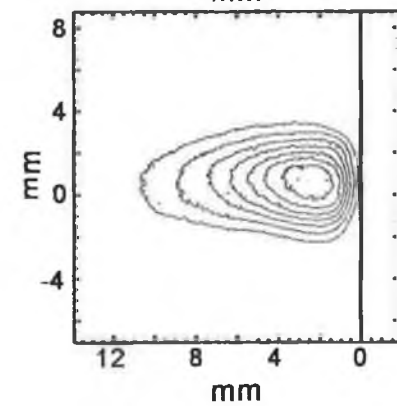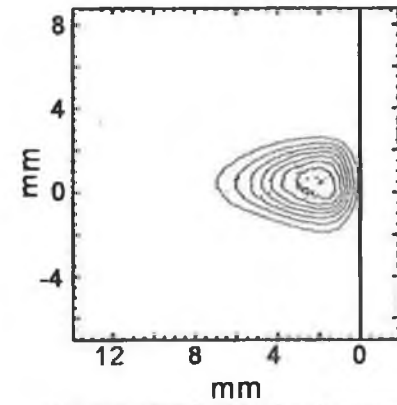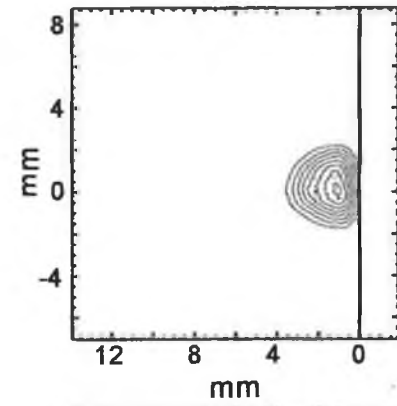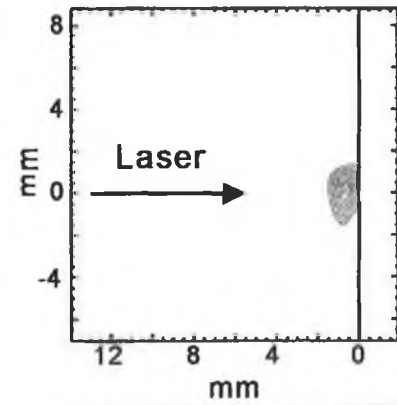
Fig. 2.14: The temporal and spatial evolution of Li⁰ (670.7 nm) in vacuum.
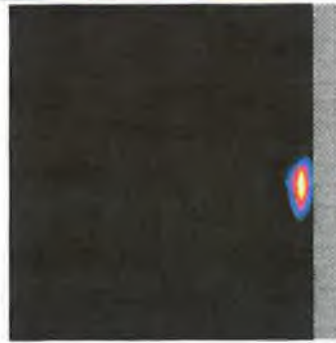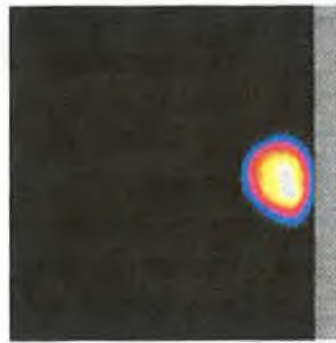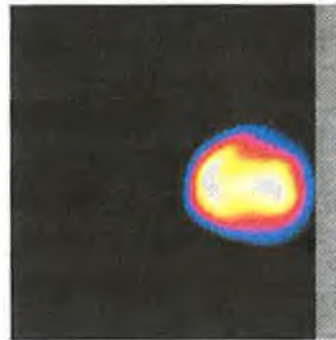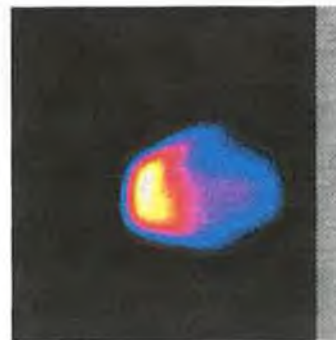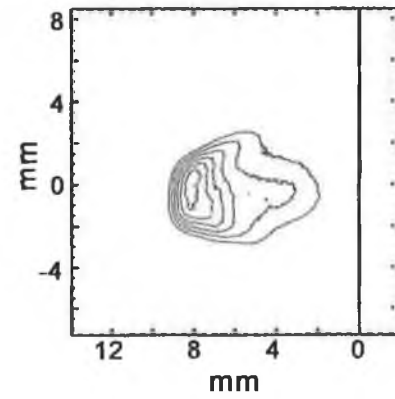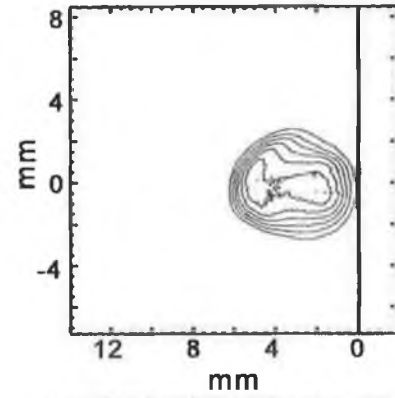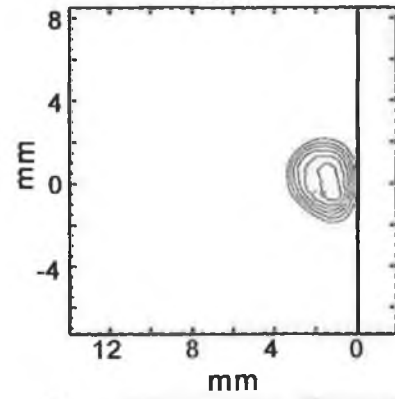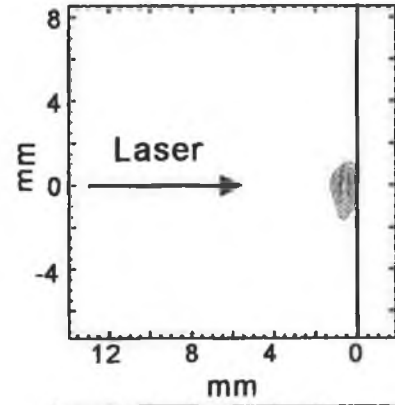
Fig. 2.15: The temporal and spatial evolution of Li⁰ (670.7 nm) in 200 mTorr of argon.

Fig. 2.16: The temporal and spatial evolution of Li° (610.3 nm) in vacuum.

73
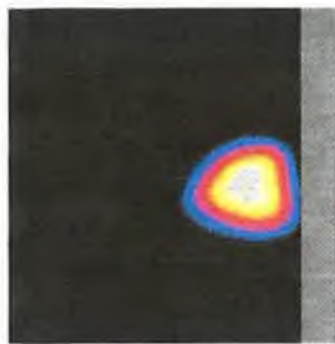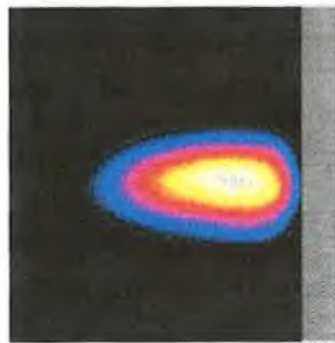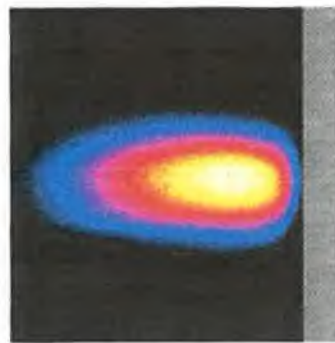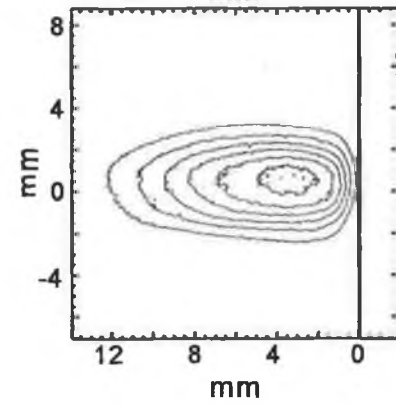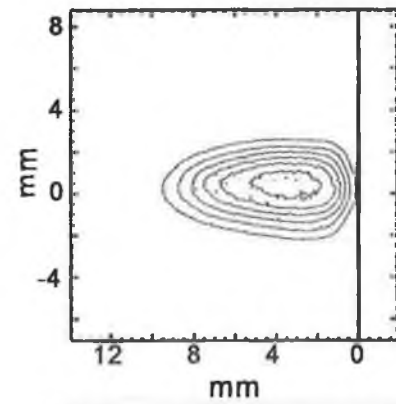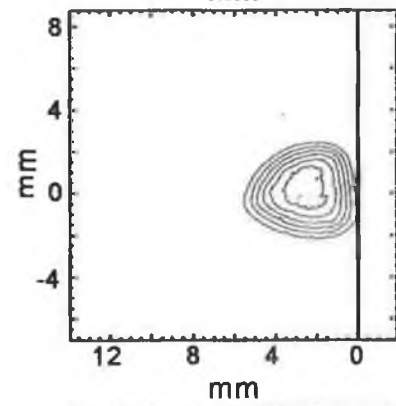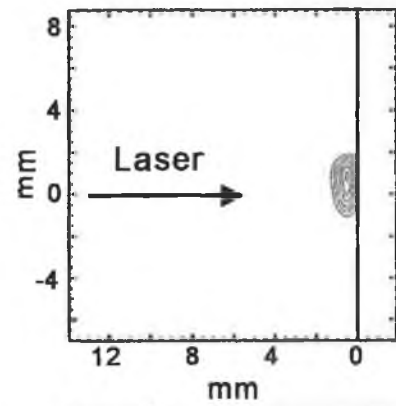
Fig. 2.17: The temporal and spatial evolution of Li⁰ (610.3 nm) in 200 mTorr of argon.
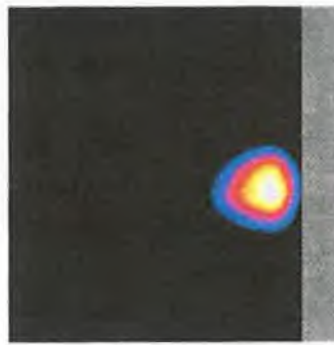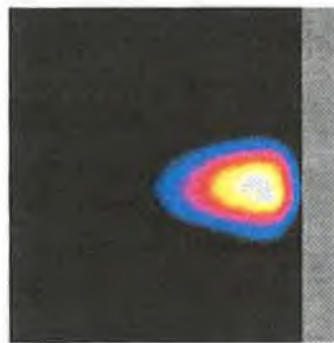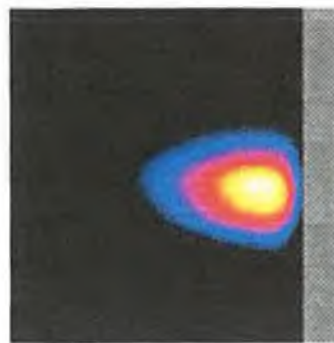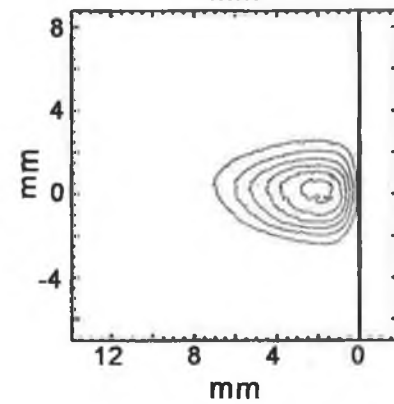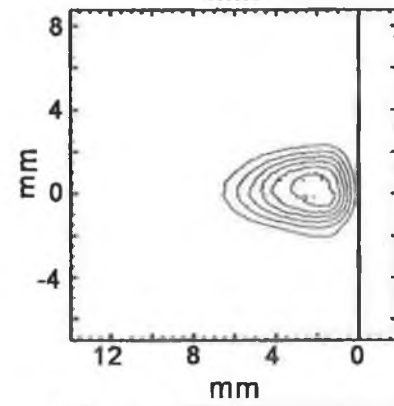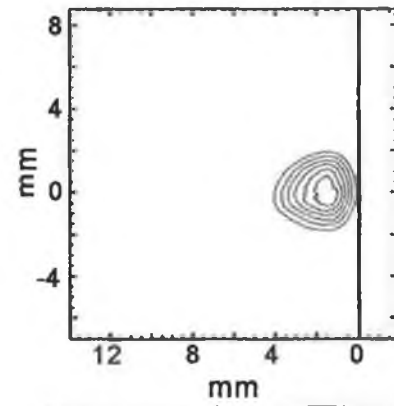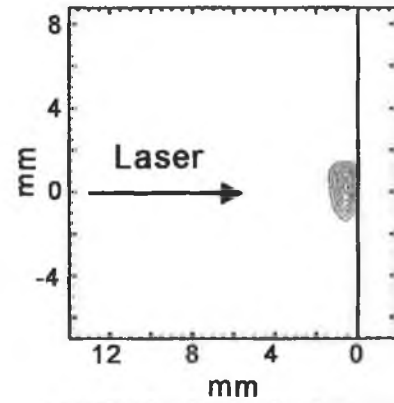
Fig. 2.18: The temporal and spatial evolution of Li$^+$ (548.4 nm) in vacuum.
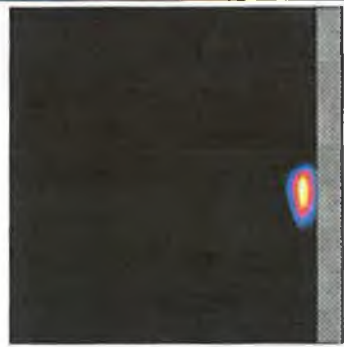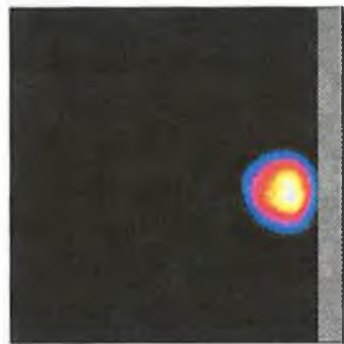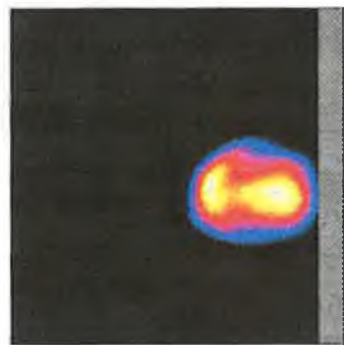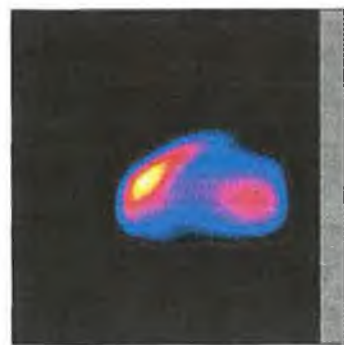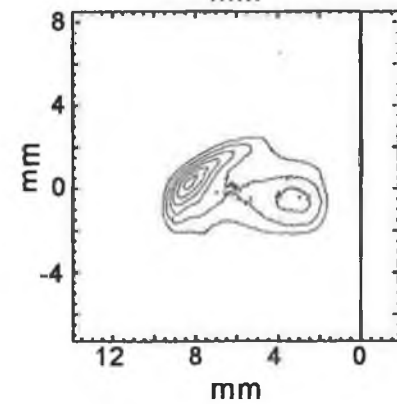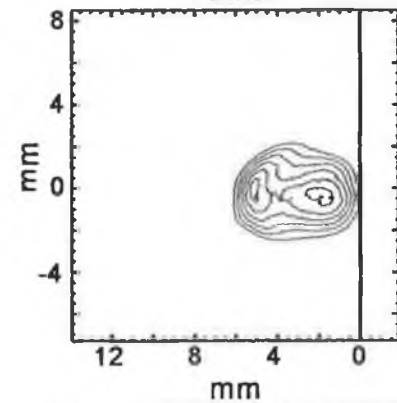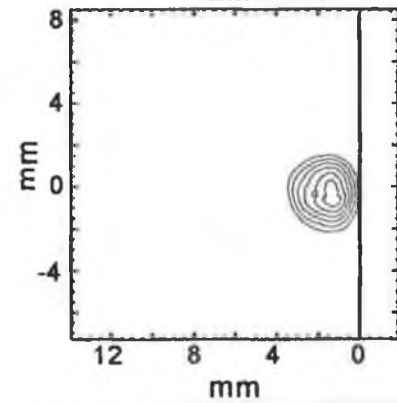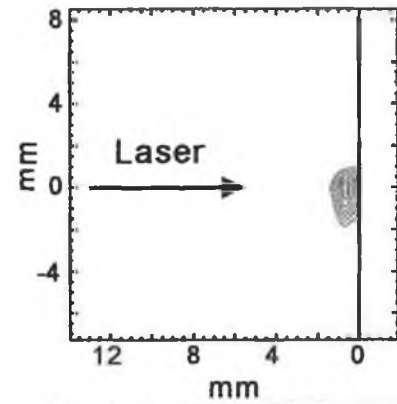
Fig. 2.19: The temporal and spatial evolution of Li$^+$ (548.4 nm) in 200 mTorr of argon.
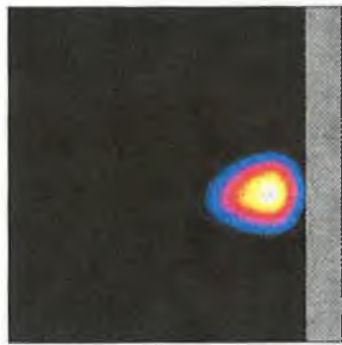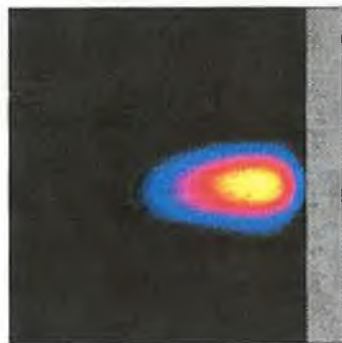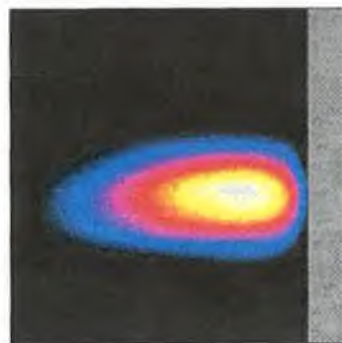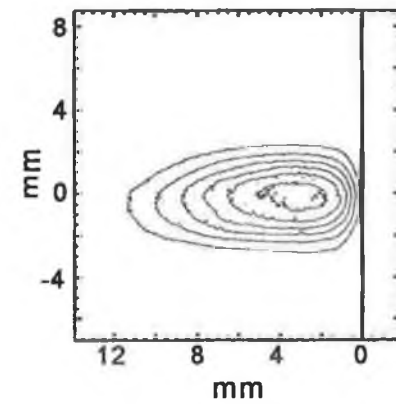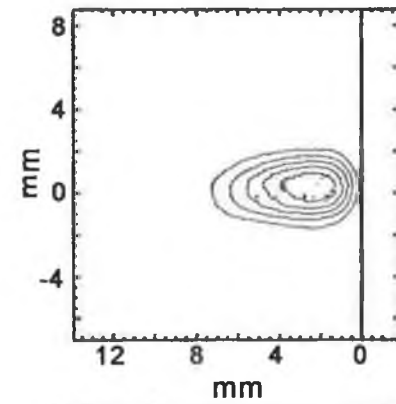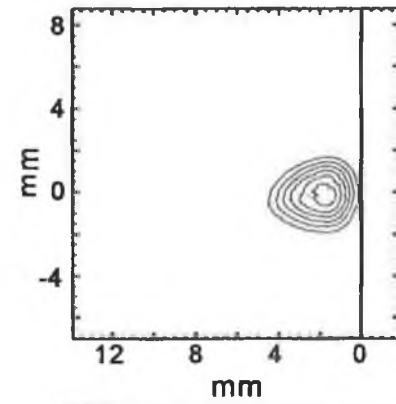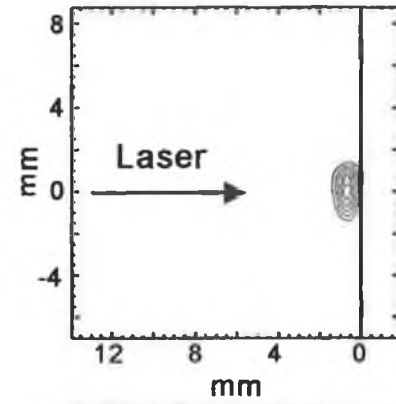
Fig. 2.20: The temporal and spatial evolution of a laser produced lithium plasma (broadband) in vacuum.
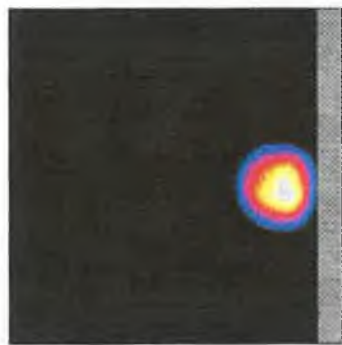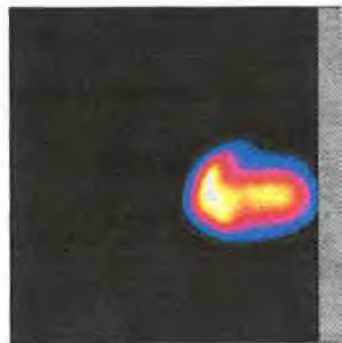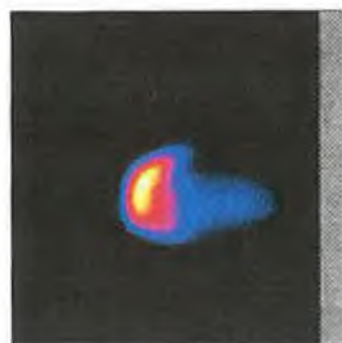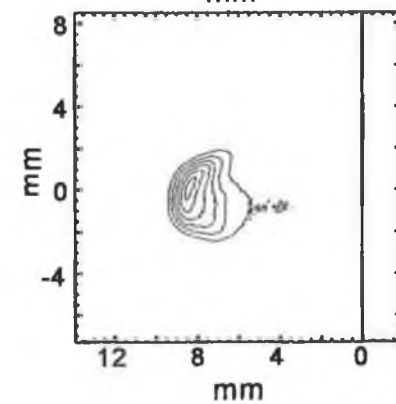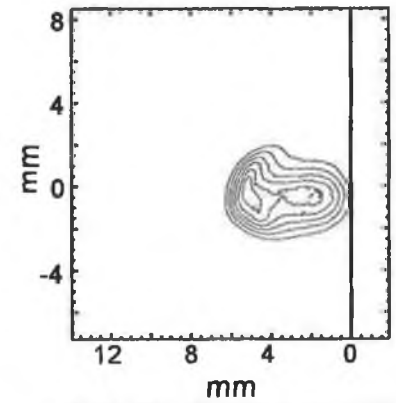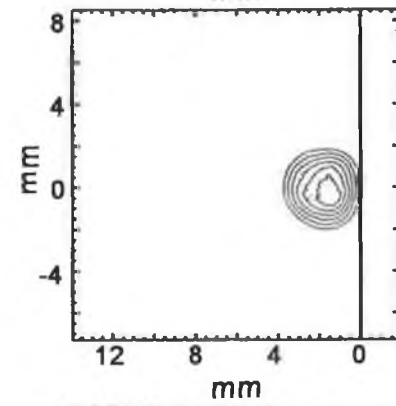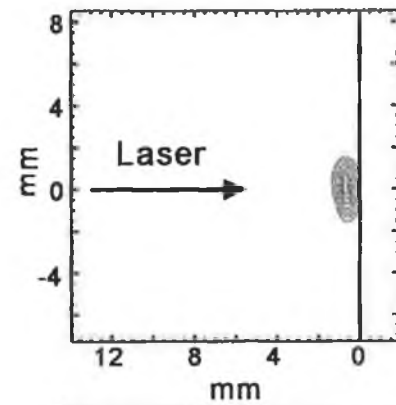
Fig. 2.21: The temporal and spatial evolution of a laser produced lithium plasma (broadband) in 200 mTorr of argon.
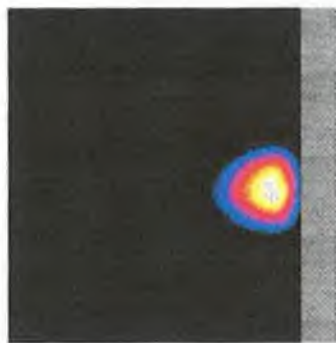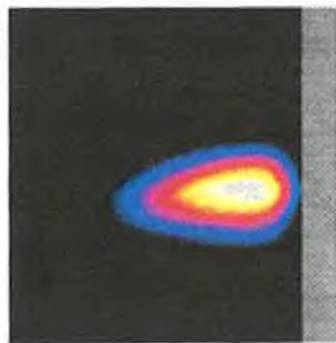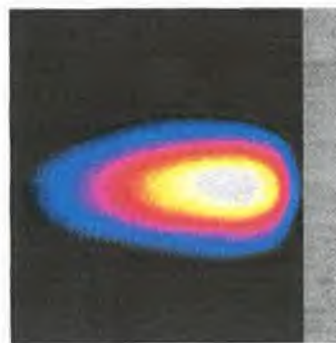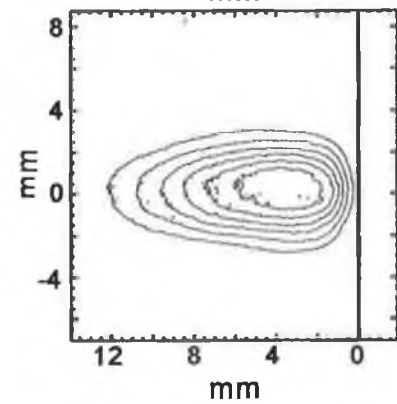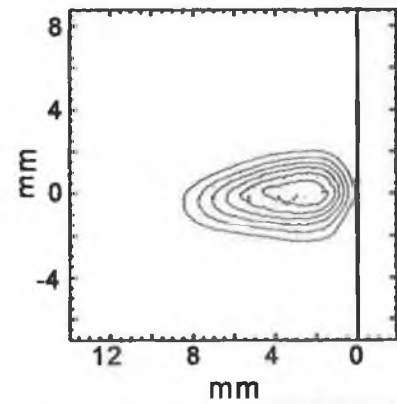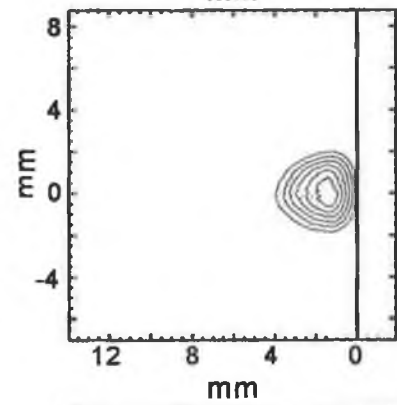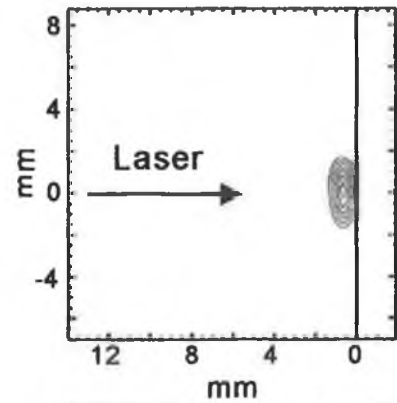
Fig. 2.22: The temporal and spatial evolution of a laser produced lithium plasma using a high wavelength pass filter (R-62) in vacuum.
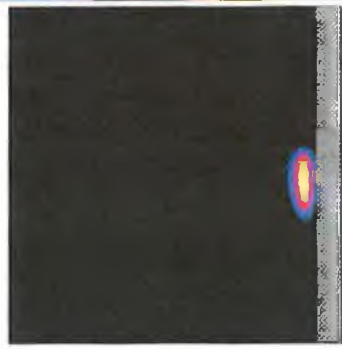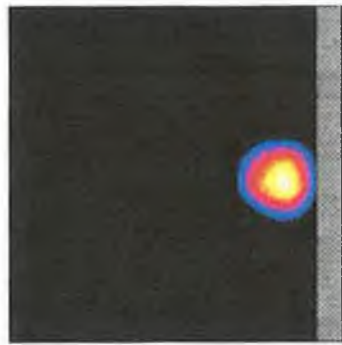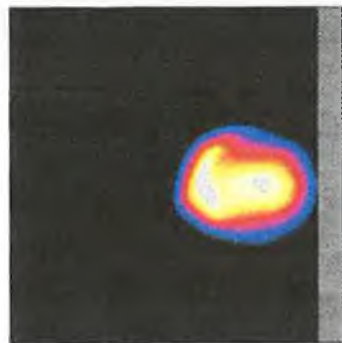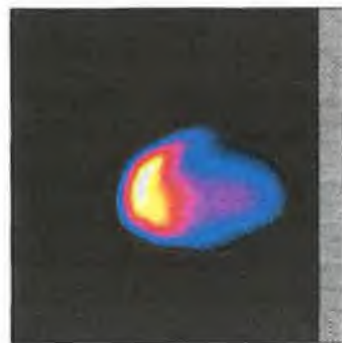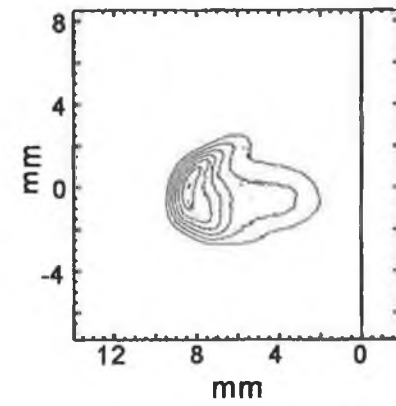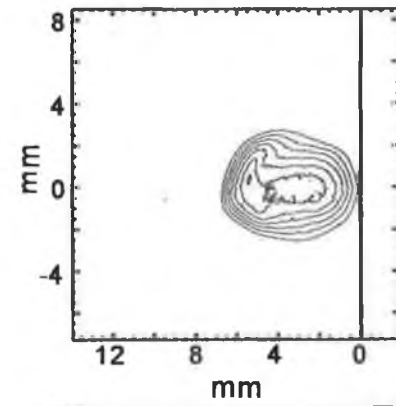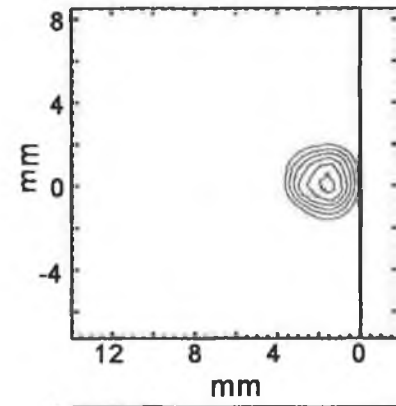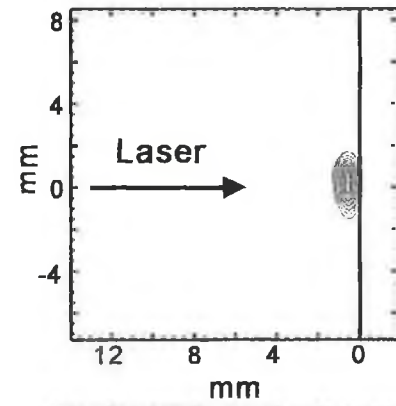
Fig. 2.23: The temporal and spatial evolution of a laser produced lithium plasma using a high wavelength pass filter (R-62) in 200 mTorr of argon.

2.2 The Shadowgraph Technique

2.2.1 Experimental Set-up

Temporally resolved shadowgraphs of an expanding laser produced lithium plasma in vacuum (~1 x 10^{-5} mbar) were obtained using the set-up depicted in figs. 2.24 and 2.25. A lithium plasma was formed by focussing the output from a Nd:YAG (0.8 J, 15 ns) using an uncorrected plano-convex lens (f = 110 mm) onto a planar lithium target. The spot size was estimated from the target crater to be ~500 μm in diameter; approximately 25 times the diffraction limited spot size diameter. The irradiance range over which the experiments were performed varied between ~1 x 10^{14} W m^{-2} and ~3 x 10^{14} W m^{-2}. Synchronisation was achieved, as before, using the Stanford digital delay generator. The timing diagram is shown in fig. 2.26.
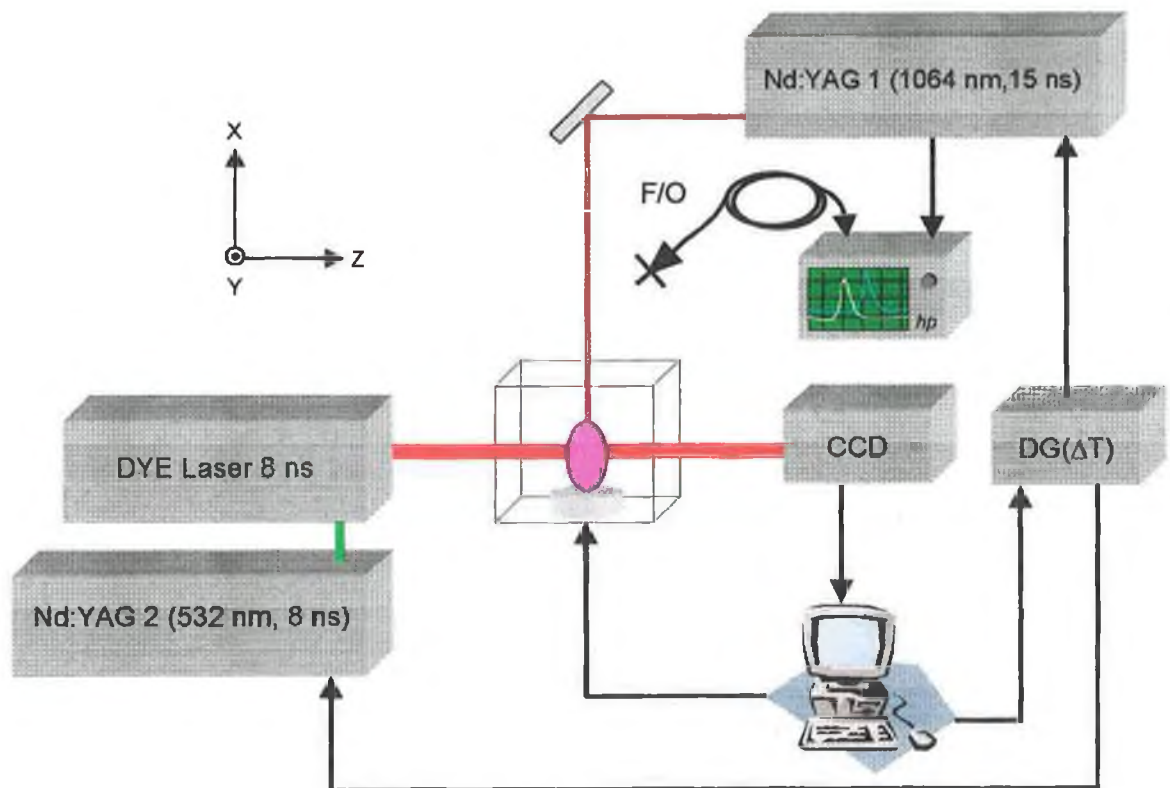

Fig. 2.24: The experimental set-up used to record a sequence of shadowgraph frames of a laser produced lithium plasma: (CCD) Charge coupled device, (DG(ΔT)) Stanford digital delay generator, (F/O) BPX 65 Fast photodiode connected to ~14.2 m of fibre optic cable.
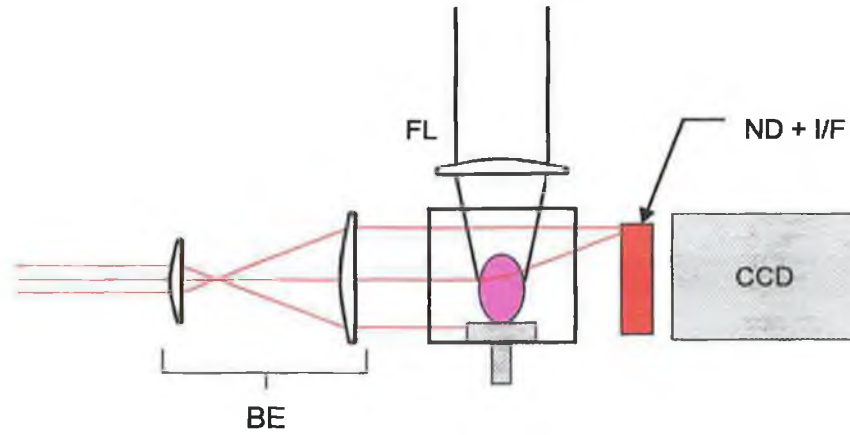
Fig. 2.25: A detailed view of the target chamber area and detection system: (FL) Plano-convex focussing lens (f = 110 mm), (BE) Beam expander, (ND + I/F) Neutral density + tuned interference filters, (CCD) Charge coupled device.
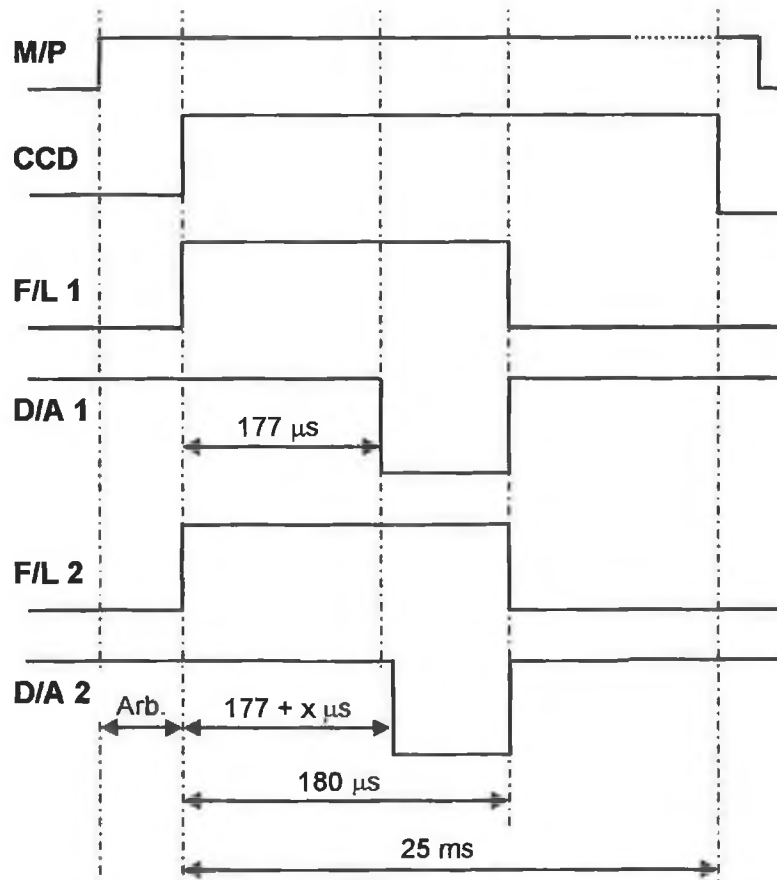

Fig. 2.26: A timing diagram of the triggering sequence used to record shadowgraphs of the lithium plume: (M/P) Master pulse (TTL), (CCD) CCD Shutter Trigger, (F/L 1) Nd:YAG 1 Flashlamp trigger (15 V), (D/A 1) Nd:YAG 1 Direct Access trigger (-15 V), (F/L 2) Nd:YAG 2 Flashlamp trigger (15 V), (D/A 2) Nd:YAG 2 Direct Access trigger (-15V).

The output from a dye laser, pumped by a frequency doubled Nd:YAG (532 nm) laser was used to probe to lithium plume. The output energy of the dye beam was typically a few mJ [104]. The beam was initially expanded using a beam expander (BE), before falling directly onto the CCD. The beam expander comprised a plano-convex lens of 18 mm focal length and 15 mm diameter, and a second plano-convex lens of 100 mm focal length and 30 mm diameter, separated by 118 mm. Single-shot images of the plasma plume using the dye beam as a back-lighter were captured using the CCIR standard in 8-bit gray-scale format. Each image was 544 x 290 pixels in size corresponding physically to ~4 mm x ~4 mm. Self-emission from the plasma as well as background illumination noise were eliminated by placing a tuned interference filter and a combination of neutral density filters (ND+I/F) in front of the CCD. The tuned interference filter also served as a rough check on the calibration of the dye laser tuning mirror. Temporal resolution of 8 ns (FWHM) was introduced via the temporal characteristics of the Q-switched Nd:YAG used to pump the dye laser. The separation between the target centre and the CCD was ~150 mm. Three dyes in all were used to cover the spectral range of the three transitions of interest. The name(s) and concentration of each dye is given in table 2.1, along with the relevant transition investigated. The dye fluorescence curves can be found in Appendix E.

Dye Name(s)	Molec. Weight	Oscillator Conc.	Amplifier Conc.	Solvent	Transition Investigated
LDS698 Pyradin I	378	3.5×10^{-4}	2×10^{-4}	Methanol	$1s^2 2s \rightarrow 1s^2 2p$
Rhodamine 640 Rhodamine 101	591	3.6×10^{-4}	1.9×10^{-4}	Methanol	$1s^2 2p \rightarrow 1s^2 3d$
Fluorescin 548 Fluorescin 27	401	1.6×10^{-3} + NaOH (200 mg / L)	8.7×10^{-4} + NaOH (200 mg / L)	Methanol	$1s2s \rightarrow 1s2p$

Table 2.1: The dye concentrations and solvents used during this study.

Separate dye reservoirs fed the oscillator and amplifier stages. Each held a capacity of ~1 L, and had separate control circuitry to allow adjustment of the flow rate. The dye flow rate, however, was not a crucial parameter as the diagnostic involved taking single shots over relatively long time intervals. The dye laser tuning mirror was connected to an incremental shaft encoder. Each encoder pulse was equivalent to 0.001 nm [104].

The linewidth of the dye beam is typically 0.1 cm^{-1} unless the prism beam expander is removed, in which case the linewidth increases to ~1 cm^{-1} as a direct result of grating under-fill [105]. The actual linewidth is dependent on the condition of the laser, its alignment etc. The prism beam expander was removed during the course of these experiments.

2.2.2 Experimental Results

Temporally resolved shadowgraphs at different stages in the evolution of the lithium plasma plume are shown in figs. 2.27 through 2.31. The same three transitions investigated in emission were again probed. Shadowgraphs for the $1s^22s \rightarrow 1s^22p$ (670.7 nm) in Li^o are shown in figs. 2.27 and 2.28. Similar images for the $1s^22p \rightarrow 1s^23d$ (610.3 nm) in Li^o are shown in fig. 2.29 and for the $1s2s \rightarrow 1s2p$ transition (548.4 nm) in Li$^+$ in figs. 2.30 and 2.31. The laser irradiance used to generate the lithium plasma is indicated in each of the figures.
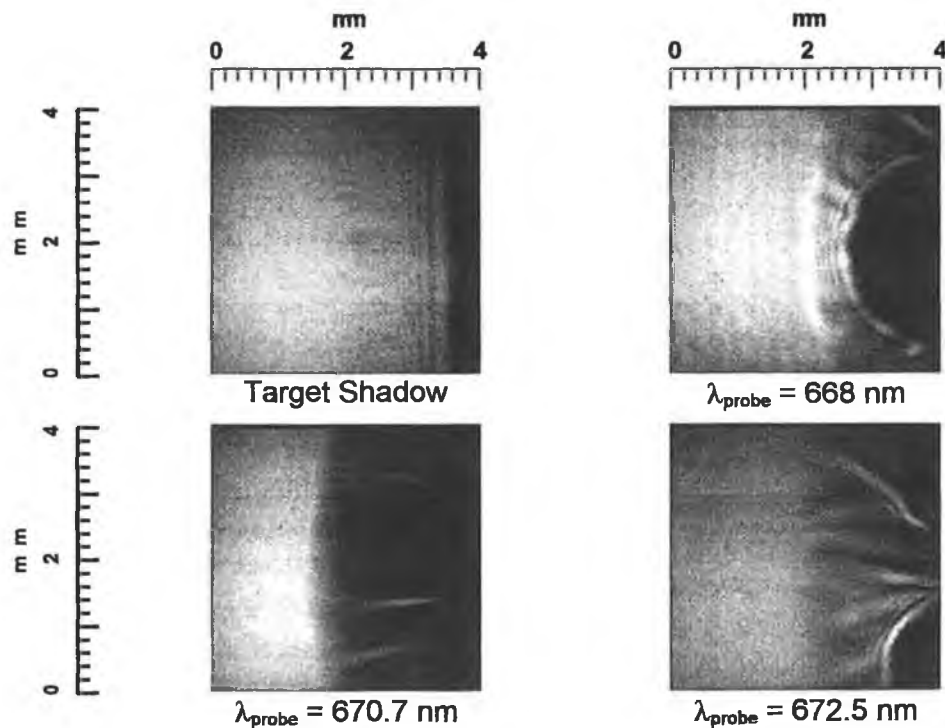

Fig. 2.27: Shadowgraphs of the lithium plume at ΔT = 80 ns. The laser irradiance was ~1.4 x 10^{14} W m^{-2}.
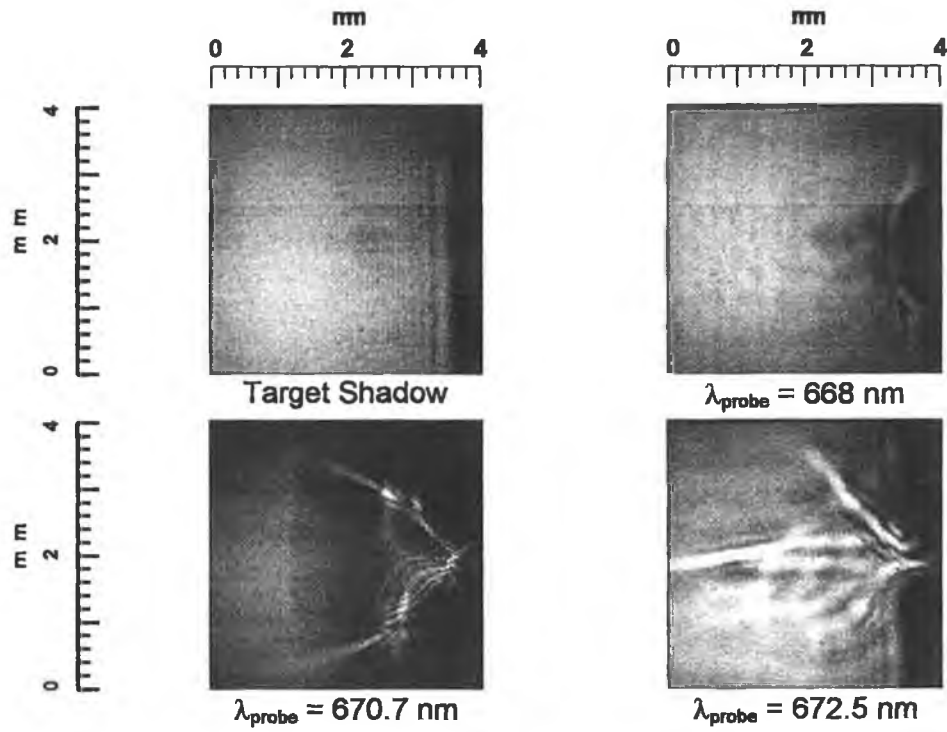
Fig. 2.28: Shadowgraphs of the lithium plume at $\Delta T = 480$ ns. The laser irradiance was ~1.4×10^{14} W m^{-2}.

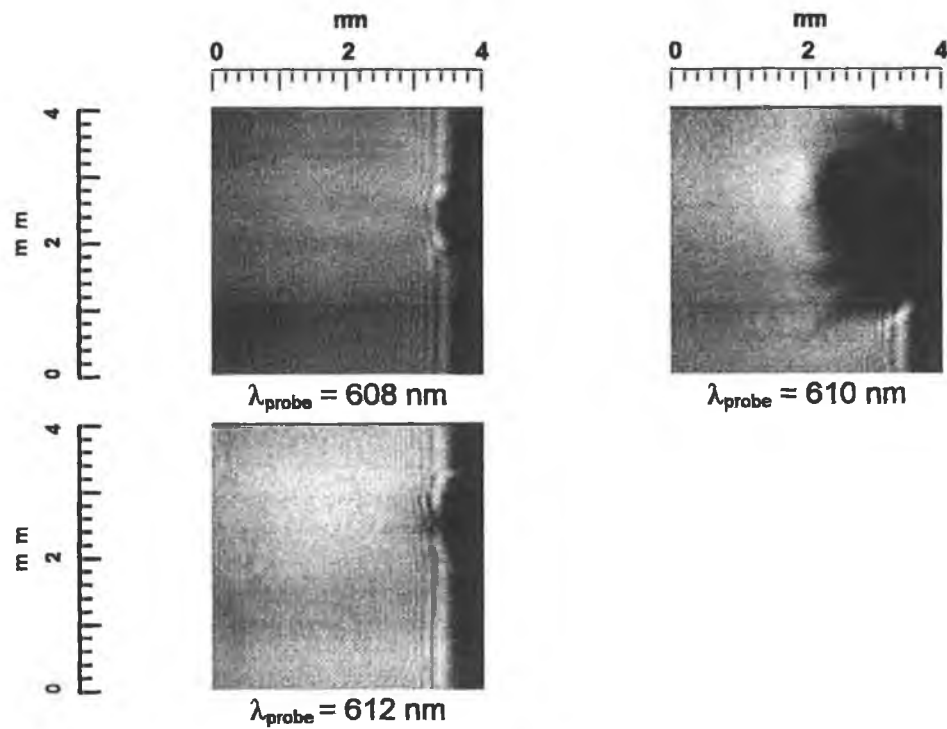**Fig. 2.29:** Shadowgraphs of the lithium plume at $\Delta T = 100$ ns. The laser irradiance was ~2.1×10^{14} W m^{-2}.

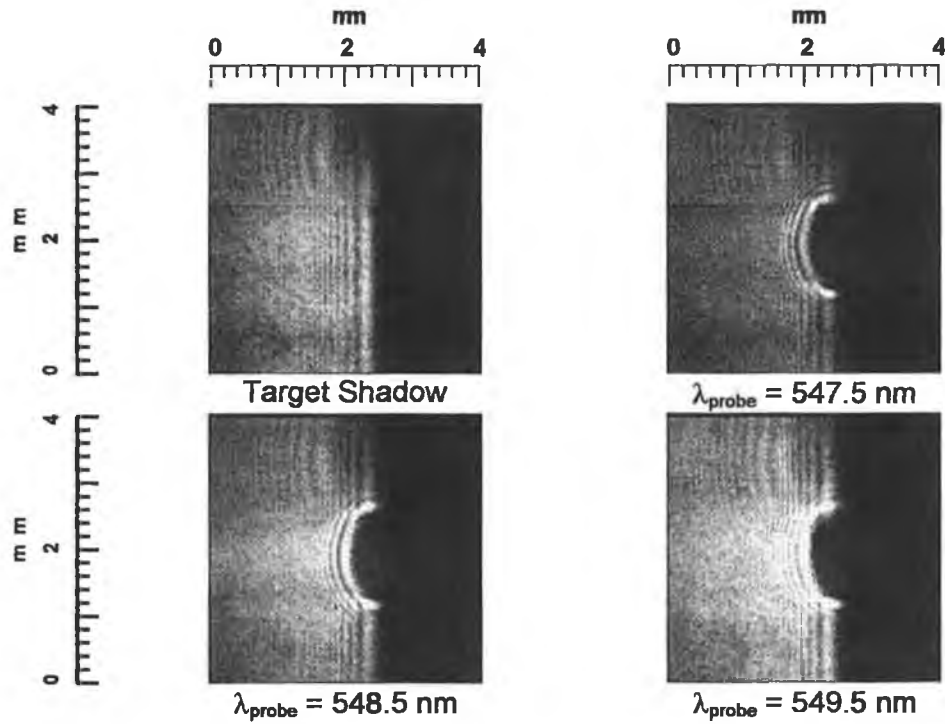Fig. 2.30: Shadowgraphs of the lithium plume at $\Delta T = 10$ ns. The laser irradiance was ~2.5 x 10^{14} W m^{-2}.
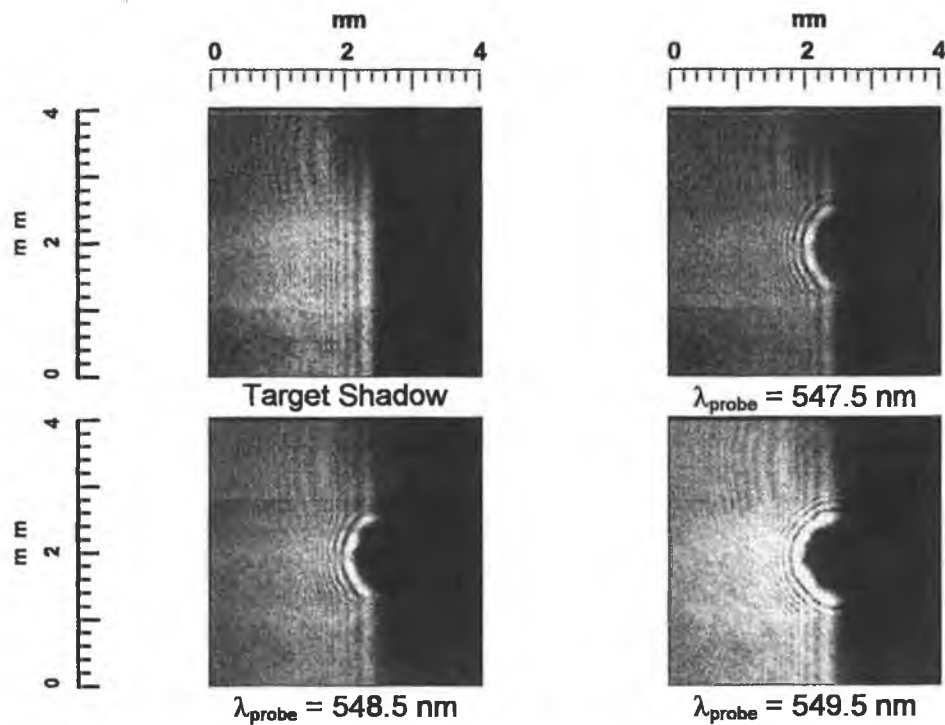

Fig. 2.31: Shadowgraphs of the lithium plume at $\Delta T = 100$ ns. The laser irradiance was ~2.5 x 10^{14} W m^{-2}.

2.3 The Dual Laser Plasma Photoabsorption Technique

2.3.1 Experimental Set-up

The experimental set-up of the DLP photoabsorption technique is depicted in fig. 2.32.
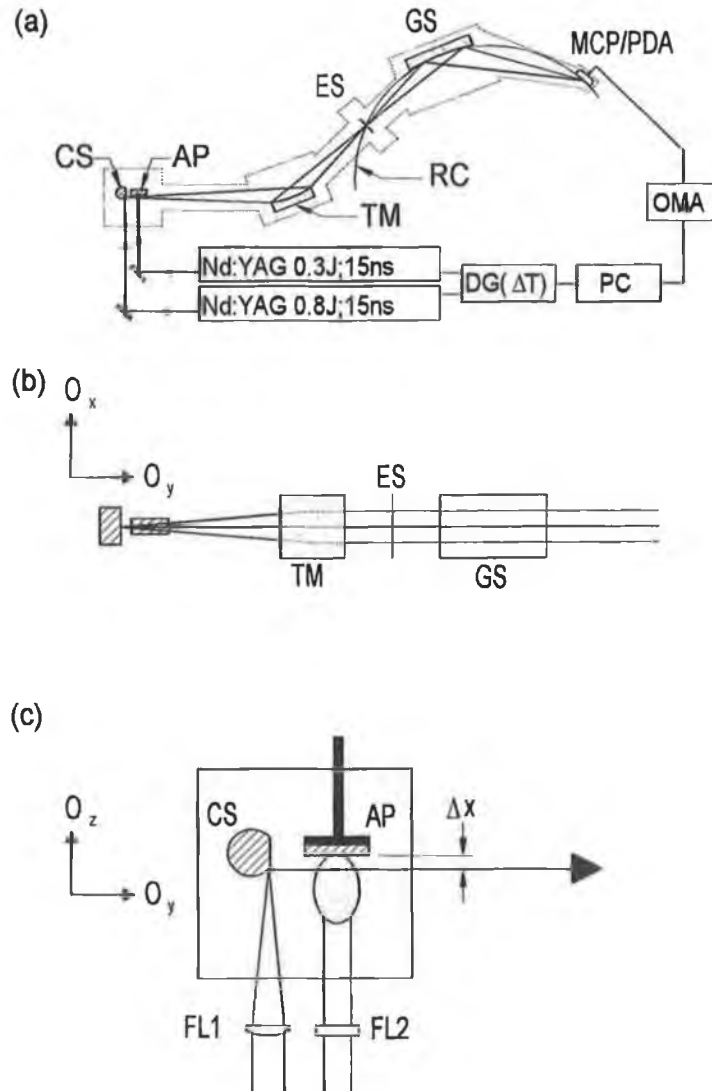

Fig. 2.32: (a) Diagram of the DLP apparatus in the horizontal plane: (CS) Continuum Source, (AP) Absorbing Plasma, (TM) Toroidal Mirror, (ES) Entrance Slit, (GS) Grating Spectrometer, (MCP / PDA) Microchannel Plate / Photodiode Array, (RC) Rowland Circle, (OMA) Optical Multichannel Analyser, (PC) Personal Computer, (DG(ΔT)) Stanford Digital Delay Generator. (b) Diagram of apparatus in the vertical plane. (c) Detailed view of the target chamber: (Δx) Distance above the plane of the sample target, (FL1) Plano-convex focusing lens, (FL2) Cylindrical focusing lens (after [106]).

The apparatus comprises three parts: (1) the lasers and the laser plasma sources, (2) the coupling toroidal optics and (3) the spectrometer and data acquisition system. The source of continuum EUV radiation (CS) was created by a Nd-YAG laser (0.8 J, 15 ns) tightly focussed onto a tungsten rod using a 100 mm uncorrected plano-convex lens (FL1). The duration of the pulse of EUV radiation was typically about the duration of the laser pulse [107]. The absorbing plasma (AP) (fig. 2.32 (c)) was created by a Nd-YAG laser (0.3 J, 15 ns) using a tightly focussed cylindrical lens (FL2) of 100 mm focal length. The irradiance on target could be varied between 10^{12} and 10^{15} W m^{-2}. The firing sequence between the two lasers (ΔT) was controlled by a digital delay generator (DG(ΔT)), the system jitter being less than 3 ns. The timing diagram is illustrated in fig. 2.33.
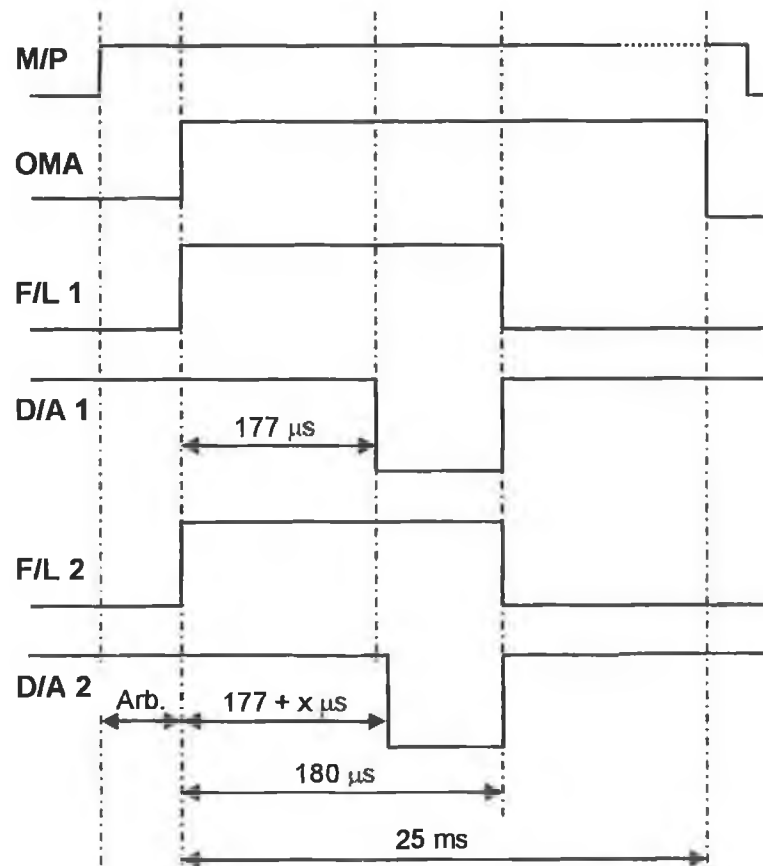

Fig. 2.33: The timing diagram for the DLP photoabsorption technique: (M/P) Master pulse (TTL), (OMA) OMA Trigger (TTL), (F/L 1) Nd:YAG (0.3 J; 15 ns) Flashlamp trigger (15 V), (D/A 1) Nd:YAG (0.3 J; 15 ns) Direct Access trigger (-15 V), (F/L 2) Nd:YAG (0.8 J; 15 ns) Flashlamp trigger (15 V), (D/A 2) Nd:YAG (0.8 J; 15 ns) Direct Access trigger (-15 V).

The optical layout conforms to the configuration prescribed by Rense and Violett [108] to increase the efficiency of a grating spectrometer by removal of astigmatism with the help of a toroidal mirror (**TM**). The radii of curvature of the toroidal mirror were chosen to produce spectral lines of uniform length on the Rowland circle (**RC**). The system is capable of imaging in the available 60 → 460 Å (27 → 207 eV) range provided by a 1,200 lines / mm grating (**GS**) operated at 84° angle of incidence. Details on stigmatic imaging of laser produced plasmas in the EUV can be found in [109]. The spectral resolving power is of the order of 1,500 at 150 eV photon energy before removal of instrumental broadening. The detector (**MCP / PDA**) was a channel electron multiplier array (CEMA) coupled using a fibre optic reducer (1.6:1) to a linear photodiode array. This has been described elsewhere [110].

2.3.2 System Characterisation

This section details the characterisation of various system parameters of the 2.2 m grazing incidence spectrometer pertinent to the quantitative interpretation of the experimentally measured spectra.

(a)   The Spatial Gain Variation across the CEMA

The spatial gain variation across the CEMA, due to changes in penetration depth of the incident radiation into the microchannels as a function of incidence angle [107], as well as possible defective pixels was estimated using the aluminium $2s^2 2p^6 \leftarrow 2s^2 2p^5 3s$ (160.074 Å) emission line. The spatial gain variation was estimated by integrating the area under the line, averaged over ten consecutive shots, for seven different overlapping CEMA settings. A fresh target surface was presented every ten shots. The resultant gain profile is shown in fig. 2.34.
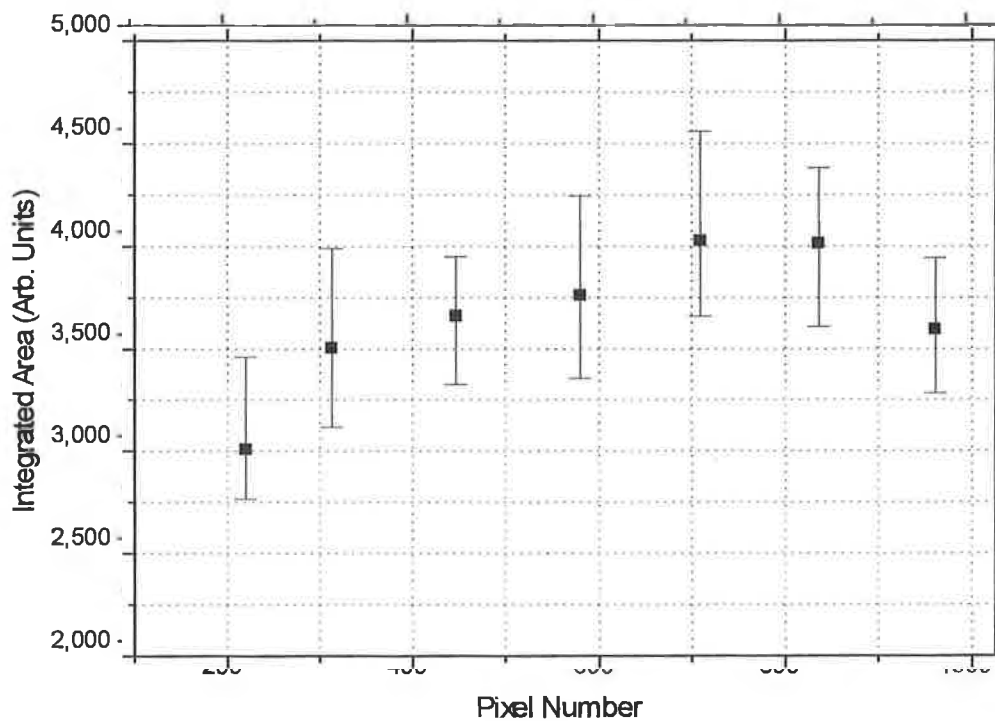
Fig. 2.34: The spatial gain variation across the CEMA.

Despite the magnitude of the error bars, a definite trend can be discerned from fig. 2.34. The gain profile shows a rapid fall-off on the left-hand (low pixel number) side of the detector i.e. for lower energies. This trend was reflected in the measurement of the emission spectrum of tungsten shown in fig. 2.35, which was obtained for three different CEMA settings with large overlaps. The fall-off in efficiency can be observed from the mismatch in the overlap of the spectra. Even more prominent, however, is the rapid fall-off in efficiency on the high pixel end of the detector i.e. for higher energies. This manifests itself at pixel locations greater than ~850. Finally, from the complete tungsten spectrum over the sensitive range of the detector (not shown here), it was possible to distinguish a small number of 'hot' pixels. The gain variation can be neglected in DLP photoabsorption measurements as it is common to both I_{v_0} and I_v, and thus cancels. However it is important in the case of emission spectra.
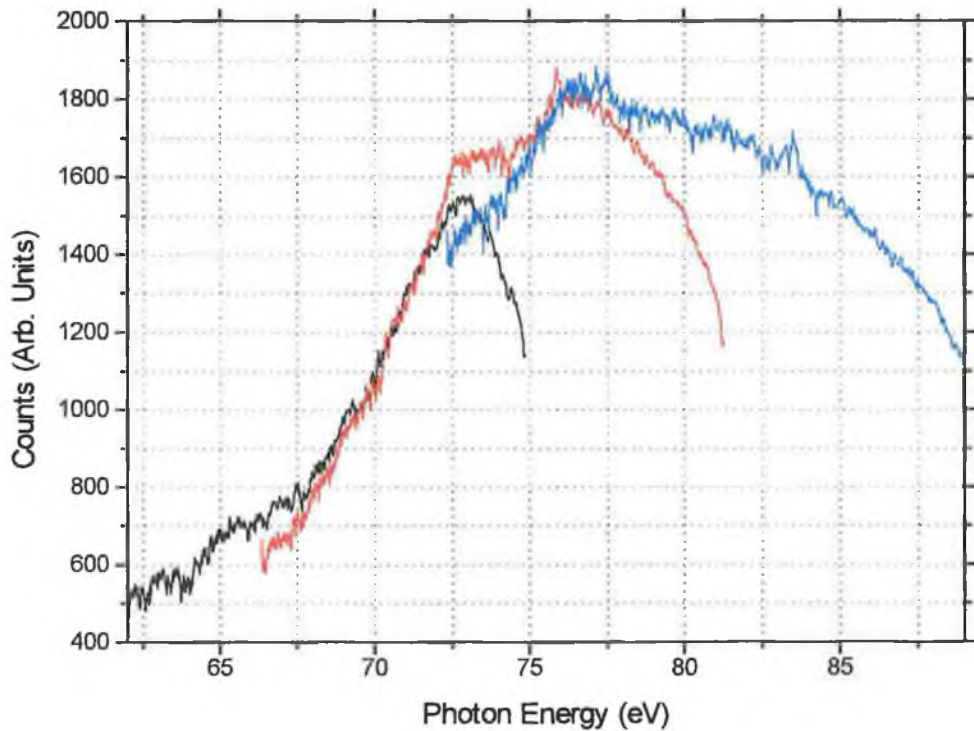
Fig. 2.35: The emission spectrum of tungsten between 62 eV and 89 eV obtained using three different CEMA settings with large overlaps between each setting. The fall-off in efficiency on both sides of the detector is easily seen, in particular for the higher energy side.

(b)   The Variation in FWHM across the CEMA

The variation in full width at half maximum (FWHM) of a spectral line across the CEMA is a consequence of positioning a flat detector on the Rowland circle as shown in fig. 2.36. The spectral lines are thus effectively 'smeared' for all pixel positions of the detector that are not tangent to the Rowland circle. In a manner similar to (a), the FWHM of the aluminium $2s^2 2p^6 \leftarrow 2s^2 2p^5 3s$ (160.074 Å) spectral emission line, averaged over ten consecutive shots, for seven different overlapping CEMA settings was determined. A fresh target surface was presented every ten shots. The resultant variation in FWHM across the face of the CEMA is shown in fig. 2.37. It should be noted that this variation also includes the small variation (typically 0.0324 Å centred at 160.618 Å) in the plate factor across the CEMA.
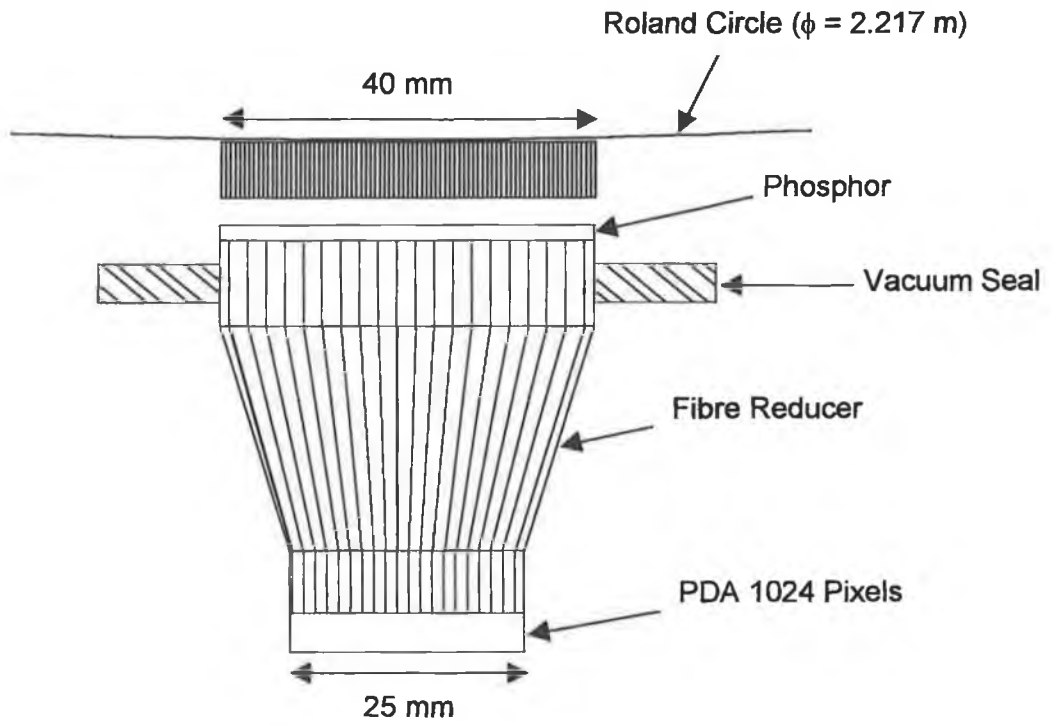
Fig. 2.36: The flat detector on the Rowland circle (to scale).
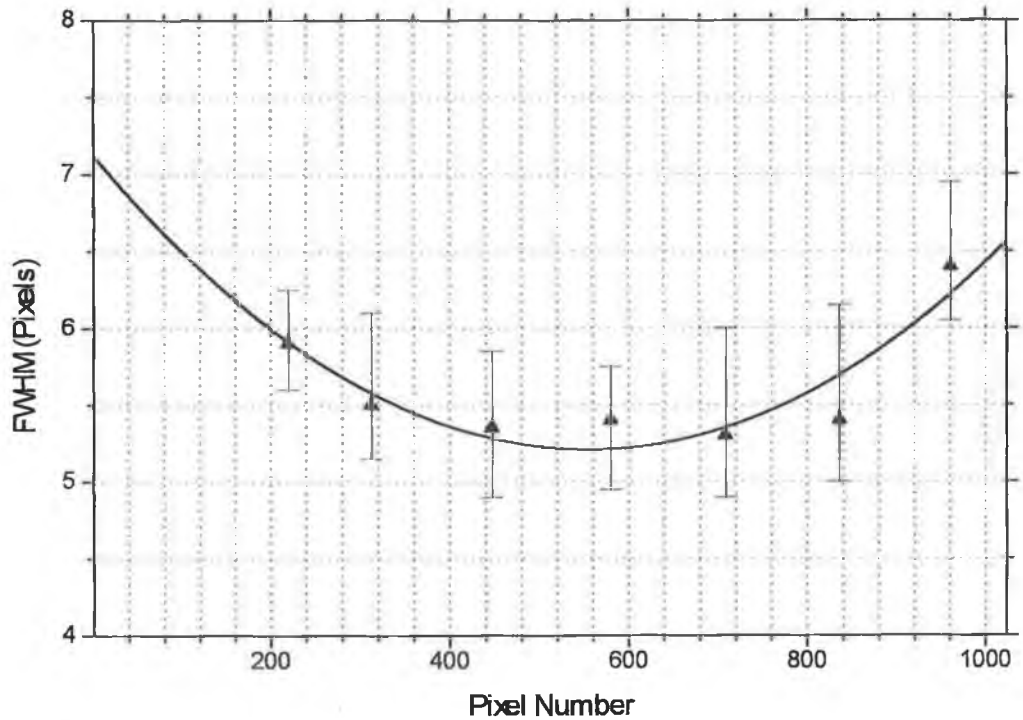

Fig. 2.37: The variation in FWHM across the face of the CEMA.

From fig. 2.37 it may be surmised that the detector is tangent to the Rowland circle, between pixel positions 500 and 600. There appears to be a marked difference between the FWHM of a spectral line positioned at this tangency point, and one that is at either extreme of the detector.

(c)   Estimation of the Instrument Function

Electron repulsion in the MCP and imperfections in the fibre reducer [107] combined with other system aberrations and diffraction effects, e.g. from the slits, the diffraction grating etc., all contribute to the broadening of spectral lines. This broadening is apart from the intrinsic broadening mechanisms discussed in §1.5. Mack *et al.* (1932) have shown that a slit width W_s gives rise to an image width on the focal curve of a concave grating in a Rowland mount, corresponding to a wavelength interval [110]

$$\Delta\lambda = \frac{W_s d_g}{R_g}$$

[2.4]

where d_g is the inter-groove spacing and R_g is the radius of curvature of the grating. The slit width, W_s, used throughout the course of these experiments was 10 μm. The corresponding wavelength interval is 0.0376 Å. This is equivalent to ~1.3 pixels centred at ~113 Å. As a first order approximation to the instrument function, the Li^{2+} Lyman β photoabsorption line was measured. Using a rough estimate for the electron density in the plasma of ~1 x 10^{24} m^{-3}, as well as the plasma temperature of ~10 eV (using the LTE model discussed in §1.3.1), one can obtain to a first order approximation the atomic frequency response. This was accomplished by convolving the computed Lorentzian (from the density estimate using the quasistatic stark broadening formula of [1.50]) and Gaussian (from the temperature estimate using [1.49]) line profiles. Deconvolving the resultant line profile from the experimentally measured Lyman β line results in an estimate for the instrument function, as shown in fig. 2.38.
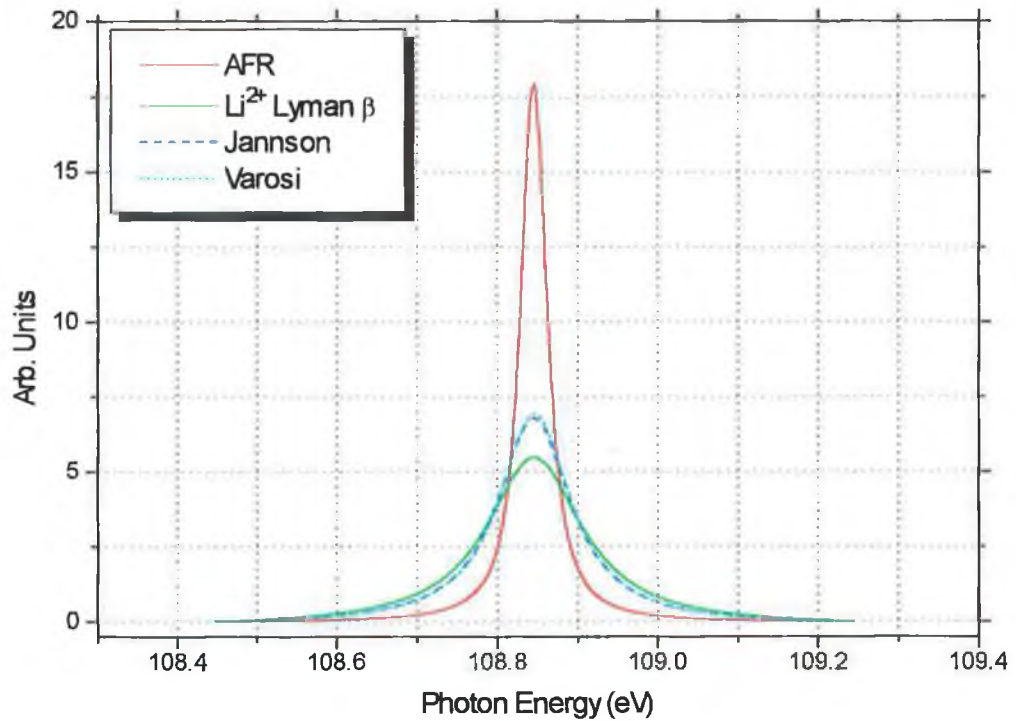
Fig. 2.38: The computed instrument function: (AFR) Atomic frequency response estimated from a convolution of the Lorentzian and Gaussian components, (Li^{2+} Lyman β) Li^{2+} Lyman β experimentally measured photoabsorption line, (Jannson) Resultant deconvolution using Jannson's algorithm, (Varosi) Resultant deconvolution using Varosi's IDL® code. The integrated area of each curve is normalised to unity for comparison.

Two procedures were used to compute the deconvolved profiles shown in fig. 2.38. The first used 20 iterations of Jannson's algorithm [111], with

$$\alpha_n \left(L_{n-1}(t) \right) = \alpha_{max} \left(L_{n-1}(t) - L_{n-1}(t)^2 \right)^{0.5} \qquad [2.5]$$

where α_{max} = 0.5. The second used 20 iterations of Varosi's maximum likelihood deconvolution technique with Poisson noise statistics. The Fast Fourier Transform (FFT) convolution procedure `convolve` (...) (see Appendix F) was arbitrarily selected over the conventional IDL® procedure `convol` (...). Defining the mean standard deviation as [64]

94

$$\sigma_{mean} = \sqrt{\frac{\sum_{i=1}^{N}(V(i) - J(i))^2}{N}}$$

[2.6]

where V(i) represents the ith data point using Varosi's maximum likelihood technique, J(i) corresponds to the ith data point using Jannson's algorithm and N is the number of data points, one can estimate the degree of correlation between the two techniques. In this case $\sigma_{mean} \cong 0.04$. The FWHM of the instrument function is ~0.11 Å (centred at 113.9049 Å) corresponding to a Lorentzian profile of approximately 3.7 pixels. This compares with typical Doppler and Stark broadened line widths of EUV lines in laser plasmas. In a similar experimental set-up [107] the instrument function was reported to be 3 pixels. Unfortunately, the shape of the profile was not disclosed. One should note that as a direct result of the variation in the FWHM of spectral lines across the face of the CEMA (see (b)), that the instrument function estimated here, centred about pixel location 390, will also vary across the detector. Finally, it should be mentioned that the instrument function may also vary with photon energy.

(d)   Higher Order Contributions

If a light source emits a continuum of wavelengths, then at the physical location of, e.g. 800 Å in first order, wavelengths of 400 Å, 266.66 Å and 200 Å in second, third and fourth orders will also be present and available to the same detector [112]. This can be eliminated through the use of bandpass filters. Higher order contributions have been estimated using boron, lithium and aluminium targets. Typically, they contribute <1% to the detected signal [113].

(e)   Scattered Light Contributions

Scattered light may be produced by either of the following [112]:

(i)   Randomly scattered light due to surface imperfections on any optical surface.

(ii)   Focused stray light due to non-periodic errors in the ruling of the grating grooves.

From experimental results using tungsten as a back-lighter (see §2.3.3 and §3.3.2), scattered light contributions appear to become substantial at energies greater than ~100 eV. In order to ascertain the region of the electromagnetic spectrum of tungsten which predominately contributes to scattered light in this region the following considerations must be observed:

(a)   The spectrum of tungsten over the sensitive range of the detector.

(b)   The quantum efficiency of the CsI coated MCP / PDA detector.

(c)   The diffraction grating / toroidal mirror efficiencies.

The contribution from higher orders will not be considered further. From (a) (see fig. 2.39), one would expect that scattered light originating in the source in the 60 → 110 Å (113 → 207 eV) range is negligible. This is an important consideration if the scattered light contribution above ~100 eV is to be quantified using the thin film filters below.
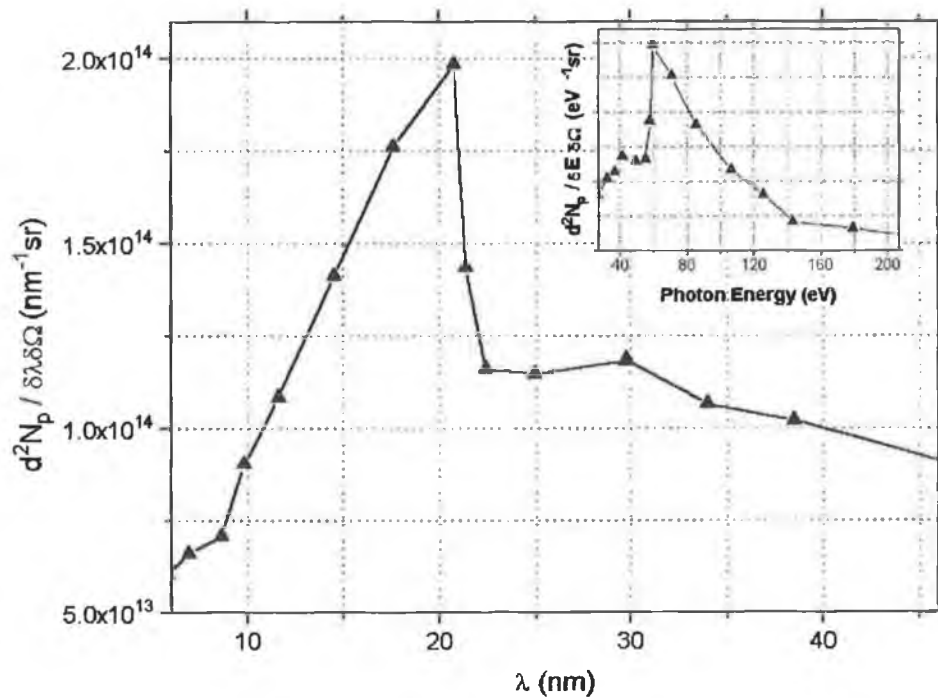

Fig. 2.39: The spectrum of tungsten over the sensitive range of the detector (after [114]) recorded using an 800 mJ Nd:YAG (1.064 μm) laser with a FWHM of 15-20 ns. The inset illustrates this on an eV scale.

This would also be substantiated by (b) where the detection efficiency of the MCP over the range of the instrument decreases with increasing energy (see fig. 2.40), and also

by (c) where the calculated efficiency of the toroidal mirror / diffraction grating combination falls off rapidly above ~130 eV as shown in fig. 2.41.
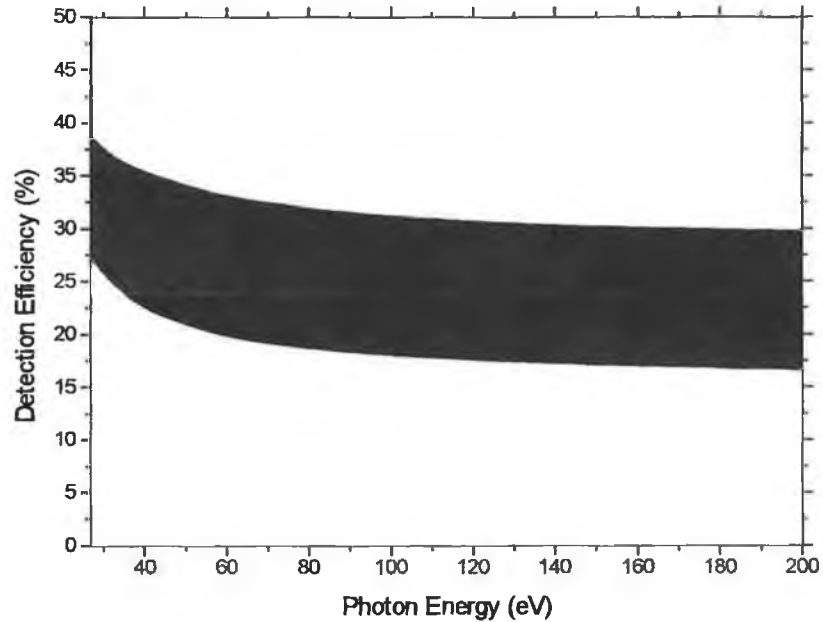

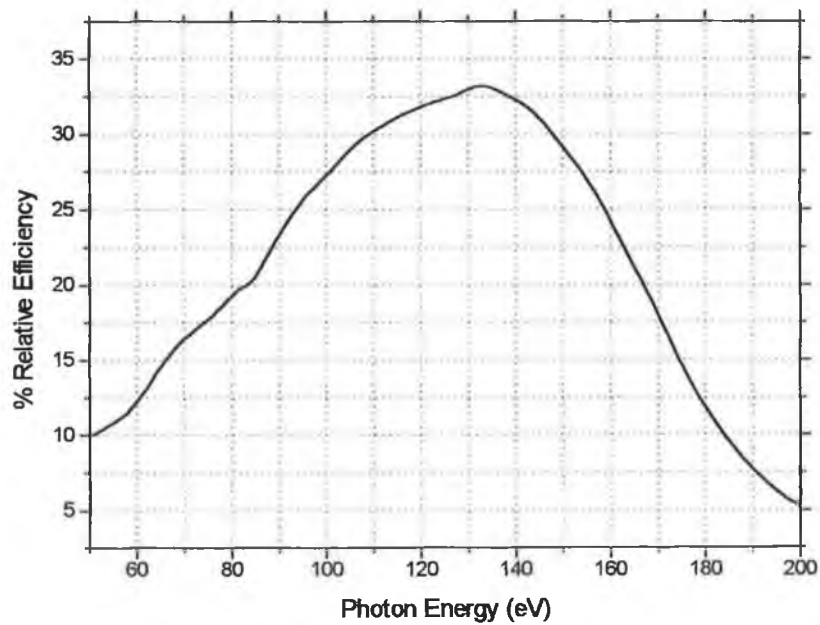Fig. 2.40: The photon detection efficiency of a CsI coated MCP [115].

Fig. 2.41: The relative efficiency (in first order) of the gold coated toroidal mirror / gold coated diffraction grating combination used in the 2.2 m grazing incidence spectrometer. The toroidal mirror reflectance was calculated using Henke's tables for an 84° angle of incidence. The efficiency of the diffraction grating was computed by [116].

97

By positioning a 0.9 μm thin film mylar filter, between the emitting tungsten plasma and the toroidal mirror, this assumption could be confirmed. The theoretical and experimentally measured transmission curves of a 0.9 μm thin film of mylar are shown in fig. 2.42. The experimental curve was obtained by averaging twenty consecutive shots for seven different CEMA settings, with large overlaps between each setting.
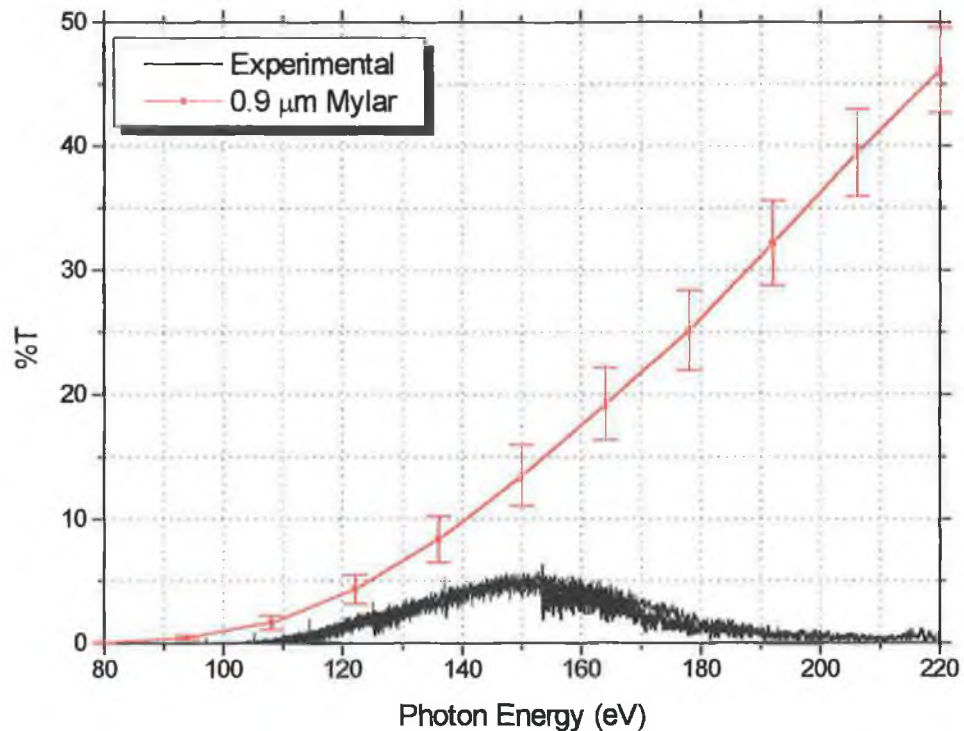

Fig. 2.42: The theoretical and experimentally measured transmission spectra of a 0.9 μm thin film of mylar ($C_{10}H_8O_4$; ρ = 1.4 g cm^{-3}) [117]. The error bars indicate the thickness tolerances specified by Goodfellow Metals (±10%).

The differences between the two transmission curves can be interpreted in a number of ways. An initial consideration involves coating of the thin film filter by blow-off material from the tungsten plasma. One would expect this to be of the order of a few Å. Secondly, errors in the measurement of the thickness of the thin film, estimated to be ±10% [5] could contribute to the discrepancy. Despite these factors, it will be assumed, taking into account the relative intensity of the spectrum of tungsten, that scattered light contributions from the 60 → 110 Å (~113 → 207 eV) are negligible. This is based on the large discrepancy shown in fig. 2.42, which, assuming negligible scattered light contributions on the measured I_v signal, i.e. (from the > ~100 eV region

98

of the tungsten spectrum), means the discrepancy can be attributed to the scattered light contributions detected on the I_{v_0} signal. The resultant transmission is thus much lower than expected. This argument is supported in the following paragraphs.

From the spectrum of tungsten, it is conceivable that the majority of scattered light originates from the 110 $\rightarrow$ 460 Å (~27 $\rightarrow$ 113 eV) range. This was verified by measuring the transmission spectrum of a 0.25 μm thin film aluminium filter (see fig. 2.43). The experimental curve was obtained by averaging twenty consecutive shots for fourteen different CEMA setting with large overlaps between each setting. The noticeable difference in fig. 2.43(a) between the theoretical and the experimental transmission curves at energies < 90 eV is not a result of inaccurate atomic scattering factors. As a result of experimental measurements on aluminium, these are expected to be accurate down to at least 25 eV [120]. Rather, the difference can be explained as follows. Powell *et al.* predict a nominal aluminium oxide (Al_2O_3) coating of 18 Å for aluminium filters at or near the time of manufacture [119]. Additionally, plasma blow-off from the tungsten target may coat the filter. Typically, one would expect this to be of the order of a few Å. Applying these corrections to a 0.3 μm (0.25 μm + 20%) Al filter with an Al_2O_3 coating of 80 Å and a tungsten coating of 10 Å, the difference between the transmission curve predicted by Henke, and the experimentally measured one at energies < 90 eV is reconciled. This is shown in fig. 2.44.
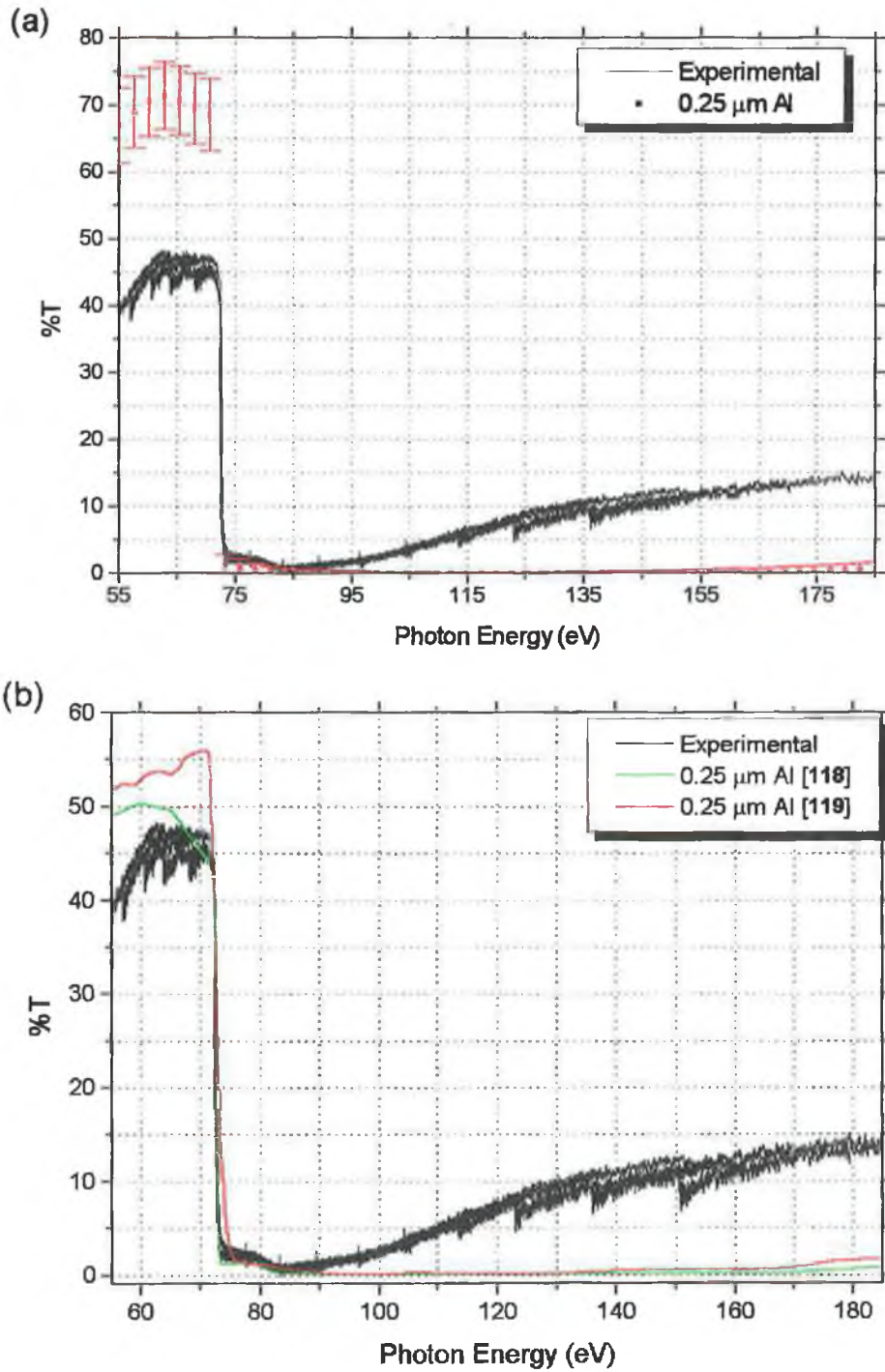
Fig. 2.43: (a) The theoretical and experimentally measured transmission spectra of a 0.25 μm aluminium filter. The error bars indicate the thickness tolerances specified by Goodfellow Metals (± 20%). (b) The experimentally measured transmission curves of similar thickness aluminium thin films by other workers [118][119].
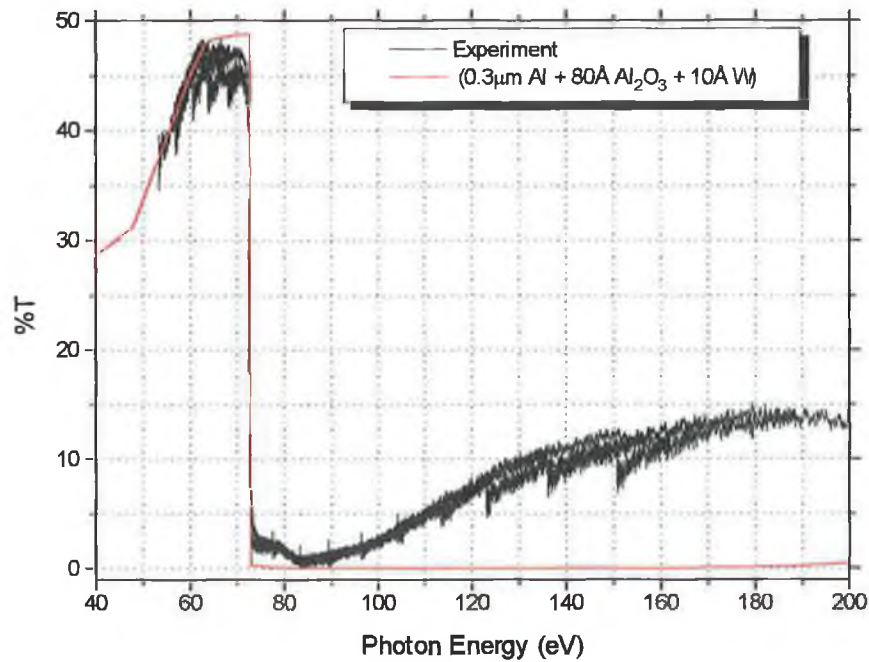
Fig. 2.44: The corrected transmission spectrum of aluminium proposing the origins of the discrepancy between the theoretical curve of Henke and the current work.

From the thickness of the Al_2O_3 coating applied to the corrected transmission curve, the aluminium filter was estimated to be less than 1 year old [119]. The differences between the experimentally measured transmission curves of fig. 2.43(b) at energies < 90 eV of [118] and [119] in comparison with the present work can be explained in terms of experimental differences in the measurement of the linear absorption coefficient μ_{abs} (cm^{-1}). Indeed, Hagemann [118] concentrated on energies greater than the L_{III} edge (72.7 eV) of aluminium.

The differences at energies greater than ~90 eV cannot readily be explained in this same manner. However, from the spectrum of tungsten (see fig. 2.39) and the measured transmittance of a 0.9 μm mylar thin film (see fig. 2.42), one can ascertain that scattered light, the majority of which originates at energies lower than 100 eV, is detected on both the I_{v_o} and I_v signals in the 100 → 200 eV energy range. The transmittance, I_v/I_{v_o}, is thus strongly affected. Comparing the theoretical and the measured transmission spectra of the mylar thin film thus provides an estimation of the

101

scattered light contribution on I_{v_o}, the back-lighting continuum in DLP photoabsorption experiments, as the I_v signal remains unaffected by scattered light contributions from the <100 eV energy range, i.e. $I_v = I_{v_{TRUE}}$. This is shown in fig. 2.45 as the fractional component of scattered light $\left(I_{o_s} \middle/ I_{v_{o\,TRUE}} \right)$ on I_{v_o} between ~120 eV and ~180 eV, where [121]

$$\frac{I_{o_s}}{I_{v_{o\,TRUE}}} = \frac{T_f - M_f}{M_f}$$

[2.7]

with

$$T_f = \frac{I_{v_{TRUE}}}{I_{v_{o\,TRUE}}}$$

[2.8]

representing the true transmission in the absence of any scattered light contributions and

$$M_f = \frac{I_v}{I_{v_o}}$$

[2.9]

is the measured transmittance, where in this case only I_{v_o} contains a scattered component I_{o_s}. In DLP experiments the absorbing plasma, however, acts as a filter, so that the scattered light contribution on I_v, cannot readily be ascertained. This difficulty can theoretically be overcome if the true transmission spectrum of the plasma is known, using the following:

$$M_f' = \frac{I_{v_{TRUE}} + I_s}{I_{v_{o\,TRUE}} + I_{o_s}}$$

[2.10]

is the experimentally measured transmission spectrum where I_s is the scattered light component on I_v. Rearranging [2.10] one obtains

102

$$M_f' = \frac{T_f + \dfrac{I_s}{I_{v_0 TRUE}}}{1 + \dfrac{I_{o_s}}{I_{v_0 TRUE}}}$$

[2.11]

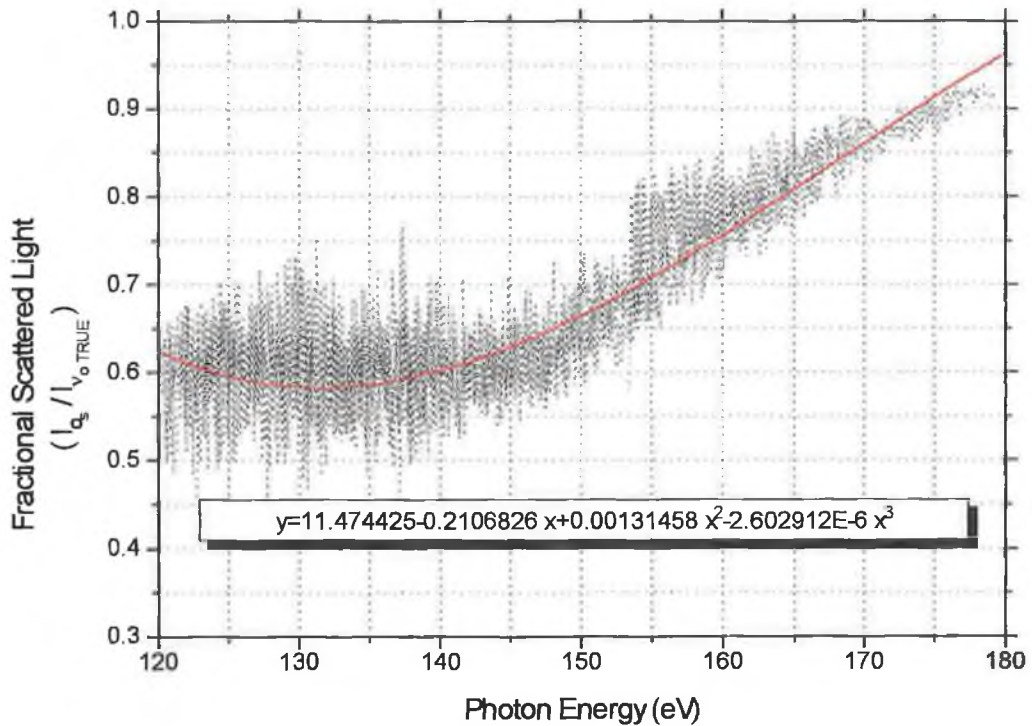$y = 11.474425 - 0.2106826\,x + 0.00131458\,x^2 - 2.602912E\text{-}6\,x^3$

Fig. 2.45: The fractional component of scattered light on I_{v_0} calculated using the theoretical and experimental transmission curves of a 0.9 μm mylar thin film filter. Also indicated in the figure is a 3rd order polynomial fit to the data.

Knowing $\dfrac{I_{o_s}}{I_{v_0 TRUE}}$ from the previous calculation using a mylar thin film, as well as T_f, the true transmission of the plasma facilitates computation of $\dfrac{I_s}{I_{v_0 TRUE}}$. T_f can be computed using Henke's tables [117] in the case of a thin film filter, or from the photoionisation cross-section data of Verner *et al.* [122], knowing the absorber density and absorbing plasma column length, in the case of a laser-produced plasma (see §3.3.2).

(f)   35 Counts Pixel Offset

A final consideration in the analysis of the DLP results presented in this chapter is the 35 counts pixel offset inherent in the MCP detector, as described by [121]. While this clearly affects the analysis of the absorption spectra presented in this chapter, it is not felt that the ratio $\ln\left(\frac{I_{v_o}}{I_v}\right)$ experiences a dramatic inaccuracy as a direct consequence of this, except perhaps at higher energies where the background continuum is weaker. This can be explained in the following manner. The true signal can be represented by $\ln\left(\frac{I_{v_o}}{I_v}\right)$, while the measured signal is described by

$$\ln\left(\frac{I_{v_o} + \Delta}{I_v + \Delta}\right) \tag{2.12}$$

where Δ represents the 35 counts pixel offset. [2.12] can be expressed as

$$\ln\left(\frac{I_{v_o} + \Delta}{I_v + \Delta}\right) = \ln\left(\frac{I_{v_o}\left[1 + \frac{\Delta}{I_{v_o}}\right]}{I_v\left[1 + \frac{\Delta}{I_v}\right]}\right)$$

$$= \ln\left(\frac{I_{v_o}}{I_v}\right) + \ln\left(\frac{1+a}{1+b}\right)$$

$$= \ln\left(\frac{I_{v_o}}{I_v}\right) + \ln(1+a) - \ln(1+b) \tag{2.13}$$

where $a = \frac{\Delta}{I_{v_o}}$ and $b = \frac{\Delta}{I_v}$. Using the Taylor series expansion [46] of the second and third terms in [2.13] to third order, this becomes

$$\ln\left(\frac{I_{v_o}}{I_v}\right) + a - \frac{a^2}{2} + \frac{a^3}{3} - b + \frac{b^2}{2} - \frac{b^3}{3} \tag{2.14}$$

104

Assuming 50% absorption, then $I_{\nu_0} = 2I_\nu$, and thus $b = 2a$, with the result that [2.14] becomes

$$\ln(2) + a - \frac{a^2}{2} + \frac{a^3}{3} - 2a + \frac{4a^2}{2} - \frac{8a^3}{3}$$

$$= \ln(2) - a + \frac{3a^2}{2} - \frac{7a^3}{3} \qquad \text{[2.15]}$$

Assuming $I_{\nu_0} = 800$ and using $\Delta = 35$ (and hence $a = 0.04375$), [2.15] results in a measured value of 0.652 in the case of 50% absorption compared with the true value of 0.693. The resulting error is thus ~6% of the true value. In the case where $I_{\nu_0} = 400$, and again assuming 50% absorption the error increases to ~11%.

2.3.3 Experimental Results

The present results were obtained with a lithium plasma expanding in vacuum at a pressure of ~3 x 10^{-6} mbar.

(a) The Temporal and Spatial Evolution of Li^0 and Li^+

The temporal and spatial evolution of Li^0 was mapped (see fig. 2.46) by integrating the optically thin spectrum of the $1s^2 2s \rightarrow 1s2s2p$ transition (line A) at 210.46 Å, for varying distances, Δx, above the target surface (see fig. 2.32), and time delays, ΔT, between the laser pulses. The irradiance used to create the back-lighting plasma was ~4 x 10^{14} W m^{-2}. The absorbing plasma was generated using a Nd:YAG (0.3 J, 15 ns) with a column length of ~2 mm. The resultant irradiance was ~9 x 10^{13} W m^{-2}. In the case of Li^+, the same procedure under the same experimental conditions was used for the $1s^2 \rightarrow 1s2p$ transition (line B) at 199.2792 Å. The results are plotted in fig. 2.47.
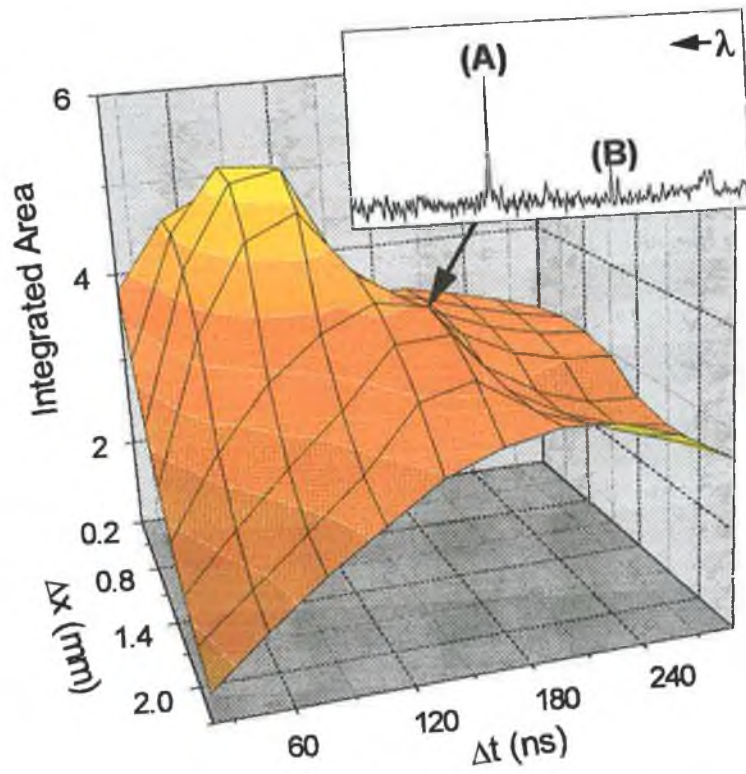
105

Fig. 2.46: The temporal and spatial evolution of Li°.
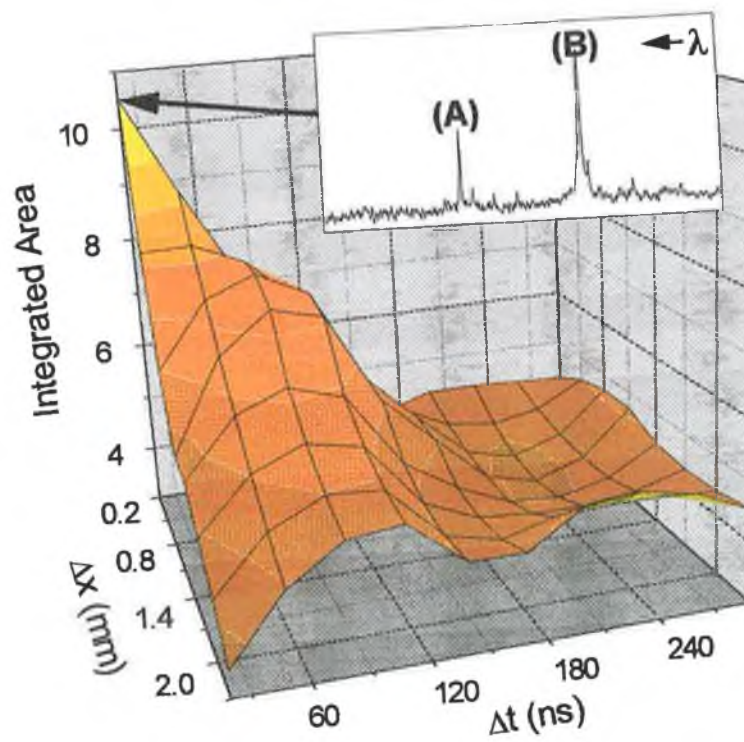

Fig. 2.47: The temporal and spatial evolution of Li⁺.

The two vertical scales are not directly comparable since the two transitions have different oscillator strengths.

(b) The Photoabsorption Spectrum of Li$^+$

With reference to figs. 2.46 and 2.47, one can immediately observe that the Li$^+$ ions appear in the earlier stages of the plume expansion and are concentrated close to the target surface along its normal. Conversely, the population of neutral atoms appears to peak at a later stage of the expansion and tends to occupy a comparatively larger area. Thus, in order to ensure that Li$^+$ is the dominant ion stage present in the plasma, one should probe the lithium plasma in conditions corresponding to $\Delta x \sim 0.4$ mm, $\Delta T \sim 30$ ns. Under these experimental conditions the relative absorption cross section spectrum of Li$^+$ as a function of photon energy was measured. This is plotted in fig. 2.48 between 61.8 eV and 74.8 eV. The observed lines correspond to the He-like resonance series $1s^2 \rightarrow np$ with n = 2, 3, 4, 5, 6 and 7.
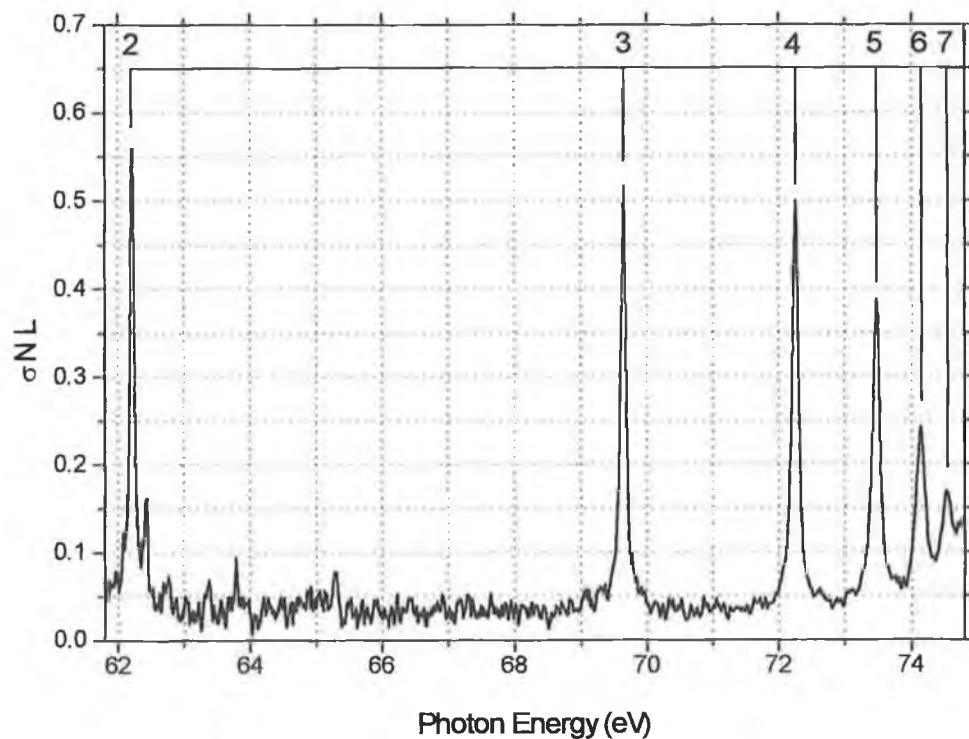

Fig. 2.48: The photoabsorption spectrum of Li$^+$ between 61.8 eV and 74.8 eV.

The irradiance of the laser beam on target was roughly estimated at ~2 x 10^{13} W m^{-2} for a column length of 0.3 mm.

(c)   The Photoionisation Spectrum of Li$^+$

Using the same experimental conditions as (b), the photoionisation spectrum of Li$^+$ was measured between threshold (75.64 eV) and 180 eV using eleven CEMA settings along the Rowland circle, with large overlaps between adjacent settings.   The cross section for Li$^+$ varies between ~2.5 Mb at threshold and ~0.3 Mb at 180 eV [122], corresponding to a factor of ~9 on the value of transmission.   Thus, in order to carry out the measurements in a satisfactory absorbance regime, the column length was increased with increasing photon energy from 2 mm at 75.64 eV to 7 mm at 180 eV. The photoionisation spectrum of Li$^+$ $1s^2 \rightarrow 1s\varepsilon p$ is plotted in fig. 2.49.
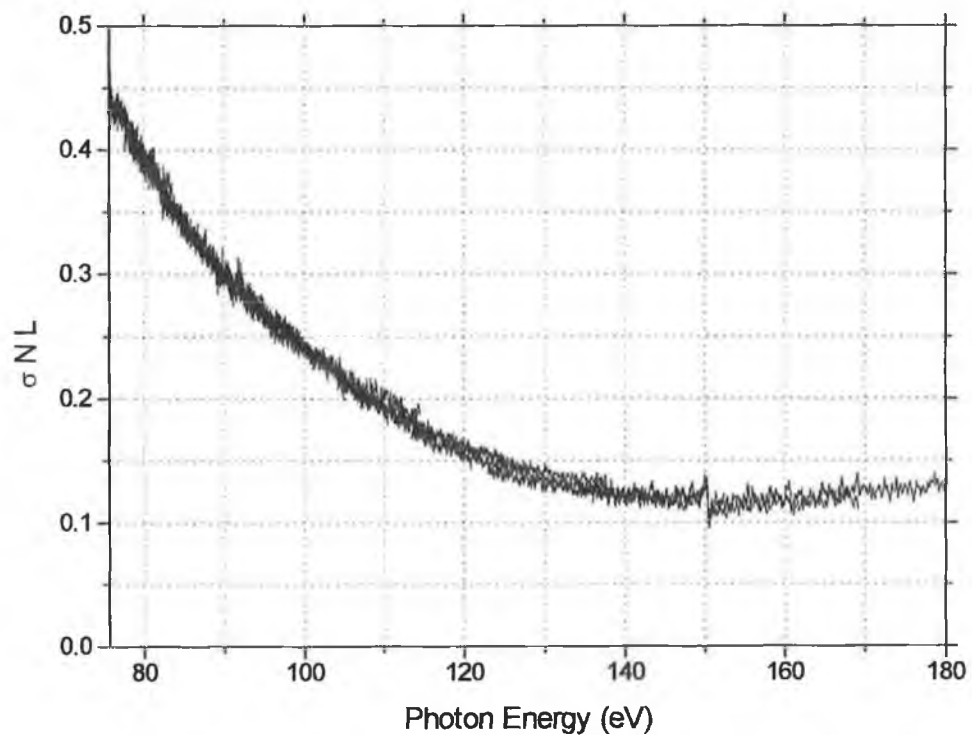
Fig. 2.49: The photoionisation spectrum of Li$^+$ between threshold (75.64 eV) and 180 eV.

The doubly excited resonance ($1s^2 \rightarrow 2s2p$) at ~150.28 eV is clearly visible in the figure. The contribution of scattered light can clearly be seen from the shape of the

108

photoionisation continuum particularly at energies > 160 eV. This topic is re-addressed in §3.3.2.

Chapter 3

The content of this chapter pertains to the analysis and discussion of the experimental results presented in chapter 2. In particular, plasma parameters such as expansion velocities, temperature and species-specific population distributions are estimated in relation to the diagnostic techniques previously outlined. Instrumental effects on the data are explored where appropriate. In all cases results are correlated with the plasma models presented in chapter 1.

3.1 The Fast-Frame Photography Technique

3.1.1 The Free-Expansion of a Lithium Plume in Vacuum

The fast-frame photography results of §2.1.3 provide insight into the spatial and temporal characteristics of the expansion of the constituent plasma species. In the early stages of expansion, the plume remains predominately confined close to the axis constituting the target normal, with a velocity component along this axis (the longitudinal component) larger than its radial counterpart, i.e. the velocity component parallel to the target surface. The plasma cloud in the early period of expansion has a minimum size in the direction normal to the target surface, i.e. along the x-axis (see fig. 2.1) [123]. As the pressure gradient is largest in this direction [124], the highest velocity is therefore along this axis giving rise to the characteristic elongated plasma shape [17]. This is consistent with a qualitative study performed by [59] on the effect of the location of the sample relative to the position of the focus of the target lens, whereby for a relatively large spot size, the plasma was very flat during the initial stages of expansion (see for example fig. 2.14). Conversely, as the sample approached the focal position, the

110

plasma became more spherical [17][59]. Furthermore, it may be observed from the isointensity contour plots of figs. 2.14, 2.16 and 2.18, that the shape of the intensity level distribution along the axis of expansion remains reasonably constant with time; indicative of a zero acceleration gradient. Assuming negligible self-absorption, this is indicative of a self-similar expansion for the plume as outlined in §1.2.1. A direct comparison of figs. 2.14 and 2.22, imaged using a narrowband interference filter centred at 671.5 nm (I/F 670IFS10-25), and a high-wavelength-pass filter (R-62) respectively, was used as an estimation for the continuum radiation level. Both sets of images represent the expansion of the $1s^22s \leftarrow 1s^22p$ (670.7 nm) transition in Li^o. The image-set obtained using the R-62 bandpass filter, however also include continuum radiation above ~610 nm. As can be seen from the similarity of the figures, the continuum level is relatively low. Indeed, from the emission spectrum of a laser produced lithium plasma measured by Kennedy [125] one would expect the continuum level to be localised to within a few mm from the target surface. This is also consistent with a spectroscopic study of aluminium plasmas performed by Knudtson *et al.* [126]. In order to estimate the peak longitudinal velocity specific to each of the species present in the plasma, the position of the leading luminous edge of the expanding plume as a function of time was measured. This is shown in fig. 3.1. The peak velocity of the Li^o transition ($1s^22s \leftarrow 1s^22p$, 670.7 nm) is ~4 x 10^6 cm s^{-1} while the peak velocity for the Li^{o*} transition ($1s^22p \leftarrow 1s^23d$, 610.3 nm) is ~5 x 10^6 cm s^{-1}. The velocity profiles of the neutral lithium transitions of fig. 3.1 show a linearity typical of the free expansion of a plasma plume [21]. On the contrary from fig. 3.1, a two velocity component structure is immediately apparent for the lithium ion (1s2s ← 1s2p, 548.4 nm), whereby the ion expands freely at a velocity of ~4 x 10^6 cm s^{-1} up to ~200 ns, whereupon it slows to a velocity of ~2 x 10^6 cm s^{-1}. This is possibly a consequence of a density related effect of the 2p level, whereby collisional ionisation processes, for example, are required to re-populate the 2p level before the radiative decay process to the 2s level is detected. Furthermore, contrary to previously reported observations [60][123] the peak velocity of the ionised species is less than that of the ground and excited states of the neutral. The error associated with each of the velocity estimates above is ~ ±25%. This is based on the spatial resolution estimate of §2.1.2(a), as well as the 'blurring' effect of a finite gate width of 9 ns for a typical velocity of 10^6 cm s^{-1}. Other sources of error such as §2.1.2(b) in the determination of the plasma boundary are not to expected to be of major significance.
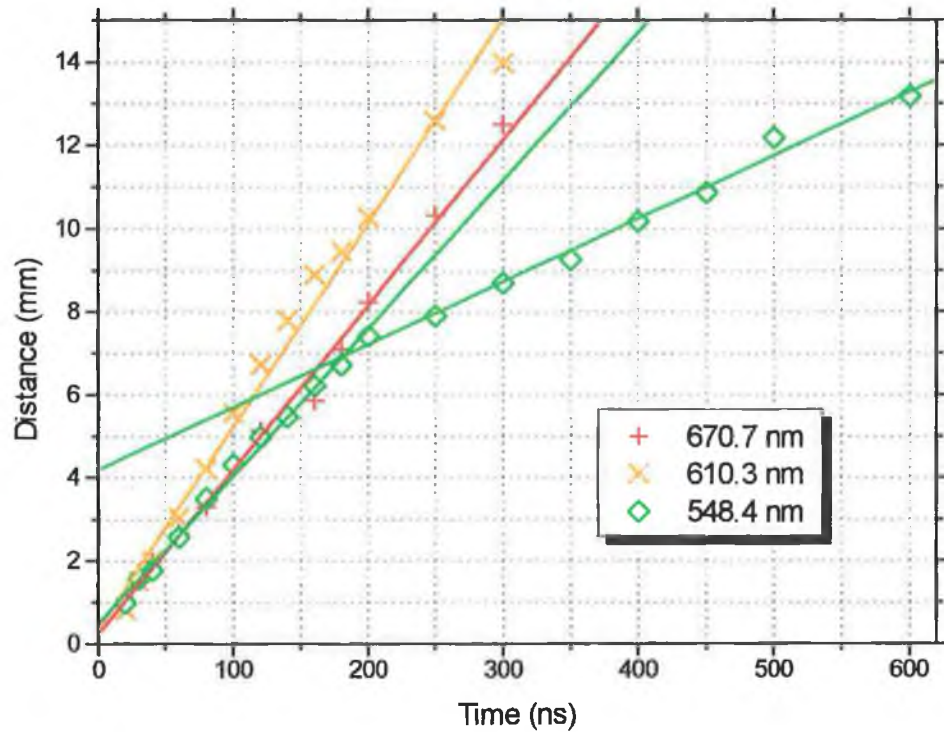
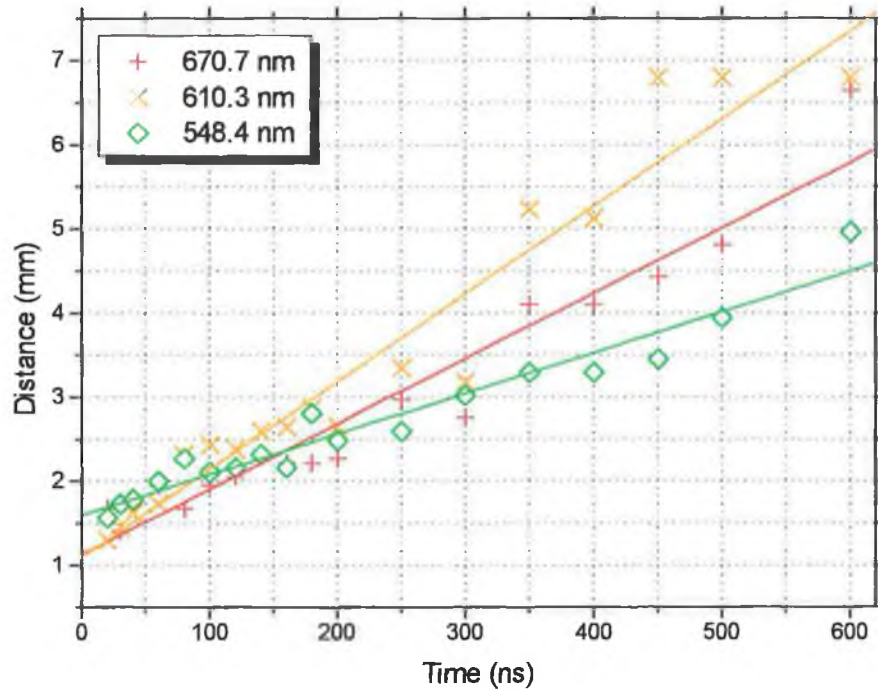Fig. 3.1: The position of the leading luminous edge of the expanding plume along the axis of expansion as a function of time for the three transitions investigated.

Comparing the peak velocities obtained in this manner with the centre of mass velocities [127] obtained by fitting the variation in the x-position of the centre of mass of the complete image, C_x, as a function of time, where C_x was computed using [128]

$$C_x = \frac{\sum\limits_{row=1}^{NR} \sum\limits_{col=1}^{NC} F_{(row,col)}.col}{area(F)}$$ [3.1]

yields velocities of ~1 x 10^6 cm s^{-1} for Li^o and ~1 x 10^6 cm s^{-1} for Li^{o*}. Again a similar trend was reflected in the ion in that a two component velocity of ~2 x 10^6 cm s^{-1} (up to ~200 ns) and ~8 x 10^5 cm s^{-1} (after ~200 ns) was observed. $F_{(row,col)}$ in [3.1] is a weighting factor representing individual non-zero pixel values in the image, col is the column number of the pixel in the image, and the area of F is calculated by a running sum of each non-zero pixel value in the image.

Applying an identical procedure to that above to obtain the peak expansion velocity in a direction normal to the expansion axis, i.e. along the y-axis (see fig. 2.1), one obtains

112

radial velocities of ~8 x 10^5 cm s^{-1} for the Li^o transition, ~1 x 10^6 cm s^{-1} for the Li^{o*} transition and ~5 x 10^5 cm s^{-1} for the Li^{+*} transition. This is illustrated in fig. 3.2.

Fig. 3.2: The position of the leading luminous edge of the expanding plume in a direction normal to the direction of expansion as a function of time for the three transitions investigated.

Assuming the plasma behaves as a high-temperature high-pressure gas [17][124], the expansion was modelled by numerically solving the equations of motion ([1.7] and [1.8]) using a fifth order Runge-Kutta integration technique with adaptive step-size control, assuming three-dimensional isothermal expansion during the time interval of the laser pulse, followed by an adiabatic expansion of the plume upon termination of the laser pulse. The initial conditions (at t = 0), used in the calculation are shown in table 3.1. The initial temperature was computed using the maximum temperature of the plasma reached in the self-similar model [21] for a plasma volume of 4 x 10^{-10} m^{-3}, an average charge of unity and an initial ion density of 10^{27} m^{-3}. The initial velocity in the x-direction was computed from the boiling point of lithium (1615 K [5]). The initial dimensions along the y- and z-axes were estimated from the laser energy burn pattern, while the estimate for the initial dimension along the x-axis was taken from [17]. In any case the critical initial values for the computation of the plasma dimensions as a function of time are the initial isothermal temperature and the specific heat ratio γ.

113

Parameter	Value	Units
T_o	5	eV
M	6.941	amu
γ	1.2	
$X_{(t=0)}$	2	mm
$Y_{(t=0)}$	2	mm
$Z_{(t=0)}$	100	μm
$V_{x\,(t=0)}$	1×10^3	m s^{-1}
$V_{y\,(t=0)}$	1×10^3	m s^{-1}
$V_{z\,(t=0)}$	2×10^3	m s^{-1}
$\Delta t_{\,laser}$ (FWHM)	15	ns

Table 3.1: Initial values of the parameters used to solve equations [1.7] and [1.8] describing the growth of a lithium plume in terms of an initial isothermal expansion followed by an adiabatic expansion.

The resultant plasma expansion as a function of time is shown in fig. 3.3, while the plasma acceleration is shown in fig. 3.4.
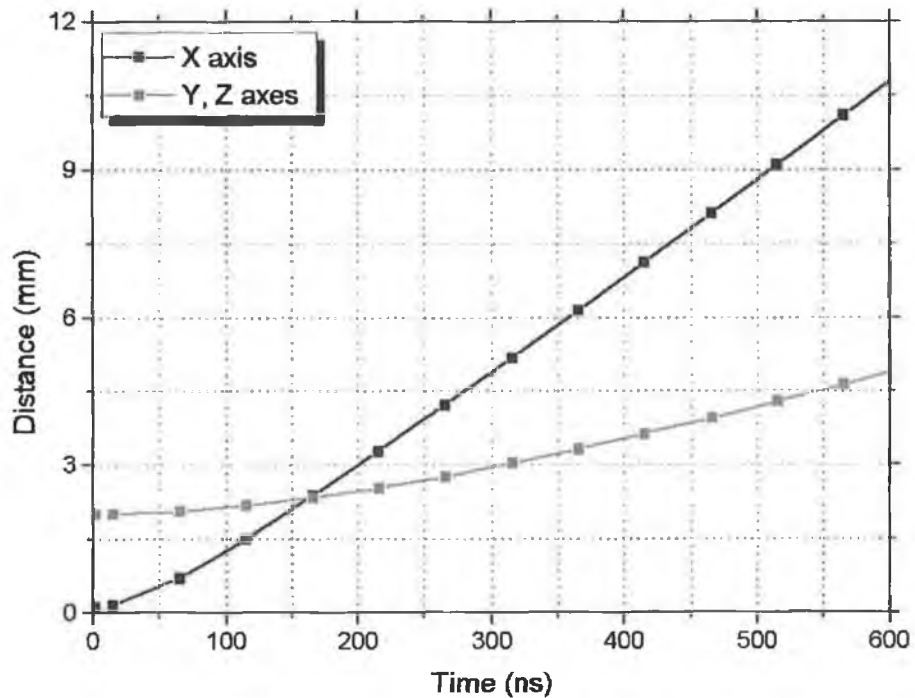
Fig. 3.3: The expansion of a lithium plume numerically modelled using the initial values shown in table 3.1.
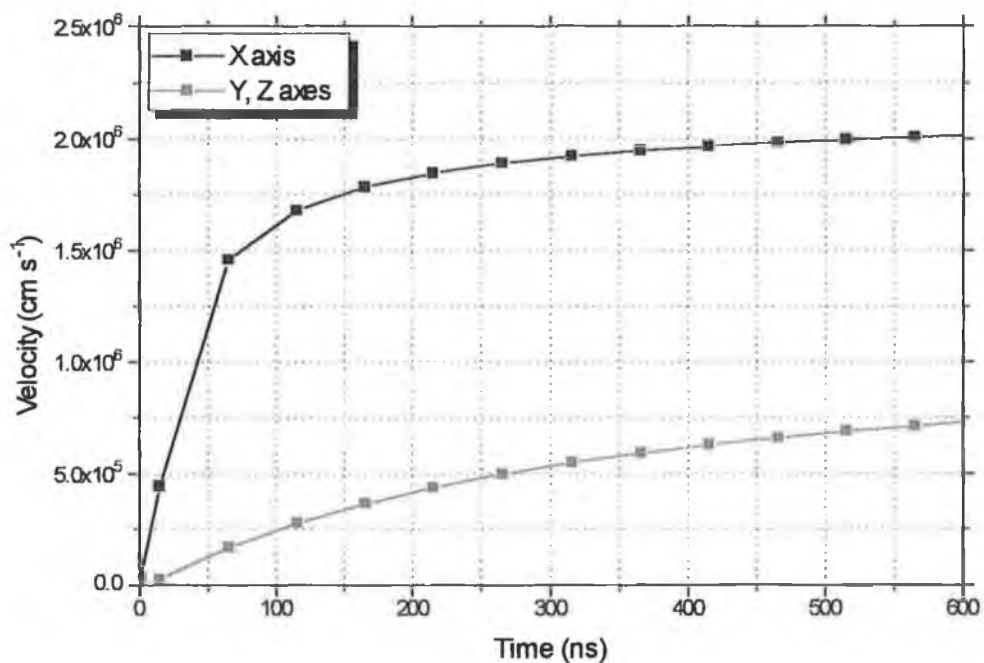
Fig. 3.4: The plasma velocity as a function of time along each of the three expansion axes resulting from the model.

The agreement between figs. 3.3 and 3.1 (for the case of the $1s^22s \leftarrow 1s^22p$ transition in Li^0) is quite reasonable, indicating that the model is applicable to the current experimental conditions. Applying a linear fit to the data shown in fig. 3.3, one obtains a longitudinal velocity of $\sim2 \times 10^6$ cm s^{-1} and a radial velocity of $\sim5 \times 10^5$ cm s^{-1}. These values are in good agreement with the experimentally measured velocities, especially if one considers that in the present model the plasma edge is defined as the distance from the centre where the density is 60.5% of the maximum value. Thus, for an exponentially decreasing density and linearly increasing velocity profile, higher velocities corresponding to 2-3 times those above are present [17]. The temperature profile resulting from the model predictions is shown in fig. 3.5. Temperatures below ~0.1 eV are not expected to be accurate as the temperature may decrease more slowly than that predicted by an adiabatic expansion due to recombination effects [17][129]. The isothermal region of expansion, advancing to the adiabatic region occurring at 15 ns is clearly discernible from fig. 3.5.
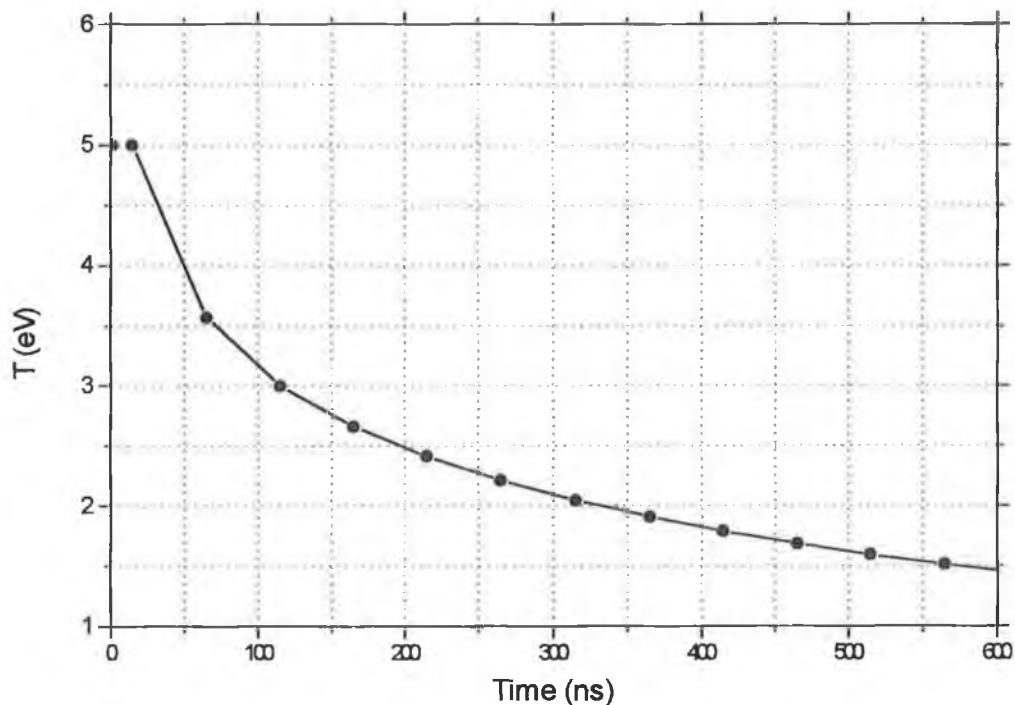
Fig. 3.5: The temperature profile resulting from the model computation.

It should be noted that the terminal velocities resulting from the model are highly dependent on the value of γ chosen. In this respect a value of 1.2 was chosen to account for the degrees of freedom associated with ionisation and excitation [17].

In addition to the technique outlined above to extract the peak longitudinal velocity from the fast-frame images, the longitudinal velocity was estimated using the technique first proposed by Boland *et al.* [60]. At fixed distances 'd' from the target surface along the axis of expansion, at y = 0 mm (see fig. 2.1), the integrated intensity variations as a function of time were recorded for the Li^o, the Li^{o*} and the Li^{+*} transitions, in a manner analogous to a time-of-flight (TOF) distribution. Correction factors were then applied to the recorded intensities to account for the ICCD gain variation (see Appendix D) as well as for the relative transmissions of the various neutral density filter combinations positioned in front of the gated image intensifier / CCD combination used to record each frame. The corrected data values are plotted in figs. 3.6 through 3.8 on a relative scale for the relevant transitions.

116
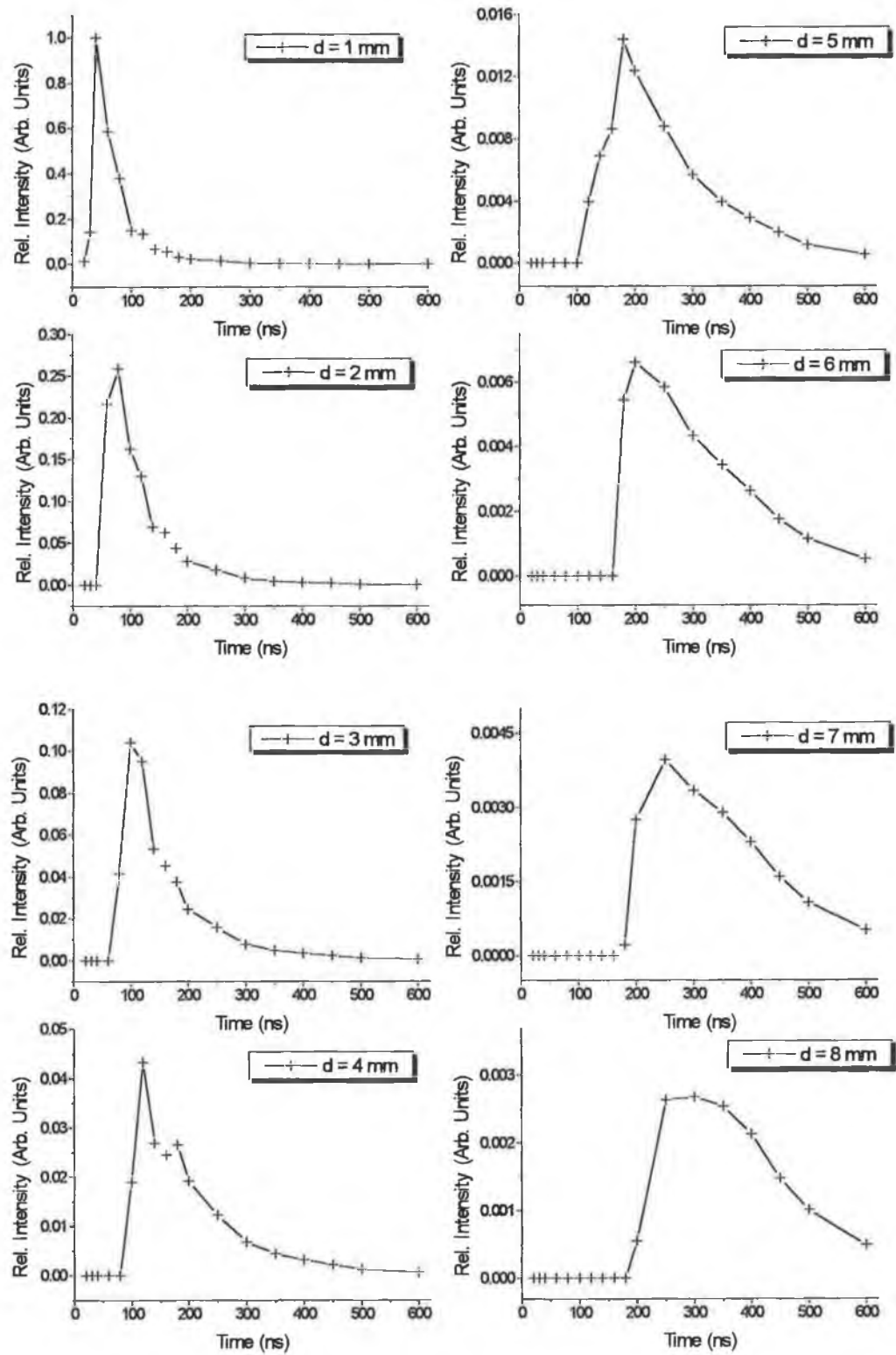
Fig. 3.6: The recorded intensity as a function of time for various fixed distances d from the target surface, along the target normal for the $1s^2 2s \leftarrow 1s^2 2p$ (670.7 nm) transition in Li^o.

117
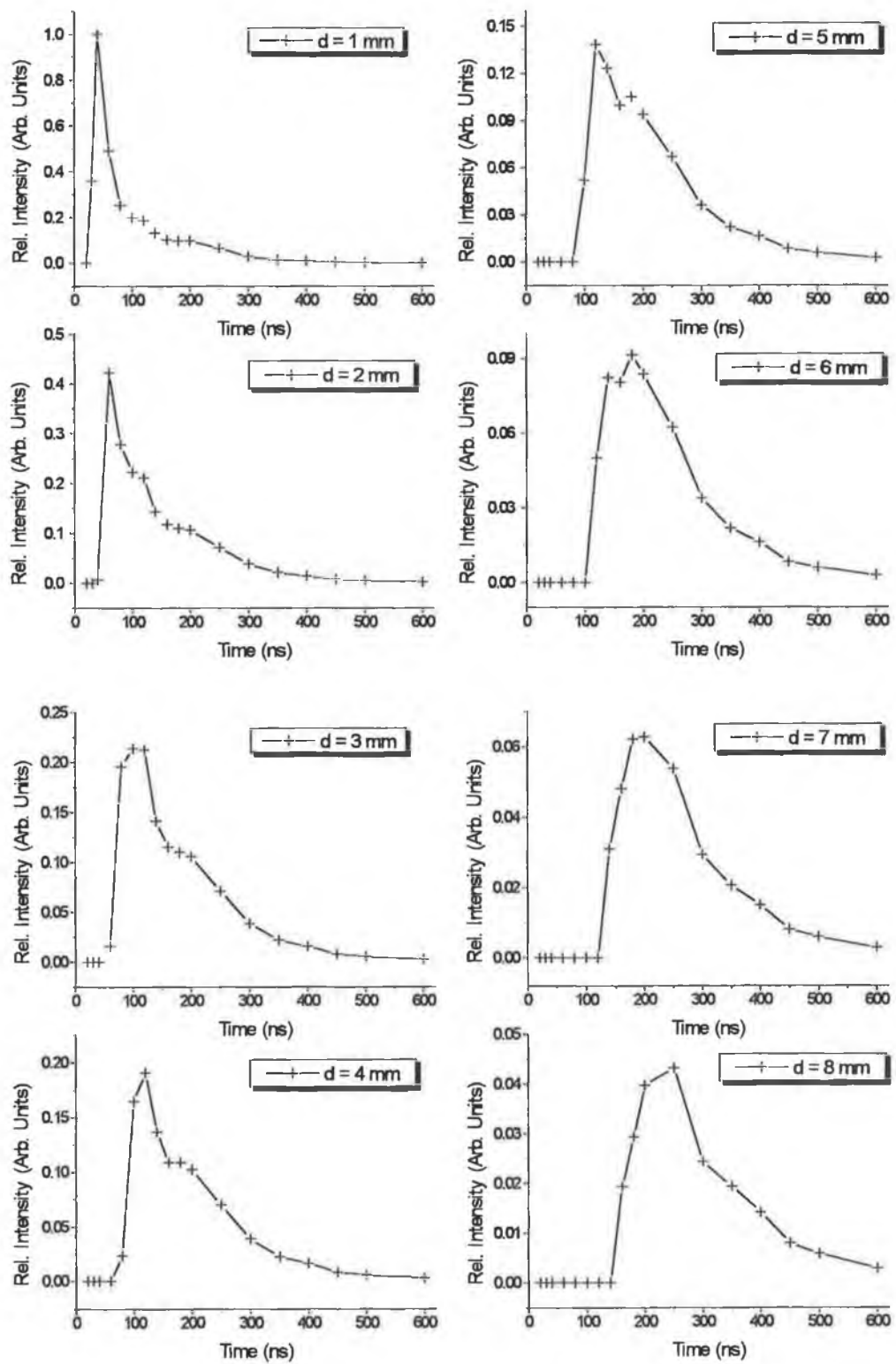
Fig. 3.7: The recorded intensity as a function of time for various fixed distances d from the target surface, along the target normal for the $1s^2 2p \leftarrow 1s^2 3d$ (610.3 nm) transition in Li^o.
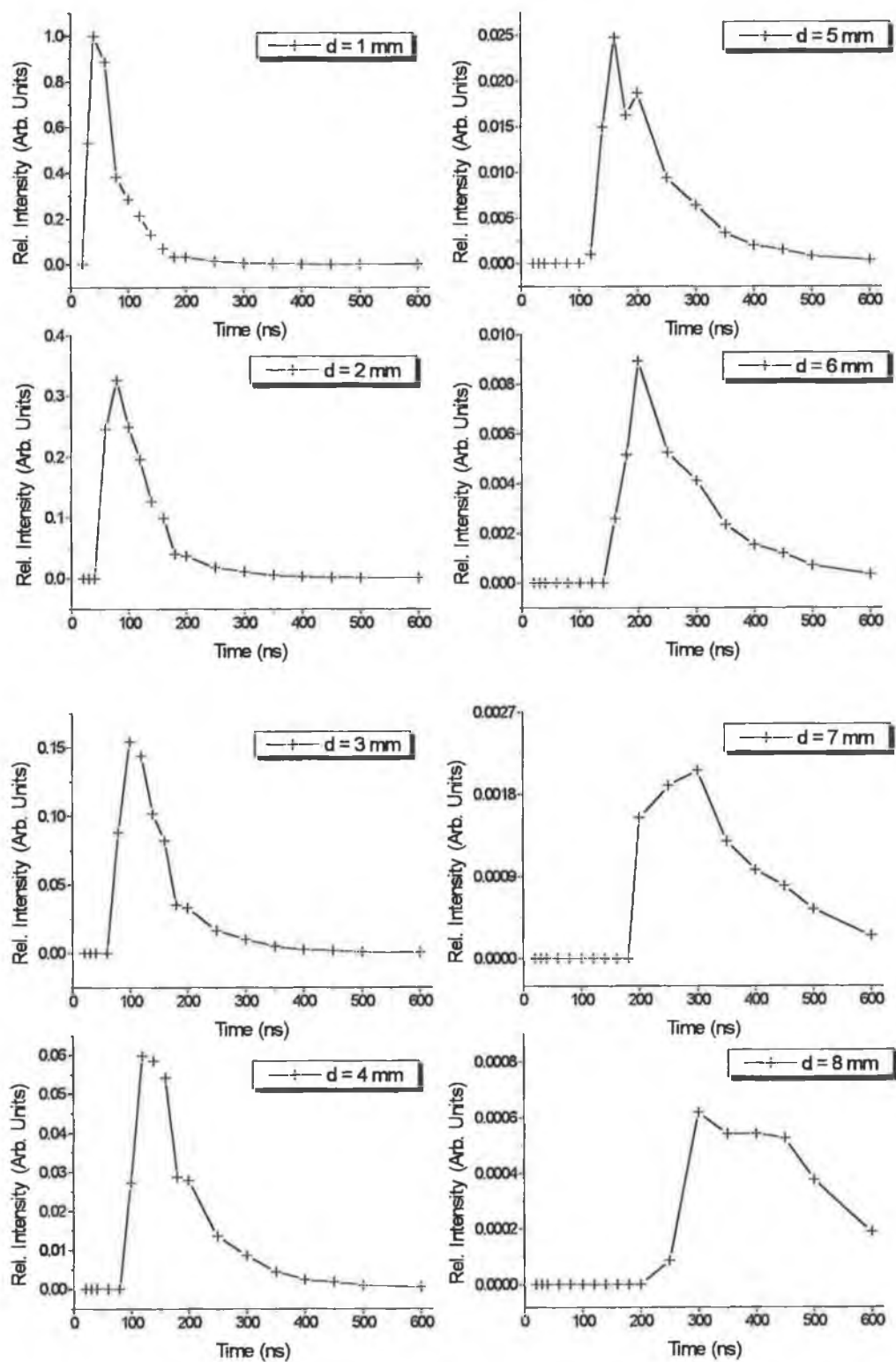
Fig. 3.8: The recorded intensity as a function of time for various fixed distances d from the target surface, along the target normal for the 1s2s ← 1s2p (548.4 nm) transition in Li$^+$.

119

A plot of d as a function of the time corresponding to the peak recorded intensity yields the desired quantity. This is plotted in fig. 3.9 for each of the transitions considered.
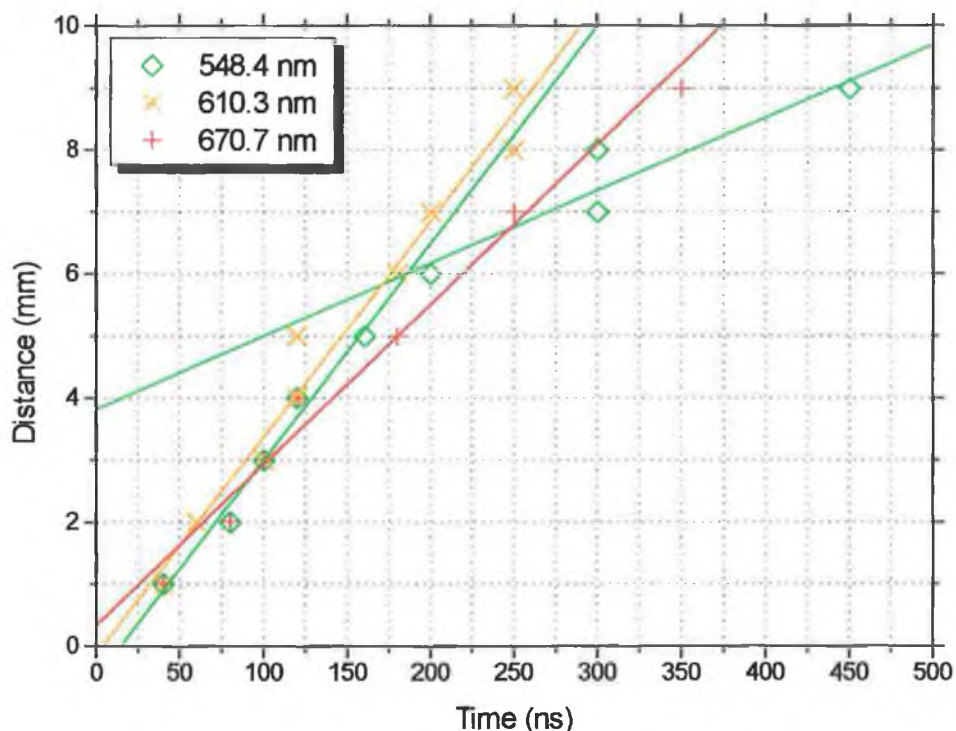
Fig. 3.9: A plot of d as a function of the time corresponding to the peak recorded intensity for the three transitions investigated.

Values of $\sim 3 \times 10^6$ cm s^{-1}, $\sim 3 \times 10^6$ cm s^{-1} and a two-component velocity of $\sim 3 \times 10^6$ cm s^{-1} and $\sim 1 \times 10^6$ cm s^{-1} were obtained for the Li^o, Li^{o*} and Li^{+*} transitions respectively.

3.1.2 The Expansion of a Lithium Plume in an Argon Environment

The spatial and temporal evolution of a lithium plume expanding in an argon environment shown in figs. 2.15, 2.17, 2.19, 2.21 and 2.23 display a characteristic difference from the equivalent vacuum expansion case. The formation of a bright peak in the emission, indicative of a shock structure is clearly evident [130]. This is also apparent from the contour plots where the isointensity lines appear to pile up at the front edge in a manner reminiscent of the spherical wavefronts of a shock wave. From the

120

figures it may be observed that the emitted light intensity in argon exceeds the vacuum case at long distances from the target surface, while the (uncorrected) measured intensities are remarkably similar at distances closer to the target surface. This is illustrated in fig. 3.10.
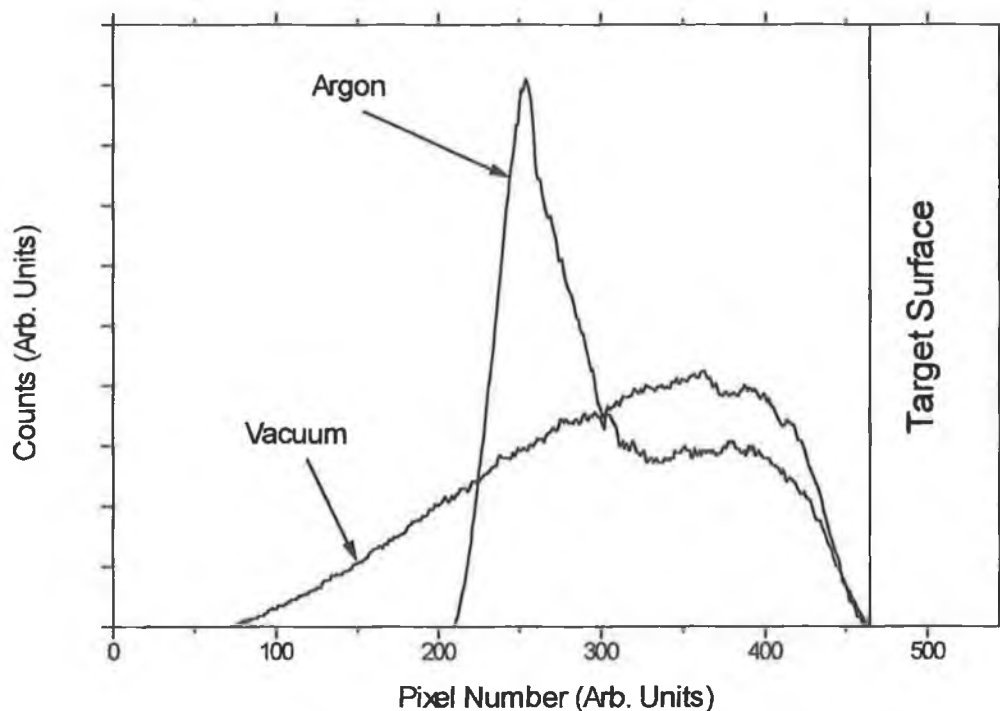
Fig. 3.10: A cross-section of the broadband emission from an expanding lithium plume in both vacuum and argon environments along the axis of expansion taken at 250 ns.

The shorter distance of expansion in the argon case as a result of gas collisions is also apparent from the figure. This is consistent with previous observations made on an yttrium plume in an argon environment [130].

The same procedure used in §3.1.1 to determine the peak longitudinal velocity in the vacuum expansion regime, was again used to ascertain the velocity of the lithium plume expanding in an argon atmosphere. The resultant graph illustrating the position of the luminous front as a function of time is shown in fig. 3.11.
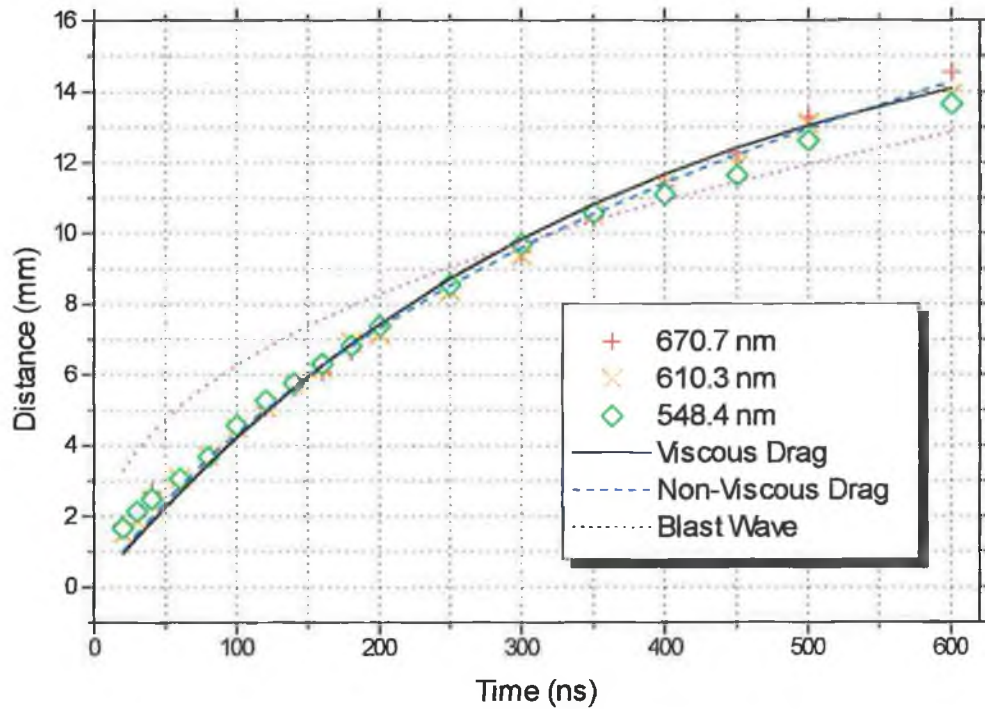
Fig. 3.11: The position of the leading luminous front for each of the three transitions as a function of time expanding in an argon environment. The pressure of the argon gas was 200 mTorr.

Immediately observable from fig. 3.11 in comparison to fig. 3.1 is the marked difference in the expansion dynamics in the presence of a background gas as discussed in chapter 1. Initially, the plasma appears to freely expand as in the vacuum case with a constant velocity of $\sim 3 \times 10^6$ cm s^{-1}. This occurs up to ~ 200 ns, after which a deviation from linearity occurs. It may also be noted that the expansion dynamics are remarkably similar for each of the three transitions unlike the vacuum expansion case. Fitting the viscous ([1.11]) and non-viscous ([1.13]) drag force models to the data one obtains values of $\beta \cong 2.8$ μs^{-1} and $x_f \cong 1.73$ cm (and therefore $v_o = 4.8 \times 10^6$ cm s^{-1}) for the viscous drag force model, while for the non-viscous case one obtains values of $\beta' \cong 1.05$ cm^{-1} and $v_o \cong 5.5 \times 10^6$ cm s^{-1}. The chi-squared value was reduced in the case of the non-viscous drag force model strengthening the validity of its application to the experimental results presented in chapter 2. In addition, the blast wave model was fitted to the data. The poor fit to the data indicates that this model is not applicable under the present experimental conditions. However, a much higher quality fit was achieved by allowing the exponent 'p' (in [1.10]) to vary as suggested by Geohegan [131]. A value of $p \cong 0.66$ resulted in the lowest chi-square value.

122

3.1.3 The Abel Transform Reconstruction Technique

High speed imaging provides information on the 'local' structure and dynamics of the constituent particles provided that a radiation model linking the observed light intensities to particle distributions exist. A complication in this recovery process arises from the fact that the intensities are necessarily integrated along the line of sight. Thus, a transformation of the data by application of the Abel transform is necessitated. As previously noted in §1.6.1, three criteria must be satisfied before the Abel inversion technique can reliably be applied to the experimental data. Criterion (a), the assumption that the rays are virtually paraxial can be validated in the following manner. The separation between the axis of expansion of the plasma, and the 21 mm circular aperture positioned in front of the imaging lens was ~190 mm. The resultant maximum acceptance angle of a cone of light originating from a point source positioned on the axis of expansion is $\alpha_{acc} = \tan^{-1}\left(\dfrac{21}{190}\right)$, which is equivalent to 110 mrad. As $\sin(\alpha_{acc}) \approx \alpha_{acc}$, the light rays originating from the plasma can be assumed to be virtually paraxial. In order to affirm criterion (b), the assumption of optical thinness, an estimate for the absorption coefficient was made using [1.30]. Assuming a Gaussian AFR with a FWHM = 4×10^{11} s^{-1} (~6 Å) centred about the $1s^2 2s \leftarrow 1s^2 2p$ transition, the resultant transmission at the line centre, for an average effective path length of 100 μm, an oscillator strength of 0.748 [40] and an average neutral density ~10^{14} cm^{-3}, is ~95%. Assuming a neutral density lower than this value, the plasma can be considered to be optically thin. Losses due to stimulated emission are not expected to be significant and the correction term for it has not been included. Finally, from the fast-frame image sequences of §2.1.3, the assumption of radial symmetry appears to be readily fulfilled, thus satisfying criterion (c). This is illustrated in figs. 3.12 through 3.14, where cross-sections of the recorded plasma emission intensity at various distances from the target surface as a function of time are shown for each of the three transitions considered. In all cases Gaussian fits to the raw data are overlaid to illustrate the symmetry. The limitation of the Gaussian profile is related to the fact that the real plasma has a definite surface and a finite expansion velocity, while the Gaussian profile distributes the plasma to any distance [21]. Thus, the minor discrepancy between the Gaussian curve fits and the raw data can in some fashion be explained. The restricted sensitivity of the CCD was perhaps a more severe limitation. Additionally, continuum contributions to the

detected signal at distances < 2 mm may contribute to the poorer quality fits in this region.
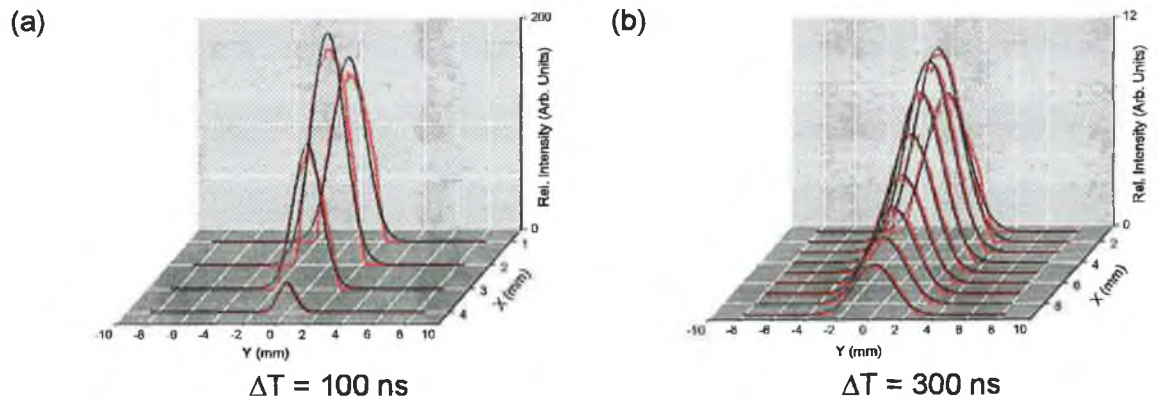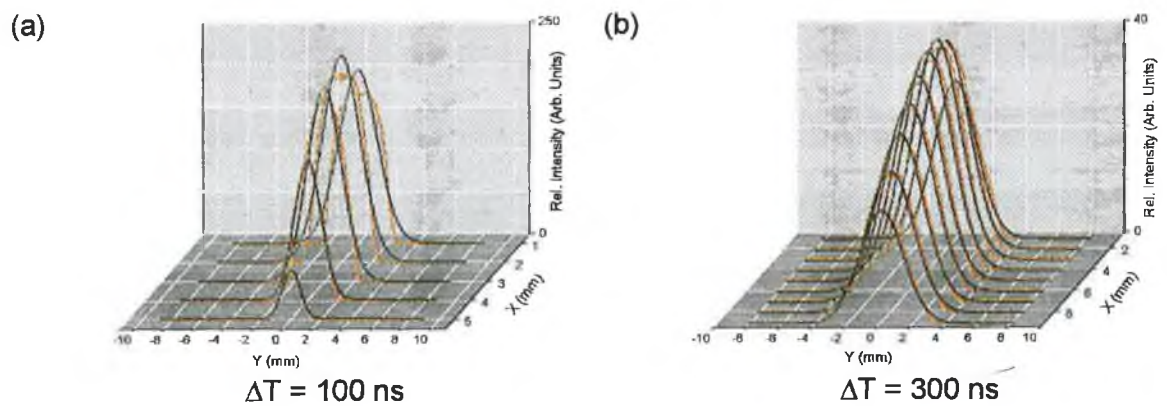
(a)

$\Delta T = 100$ ns
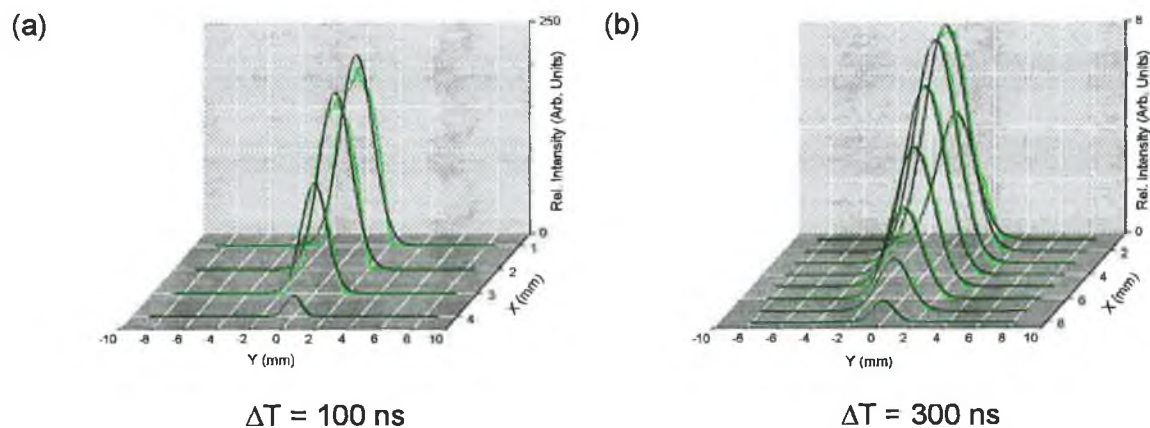
(b)

$\Delta T = 300$ ns

Fig. 3.12: Cross-sections of the recorded plasma emission intensity at various distances from the target surface as a function of time for the $1s^22s \leftarrow 1s^22p$ (670.7 nm) transition in Li^o. Also indicated in black are Gaussian fits to the raw data.

(a)

$\Delta T = 100$ ns

(b)

$\Delta T = 300$ ns

Fig. 3.13: Cross-sections of the recorded plasma emission intensity at various distances from the target surface as a function of time for the $1s^22p \leftarrow 1s^23d$ (610.3 nm) transition in Li^o. Also indicated in black are Gaussian fits to the raw data.

(a) ΔT = 100 ns   (b) ΔT = 300 ns

Fig. 3.14: Cross-sections of the recorded plasma emission intensity at various distances from the target surface as a function of time for the 1s2s ← 1s2p (548.4 nm) transition in Li$^+$. Also indicated in black are Gaussian fits to the raw data.

Multiple techniques for inverting experimental data were investigated during this study. These included the direct inversion method, employing the use of numerical differentiation (see [1.58]), a modification of the spline-based method proposed by Deutsch and Beniaminy [64], and finally an iterative technique proposed by Vicharelli and Lapatovich [65]. Incidentally, Kuthy [132] appears to have been the first to propose a spline based inversion technique. As the accuracy of the inverted data is limited by the accuracy of the integration method chosen [64], an 800 point Gauss-Legendre numerical integration technique [133] was used with a scaling error = 1 x 10^{-15}. This was found to provide improved results over the numerical implementation of the extended midpoint rule through the integration function `midpnt ( ... )` [133]. The spline method chosen [133] was a 'non-natural' spline [134]. Additionally, it should be noted that the spline-based technique is not suitable to certain test cases, namely those containing discontinuities as in [66]. This is a direct result of the unsuitability of the `spline (...)` / `splint (...)` function combination [133] to such test cases. The inversion techniques were investigated for both noiseless and noisy data for the following three widely used test cases [63][64][65]. To the best of the author's knowledge, the analytical expressions for I(y) presented in table 3.2 have only been published by Deutsch and Beniaminy [64].

i(r)	I(y)	Range
$1 - 3r^2 + 2r^3$	$u\left(1 - \dfrac{5}{2}y^2\right) + \dfrac{3}{2}y^4 \ln\left(\dfrac{1+u}{y}\right)$	$0 \le r, y \le 1$
$1 - 2r^2$	$\dfrac{4}{3}\left(1 + 2y^2\right)u - \dfrac{2}{3}\left(1 + 8y^2\right)v - 4y^2 \ln\left(\dfrac{1+u}{\frac{1}{2}+v}\right)$	$0 \le r, y \le \dfrac{1}{2}$
$2(1 - r)^2$	$\dfrac{4}{3}\left(1 + 2y^2\right)u - 4y^2 \ln\left(\dfrac{1+u}{y}\right)$	$\dfrac{1}{2} < r, y \le 1$
$\dfrac{3}{4} + 12r^2 - 32r^3$	$\dfrac{32}{27}u\left(1 - 7y^2\right) + \left(\dfrac{1}{108} + \dfrac{566}{27}y^2\right)w +$ $\dfrac{96}{27}y^2\left(1 + y^2\right)\ln\left(\dfrac{1+u}{\frac{1}{4}+w}\right) - 24y^4 \ln\left(\dfrac{\frac{1}{4}+w}{y}\right)$	$0 \le r, y \le \dfrac{1}{4}$
$\dfrac{16}{27}\left(1 + 6r - 15r^2 + 8r^3\right)$	$\dfrac{32}{27}u\left(1 - 7y^2\right) + \dfrac{96}{27}y^2\left(1 + y^2\right)\ln\left(\dfrac{1+u}{y}\right)$	$\dfrac{1}{4} < r, y \le 1$

Table 3.2: Test function pairs used in the numerical inversion of the Abel integral equation. Note: $u = \sqrt{1 - y^2}$, $v = \sqrt{\dfrac{1}{4} - y^2}$, $w = \sqrt{\dfrac{1}{16} - y^2}$.

Here I(y) denotes the observed line-of-sight experimental data, while i(r) denotes the physically relevant quantity e.g. the emission coefficient, as in this case. It should be noted that $\dfrac{3}{4}$ was published in [64] in place of $\dfrac{3}{2}$ in the first test case, and $24y^2$ in place of $24y^4$ in the third case. Long double (80 bit) precision was used in all cases to invert the data. The tests are aimed at assessing the behaviour of the various techniques for different levels of simulated experimental noise. The error free data is represented by 14-digit precision numbers, while rounding the data to two decimal places was used to simulate experimental error [64]. This was equivalent to the inclusion of normally distributed random noise with a mean standard deviation of S = 0.00275 on I(y). The tests were also carried out by adding 1% random noise to the 14-digit precision data corresponding to a mean standard deviation S = 0.00385. In all cases, a prerequisite of the techniques was that the radius of the plasma was normalised to unity. Graphical

representations of the three test function pairs analysed are shown in fig. 3.15, while tabulated results illustrating the standard deviation between the true inverted profile and those computed by the various numerical methods are shown in table 3.3. The number of data points, N, in each data set is also indicated in the table.
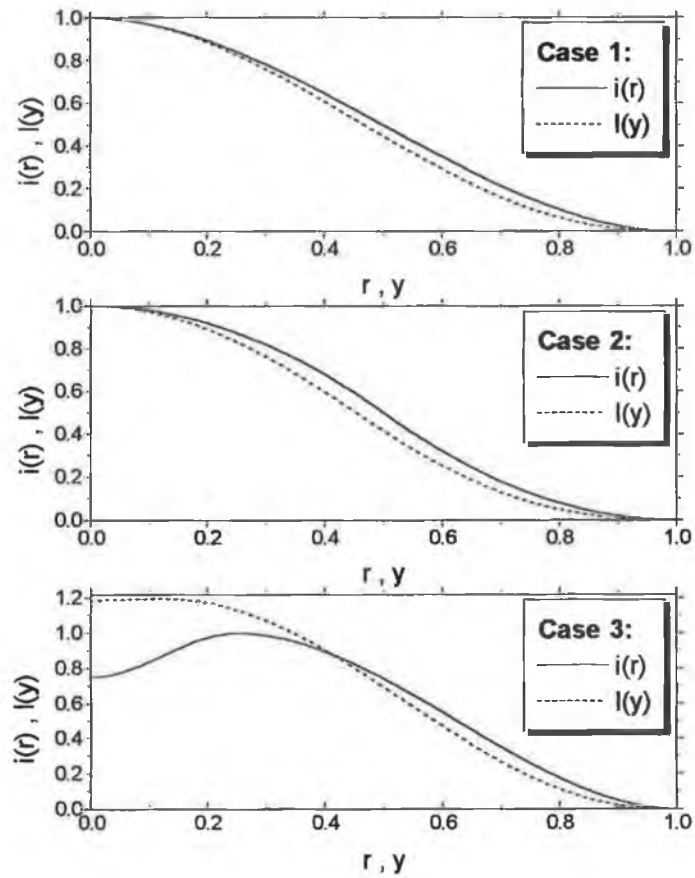
Fig. 3.15: A graphical representation of the three Abel transformed test function pairs analysed [64].

Case	N	S = 0			S = 2.75e-03		
		DIRECT	DB	VL	DIRECT	DB	VL
1	10	4.1e-04	*2.9e-04*	3.6e-03	1.12e-02	1.12e-02	*9.3e-03*
	20	3.4e-04	*1.7e-04*	1.1e-03	*1.59e-02*	*1.59e-02*	2.0e-02
	30	3.4e-04	*1.7e-04*	8.9e-04	2.1e-02	2.1e-02	*2.0e-02*
	40	3.5e-04	*1.7e-04*	8.1e-04	2.3e-02	2.3e-02	*2.1e-02*
	50	3.5e-04	*1.7e-04*	7.7e-04	1.8e-02	1.8e-02	*1.6e-02*
	100	3.5e-04	*1.8e-04*	6.7e-04	2.9e-02	2.9e-02	*2.7e-02*
	200	3.5e-04	*1.8e-04*	6.1e-04			
2	10	5.1e-04	*3.9e-04*	4.8e-03	*9.3e-03*	9.4e-03	1.1e-02
	20	3.6e-04	*1.9e-04*	1.2e-03	*1.7e-02*	1.7e-02	2.0e-02
	30	3.6e-04	*1.8e-04*	8.9e-04	*2.1e-02*	*2.1e-02*	2.5e-02
	40	3.6e-04	*1.8e-04*	8.0e-04	2.3e-02	2.3e-02	*2.2e-02*
	50	3.6e-04	*1.8e-04*	7.5e-04	2.0e-02	2.0e-02	*1.9e-02*
	100	3.7e-04	*1.8e-04*	6.6e-04	2.8e-02	2.8e-02	*2.5e-02*
	200	3.7e-04	*1.8e-04*	6.0e-04			
3	10	2.1e-03	*2.0e-03*	1.4e-02	*1.7e-02*	1.7e-02	2.2e-02
	20	4.2e-04	*2.9e-04*	1.5e-03	*1.9e-02*	1.9e-02	2.1e-02
	30	3.6e-04	*1.9e-04*	1.0e-03	*2.1e-02*	2.1e-02	2.8e-02
	40	3.5e-04	*1.8e-04*	4.3e-02	*1.9e-02*	1.9e-02	2.3e-02
	50	3.6e-04	*1.8e-04*	5.5e-04	*1.9e-02*	1.9e-02	2.2e-02
	100	3.6e-04	*1.8e-04*	4.7e-04	*2.0e-02*	2.0e-02	2.1e-02
	200	3.6e-04	*1.8e-04*	4.6e-04			

Table 3.3: Results indicating the standard deviation between the true inverted profile and those computed by each of the numerical Abel inversion techniques. The number of data points in each data set is indicated in the column labelled N. The standard deviation, S, is also indicated. The case of S=0 corresponds to noiseless data. DIRECT is used to indicate the direct solution to the Abel transform, i.e. using numerical differentiation, DB signifies the modified technique of [64], while VL indicates the iterative method of [65]. The lowest standard deviation in the case of each data set is indicated in bold.

128

Applying this to the 1% random noisy data one obtains

Case	N	DIRECT	DB	VL
		S=3.85e-03		
1	10	2.2e-02	2.2e-02	*2.1e-02*
	20	3.6e-02	3.6e-02	*2.8e-02*
	30	4.6e-02	4.6e-02	*3.0e-02*
	40	5.4e-02	5.4e-02	*3.1e-02*
	50	6.2e-02	6.2e-02	*3.2e-02*
	100	9.1e-02	9.1e-02	*3.4e-02*
	200	1.3e-01	1.3e-01	*3.7e-02*
2	10	2.2e-02	2.2e-02	*2.1e-02*
	20	2.0e-02	2.0e-02	*1.8e-02*
	30	2.7e-02	2.7e-02	*2.3e-02*
	40	3.3e-02	3.3e-02	*2.7e-02*
	50	3.8e-02	3.8e-02	*3.0e-02*
	100	5.9e-02	5.9e-02	*3.5e-02*
	200	8.9e-02	8.9e-02	*3.8e-02*
3	10	*2.7e-02*	*2.7e-02*	3.3e-02
	20	2.5e-02	2.5e-02	*2.4e-02*
	30	3.4e-02	3.4e-02	*3.1e-02*
	40	4.1e-02	4.1e-02	*3.5e-02*
	50	4.7e-02	4.7e-02	*3.5e-02*
	100	7.3e-02	7.3e-02	*4.2e-02*
	200	1.1e-01	1.1e-01	*5.0e-02*

Table 3.4: Results indicating the standard deviation between the true inverted profile and those computed by each of the Abel inversion numerical techniques applied to 1% noisy data. The notation is the same as for table 3.3. The lowest standard deviation in the case of each data set is indicated in bold.

The poor quality in the inversion of the noiseless data inferred from table 3.3 is directly attributable to the integration technique employed. This explains the discrepancy in the standard deviation for the method proposed by [64] and the modified version implemented here. In this work a numerical based splining procedure was used in place of a piece-wise cubic spline function fitted to the data. The resulting increased inaccuracy is clearly evidenced. Despite this however, the performance of the technique

was deemed adequate for the present purposes. Computationally, one finds that the iterative technique of Vicharelli and Lapatovich [65] is the most expensive, taking over 100 hours on a 66 MHz DX2 computer to complete this series of tests. From the tabulated results of tables 3.3 and 3.4, the DB technique was chosen as the preferred method of inversion due to its reasonable overall performance and acceptable execution time in comparison with the iterative technique of Vicharelli and Lapatovich [65]. The raw data as well as the Gaussian fitted profiles shown in figs. 3.12 through 3.14 were therefore inverted using this technique. The results are shown in figs. 3.16 through 3.18. The relative scales between figs. 3.12 through 3.14 and their corresponding figure below are intercomparable.
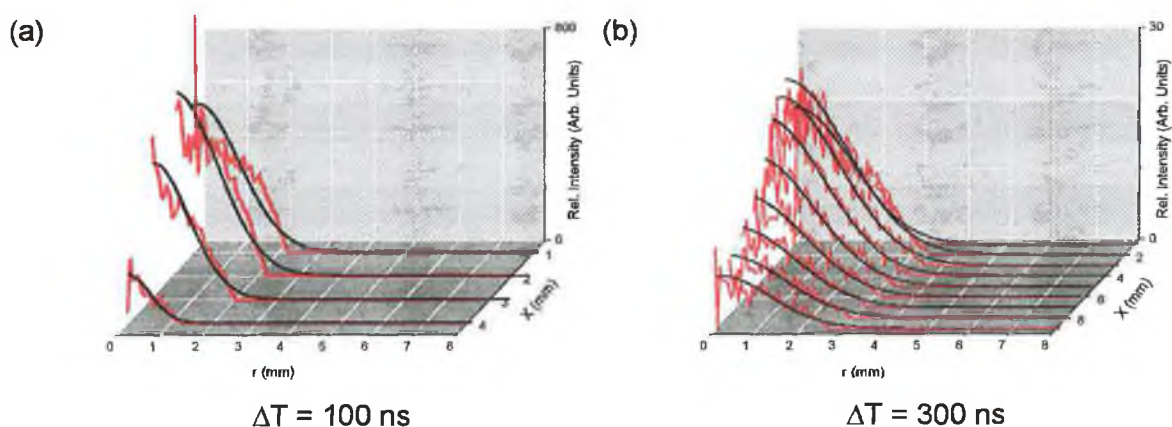
Fig. 3.16: Abel reconstruction of the Li^o (670.7 nm) data using a modified version of the DB spline based technique.
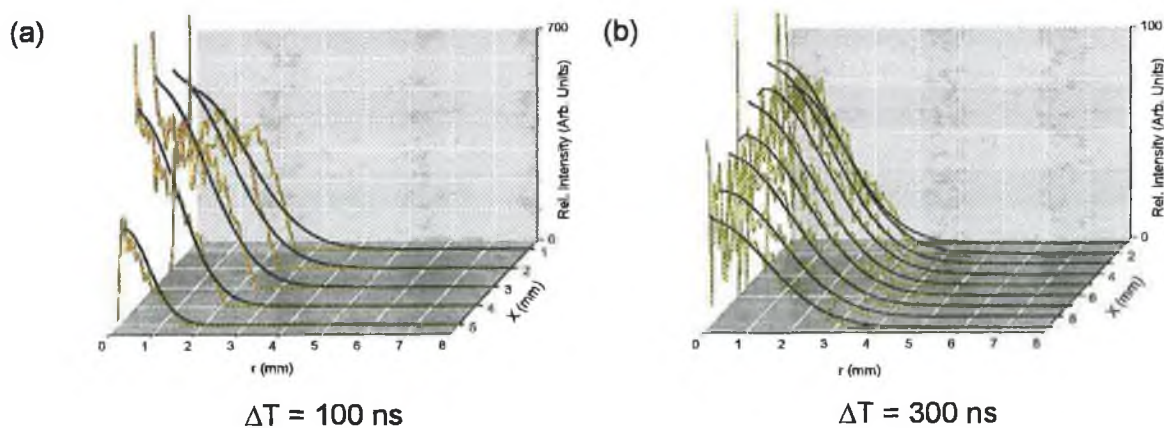
Fig. 3.17: Abel reconstruction of the Li^{o*} (610.3 nm) data using a modified version of the DB spline based technique.

$\Delta T = 100$ ns $\qquad\qquad\qquad \Delta T = 300$ ns
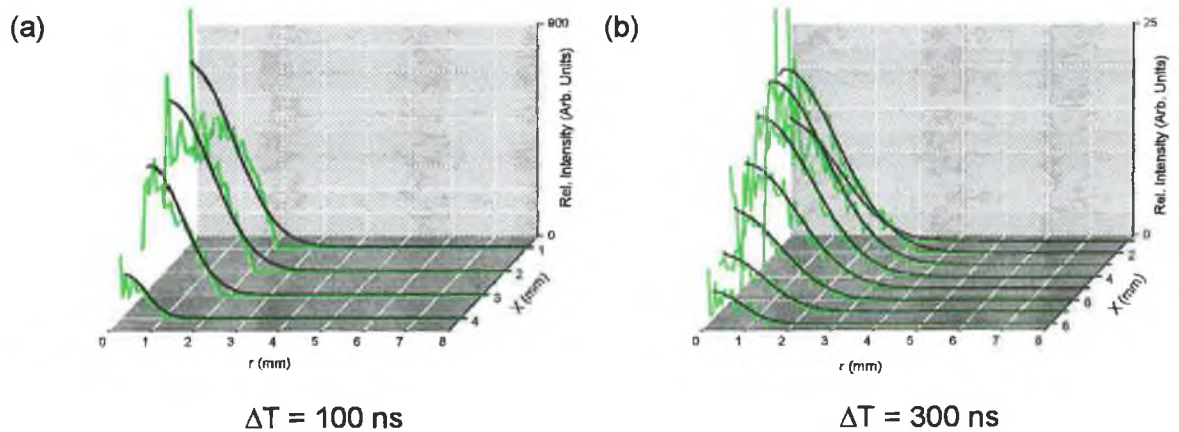
Fig. 3.18: Abel reconstruction of the Li^{+*} (548.4 nm) data using a modified version of the DB spline based method.

Initially, from the inverted data, the level of noise amplification introduced during the inversion process may be witnessed. As previously mentioned, this is most likely due to the numerics of the splining procedure. Also, it may be observed that the density profiles of the excited states appear to be Gaussian in shape, in particular at distances > 2 mm from the target surface, where the continuum contribution to the detected signal is weak, if not negligible. This Gaussian profile is indicative of a self-similar expansion (see §1.2.1) whereby the density profile retains a Gaussian shape as a function of time.

3.2 The Shadowgraph Technique

With reference to the shadowgraph figures shown in figs. 2.27 through 2.31, it is immediately apparent that two strongly competitive effects contribute to the refractive index of the plasma, one gaining dominance over the other dependent on the probe wavelength used relative to the centre wavelength of the atomic resonance transition under consideration, as seen in fig. 1.19. Using a probe wavelength lower than the centre wavelength of the transition, the electron contribution to the refractive index appears to dominate as in fig. 2.27 (λ = 668 nm). The result is an overall plasma refractive index less than unity. Consequently, the plasma's behaviour mimics that of a diverging lens. On the other hand, at probe wavelengths above the centre wavelength of the transition, the atomic and ionic contributions to the plasma refractive index eclipse the contribution due to the electrons, as in fig. 2.27 (λ = 672.5 nm). Indeed, the true

extent of the effect is not immediately clear from fig. 2.27 (λ = 672.5 nm), but can be seen in fig. 3.19 where a single lens was used to image the shadowgraph onto the CCD. The demagnification factor was ~4.
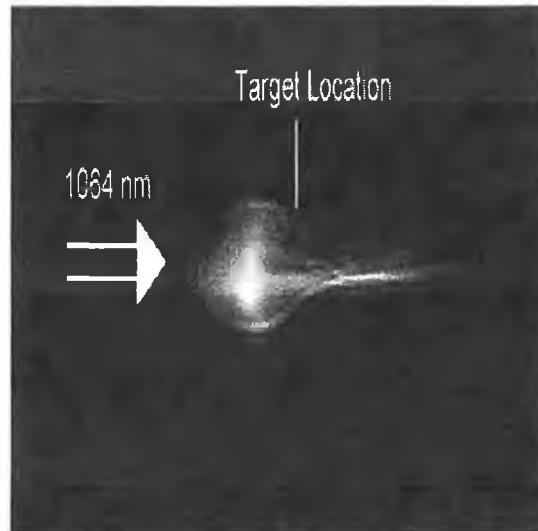
Fig. 3.19: Reduced shadowgraph taken at 100 ns after plasma initiation indicating the extent of the influence of the neutral and ionic species on the refractive index of the plasma. The dye probe beam wavelength was 671.7 nm. The approximate dimensions of the image are 12 mm x 12 mm.

The approximate location of the target surface is indicated in the figure. The striking tail of the refracted probe beam around the target is immediately discernible, indicating the dramatic effect of the neutral and ionic species on the refractive index.

This effect did not manifest itself in the case of the 1s2s $\rightarrow$ 1s2p (548.4 nm) transition. Thus, the electron contribution dominates both above and below the centre wavelengths of this transition. This is most likely related to a low (in relation to the electron density) population of the 2s level. A similar reasoning can be used to explain the comparable results obtained for the $1s^2 2p \rightarrow 1s^2 3d$ transition. The strong absorption of the probe beam at on resonance wavelengths however is clearly evident from fig. 2.27 (λ = 670.7 nm) and fig. 2.29 (λ = 610 nm). This is due to the influence of the imaginary part, κ, of the plasma refractive index as seen in fig. 1.19. This was not observed in the case of the 1s2s $\rightarrow$ 1s2p transition however, and would thus tend to indicate the low density of ground state ions in the plasma.

Using the RFD analysis of Cunningham *et al.* [86], shadowgraphs similar to that illustrated in fig. 2.27 (λ = 669 nm) may be analysed to extract electron density profiles in the plasma. This procedure was implemented for the shadowgraph shown in fig. 3.20 obtained using a probe wavelength of 669.7 nm. At this wavelength, the contribution to the refractive index due to the electrons is expected to dominate.
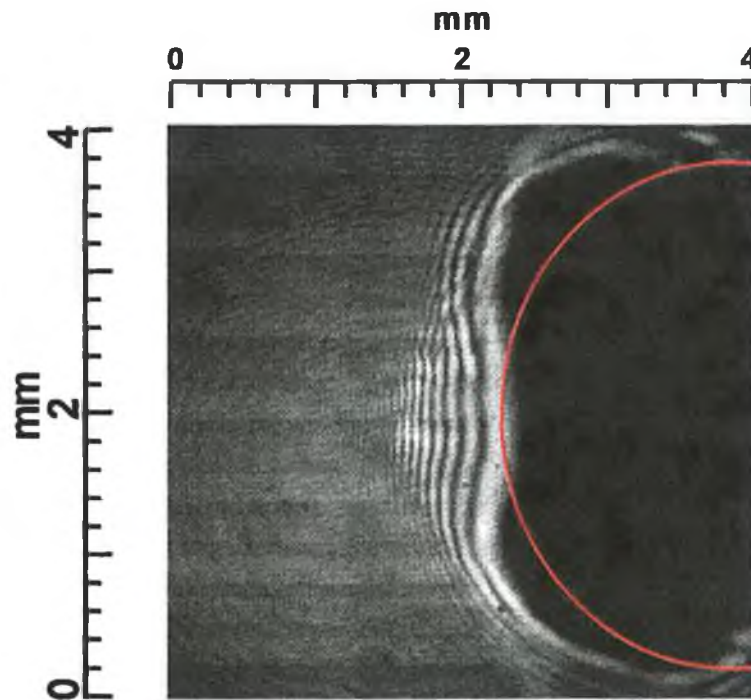
Fig. 3.20: A shadowgraph of a lithium plume taken at 70 ns. The probe beam wavelength was 669.7 nm.

The shadowgraph illustrated in fig. 3.20 was chosen due to the large number of high contrast refractive fringes. This is illustrated in fig. 3.21. As can be seen from fig. 3.20, the shape of the plasma is approximately hemi-spherical, and is thus suited to interpretation using the RFD technique. The corresponding RFD parameters calculated using the theory outlined in chapter 1 are shown in table 3.5. The resultant refractive index and electron density profiles are illustrated in figs. 3.22 and 3.23 respectively.
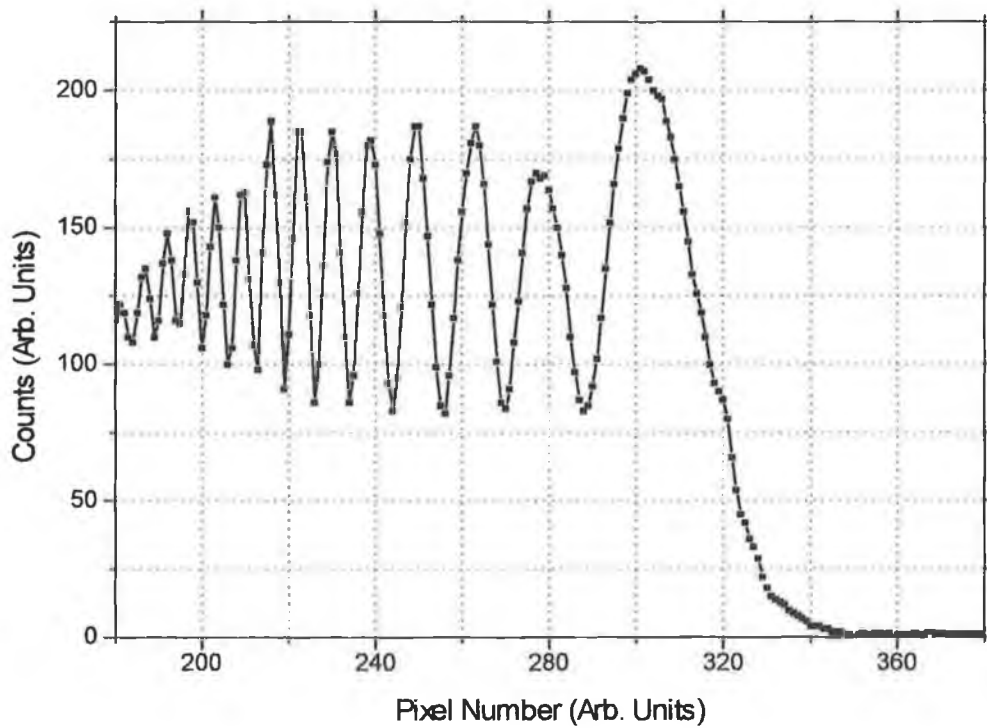
Fig. 3.21: A cross-section of the shadowgraph shown in fig. 3.20 taken at pixel row number 141 illustrating the large number of high contrast refractive fringes.

d (mm)	α_r (mrad)	R_f (mm)	β_r (rad)	r_i (mm)	$n(r_i)$	$N_e(r_i)$ ($\times 10^{19}$ cm^{-3})
0.13235	5.06	1.7206	0.7988	0.9628	0.9975	1.22
0.10294	6.51	1.8309	0.6908	0.8567	0.9961	1.94
0.08824	7.59	1.9301	0.6309	0.7937	0.9948	2.56
0.07353	9.12	2.0074	0.4981	0.6438	0.9917	4.11
0.05882	11.39	2.0735	0.2760	0.3693	0.9803	9.69
0.05147	13.01	2.1287	0.1321	0.1811	0.9534	22.65
0.04412	15.18	2.1765	0.0448	0.0652	0.8552	66.76
0.05147	13.01	2.2243	0.2044	0.2767	0.9696	14.89
0.03676	18.22	2.3125	0.2821	0.3794	0.9696	14.89
0.04412	15.18	2.3529	0.0564	0.0808	0.8816	55.38
0.03676	18.22	2.3897	0.2221	0.3015	0.9613	18.89

Table 3.5: RFD parameters calculated from fig. 3.21 and the theory presented in chapter 1. R_o (the radius of the inner most dark fringe from the target surface) was estimated to be ~1.34 mm.
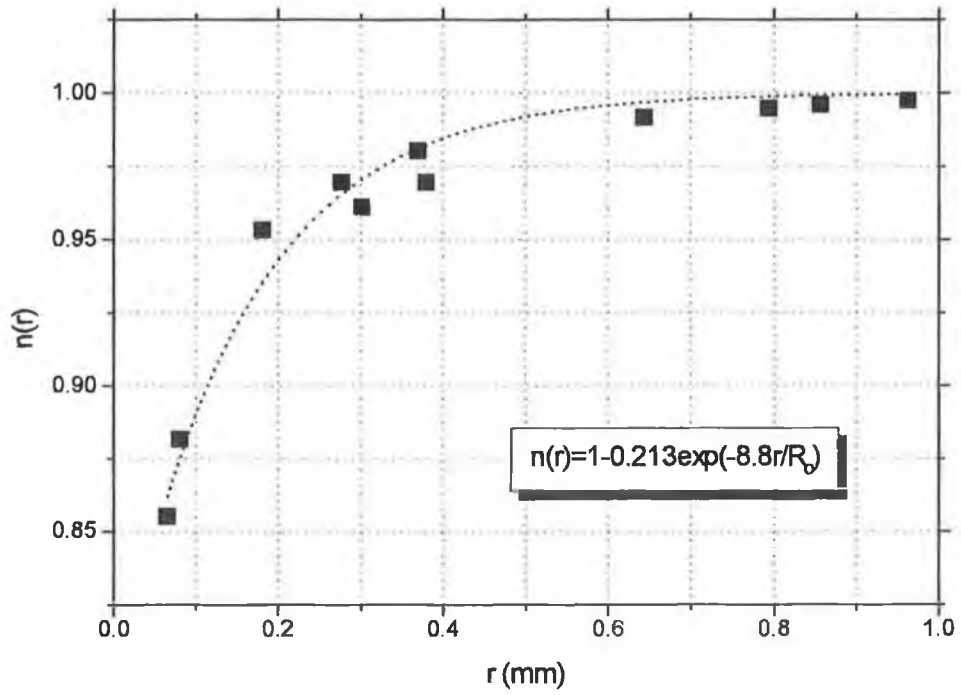
Fig. 3.22: The refractive index profile resulting from the analysis of the shadowgraph presented in fig. 3.20 using the RFD technique.
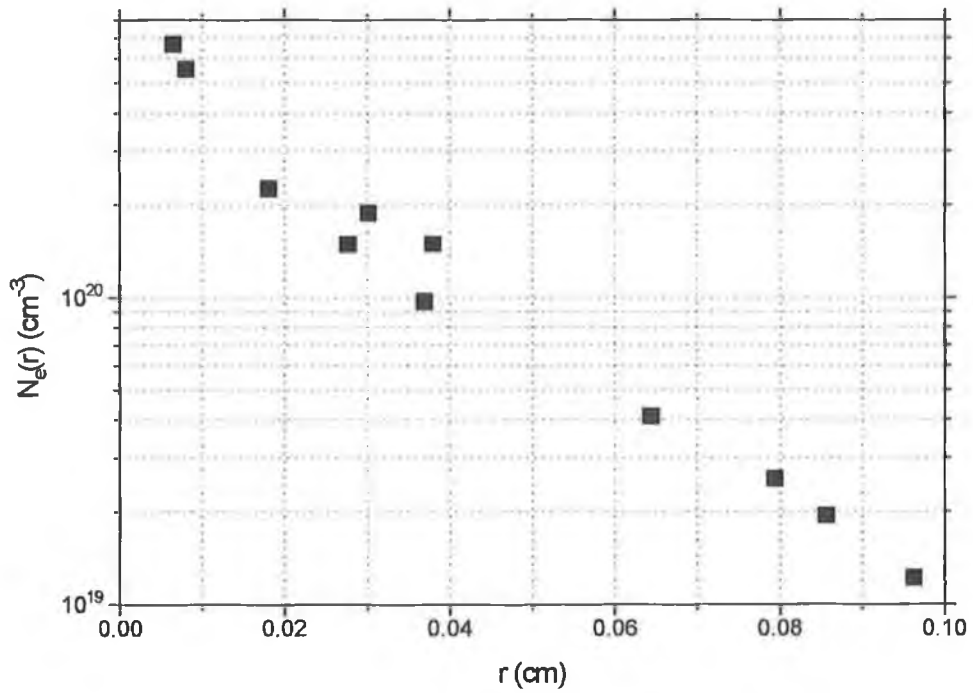
Fig. 3.23: The electron density profile resulting from the analysis of the shadowgraph presented in fig. 3.20 using the RFD technique.

135

The general profile of the electron density distribution shown in fig. 3.23, i.e. an exponentially decreasing density profile, is consistent with electron densities obtained interferometrically using cylindrically symmetric plasmas [135]. It is also typical of electron density profiles obtained using the RFD technique [86][136].

Using the refractive index profile inferred from the RFD analysis (see fig. 3.22), [1.81] was integrated using a fifth order Runge-Kutta integration technique with adaptive step-size control, assuming a hemispherical shaped plasma possessing radial symmetry of radius $R_o \cong 1.34$ mm. Initially however, the ray trace procedure was verified by examining a series of test cases [79][86]. The resultant ray traces are shown in fig. 3.24.
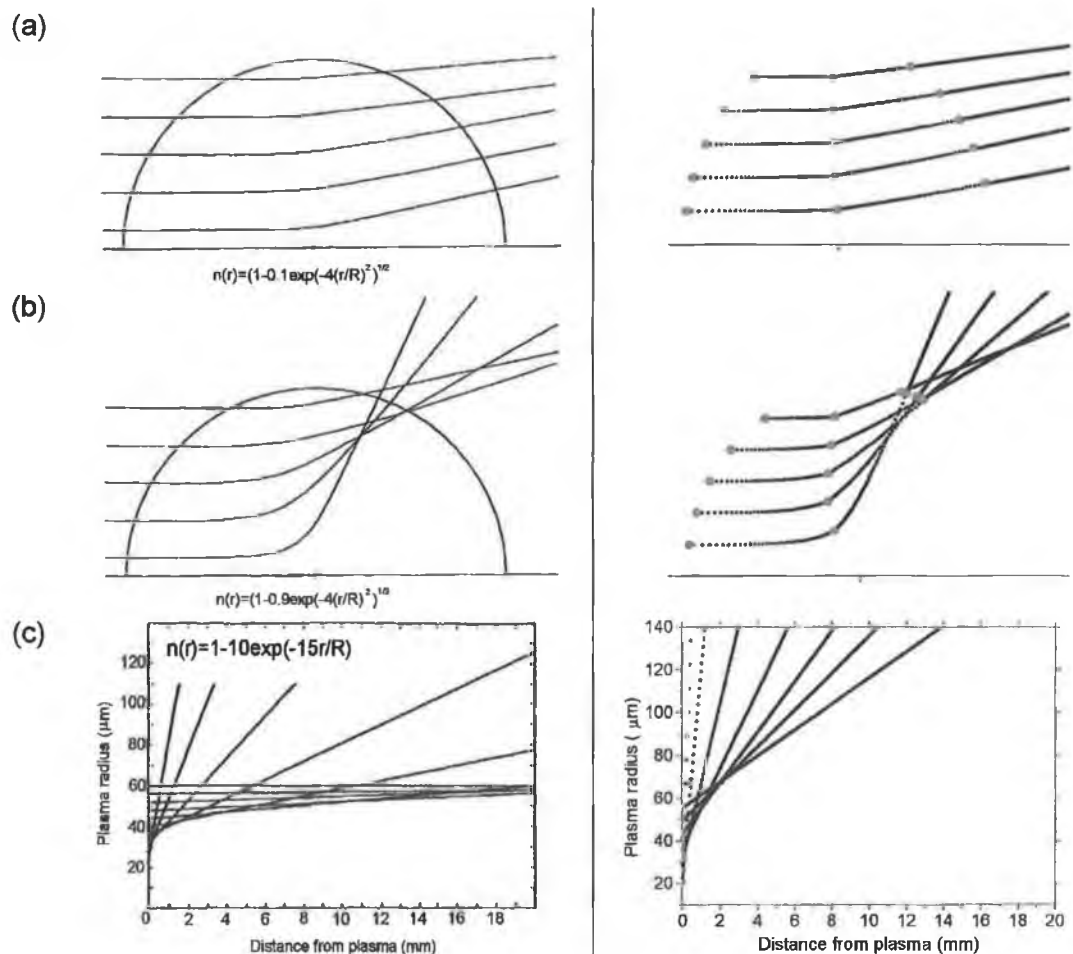
Fig. 3.24: RFD ray trace simulations using test cases from [79][86]. The left hand side shows the results given by [79][86], while the right hand side shows the results computed using [1.81]. Both (a) and (b) are plotted on a reduced scale. The radius, R_o, of the plasma in (c) was 59 μm.

Also indicated in fig. 3.24 (in red) are the entrance (P_1), turning (P_2) and exit (P_3) points of each ray (see fig. 1.20). P_2 was calculated by recognising that the function r n(r) is a monotonically increasing function. Thus, by application of Bouguer's formula ([1.62]), it was possible to compute r_i (see fig. 1.20) for each ray, by localising the range over which $rn(r) < p_r$ and $rn(r) > p_r$. Further narrowing this range until an accuracy of one part in 10^{14} was achieved facilitated accuracy in the computation. Integrating [1.81] using the

Runge-Kutta method by setting the initial value of $\theta = \pi - \beta_r = \pi - \sin^{-1}\left(\dfrac{p_r}{R_o}\right)$ for each

ray and setting the initial value of $r = R_o$, it was possible to trace individual rays through the plasma. The turning point in [1.81] was determined as the point at which $r = r_i$. Therefore P_2 in cartesian co-ordinates was computed knowing r_i and θ at the turning point for each ray. The exit point of a ray from the plasma, P_3, was calculated using the value of the exit angle α_r computed using [1.82], having previously determined r_i. As can be seen from fig. 3.24(a) and fig. 3.24(b) a high level of agreement was achieved for the case of [79]. This is not reflected in the case of [86]. While the exit angles, $\alpha_r(p_r)$, resulting from the ray trace show a high level of correlation with those computed using [1.82], the resultant ray trace differs remarkably from that of [86]. It is suspected that the ray trace presented in [86] was not computed in the usual manner, i.e. using [1.81], but that a similar form, expressed in cartesian co-ordinates, may have been used in its place [137]. Using this second order differential form of Bouguer's formula (given in [137]), the results of [86], presented in fig. 3.24(c) (left hand side), were faithfully reproduced using a fifth order Runge-Kutta integration technique. Consequently, it is believed that an error in the translation of [1.81] to cartesian co-ordinates may have occurred. Indeed, the exit angles, $\alpha_r(p_r)$, resulting from the ray trace using this modified form did not agree with those of the ray trace using [1.81], nor did they agree with those predicted by [1.82].

Applying the RFD ray trace procedure to the refractive index profile inferred from fig. 3.22, the results presented in fig. 3.25, for two different detection plane distances, were obtained. Also indicated in the figures are the points P_1, P_2 and P_3 (see fig. 1.20).
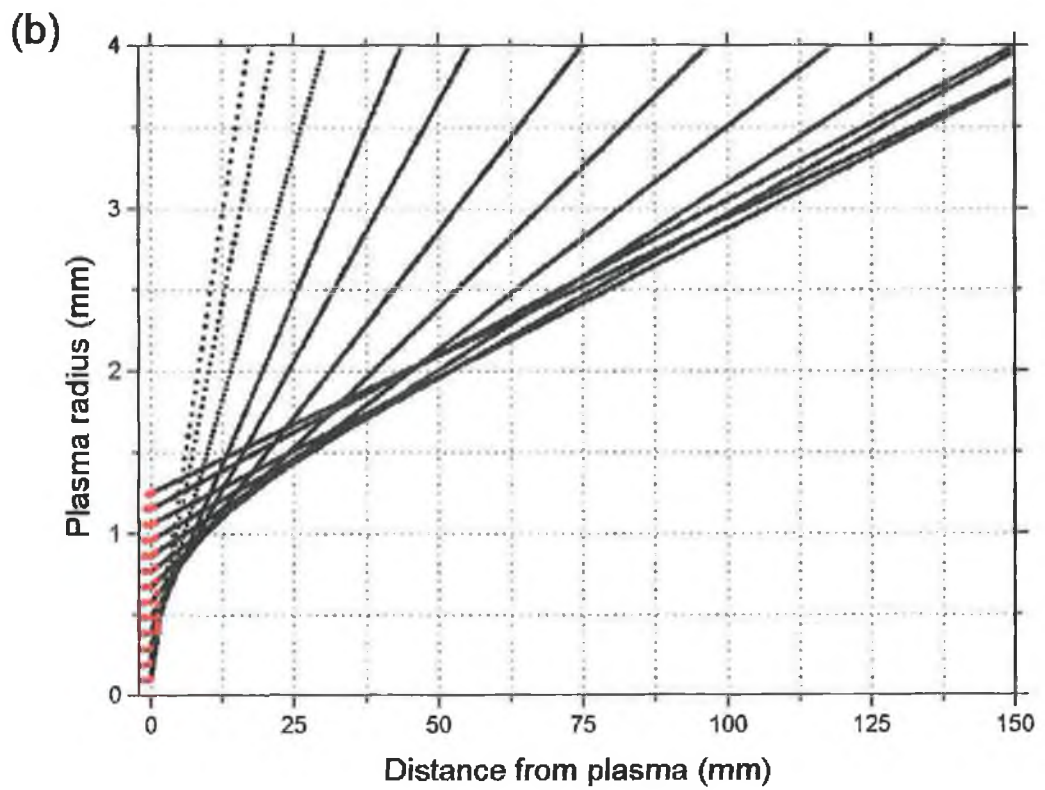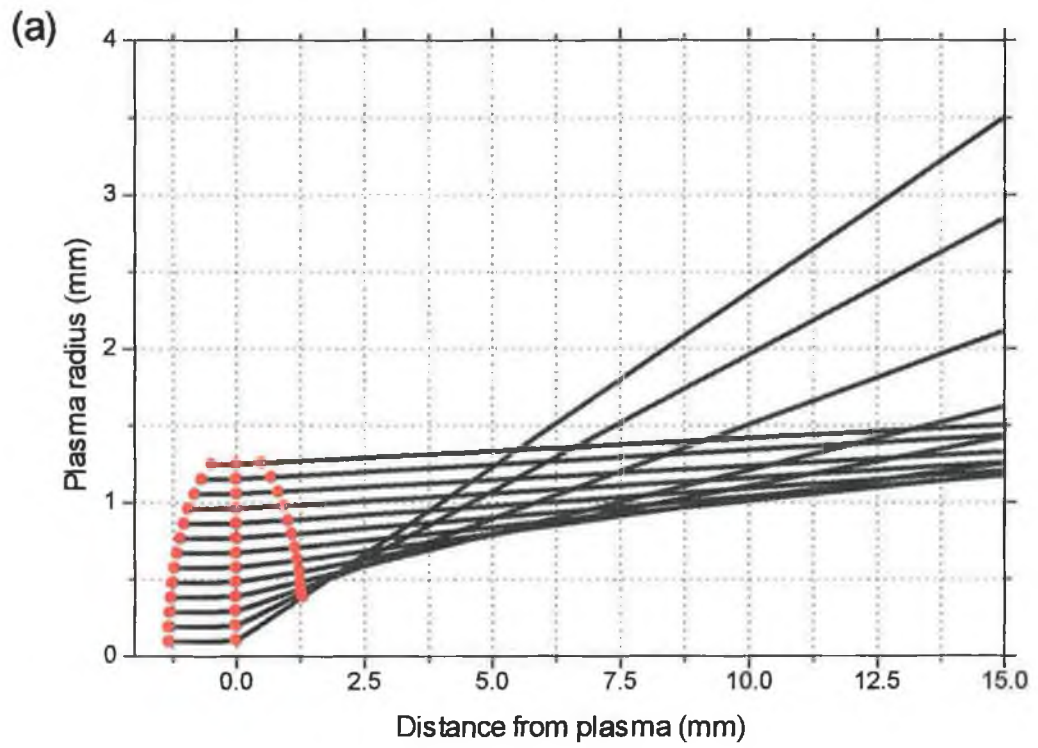
Fig. 3.25: Simulated ray traces using the refractive index profile determined from the RFD analysis of the shadowgraph shown in fig. 3.20. The distance from the plasma to the detector is 15 mm in the case of (a), and 150 mm in the case of (b).

138

One can clearly see from fig. 3.25 that a caustic surface [86][93] extends over several mm. Furthermore, no evidence for the existence of a ring focus [85] was found. The sensitivity of the technique is evident from fig. 3.25(b), where the OEPR under conditions similar to the experimentally recorded shadowgraph shown in fig. 3.20 was predicted as ~3.8 mm, approximately 2.8 times the OEPR measured from fig. 3.20 (i.e. 1.34 mm). A contributing factor may possibly be attributed to the determination of the last non-deviated ray from the shadowgraph, as well as an underestimation of α_r using [1.65] which assumes planar wavefronts at the detector plane. Campbell estimated α_r to be in the region of ~80 → 90% of the true value [137]. Additionally, it may be observed that the fringe pattern of fig. 3.20 appears to extend to ~2.5 mm from the target surface indicating a maximum deflection angle of ~17 mrad. This appears to be overestimated in the ray trace of fig. 3.25(b). As the deflection angle increases, however, the corresponding optical path difference increases, and thus the fringe pattern merges to a featureless continuum, thus masking the true maximum deflected 'ray'. The assumption of a parabolic path through the plasma can be analysed with reference to fig. 3.26, where parabolic fits of the form $y=ax^2+b$ were made to the least and most deflected rays of fig. 3.25. As can be seen from the low χ^2 values resulting from the fits, the assumption of a parabolic path is reasonable. Also, as expected, the actual path of a ray approaches that of a parabola (lower χ^2 value) for less deviated rays as in fig. 3.26(a).

(a)

Y=AX²+B
χ² = 1.1365x 10⁻⁷
A 0.01752 0.00035
B 1.24644 0.00003

■ Actual Path
······· Parabolic Fit

(b)

Y=AX²+B
χ² = 6.9968x 10⁻⁵
A 0.08359 0.0011
B 0.11078 0.00046

■ Actual Path
······· Parabolic Fit
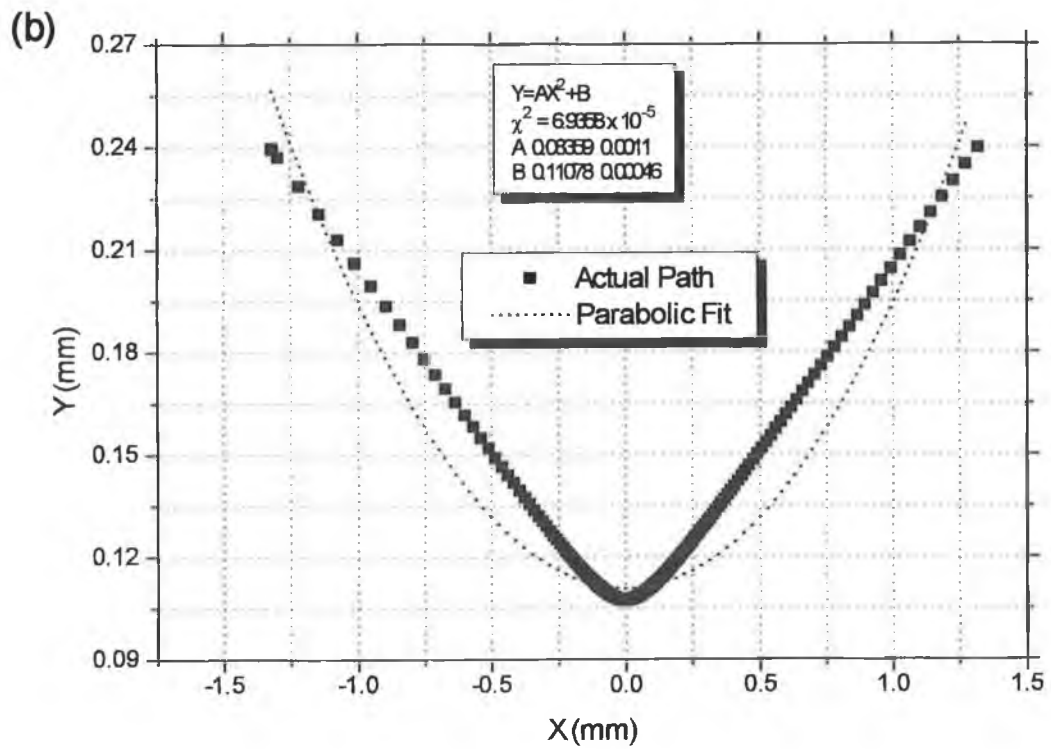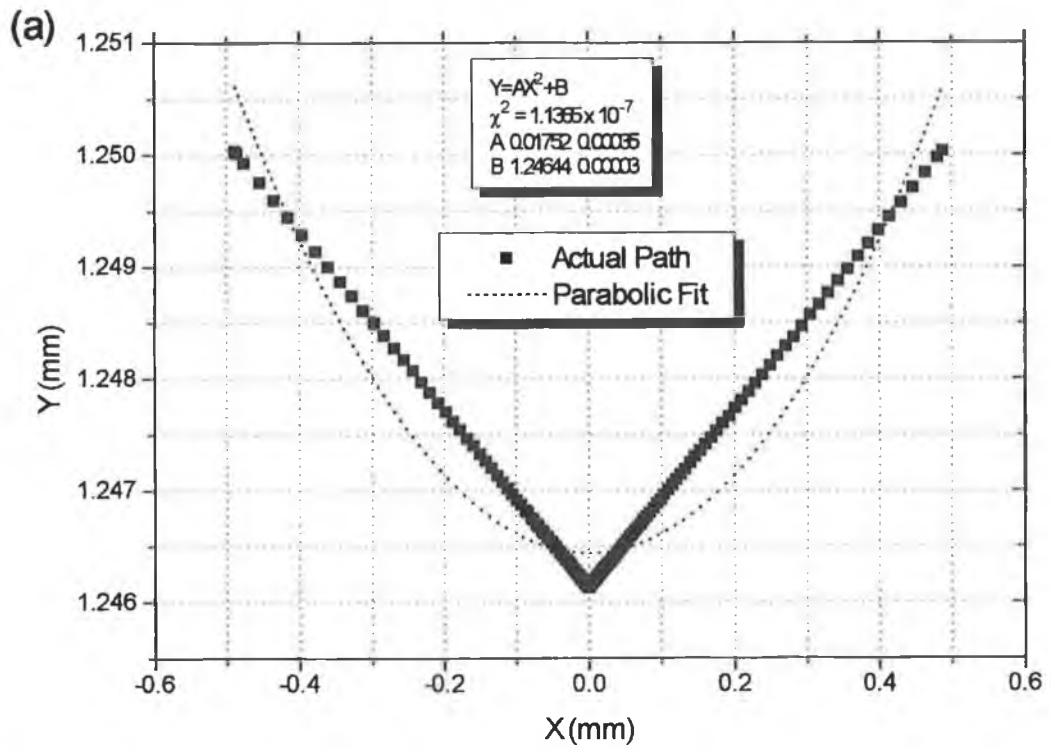
Fig. 3.26: Parabolic fits to the (a) least and the (b) most deviated rays paths through the plasma.

Finally, the applicability of the geometric optics approach to the analysis can be substantiated with reference to fig. 3.19. The maximum deflection experienced by a ray is ~7 mm. This corresponds to a deflection angle of ~47 mrad, which for an optical plume length of ~3 mm corresponds to a uniform refractive index gradient of ~16 m^{-1} using the analysis of [83]. The corresponding atomic number density gradient [83] for the transition under consideration (f_{ik} = 0.748 [40]) is ~3 x 10^{26} m^{-4} (~3 x 10^{18} cm^{-4}). Assuming a similar electron density, this gradient is much less than the maximum tolerable gradient of ~6 x 10^{24} cm^{-4} (see fig. 1.21) if an electron density not exceeding 0.8 times the critical density is to be probed, thus validating the geometric optics approach.

3.3   The Dual Laser Plasma Photoabsorption Technique

The spatio-temporal distribution maps of figs. 2.46 and 2.47 provide insight into the dynamics of the evolution of the lithium plasma. It can be seen that the Li^+ ions appear in the earlier stages of the plume expansion and are concentrated closer to the target normal. Conversely, the population of Li^o atoms appears to peak at a later stage of the expansion and tend to occupy a comparatively larger area. This observation is consistent with earlier detailed studies on the ion and velocity structure of a laser produced plasma [20].

3.3.1 The Photoabsorption Spectrum of Li^+

The photoabsorption spectrum of Li^+ shown in fig. 2.48 contains information relating to the source conditions, i.e. of temperature and density etc. The true absorption coefficient for a discrete line originating from the ground level i to an upper level k is given by [1.30]. Neglecting stimulated emission and using tabulated values for the relevant atomic parameters, one may, assuming a ground level spatial density distribution and normalised atomic frequency response, compute *ab initio* the absorption coefficient for such a transition. In our conditions, the atomic frequency response is comparable if not narrower than the estimated instrument function. The measured absorption coefficient in the vicinity of a spectral line is thus seriously distorted. Eliminating instrumental effects therefore enables the measurement of either the

absolute photoabsorption cross-section (if the density distribution is known), or the density profile (if the absolute cross-section is known). This technique has previously been applied to the He-like $1s^2 \rightarrow 1snp$ ($n \geq 4$) series in Be^{2+} by [138] using an iterative procedure involving trial values for ϕ_v, the atomic frequency response and

$$N_L = \int_{-\frac{L}{2}}^{+\frac{L}{2}} N_i(z)dz$$ (in the general case), the spatial density distribution. Using a similar

technique, the same data (extracted using a digitiser) near threshold in Be^{2+} was fitted as a proving ground for a recently developed fitting procedure. A flow-chart for the complete fitting procedure is illustrated in fig. 3.27.
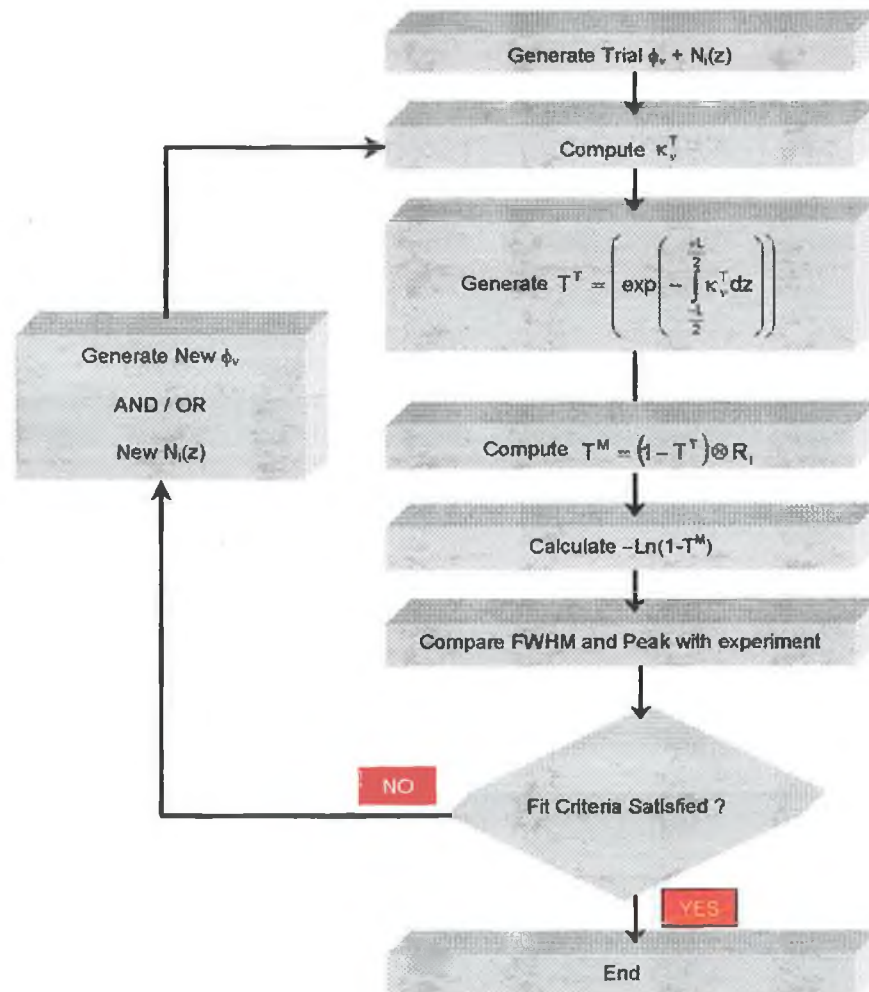
Fig. 3.27: A flow-chart illustrating the fitting procedure used to compute the true absorption coefficient data. The symbols used are explained in the text.

The procedure initiates by generating a trial normalised AFR ϕ_ν using the Voigt form described by [1.28], and a trial value for the ground state density distribution $N_i(z)$. In the absence of further information, the Lorentzian half-width Δ_L (HWHM) is calculated using the quasistatic approximation [1.50], while the Gaussian full half-width $2\Delta_G$ is evaluated using [1.49]; the temperature generally deriving from the LTE model outlined in §1.3.1. The natural line widths for the transitions investigated during the course of this work are negligible (typically 10^9 s^{-1}) and will not be considered further. The true absorption coefficient κ_ν^T defined by [1.30] accompanied by the resultant transmission

spectrum $T^T = \left(\exp\left(-\int_{\frac{-L}{2}}^{\frac{+L}{2}} \kappa_\nu^T dz \right) \right)$ were then computed by integrating along the

absorbing plasma column length using the trial value for the density distribution $N_i(z)$ and the AFR ϕ_ν. In the present experiments, a cylindrical lens was used to focus the output of a Nd:YAG (0.3 J, 15 ns) laser onto a lithium target (see §2.3.3(b)). Subsequently, the absorbing plasma column length, L, was known. As the Nd:YAG output energy distribution was uniform, a top-hat density profile was assumed. The resultant synthetic transmission spectrum T^T was inverted to enable convolution [111] with a predefined instrument function R_i estimated in §2.3.2(c). Evaluating $-Ln(1-T^M)$, where T^M represents the resultant convolved spectrum, furnishes the desired absorption spectrum. This procedure is repeated for each line in the spectrum until satisfactory convergence between experiment and model is achieved for all lines simultaneously. The criteria used to determine the degree of convergence entailed comparing the FWHM and peak absorption of the computed and experimental lines in the spectra. At each iteration, the same value for temperature and density are used for each transition in the spectrum.

Following the procedure outlined above, the photoabsorption spectrum $1s^2 \rightarrow 1snp$ (n = 4,5,6,7) of Be^{2+} measured by [138] was fitted using accurate values for the oscillator strengths. These are tabulated in table 3.6 [40].

Transition	λ (Å)	g_i	g_k	A_{ki} (s^{-1})	f_{ik}
$1s^2 \rightarrow 1s4p$	84.7580	1	3	1.53×10^{10}	4.93×10^{-2}
$1s^2 \rightarrow 1s5p$	83.2020	1	3	7.80×10^9	2.43×10^{-2}
$1s^2 \rightarrow 1s6p$	82.3770	1	3	4.49×10^9	1.37×10^{-2}
$1s^2 \rightarrow 1s7p$	81.8910	1	3	2.84×10^9	8.57×10^{-3}

Table 3.6: Atomic parameters relating to the Be^{2+} resonance absorption lines ($1s^2 \rightarrow 1snp$, n = 4,5,67) investigated as a test case for the code developed.

The instrument function was approximated by a 0.08 Å Lorentzian [138]. From the measured spectrum (at 2 mm from the target surface) (see fig. 3.28(a)) it may be observed that the FWHM of the transitions considered are comparable with the FWHM of the instrument function. As a result, the broadening is predominately instrumental, and clearly the experimental conditions correspond to the low-velocity regime defined in §1.4.3. The Lorentzian component of the AFR was calculated using the quasistatic approximation formula of [1.50] multiplied by a scaling 'stark factor' (= 0.5). The experimental and theoretical photoabsorption spectra are plotted in fig. 3.28.
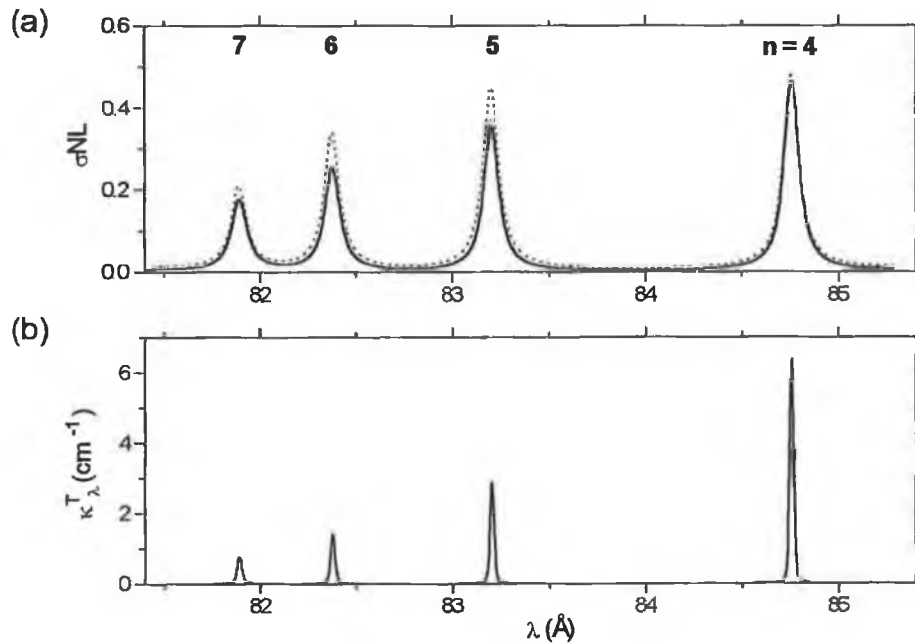
Fig. 3.28: The photoabsorption spectrum of Be^{2+} $1s^2 \rightarrow 1snp$ (n = 4,5,6,7) [138] used as a proving ground for the fitting technique developed. (a) Dotted line: experiment; solid line: absorption spectrum resulting from model. (b) The resultant theoretical absorption coefficient κ_λ^T.

144

A theoretical absorption coefficient spectrum results from the fitting procedure (see fig. 3.28(b)) where the lines have Gaussian profiles Doppler dominated, of FWHM of 2.4×10^{-2} Å. This is in good agreement with the FWHM computed by [138] of 2.5×10^{-2} Å. A value for $N_L = \int_{-\frac{L}{2}}^{+\frac{L}{2}} N_i(z)$ of $\sim 6 \times 10^{20}$ m^{-2} also results from the fitting procedure. This compares well with the value determined by [138] of $\sim 5 \times 10^{20}$ m^{-2}. The corresponding ground state Be^{2+} density for a plasma column length of 6 mm and zero density gradient is $\sim 1 \times 10^{23}$ m^{-3}.

Having successfully applied the technique to the test case of Be^{2+}, the same procedure was applied to the He-like photoabsorption spectrum of Li$^+$ 1s^2 $\rightarrow$ 1snp (n = 4,5,6,7). With reference to fig. 2.48 it may be observed that the widths of the 1s^2 $\rightarrow$ 1snp (n = 4,5,6,7) lines are comparable with the FWHM of the instrument function estimated in §2.3.2(c). The broadening is therefore mostly instrumental and, as before, it was determined that the corresponding experimental conditions belong to the low expansion velocity regime of §1.4.3. Consequently, streaming plays a negligible role. Following the fitting procedure outlined in fig. 3.27 a theoretical absorption coefficient spectrum was computed for the Li$^+$ Rydberg series (n = 4,5,6,7), for which accurate values of the oscillator strengths are tabulated in table 3.7 [40]. The Lorentzian component of the AFR for the n = 4 and 5 transitions was calculated using the electron-impact half widths (FWHM) computed by [57] shown in table 1.2 for a temperature of 40 000 K. The Stark FWHM was assumed to vary linearly with density [55]. For the n = 6 and 7 transitions the quasistatic approximation of [1.50] multiplied by a 'stark factor' (< 1) was used. The measured and theoretical spectra along with the theoretical absorption coefficient are plotted in fig. 3.29.

Transition	λ (Å)	g_i	g_k	A_{ki} (s^{-1})	f_{ik}
1s^2 $\rightarrow$ 1s4p	171.5756	1	3	3.32×10^9	4.40×10^{-2}
1s^2 $\rightarrow$ 1s5p	168.7428	1	3	1.70×10^9	2.18×10^{-2}
1s^2 $\rightarrow$ 1s6p	167.2401	1	3	9.94×10^9	1.25×10^{-2}
1s^2 $\rightarrow$ 1s7p	166.346	1	3	6.22×10^8	7.74×10^{-3}

Table 3.7: Atomic parameters relating to the Li$^+$ resonance absorption lines investigated (1s^2 $\rightarrow$ 1snp, n=4,5,6,7).
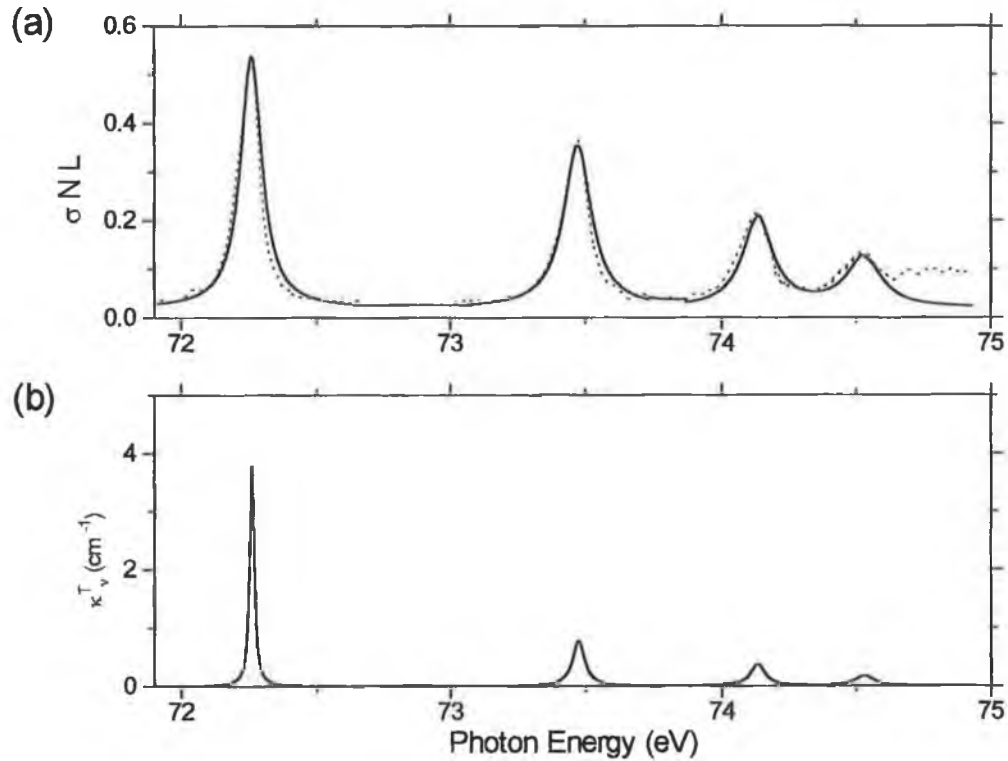
Fig. 3.29: The photoabsorption spectrum of Li$^+$. (a) Dotted line: measured at Δx = 0.4 mm, ΔT = 30 ns; solid line: absorption spectrum resulting from the model. (b) The theoretical absorption coefficient resulting from the model.

The instrument function differed slightly for each transition from that computed in §2.3.2(c) due to the variation in FWHM across the face of the CEMA (see §2.3.2(b)). However, as the variation was less than 0.1 of a pixel, a Lorentzian instrument function of 3.6 pixels FWHM was used for all transitions. From the fitting procedure one obtains an average value for $N_L \cong 2.7 \times 10^{20}$ m^{-2} in the conditions of fig. 2.48 (Δx = 0.4 mm, ΔT = 30 ns). This corresponds to a ground state Li$^+$ density of ~9 × 10^{23} m^{-3} for a plasma column length of 0.3 mm and zero density gradient along the line-of-sight. A temperature of ~4 eV results from the fitting process. This is in good agreement with the temperature conditions for an optimal Li$^+$ population density inferred from the LTE fractional ionisation plot of fig. 1.5 using an electron density of 9 × 10^{23} m^{-3}. A 'stark factor' of 0.8 was used in the fitting procedure for the n = 6 and 7 transitions. The corresponding Stark widths for the n = 4,5,6 and 7 transitions are shown in table 3.8.

Transition	λ_{centre} (Å)	Δ_L (Å) (HWHM)
$1s^2 \rightarrow 1s4p$	171.5756	0.0231
$1s^2 \rightarrow 1s5p$	168.7428	0.0610
$1s^2 \rightarrow 1s6p$	167.2401	0.0713
$1s^2 \rightarrow 1s7p$	166.346	0.0960

Table 3.8: Stark widths (HWHM) resulting from the fitting procedure for the Li$^+$ $1s^2 \rightarrow 1snp$ (n = 4,5,6 and 7) photoabsorption spectrum.

An alternative procedure to the *ab initio* fitting procedure outlined in the previous paragraphs involves deconvolving the experimentally measured transmission spectrum $\dfrac{I_\nu}{I_{\nu_o}}$, using the instrument function determined in §2.3.2(c), to obtain the true transmission spectrum. The true photoabsorption spectrum in the absence of instrumental effects is then readily computed. The true photoabsorption spectrum of Li$^+$ ($1s^2 \rightarrow 1snp$ with n = 4,5,6 and 7) generated using this method is shown in fig. 3.30. The deconvolved spectrum was computed using 20 iterations of Varosi's maximum likelihood deconvolution algorithm (see Appendix F). Also shown in the figure for comparison is the computed photoabsorption spectrum resulting from the fitting procedure above as in fig. 3.29.
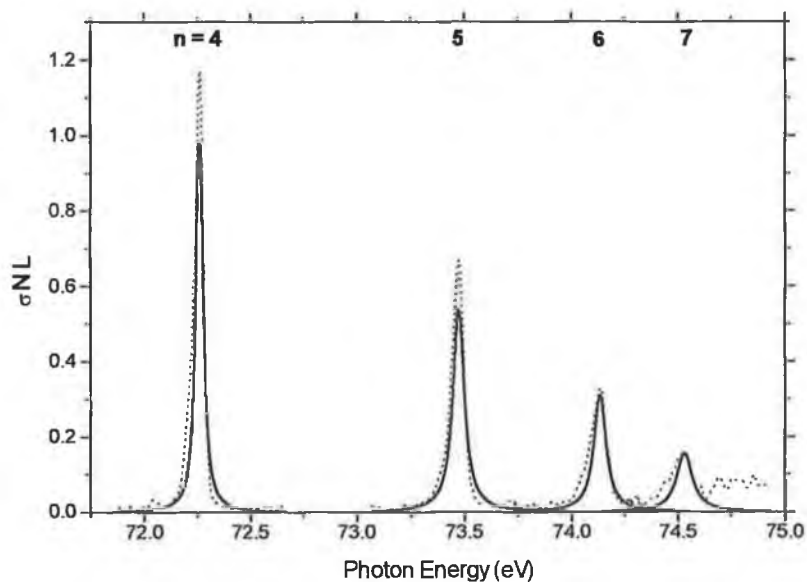
Fig. 3.30: The photoabsorption spectrum of Li$^+$ $1s^2 \rightarrow 1snp$ (n = 4,5,6 and 7). Dotted line: the photoabsorption spectrum resulting from the deconvolution process. Solid line: the computed photoabsorption spectrum resulting from fitting procedure (as in fig. 3.29).

The computed and deconvolved spectra agree well for the n = 6 and 7 transitions. The difference between the two for the n = 4 and 5 transitions corresponds to a deviation in population density of approximately ±10% for a fixed absorbing column length. This is certainly within the limits of experimental error of the instrument.

3.3.2 The Photoionisation Spectrum of Li$^+$

The photoionisation cross-section for the $1s^2 + h\nu \rightarrow 1s + \varepsilon e$ process in Li$^+$ can be accurately computed using the universal formula of Verner *et al.* [122]. The corresponding curve is overlayed in fig. 3.31 with the experimental data between threshold (75.64 eV) and 180 eV in conditions where the Li^o population was negligible (see §2.3.3).
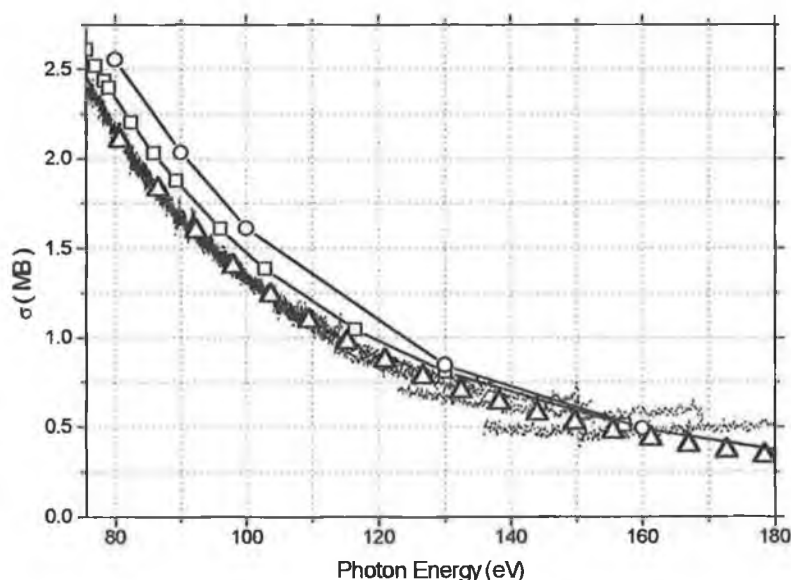
Fig. 3.31: The photoionisation spectrum of Li$^+$ between threshold (75.64 eV) and 180 eV. The triangles, squares and circles indicate the theoretical photoionisation cross-sections calculated by Verner *et al.* [122], Bell and Kingston [139] and Manson and Reilmann [140] respectively.

In this case a transmission measurement directly provided a value for N_L since the continuum cross-section does not depend on any particular line shape factor ϕ_ν. For each of the 9 overlapping CEMA settings, N_L was extracted from a non-linear least square fit of Verner's universal fitting formula to the measured absorbance data. These are shown in table 3.9.

148

Setting No.	N_L (cm^{-2})	L (cm)	N (cm^{-3})
1	2.28×10^{17}	0.25	9.12×10^{17}
2	3.13×10^{17}	0.25	1.25×10^{18}
3	3.42×10^{17}	0.25	1.37×10^{18}
4	2.89×10^{17}	0.3	9.63×10^{17}
5	5.4×10^{17}	0.4	1.35×10^{18}
6	5.05×10^{17}	0.4	1.26×10^{18}
7	5.15×10^{17}	0.55	9.36×10^{17}
8	5.76×10^{17}	0.7	8.23×10^{17}
9	5.56×10^{17}	0.7	7.94×10^{17}

Table 3.9: N_L values resulting from a non-linear least square fit using Verner's universal fitting formula applied to the photoionisation spectrum recorded at each of 9 different CEMA settings.

The excellent agreement between the curves in fig. 3.31 further confirms the high purity of Li$^+$ ions in the plasma plume under the experimental conditions used. Furthermore, the accuracy of the theoretical cross-section is augmented. Assuming a zero density gradient along the line-of sight in the absorbing plasma, the N_L values extracted using the above procedure - up to an energy of ~120 eV (i.e. the first six N_L values in table 3.9), were converted to number densities. The average value was ~1 x 10^{24} m^{-3} ±20%. This value is in excellent agreement with that predicted from modelling the discrete part of the spectrum previously described. There exists a marked discrepancy between the measured and theoretical photoionisation cross-section data at energies greater than ~120 eV. This was also observed during the fitting procedure. Despite the comparable magnitude in cross-section between Li$^+$ and Li^{2+} at energies greater that the threshold in Li^{2+} (~0.8 and ~0.7 Mb respectively at 122.5 eV) the density of Li^{2+} absorbers was markedly lower. This can be observed from the absence of the 1s → 2p resonance absorption line in Li^{2+} at 91.84 eV. Thus, it can be concluded that Li^{2+} does not contribute to the deviation at energies greater than ~120 eV. As the contribution from higher orders has already been determined to be negligible (see §2.3.2(d)), the deviation can be attributed to scattered light contributions detected on both the I_{v_o} and I_v signals (see 2.3.2(e)). The resultant transmittance is thus strongly distorted. In order to correct the spectrum of fig. 3.31 for scattered light, the scattered light contribution detected on I_v must first be determined. This was carried out in the following manner.

Knowing the fractional scattered light contribution $\left(\left.I_{o_s}\middle/I_{v_{o\,TRUE}}\right.\right)$ on I_{v_o} between ~120 eV and 180 eV (see §2.3.2(e)), one may ascertain $I_{v_{o\,TRUE}}$ using

$$I_{v_o} = I_{v_{o\,TRUE}} + I_{o_s}$$

$$\therefore I_{v_o} = I_{v_{o\,TRUE}}\left(1 + \frac{I_{o_s}}{I_{v_{o\,TRUE}}}\right) \qquad [3.2]$$

$$\Rightarrow I_{v_{o\,TRUE}} = \frac{I_{v_o}}{\left(1 + \frac{I_{o_s}}{I_{v_{o\,TRUE}}}\right)}$$

Having estimated $I_{v_{o\,TRUE}}$, $I_{v_{TRUE}}$ for each CEMA setting may readily be computed using

$$\frac{I_{v_{TRUE}}}{I_{v_{o\,TRUE}}} = \exp(-\sigma N_L L) \qquad [3.3]$$

Here, the previously determined average value for $N_L = 1.2 \times 10^{24}$ m^{-3} may be used while L, the absorbing plasma column length, and σ (Mb) (from [122]) are already known. To perform the calculation L must be constant for each CEMA setting. Otherwise the scattered light contribution on I_v may vary and thus invalidate any results. Consequently, the scattered light contribution $\left(\frac{I_s}{I_{v_{o\,TRUE}}}\right)$ on I_v may be calculated using

$$I_v = I_{v_{TRUE}} + I_s$$

$$\therefore \frac{I_s}{I_{v_{o\,TRUE}}} = \frac{I_v - I_{v_{TRUE}}}{I_{v_{o\,TRUE}}} \qquad [3.4]$$

The resultant scattered light contributions including the subsequent curve fits to the raw data are shown in fig. 3.32. It can be noted from fig. 3.32 that the scattered light contribution on I_v is, as expected, less than that on I_{v_o}. The fitted profiles can then readily be used in future calculations.

150
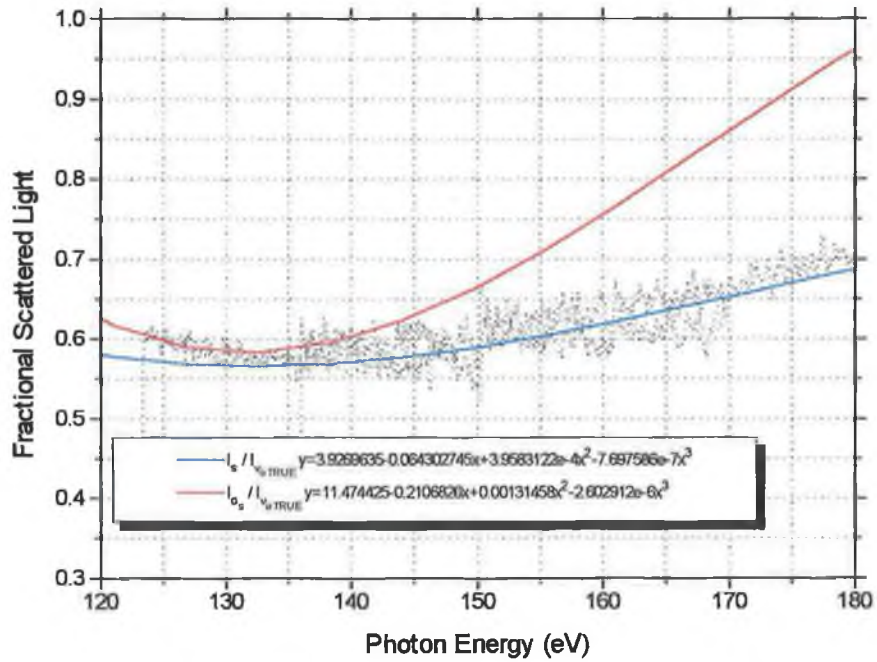
Fig. 3.32: The fractional scattered light contributions on I_{v_o} and I_v between 120 eV and 180 eV. The contribution on I_v was computed using 2 overlapping CEMA settings for which L, the absorbing plasma column length was fixed.
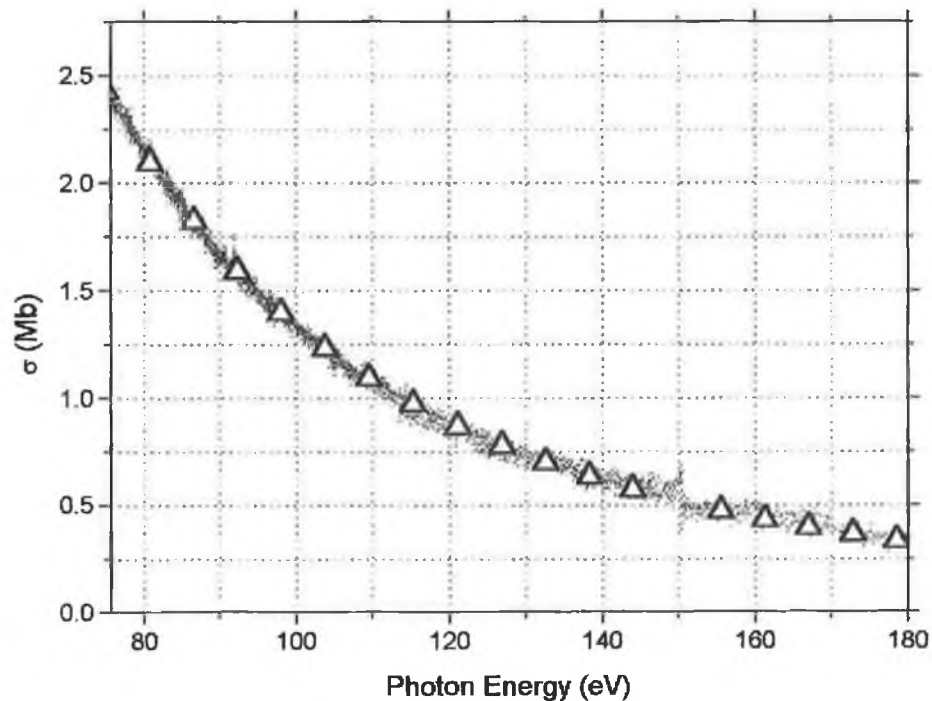
Fig. 3.33: The photoionisation spectrum of Li^+ corrected for scattered light contributions on I_{v_o} and I_v. The triangles indicate the theoretical photoionisation cross-section calculated by Verner et al. [122].

It should be emphasised that the fractional scattered light component on I_v computed above applies solely to the current experimental situation. Employing a different configuration, e.g. using a different absorbing plasma, results in a modified fractional scattered light component on I_v as a direct consequence of the plasma acting as a filter. Using the above computations, the Li^+ photoionisation spectrum of fig. 3.31 was corrected for scattered light contributions. The resultant spectrum between threshold and 180 eV is shown in fig. 3.33. The photoionisation spectrum shown in fig. 3.33 underlines the importance of correctly treating scattered light contributions if one is to reliably measure relative cross-sections.

Conclusions and Suggestions for Future Work

The development of two novel diagnostic techniques, and their application to the quantitative study of an expanding laser produced lithium plasma has been presented. Firstly, a sequence of temporally resolved frames of the luminous plume of an expanding lithium plasma were recorded using a gated image intensifier coupled to a CCD camera with a temporal resolution of ~9 ns. Secondly, shadowgraphs of the lithium plume were recorded using a CCD and a Nd:YAG pumped dye laser (FWHM = 8 ns) as a back lighter. The sensitivity of the recorded shadowgraphs to the dye laser probe wavelength in the vicinity of an atomic resonance transition was shown. Using the analysis of the so-called refractive fringe diagnostic (RFD) technique, electron density profile data was determined. Additionally, a new approach to the analysis of the photoabsorption and photoionisation spectra of Li^+ recorded using a 2.2 m extreme ultraviolet (EUV) grazing incidence spectrometer was outlined, with a view to obtaining density estimates. The importance of correcting for scattered light contributions, in the > ~100 eV range, was also underlined if relative cross-sections are to be reliably measured. In all cases, established plasma and radiation models were used in the analysis and interpretation of the experimental results, to obtain velocity, temperature and density profile estimates. Furthermore, a suggested improvement to the interpretation of the expansion of a laser-produced plasma in a gaseous environment in terms of a non-viscous drag force model was presented. For each of the experimental set-ups, system parameters pertinent to the interpretation of the results were characterised.

Some improvements and suggestions for future work include:

In relation to the fast-frame photography set-up, some potential instrumentation improvements such as the introduction of a 16-bit scientific grade CCD / frame grabber as well as the direct fibre coupling of the gated intensifier output to the CCD could be made. Additionally, an estimate of the extent of the continuum radiation from the target surface could be made through the introduction of an imaging spectrometer. Finally, a more rigorous argument in relation to the assumption of

optical thinness could be made by introducing a mirror to reflect the emitted radiation back through the plasma and onto the detector. By recording two images, one with the mirror in place, and the second without, the assumption of optical thinness could be investigated. Further characterisation of system performance would also facilitate removal of system aberrations through deconvolution techniques.

As a means of corroborating the results from both the shadowgraph and fast-frame imaging techniques, the experimental conditions under which the plasma is created could be mirrored in both set-ups. This would facilitate the determination of electron density and excited state density profiles.

An improvement to the analysis of the shadowgraphs using the RFD technique would involve the elimination of the assumption of a parabolic path through the plasma. This however, would complicate the geometry of the analysis. Additionally, a sensitivity test for the RFD technique, involving the use of Graded Refractive Index (GRIN) rod lenses of known refractive index profile, in place of the laser produced plasma, could be used. In this manner, the refractive index profile could be reconstructed and verified against the known profile. Finally, using Kirchoff's diffraction integral, and the refractive index profile determined using the RFD analysis, it may be possible to computationally reconstruct the shadowgraph images.

The extension of the analysis of the photoabsorption spectra recorded using the DLP technique to different elements is also a possibility. Indeed, through the introduction of a gated MCP one could potentially obtain temporally resolved density information. This would involve further analysis of the absorbing volume effectively 'seen' by the detector.

References

[1] Weast, *CRC Handbook of Chemistry and Physics, 68th Edition 1987-1988*, CRC Press

[2] T.P. Hughes, *Plasmas and Laser Light*, Adam Hilger, London, 1975

[3] AIP Conference Proceedings 288, *Laser Ablation: Mechanisms and Applications-II*, John C. Miller, David B. Geohegan (Eds.) (1993), New York: AIP Press

[4] Richard H. Huddlestone and Stanley, *Plasma Diagnostic Techniques*, New York: Academic Press, 1965

[5] Goodfellow Metals (UK) Catalogue 1996 / 97

[6] Akos Vertes, Renaat Gijbels and Fred Adams, *Laser Ionization Mass Analysis*, Wiley (1993)

[7] S.C. Wilks, W.L. Kruer, M. Tabak, and A.B. Langdon, Physical Review Letters, Vol. 69 No. 9 p.1383-1386 (1992)

[8] John M. Dawson, The Physics of Fluids, Vol. 7 No. 7 p.981-987 (1964)

[9] Tudor Wyatt Johnston and John M. Dawson, The Physics of Fluids, Vol. 16 No. 5 p.722 (1973)

[10] P.K Carroll and E.T. Kennedy, Contemp. Phys., Vol. 22 No. 1 p.61-96 (1981)

[11] J. Lunney, Appl. Surf. Sci., Vol. 127-129, p.941-946 (1998)

[12] James R. Stallcop, J. Plasma Physics, Vol. 11 Pt. 1 p.111-129 (1974)

[13] C.L. Chan and J. Mazumder, J. Appl. Phys., Vol. 62 No. 11 p.4579-4586 (1987)

[14] Appl. Surf. Sci. Vol. 96-98 (1996), Vol. 127-129 (1998)

[15] C. Fauquignon and F. Floux, The Physics of Fluids, Vol. 13 No. 2 p.386-391 (1970)

[16] David B. Geohegan and Alexander A. Puretzky, Appl. Surf. Sci., Vol. 96-98 p. 131-138 (1996)

[17] Rajiv K. Singh and J. Narayan, Physical Review B, Vol. 41 No. 13 p.8843-8859 (1990)

[18] M.J. Bernstein and G.G. Comisar, Journal of Applied Physics, Vol. 41 No. 2 p.729-733 (1970)

[19] I.H. Hutchinson, *Principles of Plasma Diagnostics*, Cambridge University Press (1987)

[20] F.E. Irons, R.W.P. McWhirter and N.J. Peacock, J. Phys. B: Atom. Molec. Phys., Vol. 5 p.1975-1989 (1972)

[21] Heinrich Hora, *Plasmas at High Temperature and Density: Applications and Implications of Laser-Plasma Interaction*, Berlin; New York: Springer-Verlag (1991)

[22] J. Dawson, P. Kaw and B. Green, The Physics of Fluids, Vol. 12 No. 4 p.875-882 (1969)

[23] Heinrich Hora, *Physics of Laser Driven Plasmas*, New York: Wiley (1981)

[24] J.L. Bobin, Y.A. Durand, Ph.P. Langer and G. Tonon, Journal of Applied Physics, Vol. 39 No. 9 p.4184-4189 (1968)

[25] K.R. Chen, J.N. Leboeuf, R.F. Wood, D.B. Geohegan, J.M. Donato, C.L. Liu and A.A. Puretzky, Appl. Surf. Sci., Vol. 96-98 p.45-49 (1996)

[26] R.A. Al-Wazzan, C.L.S. Lewis and T. Morrow, Rev. Sci. Instrum. Vol. 67 No. 1 p.1-4 (1996)

[27] J.C. Miller (Ed.), *Laser Ablation: Principles and Applications*, Berlin; New York: Springer-Verlag (1994)

[28] David B. Geohegan, Appl. Phys. Lett., Vol. 60 No. 22 p.2732-2734 (1992)

[29] J. Gonzalo, C.N. Afonso and I. Madariaga, J. Appl. Phys., Vol. 81 No. 2 p.951-955 (1997)

[30] Richard B. Hall, Journal of Applied Physics, Vol. 40 No. 4 p. 1941-1945 (1969)

[31] J. Grun, J. Stamper, C. Manka, J. Resnick, R. Burris and B.H. Ripin, Appl. Phys. Lett., Vol. 59 No. 2 p.246-248 (1991)

[32] J. Gonzalo, F. Vega and C.N. Afonso, J. Appl. Phys., Vol. 77 No. 12 p.6588-6593 (1995)

[33] P.E. Dyer and J. Sidhu, J. Appl. Phys., Vol. 64 No. 9 p.4657-4663 (1988)

[34] T. Kerdja, S. Abdelli, D. Ghobrini and S. Malek, J. Appl. Phys., Vol. 80 No. 9 p.5365-5371 (1996)

[35] R.A. Al-Wazzan, Ph.D Thesis (unpublished) (1997)

[36] W. Lochte-Holtgreven, *Plasma Diagnostics*, AIP Press New York (1995)

[37] D. Colombant and G.F. Tonon, J. Appl. Phys., Vol. 44 No. 8 p.3524-3537 (1973)

[38] D.A. Verner, G.J. Ferland, Astrophys. J. Suppl., Vol. 103 p.467 (1996)

[39] Alan Corney, *Atomic and Laser Spectroscopy*, Clarendon Press, Oxford (1977)

[40] D.A. Verner, E.M. Verner and G.J. Ferland, Atomic Data Nucl. Data Tables, Vol. 64 No. 1 (1996)

[41] George B. Rybicki and Alan P. Lightman, *Radiative Processes in Astrophysics*, New York: Wiley (1979)

[42] G.A. Martin, J.R. Fuhr and W.L. Wiese, J. Phys. Chem. Vol. 17 Suppl. 3 (1988)

[43] Joseph Reader, Charles H. Corliss, W.L. Wiese and G.A. Martin, NSRDS-NBS 68 (1980)

[44] Stephen P. Fels, Applied Optics, Vol. 18 No. 15 p.2634-2637 (1979)

[45] A.B. McLean, C.E.J. Mitchell, D.M. Swanston, Journal of Electron Spectroscopy and Related Phenomena, Vol. 69 p.125-132 (1994)

[46] Peter V. O'Neill, Advanced Engineering Mathematics 3rd Edition, Wadsworth (1991)

[47] F.E. Irons, J. Phys. B:Atom. Molec. Phys., Vol. 8 No. 18 p.3044-3068 (1975)

[48] A.M. Malvezzi, L. Garifo, E. Jannitti, P. Nicolosi and G. Tondello, J. Phys. B:Atom. Molec. Phys., Vol. 12 No. 8 p.1437-1447 (1979)

[49] G. Tondello, E. Jannitti and A.M. Malvezzi, Physical Review A, Vol. 16 No. 4 p.1705-1714 (1977)

[50] Douglas W. Jones, W.L. Wiese and L.A. Woltz, Physical Review A, Vol. 34 No. 1 p.450-456 (1986)

[51] A. Carillon, P. Jaegle and P. Dhez, Physical Review Letters, Vol. 25 No. 3 p.140-143 (1970)

[52] P.K. Carroll and E.T. Kennedy, Phys. Rev. Lett., Vol. 38 No. 19 p.1068-1071 (1977)

[53] George Bekefi, Claude Deutsch and Barukh Yaakobi in *Principles of Laser Plasmas*, George Bekefi (Ed.), John Wiley and Sons (1976)

[54] Hans R. Griem, Physical Review, Vol. 128 No. 2 p.515-523 (1962)

[55] Hans R. Griem, *Spectral line broadening by plasmas*, Academic Press, New York (1974)

[56] Hans R. Griem, *Plasma Spectroscopy*, McGraw-Hill, New York (1964)

[57] Milan S. Dimitrijevic and Sylvie Sahal-Bréchot, Physica Scripta, Vol. 54 p.50-55 (1996)

[58] H.R. Griem and K.Y. Shen, Physical Review, Vol. 122 No. 5 p.1490-1496 (1961)

[59] Valery Bulatov, Liang Xu and Israel Schechter, Anal. Chem., Vol. 68 p.2966-2973 (1996)

[60] B.C. Boland, F.E. Irons and R.W.P. McWhirter, J. Phys. B.(Proc. Phys. Soc.), Ser. 2 Vol. 1 p.1180-1191 (1968)

[61] M. Ohkoshi, T. Yoshitake and K. Tsushima, Appl. Phys. Lett., Vol. 64 No. 24 p.3340-3342 (1994)

[62] Rudolf Gorenflo and Sergio Vessella, *Abel Integral Equations: Analysis and Applications*, Berlin; NewYork: Springer-Verlag (1991)

[63] Clifford J. Cremers and Richard C. Birkebak, Applied Optics, Vol. 5 No. 6 p.1057-1064 (1966)

[64] Moshe Deutsch and Israel Beniaminy, J. Appl. Phys., Vol. 54 No. 1 p.137-143 (1983)

[65] Pablo A. Vicharelli and Walter P. Lapatovich, Appl. Phys. Lett., Vol. 50 No. 10 p.557-559 (1987)

[66] R.N. Bracewell, Austral. J. Phys., Vol. 9 p.198-217 (1956)

[67] L. Montgomery Smith, Dennis R. Keefer and S.I. Sudharsanan, J. Quant. Spectrosc. Radiat. Transfer, Vol. 39 No. 5 p.367-373 (1988)

[68] Mark P. Freeman and S. Katz, J. Opt. Soc. Am., Vol. 50, No. 8 p.826-830 (1960)

[69] Charles M. Vest, Applied Optics, Vol. 24 No. 23 p.4089-4094 (1985)

[70] Ignacio H. Lira, Meas. Sci. Technol., Vol. 5 p.226-232 (1994)

[71] Y.A. Andrienko, M.S. Dubovikov, A.D. Gladun and Pak Un, Applied Optics, Vol. 31 No. 14 p.2615-2620 (1992)

[72] Shay Gueron and Moshe Deutsch, J. Appl. Phys., Vol. 79 No. 12 p.8879-8885 (1996)

[73] Ron J. Litchford and Wim M. Ruyten, Applied Optics, Vol. 34 No. 21 p.4530-4541 (1995)

[74] P. Elder, T. Jerrick and J.W. Birkeland, Applied Optics, Vol. 4 No. 5 p.589-592 (1965)

[75] R.W. Ladendurg (Ed.), *Physical Measurements in Gas Dynamics and Combustion*, Oxford University Press (1955)

[76] B.J. Rye and J.C. Taylor (Eds.), *Physics of Hot Plasmas (Scottish Univeristies: Summer School)*, Oliver and Boyd (Edinburgh) (1968)

[77] Ralph A. Alpher and Donald R. White, The Physics of Fluids, Vol. 2 No. 2 p.162-169 (1959)

[78] Ma. I. de la Rosa García, Ma. C. Pérez García, A.M. de Frutos Baraja and S. Mar Sardaña, Physical Review A, Vol. 42 No. 12 p.7389-7394 (1990)

[79] C.M. Vest, Applied Optics, Vol. 14 No. 7 p.1601-1606 (1975)

[80] R.W. Ditchburn, *Light* (3rd Edition), Academic Press London, New York, San Francisco (1976)

[81] Georg Pretzler, Christian Haas, Theo Neger and Helmut Jäger, Applied Optics, Vol. 36 No. 33 p.8806-8814 (1997)

[82] P.W. Schreiber, A.M. Hunter II and D.R. Smith Jr., Plasma Physics, Vol. 15 p.635-646 (1973)

[83] A.H. El-Astal and T. Morrow, J. Appl. Phys., Vol. 80 No. 2 p.1156-1160 (1996)

[84] K. Horioka, N. Tazima and K. Kasuya, Rev. Sci. Instrum., Vol. 61 No. 1 p.610-612 (1990)

[85] M.M. Michaelis and O. Willi, Optics Communications, Vol. 36 No. 2 p.153-158 (1981)

[86] P.F. Cunningham, R.N. Campbell and M.M. Michaelis, J. Phys. E:Sci. Instrum., Vol. 19 p.957-960 (1986)

[87] R.S. Craxton, F.S. Turner, R. Hoefen, C. Darrow, E.F. Grab and Gar. E. Busch, Phys. Fluids B, Vol. 5 No. 12 p.4419-4431 (1993)

[88] Ronald M. Gilgenbach and Peter L. G. Ventzek, Appl. Phys. Lett., Vol. 58 No. 15 p.1597-1599 (1991)

[89] Peter L. G. Ventzek, Ronald M. Gilgenbach, Chi Hong Ching and Roger A. Lindley, J. Appl. Phys., Vol. 72 No. 5 p.1696-1706 (1992)

[90] A. Snigirev, I. Snigireva, V. Kohn, S. Kuznetsov and I. Schelokov, Rev. Sci. Instrum., Vol. 66 No. 12 p.5486-5492 (1995)

[91] C. Raven, A. Snigirev, I. Snigireva, P. Spanne, A. Suvorov and V. Kohn, Appl. Phys. Lett., Vol. 69 No. 13 p.1826 (1996)

[92] J.M. Cowley, *Diffraction Physics* 2nd Rev. Ed., Amsterdam: North-Holland Publishing Co. (1981)

[93] D.W. Sweeney, D.T. Attwood and L.W. Coleman, Applied Optics, Vol. 15 No. 5 p.1126-1128 (1976)

[94] M. Born and E. Wolf, *Principles of Optics* 6th Edition, Oxford; New York: Pergamon Press (1980)

[95] F. Kielmann, Plasma Physics, Vol. 14 p.111-122 (1972)

[96] John T. Costello, Jean-Paul Mosnier and Eugene T. Kennedy, Physica Scripta, Vol. T34 p.77-92 (1991)

[97] E.T. Kennedy, J.T. Costello and J.P. Mosnier, J. Elec. Spec. Rel. Phenom., Vol. 79 p283-288 (1996)

[98] Eugene Hecht, *Optics* (2nd Edition), Addison-Wesley (1987)

[99] Andor Technology Ltd., Belfast, N. Ireland.

[100] Minitron OS-25 CCD Manual

[101] M.J. Howes and D.V. Morgan (Eds.), *Charge-Coupled Devices and Systems*, New York Wiley (1979)

[102] Photometrics Ltd., http://www.photomet.com/

[103] Hamamatsu Photomultipler Tube Catalogue (OCT/90)

[104] Spectron Laser Systems Dye Manual

[105] Spectron Laser Systems *private communication*

[106] W. Whitty, J. Costello, E. Kennedy, C. Moloney and J.P. Mosnier, Appl. Surf. Sci., Vol. 127-129 p.686-691 (1998)

[107] J.M. Bridges, C.L. Cromer and Thomas J. McIlrath, Applied Optics, Vol. 25, No. 13 p.2208-2214 (1986)

[108] W.A. Rense and T. Violett, J. Opt. Soc. Am., Vol. 49 No. 2 p.139-141 (1959)

[109] G. Tondello, Optica Acta, Vol. 26 No. 3 p.357-371 (1979)

[110] L. Kiernan, Ph. D. Thesis (unpublished) (1994)

[111] W.E. Blass and G.W. Halsey, *Deconvolution of Absorption Spectra*, New York: Academic Press (1981)

[112] J.M. Lerner and A. Thevenon, *The Optics of Spectroscopy: A Tutorial V2.0*, J-Y Optical Systems (1988)

[113] Andrew Gray (Centre for Laser Plasma Research, Dublin City University), *private communication*

[114] J. Fischer, M. Kühne and B. Wende, Applied Optics, Vol. 23 No. 23 p.4252-4260 (1984)

[115] Galileo Corporation, *private communication*

[116] J. Feldhaus (HASYLAB at DESY), *private communication*

[117] Henke atomic scattering factors available from ftp://grace.lbl.gov/pub/sf/

[118] H.J. Hagemann, W. Gudat and C. Kunz, DESY SR-74/7 Internal Report (1974)

[119] Forbes R. Powell, Peter W. Vedder, Joackim F. Lindblom and Stephen F. Powell, Optical Engineering, Vol. 29 No. 6 p.614-624 (1990)

[120] E.M. Gullickson, P. Denham, S. Mrowka and J.H. Underwood, Physical Review B, Vol. 49 No. 23 p.16283-16288 (1994)

[121] M. Shaw M.Sc. Thesis (unpublished) (1996)

[122] D.A. Verner, G.J. Ferland and K.T. Korista, Ap. J., Vol. 465 p. 487 (1996)

[123] S.S. Harilal, Riju C. Issac, C.V. Bindhu, V.P.N. Nampoori and C.P.G. Vallabhan, J. Appl. Phys., Vol. 81 No. 8 p.3637-3643 (1997)

[124] J. Dawson, P. Kaw and B. Green, The Physics of Fluids, Vol. 12 No. 4 p.875-882 (1969)

[125] E.T. Kennedy Ph.D. Thesis (unpublished) (1977)

[126] J. Thomas Knudtson, William B. Green and David G. Sutton, J. Appl. Phys., Vol. 61 No. 10 p.4771-4780 (1987)

[127] B. Angerlaud, C. Girault, C. Champeaux, F. Garrelie, C. Germain and A. Catherinot, Appl. Surf. Sci., Vol. 96-98 p.117-121 (1996)

[128] J.R. Parker, *Practical Computer Vision using C*, New York: Wiley (1994)

[129] A.A. Puterzky, D.B. Geohegan, G.E. Jellison Jr. and M.M. McGibbon, Appl. Surf. Sci., Vol. 96-98 p.859-865 (1996)

[130] David B. Geohegan and Alexander A. Puretzky, Appl. Phys. Lett., Vol. 67 No. 2 p.197-199 (1995)

[131] David B. Geohegan, Thin Solid Films, Vol. 220 p.138-145 (1992)

[132] András Kuthy, Nucl. Inst. and Meth., Vol. 180 p.7-16 (1981)

[133] W.T. Vetterling, S.A. Teukolsky, W.H. Press and B.P. Flannery, *Numerical Recipes in C: The Art of Scientific Computing 2nd Edition*, Cambridge; New York: Cambridge University Press (1992)

[134] Randall L. Eubank, *Spline Smoothing and Non-Parametric Regression*, New York: M. Dekker (1988)

[135] J.F. Reintjes, T.N. Lee, R.C. Eckardt and R.A. Andrews, J. Appl. Phys., Vol. 47 No. 10 p.4457-4463 (1976)

[136] S. Siano, G. Pacini, R. Pini and R. Salimbeni, AIP Conference Proceedings, Vol. 386 p.51-52 (1997)

[137] R.N. Campbell Ph.D Thesis (unpublished) (1986)

[138] E. Jannitti, P. Nicolosi and G. Tondello, Optics Communications, Vol. 50 No. 4 p.225-230 (1984)

[139] K.L. Bell and A.E. Kingston, J. Phys. B:Atom. Molec. Phys., Vol. 4 p.1308-1317 (1971)

[140] R.F. Reilmann and S.T. Manson, ApJS, Vol. 40 p. 815 (1979)

[141] E. Richard Cohen and Barry N. Taylor, The 1986 CODATA Recommended Values of the Fundamental Constants, Journal of the Research of the National Bureau of Standards, Vol. 92 No. 2 (1987)

Appendix A

A Note on Gaussian Profiles

The standard form for a Gaussian profile is given by

$$\phi_v = \frac{2}{\sqrt{\pi}\Delta}\exp\left[-4\left(\frac{v-v_o}{\Delta}\right)^2\right] \qquad \text{[A1.1]}$$

The Full Width at Half Maximum (FWHM) is found by setting $v = v_o$, so that

$\phi_{v=v_o} = \dfrac{2}{\sqrt{\pi}\Delta}$. At $\phi_v = \dfrac{1}{\sqrt{\pi}\Delta}$ (half the maximum value), $\exp\left[-4\left(\dfrac{v-v_o}{\Delta}\right)^2\right]$ must

equal $\dfrac{1}{2}$ so that

$$4\left(\frac{v-v_o}{\Delta}\right)^2 = Ln2$$

$$2\left(\frac{v-v_o}{\Delta}\right) = (Ln2)^{\frac{1}{2}}$$

$$2(v-v_o) = \Delta(Ln2)^{\frac{1}{2}} = \text{FWHM} \qquad \text{[A1.2]}$$

Substituting the FWHM for 2 x (HWHM) = 2Γ we get $\Delta = \dfrac{2\Gamma}{(Ln2)^{\frac{1}{2}}}$. Replacing Δ in

equation [A1.2] yields

$$\phi_v = \frac{2(Ln2)^{\frac{1}{2}}}{2\Gamma\sqrt{\pi}}\exp\left[-4\left(\frac{v-v_o}{\frac{2\Gamma}{(Ln2)^{\frac{1}{2}}}}\right)^2\right]$$

$$= \sqrt{\frac{\text{Ln2}}{\pi}} \frac{1}{\Gamma} \exp\left[-\text{Ln2}\left(\frac{\nu - \nu_o}{\Gamma}\right)^2\right] \qquad \text{[A1.3]}$$

Finally Replacing Γ with Δ_G results in equation [1.26].

Appendix B

Voigt Profile Generation using 'vs' function

a_L = 1.0 (amplitude)

pos = centre energy

gamma_L = 2.0 Δ_L (FWHM)

gamma_G = 2.0 Δ_G (FWHM)

x = *running variable*

```
double    vs(double    a_L,double    pos,double    gamma_L,double
gamma_G,double x)
{
  unsigned i;
  double A[4],B[4],C[4],D[4],V=0;
  const double sqrtln2=0.832554611;
  const double sqrtpi=1.772453851;
  double X=(x-pos)*2*sqrtln2/gamma_G;
  double Y=gamma_L*sqrtln2/gamma_G;


  A[0]=-1.2150; B[0]= 1.2359;
  A[1]=-1.3509; B[1]= 0.3786;
  A[2]=-1.2150; B[2]=-1.2359;
  A[3]=-1.3509; B[3]=-0.3786;
  C[0]=-0.3085; D[0]= 0.0210;
  C[1]= 0.5906; D[1]=-1.1858;
  C[2]=-0.3085; D[2]=-0.0210;
  C[3]= 0.5906; D[3]= 1.1858;

  for(i=0;i<=3;i++)
    V+=(C[i]*(Y-A[i])+D[i]*(X-B[i]))/(SQR(Y-A[i])+SQR(X-B[i]));

  return(gamma_L*a_L*sqrtpi*sqrtln2/gamma_G)*V;
}
```

Appendix C

System Specifications

The Stanford DG535 Delay Generator

Parameter	Range / Specification
Resolution	5 ps
Range	1000 s
Slew Rate	1 V / ns
Interface	GPIB
Accuracy	1500 ps + timebase error x delay
Timebase	25 ppm crystal oscillator
RMS Jitter	Ext. trigger to any output: 60 ps + delay x 10^{-8}
	T0 to any output: 50 ps + delay x 10^{-8}
Trig. Delay	Ext. trigger to T0 output: 85 ns
Ext. Trigger	Rate DC to $\dfrac{1}{(1\,\mu s + longest\,delay)}$
	Threshold $\pm$ 2.56 V_{DC}
	Impedence 1 MΩ + 40 pF or 50 Ω
Outputs	Load 50 Ω or high impedence
	Risetime ECL: 2 ns TTL: 3 ns
	Slew 1 V / ns
	Overshoot < 100 mV + 10% of pulse amplitude
Optional Outputs	On rear
	Adjustable to $\pm$ 35 V
	Width 1 μs
	Edge 2 $\rightarrow$ 3 ns

Laser Specifications

The second harmonic generation crystal (KD*P Type II) of the Nd:YAG laser used to pump the dye laser is kept in a temperature stabilised mount. As the crystal is hygroscopic, the temperature is generally maintained at 40° C to protect it from moisture. Temperature stability is essential, as the angle tuning of the crystal is extremely sensitive to small temperature variations.

165

Cyclops 152 Pyrometer

Model:	Minolta / LAND Cyclops 152 IR pyrometer
Measurement range:	600 → 3000 °C
Spectral response:	0.8 → 1.1 µm
Measurement Area at 1 m:	4.8 mm

(from Minolta / LAND Cyclops portable infrared thermometer catalogue)

The Emissivity of Tungsten

Temperature (K)	$\lambda = 0.8$ µm	$\lambda = 0.9$ µm	$\lambda = 1.0$ µm	$\lambda = 1.1$ µm
1600	0.431	0.413	0.39	0.366
1800	0.425	0.407	0.385	0.364
2000	0.419	0.401	0.381	0.361
2200	0.415	0.396	0.378	0.359
2400	0.408	0.391	0.372	0.355
2600	0.404	0.386	0.369	0.352
2800	0.400	0.383	0.367	0.352

(data taken from [1]).

Appendix D

Image Intensifier Specifications

Intensifier Details

Serial No.:	ICE-170-170
Diameter	18 mm
Photocathode	W (180 → 850 nm) S25
Phosphor	P43
Taper Magnification	1:1

Summary of System Test Data

Peak Quantum Efficiency of Photocathode:	16.6%
Minimum Spatial Resolution (FWHM)	< 80 μm
Specified Optical Gate (FWHM)[1]	5 ns
Irising at Specified Optical Gate[2]	0.25 ns
Minimum Optical Gate[3]	2.6 ns
Irising at Minimum Optical Gate	0.25 ns
Response Uniformity[4]	> 3.5%
EBI[5]	0.02 μlux

---

[1] Specified optical gate width (must be > 50% of CW gain).

[2] There is a time delay between the centre and the edge of the tube turning ON and OFF – the centre lags the edge. We define irising as the time delay between achieving 63% of final peak values in the centre compared to edge regions.

[3] Optical gate width for 20% of CW gain.

[4] RMS deviation from the average response of the ICCD in fully binned operation illuminated with uniform white light.

[5] Equivalent Background Illuminance. Measured with 10°C coolant circulating. The temperature of the photocathode follows the temperature of the ICCD head / coolant. EBI increases by ~x2 for 5°C increase in temperature.

Gain Settings

Setting	Relative Gain
0	0.1
1	0.6
2	2
3	4
4	11
5	16
6	23
7	30
8	94
9	100

Gating Characteristics

Gate I/P (TTL) (ns)	Optical Gate @ centre[6] (ns)	Intensity[7] (% of CW)	Optical Gate @ edge[8] (ns)	Intensity (% of CW)
10	2.62	31	2.73	31
11	3.28	48	3.35	47
12	3.46	71	3.59	70
13	3.72	92	3.79	90
14	4.14	100	4.18	100
15	4.80	100	4.87	100
16	5.46	100	5.51	100
17	6.09	100	6.17	100
18	6.84	100	6.88	100
19	7.70	100	7.83	100
20	8.83	100	8.85	100
21	10.22	100	10.25	100
22	11.40	100	11.40	100
23	12.20	100	12.26	100
24	14.44	100	14.60	100
25	14.76	100	14.83	100

Thereafter, subtract ~ 11 ns from TTL gate input pulse to calculate the optical width

---

[6] FWHM of optical gate averaged over central 100 pixels.

[7] Expressed as percentage of the signal level recorded with the same source but 100 ns gate width.

[8] FWHM of optical gate averaged over edge 100 pixels.

Appendix E

Dye Fluorescence Curves
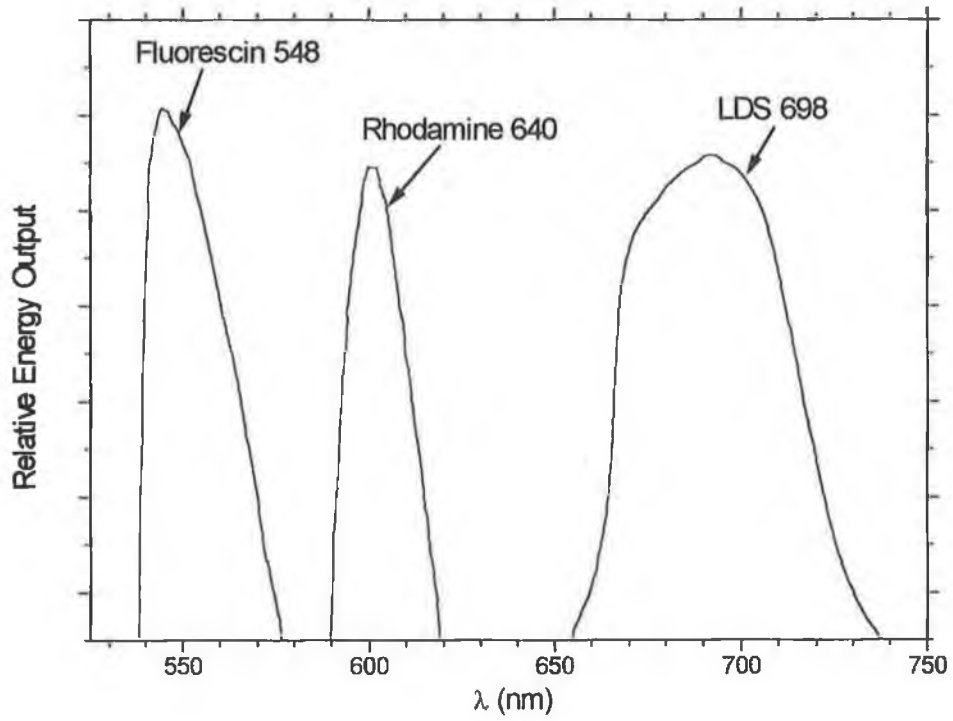
Appendix F

Varosi's IDL® Maximum Likelihood Deconvolution Code

max_likelihood.pro

```
;+
; NAME:
;     MAX_LIKELIHOOD
;
; PURPOSE:
;     Maximum likelihood deconvolution of an image or a
;     spectrum.
; EXPLANATION:
;     Deconvolution of an observed image (or spectrum) given
;       the instrument point spread response function (spatially
;       invariant psf).
;     Performs iteration based on the Maximum Likelihood
;       solution for the restoration of a blurred image (or
;       spectrum) with additive noise.
;     Maximum Likelihood formulation can assume Poisson noise
;       statistics or Gaussian additive noise, yielding two types
;       of iteration.
;
; CALLING SEQUENCE:
;       for i=1,Niter do Max_Likelihood, data, psf, deconv,
;         FT_PSF=psf_ft
;
; INPUTS PARAMETERS:
;     data = observed image or spectrum, should be mostly
;       positive, with mean sky (background) near zero.
;     psf = Point Spread Function of the observing instrument,
;           (response to a point source, must sum to unity).
; INPUT/OUTPUT PARAMETERS:
;     deconv = as input: the result of previous call to
;           Max_Likelihood,
;     (initial guess on first call, default = average of data),
;       as output: result of one more iteration by
;       Max_Likelihood.
;     Re_conv = (optional) the current deconv image reconvolved
;       with PSF for use in next iteration and to check
;       convergence.
;
; OPTIONAL INPUT KEYWORDS:
;       /GAUSSIAN causes max-likelihood iteration for Gaussian
;         additive noise
;     to be used,  otherwise the default is Poisson statistics.
;     FT_PSF = passes (out/in) the Fourier transform of the
;       PSF, so that it can be reused for the next time
;       procedure is called,
```

```
;          /NO_FT overrides the use of FFT, using the IDL function
;          convol() instead.
;          POSITIVITY_EPS = value of epsilon passed to function
;          positivity,
;                     default = -1 which means no action (identity).
;          UNDERFLOW_ZERO = cutoff to consider as zero, if numbers
;          less than this.
;
; EXTERNAL CALLS:
;     function convolve( image, psf ) for convolutions using
;          FFT or otherwise.
;     function positivity( image, EPS= ) to make image
;          positive.
;
; METHOD:
;     Maximum Likelihood solution is a fixed point of an
;     iterative eq.
;     (derived by setting partial derivatives of
;     Log(Likelihood) to zero).
;     Poisson noise case was derived by Richardson(1972) &
;     Lucy(1974).
;     Gaussian noise case is similar with subtraction instead
;     of division.
; HISTORY:
;     written: Frank Varosi at NASA/GSFC, 1992.
;     F.V. 1993, added optional arg. Re_conv (to avoid doing it
;     twice).
;-

pro Max_Likelihood, data, psf, deconv, Re_conv, FT_PSF=psf_ft,
NO_FT=noft, $
                              GAUSSIAN=gaussian, $
                              POSITIVITY_EPS=epsilon, $
                              UNDERFLOW_ZERO=under

     if N_elements( deconv ) NE N_elements( data ) then begin
          deconv = data
          deconv(*) = total( data )/N_elements( data )
          Re_conv = 0
     endif

     if N_elements( under ) NE 1 then under = 1.e-22
     if N_elements( epsilon ) NE 1 then epsilon = -1

     if N_elements( Re_conv ) NE N_elements( deconv ) then $
          Re_conv = convolve( positivity( deconv, EPS=epsilon
), psf, $
                              FT_PSF=psf_ft, NO_FT=noft )

     if keyword_set( gaussian ) then begin

          deconv = deconv + convolve( data - Re_conv, psf,
/CORREL, $
                              FT_PSF=psf_ft, NO_FT=noft )
     endif else begin

          wp = where( Re_conv GT under, npos)
```

171

```
              wz = where( Re_conv LE under, nneg)
              if    (npos    GT     0)    then    Re_conv(wp)    =    (
data(wp)/Re_conv(wp) ) > 0
              if (nneg GT 0) then Re_conv(wz) = 1

              deconv   =   deconv   *   convolve(   Re_conv,   psf,
FT_PSF=psf_ft, $
                                          /CORREL, NO_FT=noft )
         endelse

    if N_params() GE 4 then $
         Re_conv = convolve( positivity( deconv, EPS=epsilon
), psf, $
                                  FT_PSF = psf_ft, NO_FT = noft
)
 end
```

convolve.pro

```
function convolve,  image, psf, FT_PSF=psf_FT,  FT_IMAGE=imFT,
NO_FT=noft, $
                 CORRELATE=correlate, AUTO_CORRELATION=auto
;+
; NAME:
;     CONVOLVE
; PURPOSE:
;     Convolution  of  an  image  with  a  Point  Spread  Function
(PSF)
; EXPLANATION:
;     The  default  is  to  compute  the  convolution using a product
of
;     Fourier transforms (for speed).
;
; CALLING SEQUENCE:
;
;     imconv = convolve( image1, psf, FT_PSF = psf_FT )
;   or:
;     correl = convolve( image1, image2, /CORREL )
;   or:
;     correl = convolve( image, /AUTO )
;
; INPUTS:
;     image = 2-D array (matrix) to be convolved with psf
;     psf = the Point Spread Function, (size < or = to size of
image).
;
; OPTIONAL INPUT KEYWORDS:
;
;     FT_PSF = passes out/in the Fourier transform of the PSF,
;            (so that it can be re-used the next time function
is called).
;     FT_IMAGE = passes out/in the Fourier transform of image.
```

172

```
;
;      /CORRELATE uses the conjugate of the Fourier transform of
PSF,
;              to compute the cross-correlation of image and PSF,
;              (equivalent  to  IDL  function  convol()  with  NO
rotation of PSF)
;
;      /AUTO_CORR  computes  the  auto-correlation  function  of
image using FFT.
;
;      /NO_FT  overrides  the  use  of  FFT,  using  IDL  function
convol() instead.
;              (then PSF is rotated by 180 degrees to give same
result)
; METHOD:
;      When using FFT, PSF is centered & expanded to size of
image.
; HISTORY:
;      written, Frank Varosi, NASA/GSFC 1992.
;-
      sp = size( psf_FT )  &  sif = size( imFT )
      sim = size( image )  &  sc = sim/2  &  npix = N_elements(
image )

      if (sim(0) NE 2) OR keyword_set( noft ) then begin
          if keyword_set( auto ) then begin
                message,"auto-correlation only for images with
FFT",/INF
                return, image
            endif else if keyword_set( correlate ) then $
                    return, convol( image, psf ) $
                else return, convol( image, rotate( psf, 2 )
)
        endif

      if (sif(0) NE 2) OR (sif(sif(0)+1) NE 6) OR $
          (sif(1) NE sim(1)) OR (sif(2) NE sim(2)) then imFT =
FFT( image,-1 )

      if keyword_set( auto ) then $
       return, shift( npix*float( FFT( imFT*conj( imFT ),1 ) ),
sc(1),sc(2) )

      if (sp(0) NE 2) OR (sp(sp(0)+1) NE 6) OR $
          (sp(1) NE sim(1)) OR (sp(2) NE sim(2)) then begin
            sp = size( psf )
            if (sp(0) NE 2) then begin
                message,"must  supply  PSF  matrix  (2nd
arg.)",/INFO
                return, image
              endif
            Loc = ( sc - sp/2 ) > 0           ;center PSF in new
array,
            s = (sp/2 - sc) > 0        ;handle all cases: smaller
or bigger
            L = (s + sim-1) < (sp-1)
            psf_FT = complexarr( sim(1), sim(2) )
```

```
            psf_FT( Loc(1), Loc(2) ) = psf( s(1):L(1),
s(2):L(2) )
            psf_FT = FFT( psf_FT, -1, /OVERWRITE )
        endif

    if keyword_set( correlate ) then $
        conv = npix * float( FFT( imFT * conj( psf_FT ), 1
) ) $
    else      conv = npix * float( FFT( imFT * psf_FT, 1 ) ) )

    sc = sc + (sim MOD 2) ;shift correction for odd size
images.

return, shift( conv, sc(1), sc(2) )
end
```

positivity.pro

```
function positivity, x, DERIVATIVE=deriv, EPSILON=epsilon
;+
; NAME:
;     POSITIVITY
; PURPOSE:
;     Map an image uniquely and smoothly into all positive
values.
; EXPLANATION:
;     Take unconstrained x (usually an image), and map it
uniquely and
;     smoothly into positive values.   Negative values of x get
mapped to
;     interval ( 0, sqrt( epsilon )/2 ], positive values go to
;     ( sqrt( epsilon )/2, oo ) with deriv approaching 1.
Derivative is
;     always 1/2 at x=0.    Derivative is used by the MRL
deconvolution
;     algorithm.
;
; CALLING SEQUENCE:
;     result = POSITIVITY( x, [ /DERIVATIVE, EPSILON = )
;
; INPUTS:
;     x - input array, unconstrained
;
; OUTPUT:
;     result =  output array = ((x + sqrt(x^2 + epsilon))/2
;          if the /DERIV keyword is set then instead the
derivative of
;          the above expression with respect to X is returned
;
; OPTIONAL INPUT KEYWORDS:
;     DERIV - if this keyword set, then the derivative of the
positivity
;          mapping is returned, rather than the mapping itself
```

174

```
;       EPSILON - real scalar specifying the interval into which
to map
;            negative values.       If EPSILON EQ 0 then the
mapping reduces to
;            positive truncation.      If EPSILON LT then the
mapping reduces to
;            an identity (no change).  Default is EPSILON = 1e-9
;
; REVISION HISTORY:
;       F.Varosi NASA/GSFC 1992, as suggested by R.Pina UCSD.
;-

        if N_elements( epsilon ) NE 1 then epsilon = 1.e-9

        if keyword_set( deriv ) then begin
            if (epsilon GT 0) then return,(1 + x/sqrt( x^2 +
epsilon ))/2 $
                            else if (epsilon LT 0) then return,(1)
$
                            else return,( x GT 0 )
        endif else begin
            if (epsilon GT 0) then return,( x + sqrt( x^2 +
epsilon ) )/2 $
                            else if (epsilon LT 0) then return, x
$
                            else return,( x > 0 )
        endelse
end
```

175

Appendix G

Table Of Symbols

Symbol	Description	SI Units	Introduced
σ'	Conductivity	mhos m^{-1}	[1.1]
δ	Skin depth	m	[1.1]
C_o	Constant (depends on p)	m s^{-p}	[1.10]
N_e	Electron density	m^{-3}	§1.1
p	Constant (> 0.4)		[1.10]
T_e	Electron temperature	K	§1.1
T_i	Ion temperature	K	§1.1
β	Slowing coefficient	s^{-1}	[1.11]
v_o	velocity at time t=0	m s^{-1}	[1.11]
x_f	Stopping Distance	m	[1.11]
υ	Viscosity	kg s^{-1} m^{-1}	[1.12]
d_ϕ	Cross sectional diameter	m	[1.12]
R_n	Reynold's number		[1.12]
β'	Non-viscous model slowing coefficient	m^{-1}	[1.13]
dn_v	The number of electrons with velocities between v and v + dv		[1.14]
$\chi(i,k)$	Energy different between lower and upper levels	J	[1.15]
g	Statistical weight		[1.15]
i	Denotes lower level		[1.15]
k	Denotes upper level		[1.15]
$\chi(Z-1)$	Ionisation energy	J	[1.16]
α_r	Radiative recombination coefficient	m^3 s^{-1}	[1.18]
S	Collisional ionisation coefficient	m^3 s^{-1}	[1.18]
α_{3b}	Coefficient for three-body recombination	s^{-1}	[1.19]
δ'	Penetration depth	m	[1.2]
κ_D	Thermal diffusivity	m^2 s^{-1}	[1.2]
A_{ki}	Einstein A coefficient for spontaneous emission	s^{-1}	[1.20]
t_p	Laser pulse duration (FWHM)	s	[1.2]

Symbol	Description	Units	Ref
B_{ik}	Einstein B coefficient for absorption	$m^3\ J^{-1}\ s^{-2}$	[1.21]
B_{ki}	Einstein B coefficient for stimulated emission	$m^3\ J^{-1}\ s^{-2}$	[1.21]
f_{ik}	Absorption oscillator strength		[1.22]
ϕ_v	Atomic frequency response	s^{-1}	[1.24]
Δ_L	Lorentzian HWHM	s^{-1}	[1.25]
Δ_G	Gaussian HWHM	s^{-1}	[1.26]
C_n	Normalisation constant		[1.27]
E	Energy	J	[1.34]
ε_v	Emission coefficient		[1.29]
ρ_o	Density	$kg\ m^{-3}$	[1.3]
C	Specific heat	$J\ K^{-1}\ kg^{-1}$	[1.3]
R	Reflectance		[1.3]
T	Temperature	K	[1.3]
T_o	Initial temperature	K	[1.3]
f_c	Oscillator strength for the whole continuum associated with absorption from a level m		[1.32]
S_L	Series limit		[1.32]
$\sigma_m(v)$	Cross section	m^2	[1.33]
I_v	Frequency dependent intensity	$J\ s^{-1}$	[1.34]
ω	Frequency	radians	[1.4]
λ	Wavelength	m	[1.4]
a	Acceleration	$m\ s^{-2}$	§1.2.2
n	Real part of refractive index		[1.4]
N_{ec}	Critical electron density	m^{-3}	[1.4]
C_{int}	Integration constant	$J\ s^{-1}$	[1.40]
I_{v_o}	Intensity of back lighting radiation	$J\ s^{-1}$	[1.42]
a_r	Constant of proportionality	$m^{-1/2}\ s^{-1}$	[1.45]
τ	Transition Lifetime	s	[1.46]
ΔE	Energy spread	J	[1.46]
$\Delta\lambda_{D_{1/2}}$	Doppler width (FWHM)	m	[1.48]
μ	atomic mass	kg	[1.49]
γ	Ratio of specific heats		[1.5]
$\Delta\lambda_{1/2}$	Quasistatic FWHM of Stark broadened line	m	[1.50]
N_D	Number of particles in a Debye sphere		[1.50]
n_i	Principal quantum number of lower level		[1.50]

Symbol	Description	Units	Equation
n_j	Principal quantum number of upper level		[1.50]
Z_e	Nuclear charge		[1.50]
Z_p	Ionic charge		[1.50]
$\Delta\lambda_{\frac{1}{2}_{impact}}$	Impact FWHM of Stark broadened line	m	[1.52]
A	Stark broadening coefficient		[1.52]
D	Stark broadening coefficient	m	[1.52]
W	Stark broadening coefficient	m	[1.52]
$\Delta\lambda_{shift}$	Impact approximation Stark shift	m	[1.53]
$I_{(x,y)}$	Pixel intensity		[1.54]
$i(r)$	Spectrally integrated emission coefficient		[1.55]
$\tilde{n}$	Complex refractive index		[1.59]
ζ	Spectral width of resonance line	m	[1.59]
ω_o	Centre frequency	radians	[1.59]
K	Constant in self-similar expansion model	s^{-1}	[1.6]
n_e	Free electron contribution to the refractive index		[1.59]
v	Velocity	$m\ s^{-1}$	[1.6]
ω_p	Plasma frequency	radians	[1.60]
p_r	Impact parameter of a ray		[1.62]
$\dfrac{d^2X}{dt^2}$ $\dfrac{d^2Y}{dt^2}$ $\dfrac{d^2Z}{dt^2}$	X, Y, Z accelerations	$m\ s^{-2}$	[1.7]
$\dfrac{dX}{dt}\ \dfrac{dY}{dt}$ $\dfrac{dZ}{dt}$	X, Y, Z velocities	$m\ s^{-1}$	[1.7]
M	atomic weight	kg	[1.7]
m_u	Atomic mass unit	kg	§1.5.2
$X(t), Y(t), Z(t)$	X, Y, Z co-ordinates as a function of time	m	[1.7]
κ	Imaginary part of refractive index		§1.6.2
τ_v	Frequency dependent optical depth		§1.4.2
λ_D	Debye length	m	§1.5.3

Symbol	Description	Units	Reference
β_r	The entrance angle of a ray	radians	§1.6.2
α_r	The exit angle of a ray	radians	§1.6.2
d	The fringe thickness	m	§1.6.2
i_r	The instantaneous angle that the tangent to a ray makes with the vector r	radians	§1.6.2
L	The plasma-detector separation	m	§1.6.2
N_p	Perturber density	m^{-3}	§1.5.3
P_1, P_2, P_3	The entrance, turning and exit points of a ray		§1.6.2
R_f	The distance from the target to the central maximum of a fringe	m	§1.6.2
r_i	The distance r for which the angle $i_r = \dfrac{\pi}{2}$	m	§1.6.2
R_o	The plasma radius (OEPR)	m	§1.6.2
X_o, Y_o, Z_o	initial orthogonal edges of the plasma after termination of the laser pulse	m	[1.8]
λ_o	Centre wavelength	m	§1.4.3
A_z	Constant	$m^3\,s^{-1}$	§1.4.3
E_B	Laser energy that contributes to blast wave	J	[1.9]
L_c	Length of plasma chord	m	§1.4.3
R_p	Plasma radius	m	§1.4.3
t	Time	s	[1.9]
t_s	Boundary condition: Time	s	[1.9]
I_s	Fractional component of scattered light on I_v		[2.10]
M'_f	Measured transmission		[2.10]
γ_c	Gamma correction		[2.1]
G	Gray level		[2.1]
I_T	True Intensity	$W\,m^{-2}$	[2.1]
μ_s	σ_s^2		[2.2]
σ_s	Standard deviation		[2.3]
ν, ν'	Frequency	Hz	[1.1], [1.27]
κ_v	Absorption coefficient	m^{-1}	§1.1, [1.30]
$\Delta\lambda$	Wavelength interval	m	[2.4]
d_g	Inter-groove spacing	m	[2.4]
I	Laser irradiance	$J\,s^{-1}\,m^{-2}$	§1.1, [1.3]
R_g	Radius of curvature of the grating	m	[2.4]

Symbol	Description	Units	Reference
W_s	Slit width	m	[2.4]
μ_{abs}	Linear absorption coefficient	cm^{-1}	§2.3.2(e)
$\alpha_n(L_{n-1})$	A relaxation parameter which results in the Jannson deconvolution algorithm being inherently non-linear		[2.5]
L_{n-1}	The n-1th estimate of L, the true spectrum		[2.5]
σ_{mean}	Mean standard deviation		[2.6]
$J(i)$	i[th] data point using Jannson's deconvolution algorithm		[2.6]
N	Number of data points		[2.6]
$V(i)$	i[th] data point using Varosi's maximum likelihood deconvolution technique		[2.6]
$\sigma(v)$	Cross section	m^2	[1.31]
v_o	Centre frequency	s^{-1}	§1.4.1, [1.25]
I_{o_s}	Scattered light contribution on I_{v_o}		[2.7]
$I_{v_o TRUE}$	True I_{v_o} in the absence of scattered light		[2.7]
M_f	Measured fractional transmittance		[2.7]
T_f	True fractional transmittance (i.e. in the absence of any scattered light)		[2.7]
$I_{v TRUE}$	True I_v in the absence of scattered light		[2.8]
$F_{(row,col)}$	A weighting factor		[3.1]
C_x	The x co-ordinate of the centre of mass		§3.1.1
r, y, z	Spatial coordinates	m	[1.5], §1.4.3

Appendix H

Table of Constants

Data taken from [141]:

Symbol	Description	Value	Units	Relative uncertainty (ppm)
h	Planck constant	6.6260755(40)	10^{-34} J s	0.60
$\hbar$	$h/2\pi$	1.05457266(63)	10^{-34} J s	0.60
μ_o	Permeability of vacuum	12.566370614... $=4\pi \times 10^{-7}$	10^{-7} N A^{-2}	exact
ε_o	Permittivity of free vacuum	8.854187817...	10^{-12} F m^{-1}	exact
c	Speed of light in vacuum	299792458	m s^{-1}	exact
e	Elementary charge	1.60217733(49)	10^{-19} C	0.30
k_B	Boltzmann constant	1.380658(12)	10^{-23} J K^{-1}	8.5
m_e	Electron mass	9.1093897(54)	10^{-31} kg	0.59
m_u	Atomic mass unit	1.6605402(10)	10^{-27} kg	0.59

Appendix I

List of Tables

List of Figures

185

10^{24} m^{-3}, $N_e(r) = 1 \times 10^{25}$ cm^{-3}, $f_{ik} = 0.75$, $\lambda_o = 670.78$ nm). Also shown is the electronic contribution, n_e, to the plasma refractive index.

186

plasma (broadband) in vacuum.

R_o, of the plasma in (c) was 59 μm.